Développement de sources supercontinuum et applications biomédicales

Philippe Leproux

Université de Limoges

HABILITATION A DIRIGER DES RECHERCHES

Spécialité : Biophotonique

Présentée et soutenue publiquement le 19 décembre 2023 par

Philippe LEPROUX

Développement de sources supercontinuum et applications biomédicales

Chargé de suivi : **Philippe ROY**

Composition du jury

Rapporteurs
Marie-Claire SCHANNE-KLEIN, DR CNRS, LOB, Ecole Polytechnique
Sophie LECOMTE, DR CNRS, CBMN, Université de Bordeaux
Arnaud MUSSOT, Prof. Université de Lille, PhLAM

Examinateurs
Olivier PIOT, Prof. Université de Reims Champagne-Ardenne, BioSpecT
Éric CHAMPION, Prof. Université de Limoges, IRCER
Catherine YARDIN, PU-PH Université de Limoges, Chef de service CHU
Philippe CARRÉ, Prof. Université de Poitiers, XLIM-ASALI
Philippe ROY, DR CNRS, XLIM-Photonique, Université de Limoges

Invités
Denis BARATAUD, Prof. Université de Limoges, XLIM-SRF
Guillaume HUSS, PhD, CEO LEUKOS SAS

Table des matières

Introduction 5

Partie 1 - Architectures de sources supercontinuum à fibre microstructurée 7

I. Positionnement 7

II. Utilisation d'une double excitation 532/1064 nm 8

III. Exploitation du mélange à quatre ondes intermodal 12

IV. Combinaison de l'amplification et de la non-linéarité 15

Synthèse Partie 1 avec indicateurs 19

Publications majeures Partie 1 22

Partie 2 - Développement de sources supercontinuum dédiées à des applications biomédicales ... 43

I. Contexte 43

II. Source déclenchée pour la cytométrie en flux 44

III. Source optimisée pour la tomographie optique cohérente 48

IV. Emission dans les fenêtres biologiques pour l'imagerie à travers un tissu épais 49

V. Source à double sortie pour la microspectroscopie CARS 51

Synthèse Partie 2 avec indicateurs 57

Publications majeures Partie 2 60

Partie 3 - Microspectroscopie non linéaire multimodale sous excitation supercontinuum 77

I. Développement instrumental centré sur la microspectroscopie CARS 77

II. Application à l'imagerie d'échantillons biologiques sans marquage 80

III. Nouvelles approches de traitement et analyse de données hyperspectrales CARS 85

IV. Mise en place d'une chaîne complète pour l'étude d'un dispositif biocéramique 91

Synthèse partie 3 avec indicateurs 94

Publications majeures Partie 3 98

Conclusion et perspectives 127

Bibliographie 129

Liste des publications 132

Annexe 1 : liste des conférences invitées 139

Annexe 2 : liste des actes de congrès 141

Annexe 3 : bilan de la production scientifique 144

Annexe 4 : bilan des contrats de recherche 145

Annexe 5 : activités d'enseignement 148

Introduction

Depuis ma nomination en 2002, mes travaux de recherche portent sur le développement de sources supercontinuum et sur leurs applications biomédicales. Ces sources optiques particulières permettent de combiner la qualité de faisceau d'un laser (cohérence spatiale) avec la largeur spectrale d'une lampe incohérente (halogène, arc au xénon), d'où la dénomination de « laser blanc ». Si le principe de génération d'un supercontinuum de lumière date de 1970 [Alfano & Shapiro, 1970], ce n'est qu'au début des années 2000 qu'apparaissent les premiers dispositifs portables, en corrélation avec le développement des fibres optiques microstructurées. Ainsi, l'architecture standard d'une source supercontinuum se compose d'un laser impulsionnel monochromatique (laser dit de pompe) injecté dans une fibre microstructurée, dans laquelle est généré, grâce à la forte puissance crête couplée, un ensemble de phénomènes non linéaires (automodulation de phase, modulation de phase croisée, mélange à quatre ondes, instabilité de modulation, diffusion Raman stimulée, effets solitoniques, etc.). L'onde optique recueillie à la sortie de la fibre se caractérise alors par un spectre continu, plus ou moins large, plus ou moins plat, en fonction des caractéristiques de la fibre (taille du cœur, proportion d'air, longueur, etc.) et de celles du laser de pompe (longueur d'onde, puissance crête, durée d'impulsion, etc.).

Dans ce cadre, je me suis tout d'abord attaché à **proposer de nouvelles architectures de sources supercontinuum** visant à en améliorer les performances (couverture/planéité spectrale, puissance moyenne) tout en maximisant la compacité du système. Cette activité, qui fait l'objet de la **Partie 1** de ce manuscrit, s'est fortement appuyée sur le savoir-faire présent à XLIM en matière de design et fabrication de fibres optiques microstructurées. En ce qui concerne le laser de pompe, j'ai majoritairement travaillé avec des microlasers, émettant des impulsions de durée sub-nanoseconde, afin de prendre en compte la question de la compacité au regard du potentiel applicatif de ces sources laser large bande. Les performances et l'originalité des architectures de sources supercontinuum introduites m'ont amené à prendre activement part à un projet de transfert de technologie vers l'industrie, me conduisant à cofonder la start-up LEUKOS en 2006 en compagnie de Guillaume Huss, alors post-doctorant au laboratoire.

La nécessité de concevoir des sources supercontinuum répondant aux besoins d'applications particulières, notamment dans le domaine biomédical, est vite apparue. Pour adresser efficacement cette problématique, je me suis naturellement tourné vers des partenaires possédant une expertise dans les champs applicatifs visés, comme l'imagerie cellulaire/tissulaire sans marquage ou l'analyse cellulaire en flux. Ensemble, nous avons pu démontrer des applications innovantes des sources supercontinuum (le système d'imagerie ou d'analyse étant développé chez le partenaire). À cet égard, la création de la société LEUKOS a été bénéfique, dans la mesure où des solutions supercontinuum intégrées et opérationnelles pouvaient être régulièrement testées sur les dispositifs applicatifs des partenaires. **Dans la Partie 2, nous présentons quatre problématiques d'applications biomédicales ayant donné lieu au développement de sources supercontinuum dédiées en collaboration avec les partenaires correspondants.** Les applications concernées sont la cytométrie en flux, la tomographie optique

cohérente, l'imagerie à travers un tissu épais et enfin la microspectroscopie CARS (*coherent anti-Stokes Raman scattering*).

Enfin, c'est dans la continuité de ces projets partenariaux que j'ai par la suite proposé de développer au sein même du laboratoire XLIM une activité allant des sources supercontinuum jusqu'aux systèmes d'imagerie, en capitalisant sur une collaboration historique avec le Japon (universités de Tokyo, Tsukuba, Kyushu). **Cette activité, introduite dans la Partie 3, porte plus précisément sur la micro(spectro)scopie non linéaire multimodale sous excitation supercontinuum, avec comme modalité centrale la diffusion Raman anti-Stokes cohérente (CARS).** Nous en décrivons tout d'abord le développement instrumental correspondant et l'application à l'imagerie d'échantillons biologiques sans marquage, puis nous présentons de nouvelles approches de traitement et analyse de données hyperspectrales en cours de développement avec les chercheurs de l'axe ASALI d'XLIM. Enfin, la mise en place d'une chaîne complète d'imagerie (acquisition, traitement et analyse des données), également en cours, est proposée et discutée, dans un contexte applicatif lié à l'étude d'un dispositif biocéramique implantable en collaboration avec l'équipe « Biomatériaux » de l'IRCER.

Pour chacune des trois thématiques décrites ci-dessus, nous avons sélectionné dans ce manuscrit les résultats les plus marquants afin de donner une vision la plus synthétique possible des activités de recherche correspondantes. Dans la conclusion finale, nous revenons sur le projet de recherche actuel et nous en décrivons quelques perspectives.

Partie 1 - Architectures de sources supercontinuum à fibre microstructurée

I. Positionnement

Au début des années 2000, l'équipe « Optique guidée et intégrée » (OGI) de l'Institut de Recherche en Communications Optiques et Microondes (IRCOM, UMR CNRS 6615) est fortement positionnée sur le design et la fabrication de fibres optiques microstructurées ou fibres à cristal photonique (PCF pour *photonic crystal fibers*) [Knight *et al.*, 1996]. Ayant pris part à certains développements de ce type de fibre au sein de l'équipe OGI [2,6], je commence à collaborer avec l'équipe « Optique non linéaire » (ONL) de l'IRCOM sur la propagation non linéaire dans les PCF. C'est dans ce contexte que naît à Limoges une thématique autour de la génération de supercontinuum, associant les savoir-faire complémentaires des deux équipes d'optique. Ainsi, **le premier élément de positionnement de cette nouvelle thématique consiste à proposer - et fabriquer localement - des designs originaux de PCF** (dites « non linéaires » en raison de la faible taille du cœur) afin d'exploiter des mécanismes de propagation non linéaire particuliers.

Par ailleurs, le renouveau apporté par les PCF au domaine de la génération de supercontinuum, diffusé largement à travers des articles comme celui de [Ranka *et al.*, 2000], engendre une envolée du nombre de publications sur le sujet (**Figure 1**). Ces nombreux travaux concernent tant l'optimisation des designs de fibre que l'utilisation de régimes laser différents : **femtoseconde** [Dudley & Coen, 2002 ; Herrmann *et al.*, 2002 ; Gaeta, 2002 ; Hilligsøe *et al.*, 2004], **picoseconde** [Coen *et al.*, 2001 ; Coen *et al.*, 2002 ; Travers *et al.*, 2005], **(sub)nanoseconde** [Provino *et al.*, 2001 ; Wadsworth *et al.*, 2004 ; Leon-Saval *et al.*, 2004] et même **continu** [Avdokhin *et al.*, 2003 ; Kudlinski & Mussot, 2008 ; Travers *et al.*, 2008] (cette sélection de références n'étant aucunement exhaustive). Dans ce cadre, et devant l'intérêt grandissant pour les sources supercontinuum et leur potentiel applicatif, nous faisons le choix de privilégier la **compacité** et la **simplicité** des systèmes développés. **Notre second élément de positionnement consiste ainsi à utiliser majoritairement des microlasers (*microchip lasers*) sub-nanoseconde comme source de pompe.**

Nous présentons ci-après trois exemples majeurs d'architectures de source supercontinuum introduites dans le cadre de cette stratégie de positionnement.

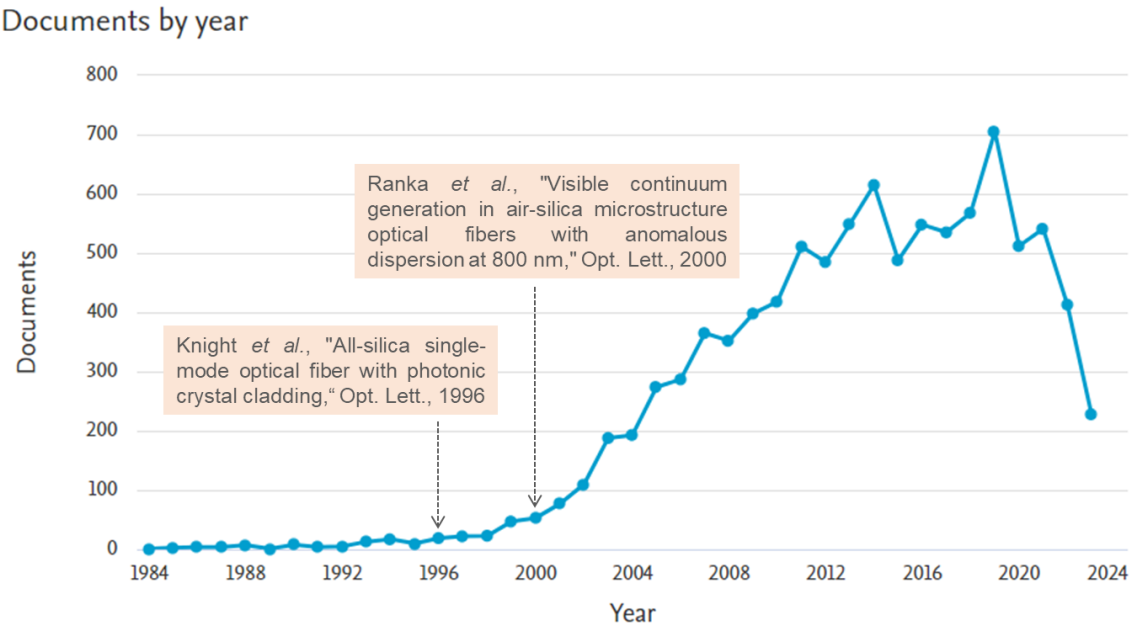

Figure 1 : Nombre de documents publiés par an sur la thématique « supercontinuum » (données fournies par Scopus). Mise en évidence de l'introduction des PCF en 1996 [Knight *et al.*, 1996] et de la génération d'un supercontinuum visible dans une PCF [Ranka *et al.*, 2000].

II. Utilisation d'une double excitation 532/1064 nm

Cette architecture s'inspire de travaux antérieurs menés à l'IRCOM par Alain Barthélémy et Claude Froehly sur l'interaction par modulation de phase croisée (XPM) de faisceaux pompe et sonde de longueurs d'onde différentes dans un milieu Kerr homogène [De La Fuente *et al.*, 1991]. Il s'agit dans notre cas de pomper une PCF de part et d'autre de la longueur d'onde de dispersion nulle (ZDW) du mode fondamental (LP_{01}) [7]. Ce double pompage est mis en œuvre aux longueurs d'onde de 1064 et 532 nm grâce à l'utilisation d'un microlaser Nd:YAG sub-nanoseconde doublé en fréquence (**Figure 2a**). La fibre microstructurée air-silice, conçue et fabriquée au laboratoire, présente un diamètre moyen de trou $d \simeq 1{,}5$ µm et un espacement entre trous $\Lambda \simeq 2{,}2$ µm, résultant en un rapport $d/\Lambda \simeq 0{,}68$ et une ZDW $\simeq 870$ nm pour le mode LP_{01} (**Figures 2b, 2c**). Cette fibre, légèrement multimode, peut guider les modes LP_{01} et LP_{11}. Aussi, dans l'expérience introduite ici, l'injection du laser est réalisée de façon à exciter majoritairement le mode fondamental.

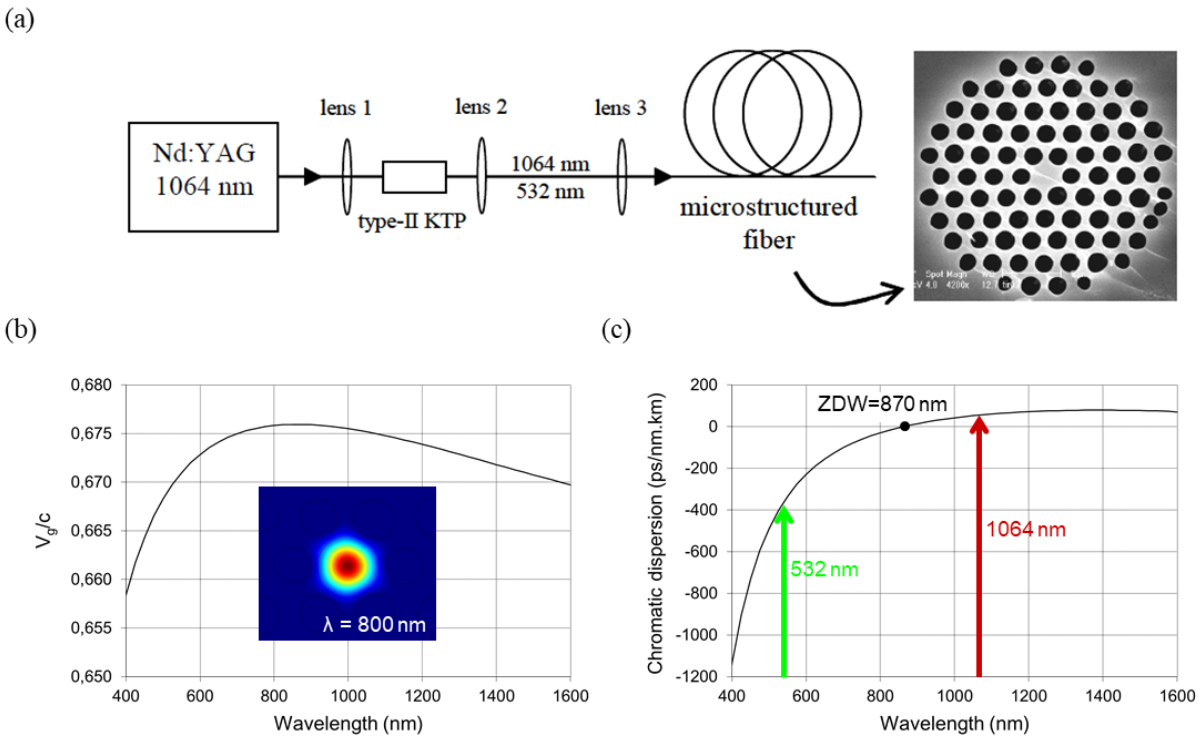

Figure 2 : (a) Montage expérimental pour la génération de supercontinuum par double pompage dans une PCF (image MEB associée, d ≃ 1,5 µm, Λ ≃ 2,2 µm). (b) Courbe de vitesse de groupe (normalisée par la vitesse de la lumière dans le vide) calculée pour le mode fondamental de la PCF (encart : distribution transversale d'énergie calculée à λ = 800 nm). (c) Courbe de dispersion chromatique correspondante, faisant apparaître une dispersion nulle à 870 nm. Figure adaptée à partir de [7].

Lorsque la radiation de pompe verte est injectée seule dans la fibre, le phénomène de diffusion Raman stimulée (SRS) est le mécanisme non linéaire prédominant du fait du régime de dispersion fortement normal à 532 nm. Une cascade Raman vers les hautes longueurs d'onde est clairement observée dans ce cas (**Figure 3a**). Lorsque les radiations de pompe verte et infrarouge sont injectées simultanément dans la fibre, on obtient cette fois-ci, dans le domaine visible, un élargissement spectral homogène de part et d'autre de la pompe à 532 nm, couvrant la plage 400-700 nm (**Figure 3b**). Dans le domaine infrarouge, on observe une extension spectrale régulière vers les hautes longueurs d'onde à partir de la pompe à 1064 nm (**Figure 3c**).

Afin d'élucider le mécanisme non linéaire à l'origine de l'élargissement spectral dans le visible, différentes expériences ont été réalisées, prenant en compte la puissance crête injectée dans la PCF à 532 nm (P_{532}) et 1064 nm (P_{1064}), ainsi que la longueur de la fibre (**Figure 4**) [14]. Nous listons ces expériences ci-après, ainsi que les principales observations et conclusions correspondantes.

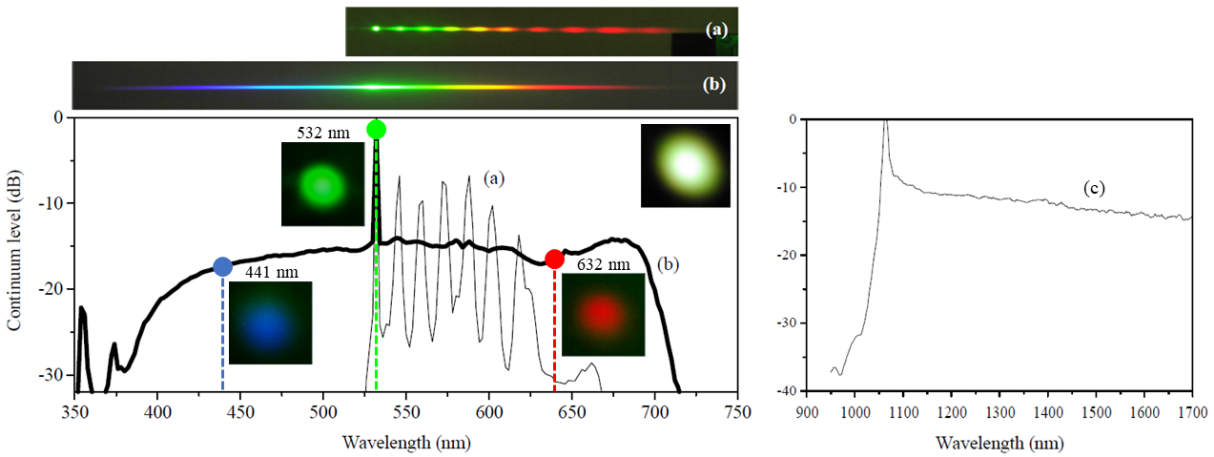

Figure 3 : Génération de supercontinuum dans une PCF dans le cas (a) du pompage unique à 532 nm et (b,c) du double pompage à 532/1064 nm. Dans chaque cas, une photographie du faisceau visible diffracté par un réseau et le spectre correspondant sont présentés. Dans le cas du double pompage, la distribution transversale d'énergie (figure de champ lointain) est mise en évidence à 441, 532 et 632 nm, ainsi que sur la totalité du domaine visible, et le spectre mesuré dans le domaine infrarouge (c) est également exposé. Figure adaptée à partir de [7].

(1) Étude de l'élargissement spectral en fonction de P_{1064} avec P_{532} fixée à 200 W (Figure 4a) : lorsque P_{1064} augmente, le spectre infrarouge s'étend progressivement vers les hautes longueurs d'onde sous l'impact du phénomène initial d'instabilité de modulation (MI) et des effets solitoniques en présence de gain Raman et en régime de dispersion anormale ; le spectre visible s'étend dans un premier temps vers les hautes longueurs d'onde ($P_{1064} < 2$ kW), puis vers les basses longueurs d'onde ($P_{1064} > 2$ kW). Or, on observe que pour $P_{1064} \sim 2$ kW, l'extension spectrale dans l'infrarouge atteint une longueur d'onde d'environ 1400 nm, pour laquelle la vitesse de groupe égale celle de la pompe à 532 nm (voir la **Figure 2b**). En d'autres termes, les ondes solitoniques infrarouges avec $\lambda < 1400$ nm (respectivement, $\lambda > 1400$ nm) se propagent plus rapidement (respectivement, plus lentement) que l'onde à 532 nm. C'est donc la différence de vitesse de groupe entre les solitons infrarouges et la pompe verte qui gouverne l'élargissement spectral autour de cette dernière. Cette observation est fortement compatible avec l'hypothèse de l'effet XPM comme étant à l'origine de la génération du supercontinuum visible.

(2) Étude de l'élargissement spectral en fonction de P_{532} avec P_{1064} fixée à 4 kW (Figure 4b) : lorsque P_{532} augmente, le spectre infrarouge n'est pas modifié, contrairement au spectre visible qui voit sa densité spectrale de puissance croître. Néanmoins, le profil et l'extension de ce dernier restent stables, indiquant que l'élargissement spectral autour de la pompe verte est fixé par les solitons constituant le supercontinuum infrarouge. Cette observation confirme l'impact par XPM des solitons infrarouges sur l'onde à 532 nm.

(3) Étude de l'élargissement spectral en fonction de la longueur L de la PCF (Figure 4c) : lorsque L augmente, le spectre infrarouge s'étend progressivement vers les hautes longueurs d'onde, de façon comparable à l'étude (1) ; de même, on retrouve le mécanisme d'élargissement spectral en deux étapes dans le domaine visible, c'est-à-dire en premier lieu une extension vers le rouge puis

une extension vers le bleu. La transition entre ces deux étapes est observée pour une valeur de L comprise entre 70 et 90 cm, correspondant à une longueur d'onde d'extension maximale dans l'infrarouge de l'ordre de 1400 nm. Ceci est en très bon accord avec (1) et corrobore le rôle joué par la XPM.

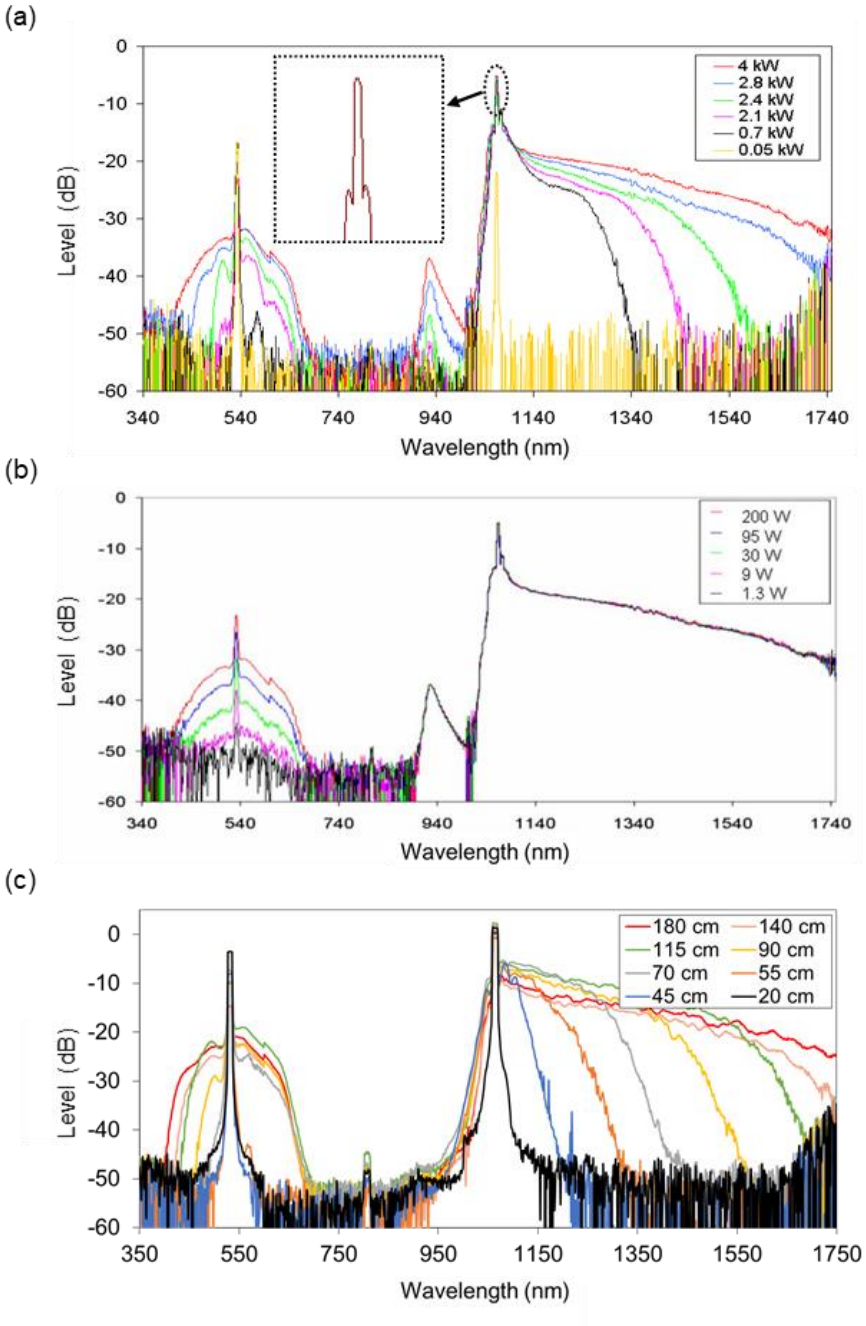

Figure 4 : Génération de supercontinuum par double pompage 532/1064 nm dans une PCF. (a) Variation de P_{1064} (valeurs données en légende) avec P_{532} = 200 W (valeur inférieure au seuil de SRS). (b) Variation de P_{532} (valeurs données en légende) avec P_{1064} = 4 kW (valeur permettant de générer un supercontinuum infrarouge au-delà de 1750 nm). (c) Variation de la longueur de fibre avec P_{532} = 200 W et P_{1064} = 4 kW. P_{532} et P_{1064} désignent la puissance crête injectée dans la PCF à 532 et 1064 nm, respectivement. La longueur de fibre est de 4 m pour (a) et (b). Figure adaptée à partir de [14].

III. Exploitation du mélange à quatre ondes intermodal

Toujours dans l'objectif de favoriser la génération de supercontinuum dans le domaine visible, une approche alternative à celle du double pompage consiste à utiliser une seule onde de pompe externe et à générer une onde de pompe secondaire dans la PCF. Cette approche s'inspire de résultats préliminaires obtenus dans la même fibre que précédemment (**Figure 2**), mais cette fois-ci en excitant à la fois les modes LP_{01} et LP_{11} à la longueur d'onde de 1064 nm. Dans ces conditions, il est possible de générer un supercontinuum dans le visible et l'infrarouge, avec la particularité d'obtenir les longueurs d'onde visibles spécifiquement sur le mode LP_{11} [9] (**Figure 5a**).

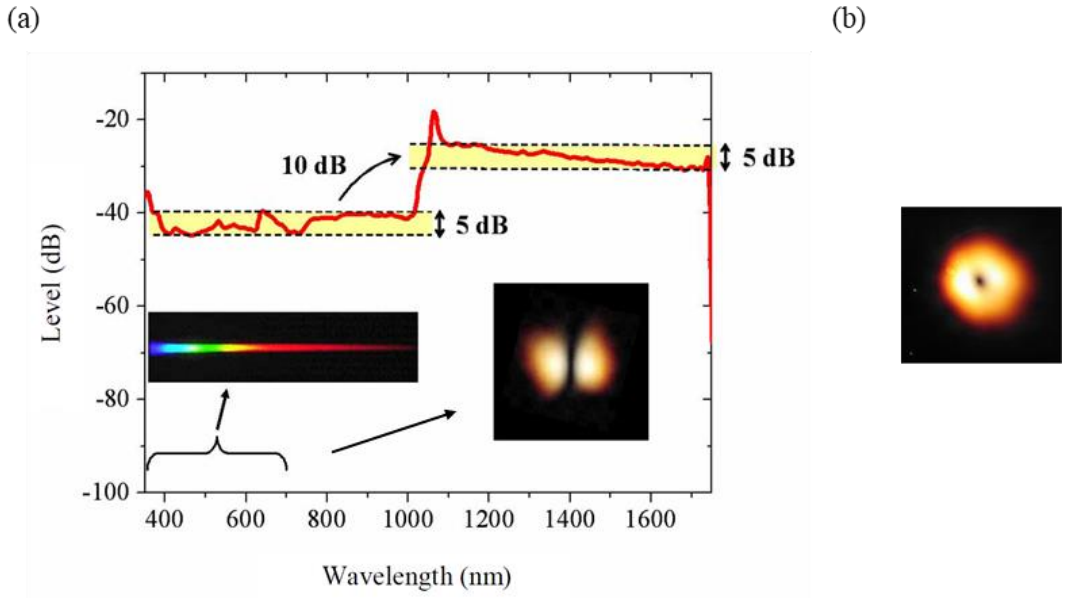

Figure 5 : Génération de supercontinuum dans une PCF légèrement multimode par pompage unique à 1064 nm. (a) Le mode LP_{01} et un seul des modes LP_{11} sont excités à la longueur d'onde de pompe. Encarts : faisceau visible diffracté et distribution transversale d'énergie (figure de champ lointain), mettant en évidence la présence unique d'un mode LP_{11} dans le visible. (b) Figure de champ lointain observée lorsque le mode LP_{01} et les deux modes LP_{11} sont excités. Figure adaptée à partir de [9].

Plus précisément, la fibre microstructurée utilisée peut en fait guider le mode LP_{01} et deux modes LP_{11}, l'un à annulation de champ verticale (LP_{11a}) et l'autre à annulation de champ horizontale (LP_{11b}). Ces trois modes transverses se décomposent également selon la direction de la polarisation, conduisant à l'existence des modes $LP_{01,x}$, $LP_{01,y}$, $LP_{11a,x}$, $LP_{11a,y}$, $LP_{11b,x}$ et $LP_{11b,y}$. Ainsi, chacun de ces six modes peut être excité à la longueur d'onde de pompe, avec un coefficient de couplage dépendant des conditions d'injection (spatiales et de polarisation). Il résulte de cela une certaine difficulté à obtenir et surtout stabiliser le résultat de la **Figure 5a** (mode LP_{11} dans le visible avec nette annulation du champ selon x ou y), qui tend à laisser la place à une figure de champ lointain plus complexe (**Figure 5b**).

Afin de simplifier le problème et de bien cerner le mécanisme non linéaire à l'origine de la génération du spectre visible, une nouvelle PCF a été conçue et fabriquée à XLIM. Celle-ci possède un cœur fortement elliptique grâce à l'introduction de deux gros trous dans le profil (**Figure 6a**),

lui conférant une forte biréfringence (2.10^{-3} à 1064 nm) et conduisant au guidage des seuls modes $LP_{01,x}$, $LP_{01,y}$, $LP_{11b,x}$ et $LP_{11b,y}$ à 1064 nm (la longueur d'onde de coupure des modes $LP_{11a,x}$ et $LP_{11a,y}$ étant inférieure à 1064 nm). Les courbes de dispersion chromatique de ces quatre modes sont données en **Figure 6b** (le mode LP_{11b} étant désormais noté LP_{11} à des fins de clarté). **Dans cette fibre, il devient aisé de contrôler les conditions d'injection afin de sélectionner précisément le(s) mode(s) excité(s) parmi les quatre possibilités.**

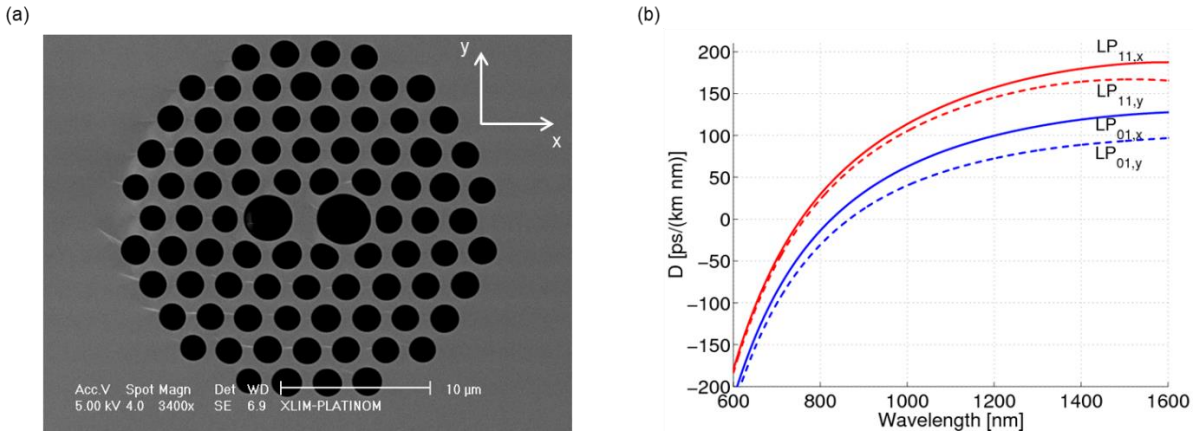

Figure 6 : Caractéristiques d'une PCF fortement biréfringente pour la génération de supercontinuum par mélange à quatre ondes intermodal. (a) Image MEB. (b) Courbes de dispersion chromatique des quatre modes guidés de la fibre à la longueur d'onde de pompe (1064 nm). Figure adaptée à partir de [17].

Nous nous plaçons dans le cas où la direction de polarisation de l'onde de pompe est parallèle à l'axe rapide de la fibre (x). Lorsque seul le mode $LP_{01,x}$ est excité, un élargissement spectral vers les hautes longueurs d'onde est observé dans l'infrarouge (**Figure 7a**, courbe noire). Lorsque les modes $LP_{01,x}$ et $LP_{11,x}$ sont excités simultanément, un élargissement spectral est obtenu à la fois dans les domaines visible et infrarouge (**Figure 7a**, courbe rouge). Dans ce dernier cas, deux contributions particulières apparaissent respectivement à 831 et 1478 nm. Une étude en puissance avec une fibre courte permet alors de constater la construction du spectre à partir de ces deux raies et la présence respective du mode $LP_{11,x}$ à 831 nm et du mode $LP_{01,x}$ à 1481 nm (**Figure 7b**). Une étude numérique confirmera la génération des deux contributions par **mélange à quatre ondes (FWM) intermodal large bande** (~ 79 THz), se produisant donc uniquement lorsque les modes $LP_{01,x}$ et $LP_{11,x}$ à la fois sont mis en jeu à la longueur d'onde de pompe [17]. **L'onde anti-Stokes à λ_{AS} = 831 nm peut ainsi jouer le rôle de pompe secondaire,** se propageant en régime de dispersion anormal ($D_C \simeq 46$ ps/nm.km pour le mode $LP_{11,x}$ à cette longueur d'onde). Son élargissement relativement symétrique quand P_{1064} augmente (**Figure 7b**) semble indiquer la mise en jeu de différents effets non linéaires qui au final permettent d'atteindre, de façon intéressante, les longueurs d'onde bleues. Enfin, le même phénomène de FWM intermodal large bande est observé lorsque la direction de polarisation de l'onde de pompe est parallèle à l'axe lent de la fibre (y). Dans ce cas, un décalage fréquentiel supérieur est obtenu (~ 120 THz) mais la génération des fréquences bleues est moins efficace.

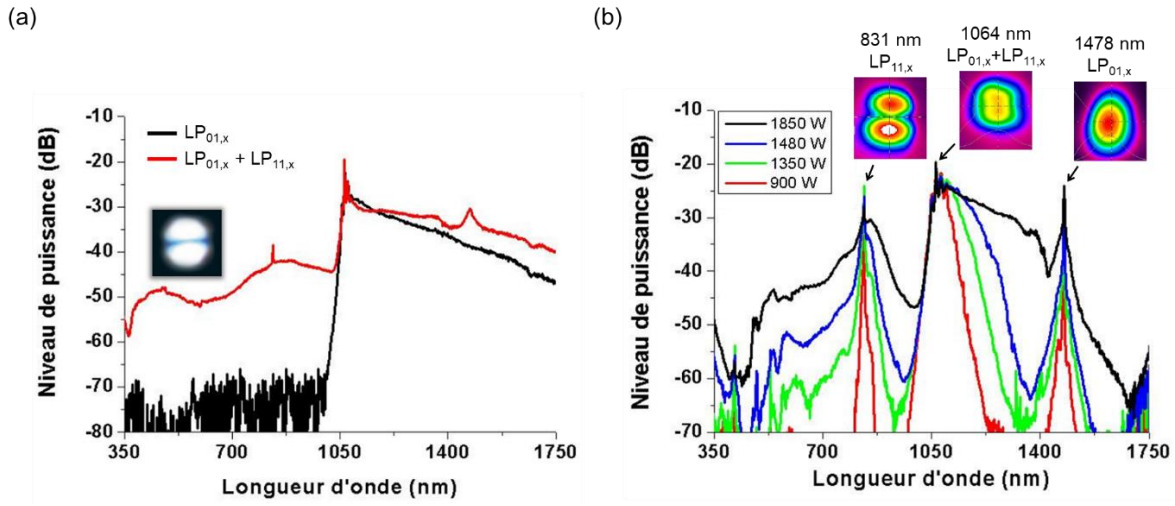

Figure 7 : Génération de supercontinuum assistée par FWM intermodal dans une PCF fortement biréfringente et légèrement multimode pompée à 1064 nm. (a) Excitation à la longueur d'onde de pompe du mode $LP_{01,x}$ seul (courbe noire) et des modes $LP_{01,x}$ et $LP_{11,x}$ simultanément (courbe rouge) dans un tronçon de fibre de longueur ~ 2 m. Encart : distribution transversale d'énergie (figure de champ lointain), mettant en évidence la présence unique du mode $LP_{11,x}$ dans le visible. (b) Variation de P_{1064} (valeurs données en légende) dans un tronçon de fibre de longueur ~ 50 cm. Encarts : distribution transversale d'énergie (figure de champ proche) aux longueurs d'onde de la pompe et des bandes latérales générées par FWM intermodal. P_{1064} désigne la puissance crête injectée dans la PCF à 1064 nm.

Nous avons également pu mettre en œuvre le mécanisme de FWM intermodal **dans une PCF à cœur structuré dopé au germanium** (**Figure 8**). Ce type de fibre se caractérise par la présence au centre du cœur d'une petite zone (notée A) de silice fortement dopée en germanium (différence d'indice de réfraction $\Delta n \sim 5.10^{-2}$ à 1064 nm), visant à la fois à augmenter l'indice non linéaire et à donner des possibilités d'accord de phase pour du FWM très large bande. Les fibres PCF I et II présentées en **Figure 8** ont permis de démontrer, respectivement, l'obtention d'un FWM intermodal avec un décalage fréquentiel de 140 THz (λ_{AS} = 710 nm) et d'un FWM unimodal avec un décalage de 144 THz (λ_{AS} = 704 nm). Il est intéressant de noter que dans les deux cas, l'onde anti-Stokes est générée sur le mode LP_{01}, ce qui facilite son utilisation comme pompe secondaire d'une seconde PCF en vue de générer un supercontinuum très large bande et transversalement monomode (voir la courbe rouge de la **Figure 8**).

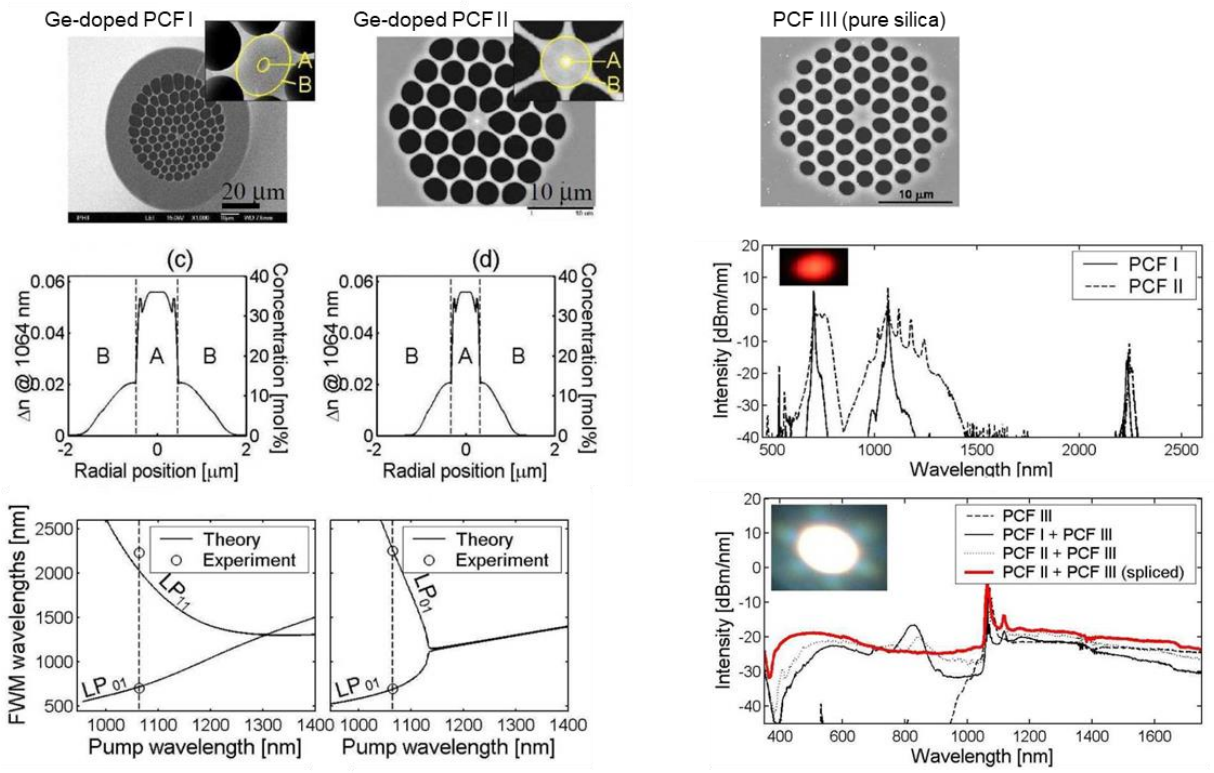

Figure 8 : FWM dans une PCF à cœur structuré dopé au germanium (Ge) et gaine microstructurée air-silice. Mise en jeu des modes LP_{01} / LP_{11} dans la PCF I (FWM intermodal) et du mode LP_{01} seul dans la PCF II (FWM unimodal). Utilisation de l'onde anti-Stokes générée par FWM comme pompe secondaire dans une PCF en silice pure (PCF III). Courbe rouge : supercontinuum mesuré en sortie de l'ensemble PCF II + PCF III (fibres soudées). Figure adaptée à partir de [33].

IV. Combinaison de l'amplification et de la non-linéarité

Nous présentons maintenant une dernière approche d'architecture pour favoriser la génération de supercontinuum, cette fois-ci basée sur l'idée de combiner le phénomène d'amplification et les effets non linéaires. Auparavant, ce type d'approche a pu être utilisé pour mettre en œuvre un laser « supercontinuum » à fibre dopée ytterbium déclenché passivement [Chernikov *et al.*, 1997] ou bien pour réaliser une source laser femtoseconde accordable à amplificateur à PCF dopée ytterbium [Price *et al.*, 2002]. Néanmoins, aucune étude ne proposait, à notre connaissance, une architecture permettant de générer et d'optimiser un supercontinuum dans le domaine visible. **La solution que nous avons introduite consiste à exploiter les propriétés d'amplification, de dispersion et de non-linéarité d'une PCF à cœur dopé ytterbium et à double gaine microstructurée,** dont la **Figure 9** montre l'ensemble des caractéristiques.

Dans un premier temps, la méthode du faisceau propagé (BPM) a permis d'étudier l'influence des paramètres géométriques de la gaine interne (taille des trous, utilisation de trous de diamètre différent) et de la gaine externe (longueur et largeur des pontons de silice, courbure des alvéoles d'air) sur le couplage, le guidage et l'absorption par les ions ytterbium de l'onde de pompe multimode se propageant dans la gaine interne. Par exemple, la **Figure 9b** présente l'évolution

longitudinale de la puissance de pompe multimode pour différentes valeurs du rapport d/Λ dans la gaine interne d'une PCF idéale. Le logiciel COMSOL Multiphysics a par ailleurs été utilisé afin de déterminer un profil idéal de PCF à double gaine en termes de biréfringence, dispersion ou encore aire effective. Ainsi, le design d'une telle fibre microstucturée revêt une certaine complexité, dans la mesure où certains paramètres opto-géométriques interviennent à la fois dans le guidage de la pompe multimode (au sein de la gaine interne) et dans la propagation non linéaire de la pompe pour la génération de supercontinuum (au sein du cœur).

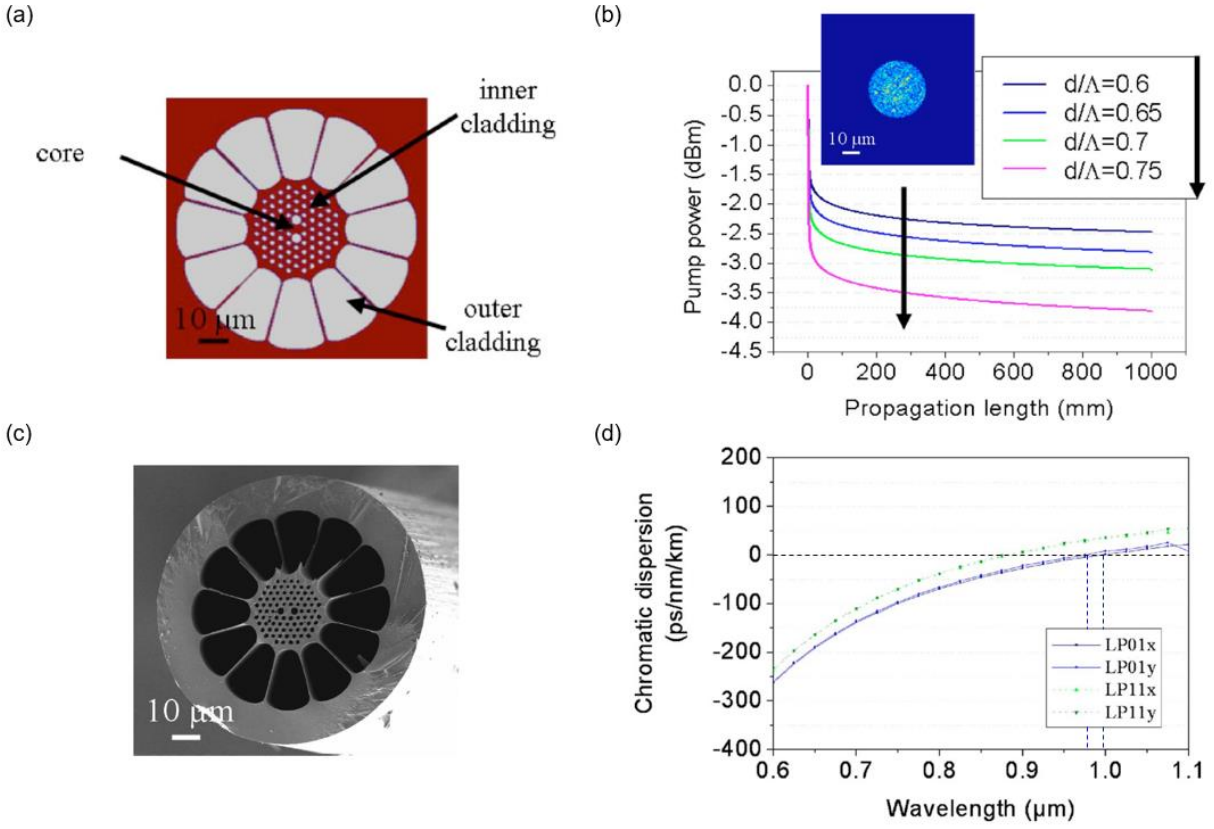

Figure 9 : Caractéristiques d'une PCF à cœur dopé ytterbium et à double gaine microstructurée pour la génération de supercontinuum assistée par amplification de la pompe. (a) Profil idéal illustrant le concept proposé. (b) Évolution longitudinale de la puissance de pompe multimode dans la gaine interne calculée par BPM pour différentes valeurs du rapport d/Λ (encart : distribution transversale de l'intensité du champ incident). (c) Image MEB de la fibre fabriquée. (d) Courbes de dispersion chromatique des quatre modes guidés de la fibre réelle à la longueur d'onde de pompe (1064 nm). Figure adaptée à partir de [16].

Dans un second temps, différents fibrages ont été réalisés, parmi lesquels un des profils de PCF retenus est exposé en **Figure 9c** avec les courbes de dispersion chromatique associées pour les modes LP_{01} et LP_{11} en **Figure 9d**. On notera que, dans le cas de l'injection sélective sur le mode fondamental dans le cœur, la pompe pulsée à 1064 nm se propagera en régime de dispersion légèrement anormal, d'une façon potentiellement similaire au cas c) rapporté dans [Wadsworth *et al.*, 2004] qui prévoit une bonne efficacité de conversion vers les longueurs d'onde visibles. La fibre fabriquée a alors été pompée simultanément par une diode multimode continue à 975 nm (couplée dans la gaine interne) et par un microlaser Nd:LSB nanoseconde à 1062 nm (couplé dans

le cœur) (**Figure 10a**). Comme attendu, le niveau de puissance du supercontinuum visible/proche infrarouge généré dans le cœur augmente avec la puissance de la pompe continue injectée dans la fibre (P_{CW}), avec un gain moyen d'un ordre de grandeur pour P_{CW} = 1,5 W seulement (**Figure 10b**). Il s'agit donc d'un résultat intéressant au vu du gain obtenu pour cette faible valeur de puissance de pompe multimode, **qui représente une voie prometteuse pour la montée en puissance des sources supercontinuum**. Enfin, nous avons tenté d'exploiter le même type de PCF à double gaine afin de réaliser un laser « supercontinuum » à déclenchement actif [20]. Même si la configuration proposée comportait plusieurs points d'amélioration majeurs, cette approche n'est pas totalement convaincante compte tenu des fluctuations d'amplitude du train d'impulsions que nous avons pu observer, de la même manière que [Chernikov *et al.*, 1997] avaient pu mettre en évidence des instabilités du taux de répétition.

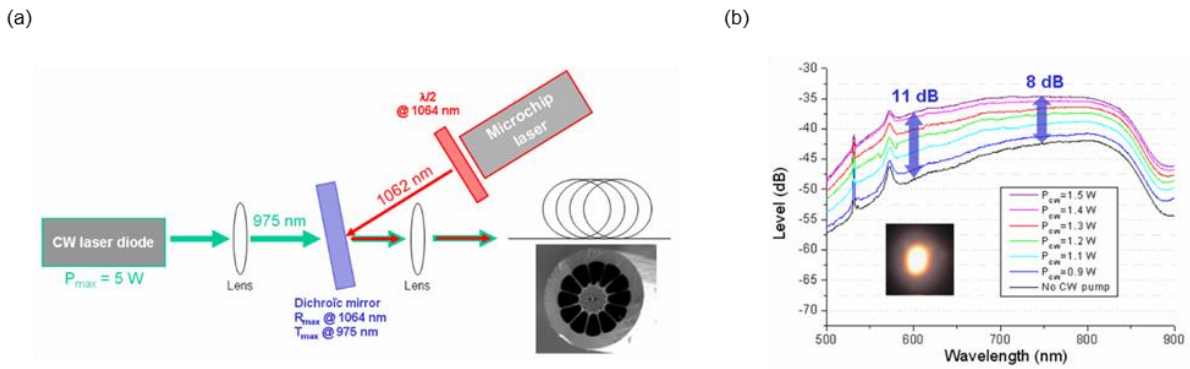

Figure 10 : Génération de supercontinuum dans une PCF à cœur dopé ytterbium et à double gaine microstructurée. (a) Montage expérimental. (b) Spectre mesuré dans le domaine visible/proche infrarouge pour différentes valeurs de puissance de pompe multimode continue injectée dans la fibre (P_{CW}) (encart : distribution transversale d'énergie en champ lointain).

Toujours dans le cadre de cette stratégie consistant à combiner amplification et non-linéarité, nous avons également démontré la génération d'un supercontinuum infrarouge dans un amplificateur à fibre (standard) dopée ytterbium disponible commercialement [18]. Cette configuration, donnant lieu à une extension du spectre initial vers les hautes longueurs d'onde uniquement (**Figure 11**), présente l'intérêt d'une relative simplicité pour analyser le mécanisme non linéaire se mettant en place en présence du gain apporté par les ions ytterbium. En particulier, notre étude a pointé l'effet d'amplification de l'auto-modulation de phase (SPM) de la pompe à 1064 nm et de son impact sur la forme de la cascade SRS sur la plage spectrale de dispersion normale (1050-1300 nm), en accord avec les observations de [Ilev *et al.*, 1996].

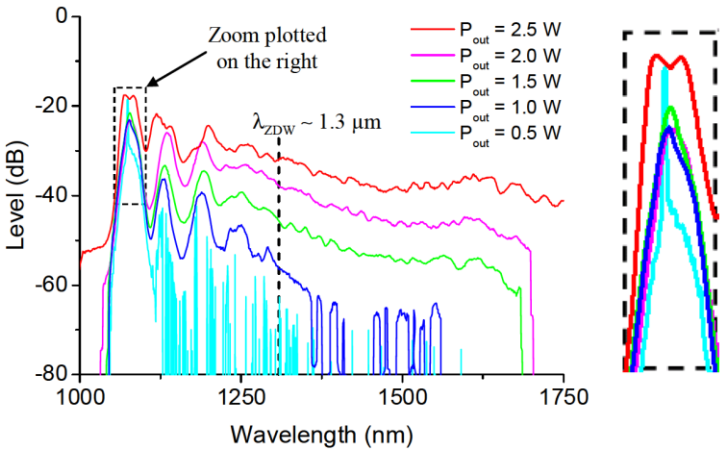

Figure 11 : Génération de supercontinuum dans un amplificateur à fibre (standard) dopée ytterbium. Figure extraite de [18].

Synthèse Partie 1 avec indicateurs

Architectures de sources supercontinuum à fibre microstructurée					
Articles	Communications internationales	Actes de congrès internationaux	Communications nationales	Brevets	Edition
27	44 dont 7 invitées	11	20 dont 2 invitées	11	1 numéro spécial de journal

Mots clés

Fibre à cristal photonique, microlaser, mécanismes non linéaires, génération de supercontinuum

Points saillants / points forts

- Activité à l'interface entre les équipes historiques « Optique guidée et intégrée » et « Optique non linéaire », permettant de capitaliser sur leurs savoir-faire respectifs
- Mise au point de systèmes supercontinuum compacts et simples (utilisation de microlasers), couvrant la totalité du domaine visible (400-700 nm) et le proche infrarouge
- Conséquemment au point précédent, facilitation du transfert de technologie et du développement des applications des sources supercontinuum

Collaborations principales

CIMAP (Caen), FEMTO-ST (Besançon), Institut d'Optique (Palaiseau), IPCMS (Strasbourg), Leibniz-IPHT (Allemagne), Polytechnique Montréal (Canada), Draka (France), Multitel (Belgique), Horiba Medical (Montpellier)

Contrats de recherche

Titre	**Type**	**Période**	**Rôle**	**Nombre de partenaires**	**Coût total**	**Financement XLIM**
Fibres Optiques à cristaux photoniques Nano Optimisées pour Télécommunications Et Applications Médicales (FONOTEAM)	Projet ANR PNANO	2005-2008	Simple participation	5		
SUPERcontinuum généré par fibre optique à cristal photonique pour	Projet ANR BLANC	2006-2009	Simple participation	4		

l'accès multiple à répartition par CODE (SUPERCODE)						
Développement d'un prototype de source laser polychromatique utilisant une fibre optique à cœur structuré (GeStruct)	Projet AVRUL-DIRECCTE Détection Innovation Laboratoires (DIL)	2011-2013	Porteur	3	70 k€	35 k€
SUPercontinuum broadband light sources covering UV to IR applications (SUPUVIR)	Projet MSCA-ITN du programme H2020	2016-2020	Partenaire (par l'inter-médiaire de LEUKOS)	10	4 M€	263 k€
TOTAL						**298 k€**

Publications majeures (insérées ci-après)

- *White-light supercontinuum generation in normally dispersive optical fiber using original multi-wavelength pumping system*, P. A. Champert, V. Couderc, **P. Leproux**, S. Février, V. Tombelaine, L. Labonté, P. Roy, C. Froehly, P. Nérin, Optics Express, vol. 12, no. 19, pp. 4366-4371, 2004 (référence [7] de la liste complète)
- *Ultra wide band supercontinuum generation in air-silica holey fibers by SHG-induced modulation instabilities*, V. Tombelaine, C. Lesvigne, **P. Leproux**, L. Grossard, V. Couderc, J. L. Auguste, J. M. Blondy, G. Huss, P. H. Pioger, Optics Express, vol. 13, no. 19, pp. 7399-7404, 2005 (référence [9] de la liste complète)
- *Structured-core GeO_2-doped photonic-crystal fibers for parametric and supercontinuum generation*, A. Labruyère, **P. Leproux**, V. Couderc, V. Tombelaine, J. Kobelke, K. Schuster, H. Bartelt, S. Hilaire, G. Huss, G. Mélin, Photonics Technology Letters, vol. 22, no. 16, pp. 1259-1261, 2010 (référence [33] de la liste complète)
- *Supercontinuum generation in a nonlinear Yb-doped double-clad microstructured fibre*, A. Roy, **P. Leproux**, P. Roy, J. L. Auguste, V. Couderc, Journal of the Optical Society of America B, vol. 24, no. 4, pp. 788-791, 2007 (référence [16] de la liste complète)

Activités d'édition

- **Editeur en chef du numéro spécial "Fiber supercontinuum sources and their applications",** Optical Fiber Technology, vol. 18, n° 5, p. 247-420, 17 articles invités (Septembre 2012) https://www.sciencedirect.com/journal/optical-fiber-technology/vol/18/issue/5
  > Structuration du numéro en 4 thématiques avec les éditeurs associés (John Dudley, Mohammed Islam, Roy Taylor et Hideaki Kano)
  > Coordination du processus d'invitation des auteurs et d'expertise des articles soumis
  > Rédaction de la préface

Encadrement de thèses de doctorat

- **Vincent Tombelaine**, « Étude de rayonnements à large bande spectrale induits dans les fibres optiques microstructurées air-silice » (2004-2007, **codirection**, directeur de thèse : Vincent Couderc)
- **Christelle Buy-Lesvigne**, « Conversions non-linéaires et élargissements spectraux dans les fibres optiques microstructurées » (2005-2008, **codirection**, directeur de thèse : Vincent Couderc)
- **Aude Roy**, « Architectures de sources lasers blanches à fibres optiques microstructurées actives » (2005-2008, **codirection**, directeur de thèse : Philippe Roy)
- **Marco Andreana**, « Soliton propagation in crystals and optical fibres » (2008-2011, **participation à l'encadrement**, directeur de thèse : Vincent Couderc)
- **Fathima Mullackalparampu**, « Sources supercontinuum dans les plages spectrales émergentes pour l'imagerie à haute résolution » (en cours, soutenance prévue début 2024, **direction de thèse**)

Autres encadrements

- Stages M2 de V. Tombelaine, C. Buy-Lesvigne, A. Roy (2004-2005)
- Anthony Martin, « Étude du mélange à quatre ondes large bande dans une fibre optique microstructurée », stage M1 Omega, Université de Nice Sophia Antipolis (2007)
- Mohamad Chakaroun, Ahmad Kanso et Ali Khalil, « Programmation et étude de la BPM », Travaux d'Étude et de Recherche M1 EEA, Université de Limoges (2005-2006)
- Samir Ghilas et Eric Suran, « Étude de la propagation de la pompe dans le cœur multimode d'une fibre air-clad », Travaux d'Étude et de Recherche M1 EEA, Université de Limoges (2004-2005)
- Lina Moustafa, Emeric Lavergne et Dany Lenox, « Étude de la propagation par BIP dans une fibre optique microstructurée air/silice à trous remplis de liquide », Travaux d'Étude et de Recherche Maîtrise EEA, Université de Limoges (2003-2004, co-encadrement avec Sébastien Février)
- Julien Drouet et Nicolas Louis, « Étude numérique de la propagation de la lumière dans les fibres optiques - Application aux fibres microstructurées air-silice et étude expérimentale », Travaux d'Étude et de Recherche Maîtrise EEA, Université de Limoges (2002-2003, co-encadrement avec Sébastien Février)

Publications majeures Partie 1

White-light supercontinuum generation in normally dispersive optical fiber using original multi-wavelength pumping system

Pierre-Alain Champert, Vincent Couderc, Philippe Leproux, Sébastien Février, Vincent Tombelaine, Laurent Labonté, Philippe Roy and Claude Froehly

Institut de Recherche en Communications Optiques et Microondes, UMR CNRS 6615
Faculté des Sciences et Techniques, 123 avenue Albert Thomas, 87060 Limoges Cedex, France
leproux@ircom.unilim.fr

Philippe Nérin

ABX, Parc Euromédecine, Rue du Caducée, BP 7290, 34184 Montpellier Cedex 4, France

Abstract: We report on the experimental demonstration of a white-light supercontinuum generation in normally dispersive singlemode air-silica microstructured fiber. We demonstrate that the simultaneous excitation of the microstuctured fiber in its normal and anomalous dispersion regimes using the fundamental and second harmonic signals of a passively Q-switched microchip laser leads to a homogeneous supercontinuum in the visible range. This pumping scheme allows the suppression of the cascaded Raman effect predominance in favor of an efficient spectrum broadening induced by parametric phenomena. A flat supercontinuum extended from 400 to 700 nm is achieved.

OCIS codes: (190.4370) Nonlinear optics, fibers; (190.1900) Diagnostic applications of nonlinear optics

References and links

1. *Optical Coherence Tomography and Coherence Techniques*, W. Drexler, ed., Proc. SPIE **5140** (2003).
2. R. R. Alfano and S. L. Shapiro, "Emission in the region 4000 to 7000 Å via four-photon coupling in glass," Phys. Rev. Lett. **24**, 584-587 (1970).
3. W. Yu, R. R. Alfano, C. L. Sam and R. J. Seymour, "Spectral broadening of picosecond 1.06 μm pulse in KBr," Opt. Commun. **14**, 344-347 (1975).
4. I. Ilev, H. Kumagai, K. Toyoda and I. Koprinkov, "Highly efficient wideband continuum generation in a single-mode optical fiber by powerful broadband laser pumping," Appl. Opt. **35**, 2548-2553 (1996).
5. W. Werncke, A. Lau, M. Pfeiffer, K. Lenz, H. J. Weigmann and C. D. Thuy, "An anomalous frequency broadening in water," Opt. Commun. **4**, 413-415 (1972).
6. P. B. Corkum, C. Rolland and T. Srinivasan-Rao, "Supercontinuum generation in gases," Phys. Rev. Lett. **57**, 2268-2271 (1986).
7. R. L. Fork, C. V. Shank, C. Hirlimann, R. Yen and W. J. Tomlinson, "Femtosecond white-light continuum pulses," Opt. Lett. **8**, 1-3 (1983).
8. C. Lin and R. H. Stolen, "New nanosecond continuum for excited-state spectroscopy," Appl. Phys. Lett. **28**, 216-218 (1976).
9. P. L. Baldeck and R. R. Alfano, "Intensity effects on the stimulated four photon spectra generated by picosecond pulses in optical fibers," J. Light. Technol. **5**, 1712-1715 (1987).
10. S. Coen, A. Hing Lun Chau, R. Leonhardt, J. D. Harvey, J. C. Knight, W. J. Wadsworth and P. St. J. Russell, "Supercontinuum generation by stimulated Raman scattering and parametric four-wave mixing in photonic crystal fibers," J. Opt. Soc. Am. B **19**, 753-764 (2002).

#4814 - $15.00 US
Received 15 July 2004; revised 31 August 2004; accepted 3 September 2004

11. A. Mussot, T. Sylvestre, L. Provino and H. Maillotte, "Generation of a broadband single-mode supercontinuum in a conventional dispersion-shifted fiber by use of a subnanosecond microchiplaser," Opt. Lett. **28**, 1820-1822 (2003).
12. B. Colombeau, J. Monneret, F. Reynaud, B. Carquille, F. Louradour and C. Froehly, "Réduction du gain de la diffusion Raman stimulée dans les fibres optiques unimodales de silice," presented at the Dixièmes Journées Nationales d'Optique Guidée, Jouy-en-Josas, France, Aug. 1989.
13. E. Golovchenko, E. M. Dianov, P. V. Mamyshev and A. N. Pilipetskii, "Parametric suppression of stimulated Raman scattering," JETP Lett. **50**, 190-193 (1989).
14. P. V. Mamyshev and A. P. Vertikov, in *Quantum Electronics and Laser Science*, Vol. 13 of OSA Technical Digest Series (Optical Society of America, Washington, D. C., 1992), p. 130.
15. S. Trillo and S. Wabnitz, "Parametric and Raman amplification in birefringent fibers," J. Opt. Soc. Am. B **9**, 1061-1082 (1992).
16. T. Sylvestre, H. Maillotte and E. Lantz, "Stimulated Raman suppression under dual-frequency pumping in singlemode fibres," Electron. Lett. **34**, 1417-1418 (1998).
17. S. Pitois, G. Millot and P. Tchofo Dinda, "Influence of parametric four-wave mixing effects on stimulated Raman scattering in bimodal optical fibers," Opt. Lett. **23**, 1456-1458 (1998).
18. P. Tchofo Dinda, S. Wabnitz, E. Coquet, T. Sylvestre, H. Maillotte and E. Lantz, "Demonstration of stimulated-Raman-scattering suppression in optical fibers in a multifrequency pumping configuration," J. Opt. Soc. Am. B **16**, 757-767 (1999).
19. T. Sylvestre, H. Maillotte, P. Tchofo Dinda and E. Coquet, "Suppression of stimulated Raman scattering in optical fibres by power-controlled multifrequency pumping," Opt. Commun. **159**, 32-36 (1999).

1. Introduction

Continuum generation has been widely studied in the past four decades due to the large potential applications such as telecommunications systems, time resolved absorption, spectroscopy, optical metrology or biomedical optics [1]. It was first demonstrated in bulk borosilicate glass [2] and later in a large variety of nonlinear media including liquid waveguides and gasses [3-6]. The progress and development in microstructured optical fibers brought a new range of fiber with manageable dispersion properties. The zero dispersion wavelength (ZDW) can thus be shifted toward the near IR and matched with the operating wavelength of a large variety of nanosecond to femtosecond high peak power lasers, yielding broadband continuum of more than 1000 nm at the -20 dB level [7-11]. Continuum generation is the result of multiple nonlinear phenomena such as stimulated Raman scattering (SRS), self-phase and cross-phase modulations (SPM and XPM), four wave mixing (FWM), high-order soliton formation and parametric mixing through modal phase matching in the case of multimode optical fibers. All these effects directly affect the continuum homogeneity and occur with different weights, according to the pump wavelength and power and to the chromatic dispersion characteristics of the fiber. Broadband continua were obtained by pumping a singlemode optical fiber near its ZDW or in regime of strong positive chromatic dispersion.

Nevertheless, no flat continuum generation has ever been demonstrated with large normal dispersion. Indeed in such conditions cascaded Raman scattering is the dominant effect and leads to an energy transfer from the pump towards discrete downshifted frequencies. To avoid the effect of SRS in optical fibers, several mechanisms have been suggested [12-16]. One of these mechanisms is based on a FWM process involving parametric Stokes and anti-Stokes sidebands and inhibiting the growth of the ordinary Raman Stokes radiation. Control of the Raman process was also investigated in high-birefringence fiber and demonstrated by means of a linearly-polarized dual-frequency pump scheme in the regime of strong positive dispersion where parametric suppression is not efficient [17-19].

In this paper, we report on the possibility to obtain a flat and homogeneous continuum in the visible range using a singlemode microstuctured optical fiber (MOF) respectively pumped in its anomalous and normal dispersion regimes by the fundamental and second harmonic signals of a passively Q-switched nanosecond pulse laser. The double excitation allows the spectacular inhibition of the cascaded Raman process in favor of FWM and XPM, yielding a

#4814 - $15.00 US Received 15 July 2004; revised 31 August 2004; accepted 3 September 2004

white light supercontinuum source ranging from the near UV to the near IR (350-750 nm).

2. Experimental set-up with double pumping scheme

The set-up is shown on Fig. 1. The pump source consists of a passively Q-switch Nd:YAG laser operating at 5.4 kHz repetition rate and delivering 600 ps pulses at $\lambda = 1064$ nm. The free space radiation of the laser is frequency doubled in a 20 mm long type-II KTP crystal, with better than 35 % conversion efficiency, yielding pulses of 420 ps at $\lambda = 532$ nm. These IR and green radiations are coupled into a 4 m long MOF. Two filters (named "RG 85" and "BG 18") are used to allow total filtering of the visible or IR radiation at the launching end of the fiber.

The MOF used in these experiments has been fabricated in our laboratory by the conventional stack and draw process. A cross sectional scanning electron microscope image of the fiber is shown in Fig. 1. The hole-to-hole spacing Λ is around 2.2 µm, leading to a core diameter approximately equal to 2.8 µm. The average hole diameter d is 1.5 µm. The resulting ratio d/Λ equal to 0.68 indicates that the fiber is slightly multimode. Indeed at the pump wavelengths of 1064 and 532 nm, we observed the guidance of LP_{01} and LP_{11} modes. Suppression of the second mode was achieved by coiling the fiber around a spool with a diameter of about 1 cm.

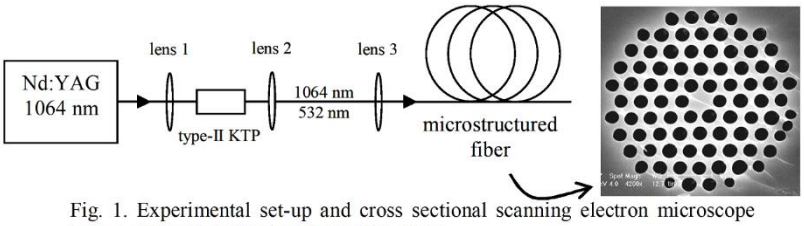

Fig. 1. Experimental set-up and cross sectional scanning electron microscope image of the microstructured air-silica fiber.

The chromatic dispersion and the effective area of the fundamental mode have been computed from 400 to 1600 nm using a full vectorial finite element algorithm and taking into account the actual cross section shown in Fig. 1. The results plotted in Fig. 2 show that the ZDW is located at $\lambda \sim 870$ nm, thus between the two pump wavelengths $\lambda = 532$ nm and $\lambda = 1064$ nm. The chromatic dispersion is respectively -410 ps/nm/km and +55 ps/nm/km at these wavelengths. The small effective area A_{eff}, calculated to be around 4 µm² at 800 nm, gives a nonlinear coefficient $\gamma = 2\pi.n_2/\lambda.A_{eff}$ equal to 0.06 $W^{-1}.m^{-1}$ at this wavelength (n_2 being the nonlinear refractive index, $n_2 \sim 3\times10^{-20}$ $m^2.W^{-1}$). The transverse energy distribution of the fundamental mode computed at 800 nm is also plotted in inset of Fig. 2(a).

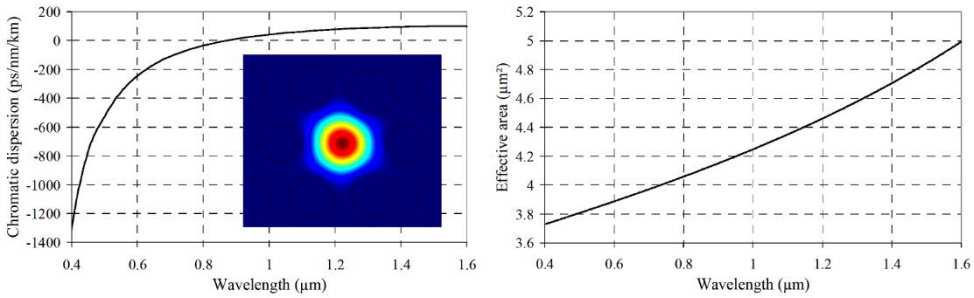

Fig. 2. Computed chromatic dispersion (a) and effective area (b) of the fundamental mode of the microstructured fiber versus the wavelength. Inset: transverse energy distribution calculated at $\lambda = 800$ nm.

#4814 - $15.00 US
Received 15 July 2004; revised 31 August 2004; accepted 3 September 2004

3. Smooth and broadened supercontinuum generation

In a first case, the IR radiation is filtered out. The green peak power propagating in the waveguide is close to 1.5 kW for an average power of 3 mW measured at the fiber output. Due to the strong normal dispersion at 532 nm (-410 ps/nm/km), Raman scattering is the dominating nonlinear process. Indeed, up to seven Raman orders are generated through cascaded Raman effect (Fig. 3(a)).

We now consider the case when both the fundamental and second harmonic radiations are co-propagating in the fiber. The chromatic aberration of the coupling lens and the implementation of a longitudinal micro-displacement of the fiber allow a variation of the visible/IR power ratio coupled into the fiber core. For a sufficient power at 1064 nm, we observe a complete modification of the nonlinear behavior, giving birth to a symmetric and homogeneous broadening of the spectrum around 532 nm (Fig. 3(b)). This new continuum displays between 350 nm to 750 nm with a significant improvement of the spectrum flatness thanks to the quasi suppression of SRS effect. Except the remaining 532 nm peak, the 5 dB bandwidth has been measured to be close to 300 nm.

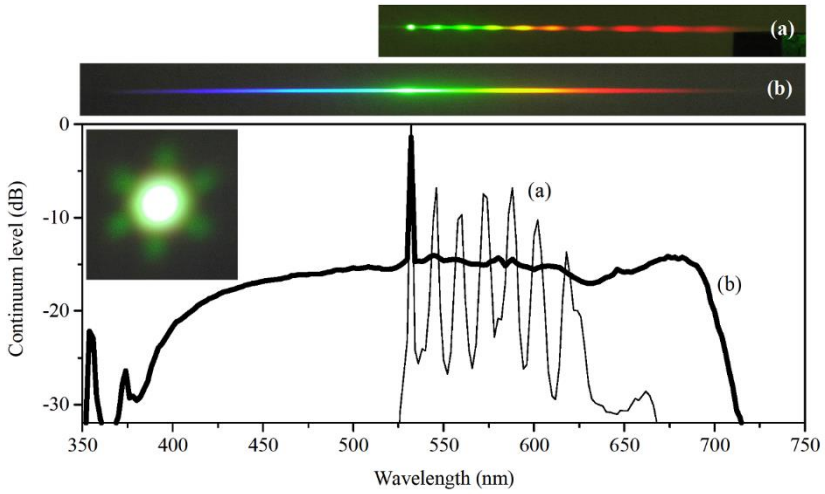

Fig. 3. Continuum generation in normal dispersion regime in the case of single (a) and dual (b) pump configuration. Pictures: diffracted beams. Graph: corresponding recorded power spectra. (a) The cascaded Raman effect is clearly visible in the presence of a single pump (532 nm). (b) The spectrum smoothly and symmetrically broadens when a second pump (1064 nm) is added. The corresponding singlemode transverse energy distribution is shown in inset (far field pattern).

The continuum can be divided into two parts. The first one at wavelengths larger than 532 nm seems to be obtained by the combination of FWM, SPM, XPM and SRS. In particular FWM and XPM are exacerbated by the presence of the second pump wavelength (1064 nm) situated in large anomalous dispersion regime (+55 ps/nm/km). Because of the high parametric gain, the SRS phenomenon is significantly reduced, allowing the growth of a continuous and flat spectral broadening. Nevertheless, the presence of some residual oscillations proves that the Raman effect is not completely suppressed and may still contribute to the broadening. The limit of the supercontinuum in the near infrared region (~ 750 nm) directly depends both on the green and IR pump powers. The higher the pump powers, the broader the supercontinuum.

In the second part (from 380 nm to 532 nm), the spectrum profile is particularly smooth without disconnections or oscillations. The wavelength growth seems to be built from the

#4814 - $15.00 US
Received 15 July 2004; revised 31 August 2004; accepted 3 September 2004

combination of XPM and parametric effects. Indeed it seems that the spectral broadening obtained in the infrared region between 1064 nm and 1750 nm (see Fig. 4) has a role in the creation of wavelengths in the blue/UV region. Moreover no contribution of the SRS phenomenon is expected in this range of wavelengths, where anti-Stokes waves receive no significant energy. The limit of the supercontinuum in the blue range directly depends on the IR pump power and seems to be less sensitive to the green energy. Below 380 nm, only two peaks centered at 355 and 365 nm are identified and seem to be created by the third harmonic generation from the infrared pump.

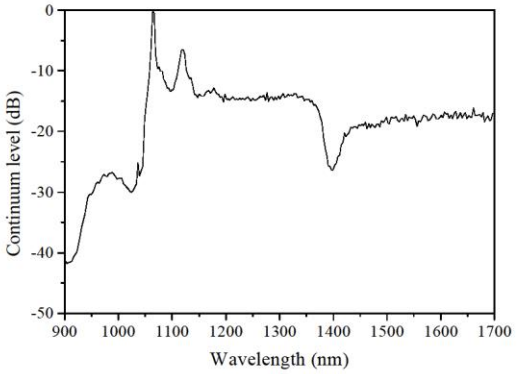

Fig. 4. Continuum power spectrum measured in the infrared range (anomalous dispersion regime).

It is worth to note that the change in the nonlinear process depends on the input IR pump power and on the power ratio $P_\omega/P_{2\omega}$ between 1064 nm and 532 nm pump wavelengths. In our experiments, the quasi complete suppression of the SRS phenomenon and the smoothing of the spectrum profile occurred notably for a ratio $P_\omega/P_{2\omega} > 2.8$. For a lower ratio, residual Raman peaks were clearly visible in the spectrum profile and no significant spectral broadening between 350 and 532 nm was observed (Fig. 5). In any case, the competition between FWM and SRS phenomena seems to be the right explanation of the continuum profile evolution.

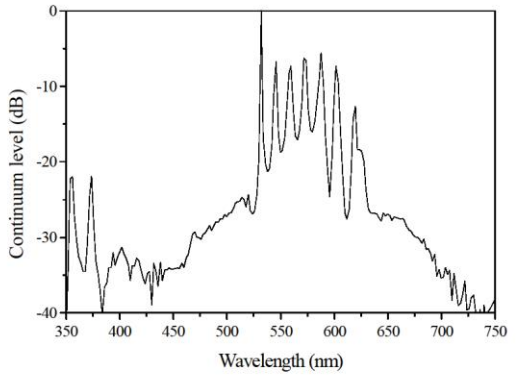

Fig. 5. Continuum power spectrum obtained in the visible range when using both 532 and 1064 nm pumps, but for an insufficient value of ratio $P_\omega/P_{2\omega}$.

The contribution of the 1064 nm pump is also visible in the infrared domain (Fig. 4). We observe a significant spectral broadening towards high wavelengths, reaching the upper limit of the optical spectrum analyzer used (1750 nm). The combination of SRS and FWM gives birth to a smooth spectrum profile. Unfortunately, the OH^- bonding present inside the MOF

#4814 - $15.00 US
Received 15 July 2004; revised 31 August 2004; accepted 3 September 2004

silica core induces a significant absorption at $\lambda \sim 1.4$ µm, restricting the usable bandwidth of this infrared continuum in optical coherent tomography applications. Nevertheless, this drawback can be avoided when fabricating the MOF by using a non flame fused silica glass, exhibiting low OH^- absorption. An example of IR spectrum obtained in an OH^--free MOF fabricated in our laboratory is shown in Fig. 6 and successfully confirms the necessity to use adequate silica material.

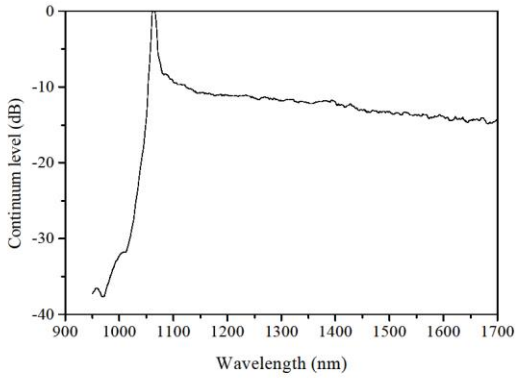

Fig. 6. Infrared continuum power spectrum obtained in a microstructured fiber fabricated at IRCOM with non flame fused silica glass. No more OH^- absorption peak is observable at 1400 nm.

4. Conclusion

We have demonstrated supercontinuum generation in normally dispersive air-silica microstuctured optical fiber using a double pumping scheme with both 532 and 1064 nm radiations. A significant and symmetrical spectrum broadening due to the synchronic excitation in large normal and anomalous dispersion regimes was observed, resulting in a flat and homogeneous continuum between 400 and 700 nm. The addition of a second pump in the infrared range permitted to exacerbate the four wave mixing processes and to significantly inhibit the stimulated Raman scattering phenomenon. Thus a singlemode and truly white laser source was achieved. Wide spectral broadening over all the infrared range between 1064 and 1750 nm (upper limit of measurement device) was also obtained.

The new pumping scheme proposed here is applicable to all optical fiber in order to broaden and flatten the spectral continuum profile by the control of Raman effect. For example, it is possible to pump a standard singlemode fiber on both sides of its zero-GVD wavelength (~ 1300 nm) for supercontinuum generation in second and third communication windows. Moreover the multi wavelength pumping can be extended to three or four synchronic radiations, generated from an efficient laser source, to cover the whole transparency window of silica fibers.

In addition, we have recently fabricated in our laboratory a new microstructured fiber, whose well-adapted dispersion properties and low UV-absorption allow to efficiently improve the continuum generation below 380 nm, resulting in a quasi constant power level from at least 350 to 532 nm (without deteriorating the broadening beyond 532 nm). These results will soon be proposed for publication.

Acknowledgments

The authors thank ABX Diagnostics (HORIBA group) for financial support, J. L. Auguste and J. M. Blondy from IRCOM for the fabrication of the fibers, S. Coen (Auckland University), J. Dudley and T. Sylvestre (Université de Besançon) for fruitful discussions.

#4814 - $15.00 US
Received 15 July 2004; revised 31 August 2004; accepted 3 September 2004

Ultra wide band supercontinuum generation in air-silica holey fibers by SHG-induced modulation instabilities

Vincent Tombelaine, Christelle Lesvigne, Philippe Leproux, Ludovic Grossard, Vincent Couderc, Jean-Louis Auguste, Jean-Marc Blondy

Institut de Recherche en Communications Optiques et Microondes, UMR CNRS 6615
Faculté des Sciences et Techniques, 123 avenue Albert Thomas, 87060 Limoges Cedex, France
leproux@ircom.unilim.fr

http://www.ircom.unilim.fr

Guillaume Huss, Paul-Henri Pioger

Projet LEUKOS, Incubateur Limousin d'entreprises, ESTER technopole, BP6935, 87069 Limoges Cedex, France
huss@ircom.unilim.fr

Abstract: Second harmonic generation in an air-silica microstructured optical fiber pumped by subnanosecond pulses is used in order to initiate modulation instability processes in normal and anomalous dispersion regimes. This allows us to generate an ultra wide and flat supercontinuum (350-1750 nm), covering the entire transparency window of silica and exhibiting a singlemode transverse profile in visible range.

OCIS codes: (190.4370) Nonlinear optics, fibers; (190.5530) Pulse propagation and solitons

References and links

1. L. Provino, J. M. Dudley, H. Maillotte, N. Grossard, R. S. Windeler and B. J. Eggleton, "Compact broadband continuum source based on microchip laser pumped microstructured fibre," Electron. Lett. **37**, 558-560 (2001).
2. A. Mussot, T. Sylvestre, L. Provino and H. Maillotte, "Generation of a broadband single-mode supercontinuum in a conventional dispersion-shifted fiber by use of a subnanosecond microchip laser," Opt. Lett. **28**, 1820-1822 (2003).
3. W. J. Wadsworth, N. Joly, J. C. Knight, T. A. Birks, F. Biancalana and P. St. J. Russell, "Supercontinuum and four-wave mixing with Q-switched pulses in endlessly single-mode photonic crystal fibres," Opt. Express **12**, 299-309 (2004), http://www.opticsexpress.org/abstract.cfm?URI=OPEX-12-2-299.
4. S. G. Leon-Saval, T. A. Birks, W. J. Wadsworth, P. St. J. Russell and M. W. Mason, "Supercontinuum generation in submicron fibre waveguides," Opt. Express **12**, 2864-2869 (2004), http://www.opticsexpress.org/abstract.cfm?URI=OPEX-12-13-2864.
5. P. A. Champert, V. Couderc, P. Leproux, S. Février, V. Tombelaine, L. Labonté, P. Roy, C. Froehly and P. Nérin, "White-light supercontinuum generation in normally dispersive optical fiber using original multi-wavelength pumping system," Opt. Express **12**, 4366-4371 (2004), http://www.opticsexpress.org/abstract.cfm?URI=OPEX-12-19-4366.
6. V. Tombelaine, V. Couderc, P. Leproux, L. Grossard, J. L. Auguste and J. M. Blondy, "Modulational instabilities in normal dispersion regime leading to white-light supercontinuum generation," CLEO/QELS, Baltimore, Maryland, USA, paper CTuJ2 (2005).
7. B. T. Kuhlmey, R. C. Mc Phedran and C. M. de Sterke, "Modal cutoff in microstructured optical fibers," Opt. Lett. **27**, 1684-1686 (2002).
8. Y. Sasaki and Y. Ohmori, "Phase-matched sum-frequency light generation in optical fibers," Appl. Phys. Lett. **39**, 466-468 (1981).
9. U. Osterberg and W. Margulis, "Dye laser pumped by Nd:YAG laser pulses frequency doubled in a glass optical fiber," Opt. Lett. **11**, 516-518 (1986).
10. R. H. Stolen and H. W. K. Tom, "Self-organised phase-matched harmonic generation in optical fibers," Opt. Lett. **12**, 585-587 (1987).
11. M. A. Saifi and M. J. Andrejco, "Second-harmonic generation in single-mode and multimode fibers," Opt. Lett. **13**, 773-775 (1988).

#8215 - $15.00 USD Received 19 July 2005; revised 1 September 2005; accepted 3 September 2005

12. R. H. Stolen and J. E. Bjorkholm, "Parametric amplification and frequency conversion in optical fibers," IEEE J. Quantum Electron. **QE-18**, 1062-1071 (1982).
13. U. Osterberg, R. I. Lawconnell, L. A. Brambani, C. G. Askins and E. J. Friebele, "Modal evolution of induced second harmonic light in an optical fiber," Opt. Lett. **16**, 132-134 (1991).
14. K. M. Hilligsøe, T. Vestergaard Andersen, H. N. Paulsen, C. K. Nielsen, K. Mølmer, S. Keiding, R. Kristiansen, K. Per Hansen and J. J. Larsen, "Supercontinuum generation in a photonic crystal fiber with two zero dispersion wavelengths," Opt. Express **12**, 1045-1054 (2004), http://www.opticsexpress.org/abstract.cfm?URI=OPEX-12-6-1045.
15. M. H. Frosz, O. Bang, A. Bjarklev, P.E. Andersen and J. Broeng, "Supercontinuum generation in photonic crystal fibers: The role of the second zero dispersion wavelength," CLEO/QELS, Baltimore, Maryland, USA, paper CWC1 (2005).

1. Introduction

The combination of microstructured optical fibers and subnanosecond microchip lasers allows to realize very compact and efficient systems leading to wide band supercontinuum generation [1-4]. In particular, homogeneous spectral broadening can be achieved in large normal dispersion regime by means of modulation instabilities (MI) induced by a double pumping system [5-6]. We show here that the same type of phenomenon can be observed by using a single pump laser and generating its second harmonic frequency directly in the fiber. We demonstrate that second harmonic generation occurring in the holey fiber is sufficiently efficient to initiate spectacular MI processes in large normal dispersion regime and to obtain a white light source with a single pump laser at 1064 nm.

The generated supercontinuum surprisingly extends from almost 350 to 1750 nm (limited by measurement), covering the entire transparency window of silica optical fibers. The spectrum is divided into two parts, on both sides of the pump wavelength, with a flatness of around 5 dB for each part. The transverse spatial profile of the output beam is singlemode and is built on the second order mode (LP_{11}) of the fiber in the visible range. No supercontinuum exhibiting such kind of performances and bringing such nonlinear processes into play was, to our knowledge, already published.

This white light source is suitable for many applications requiring low cost and compactness, such as Optical Coherence Tomography (OCT), confocal microscopy, hematological diagnosis or also spectroscopy. Some first measurements demonstrate the presence of energy in the UV range, opening a new field of possible applications of this technology.

2. Experimental set-up and characteristics of the microstructured fiber

The set-up is shown on Fig. 1. The pump source consists of a Q-switched Nd:YAG laser delivering 600 ps pulses at $\lambda = 1064$ nm. It is coupled into a 2-m long air-silica microstructured optical fiber by means of a focusing lens. A half wave plate is used to make the polarization rotate on the input end of the fiber.

The microstructured fiber, fabricated in our laboratory, has a hole-to-hole spacing Λ of around 2.2 µm and an average hole diameter of 1.5 µm, resulting in a ratio d/Λ equal to 0.68 and indicating that the fiber is highly nonlinear and slightly multimode [7]. This fiber exhibits two propagation modes (fundamental mode, LP_{01} and second order mode, LP_{11}) for wavelengths in the visible range and is strictly singlemode beyond 1200 nm. The transition between these two behaviors, around 1 µm, is gradual and permits to transfer more or less energy to the two transverse modes. The chromatic dispersion curves of these two modes have been calculated with a finite element method and are plotted on Fig. 2. For LP_{01} mode, the zero dispersion wavelength (ZDW) is located at 870 nm. For LP_{11} mode, it is shifted down to 710 nm and a second ZDW appears at 1100 nm.

#8215 - $15.00 USD Received 19 July 2005; revised 1 September 2005; accepted 3 September 2005

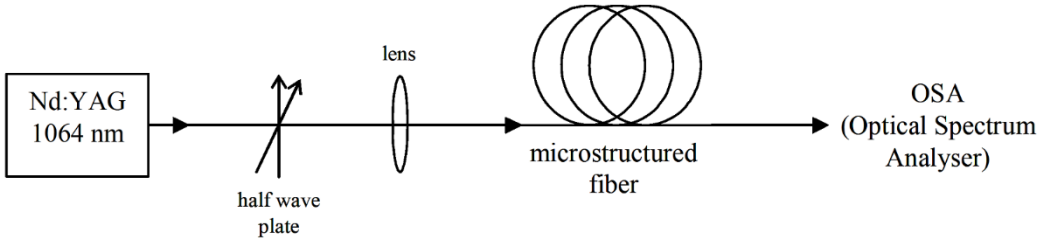

Fig. 1. Experimental set-up.

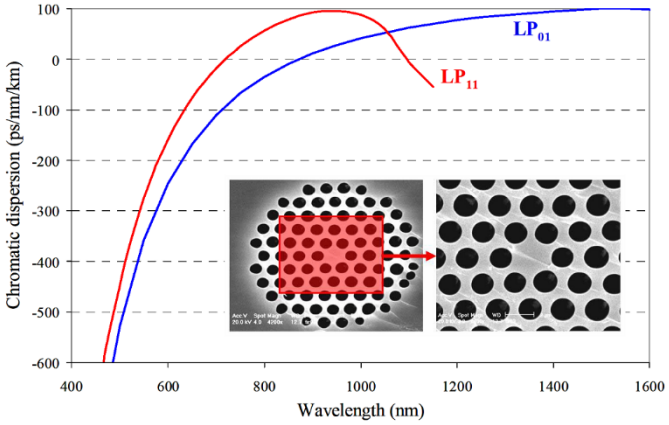

Fig. 2. Calculated chromatic dispersion curves of fundamental and second order modes of the microstructured fiber. Inset: cross sectional scanning electron microscope image of the fiber.

3. Second harmonic generation (SHG) in the microstructured fiber

When we launched the fundamental radiation (1064 nm) into the microstructured fiber, we clearly observed the generation of energy at 532 nm inside the fiber, corresponding to the doubling of the fundamental frequency [8-11]. This SHG is due to local inhomogeneities located in silica glass and also to the core-cladding interface, corresponding to the air-silica interfaces, encountered by the pump wave propagating in the core. The SHG efficiency remains weak (few %) but is sufficient to initiate MI processes and to generate a wide band supercontinuum, as shown underneath. Figure 3 shows an example of spectrum measured for a low pump power launched into the fiber: the pump line at 1064 nm is slightly broadened and the SHG line is visible at 532 nm.

4. Visible and infrared spectral broadening

It has been previously demonstrated [5-6] that a double pumping system (both 532 and 1064 nm pump wavelengths) could induce MI process leading to supercontinuum generation in large normal dispersion regime, over the whole visible range and without any presence of noticeable peaks due to stimulated Raman scattering (SRS). The phase matching condition was then achieved thanks to a strong nonlinear phase shift combined with the particular dispersion characteristics of the fiber, depending on the considered propagation mode (LP_{01}).

Identical MI process can be obtained by pumping the fiber at a single wavelength (1064 nm), the second wave (532 nm) being created directly inside the fiber by means of SHG. Indeed we obtained by this way the supercontinuum plotted on Fig. 4, which exhibits a wide and flat spectral broadening in the visible domain. A continuum was also observed in the infrared range, i.e. in anomalous dispersion regime, resulting from the combination of self and cross phase modulation, SRS and four-wave mixing. The whole broadening finally extends

#8215 - $15.00 USD Received 19 July 2005; revised 1 September 2005; accepted 3 September 2005

from 350 to 1750 nm (lowest and highest limits of the OSA used), covering the entire transparency window of silica. For each part of the spectrum, the flatness is around 5 dB. The visible part is 10 dB lower than the infrared one.

Finally, the output beam is spatially singlemode, with the typical transverse distribution of the second order mode (LP_{11}) of the fiber in the visible range, as shown in inset of Fig. 4. The IR part of the continuum above 1 µm propagates on the single LP_{01} mode whereas the energy between 750 and 1000 nm propagates on both LP_{01} and LP_{11} modes.

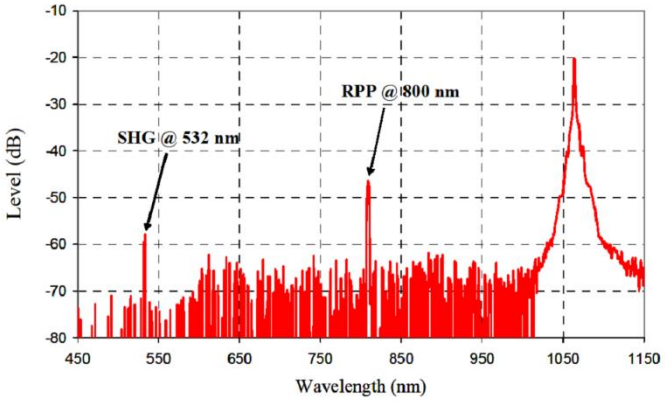

Fig. 3. Spectrum measured at the output end of the microstructured fiber (2 m), showing second harmonic generation at 532 nm from the fundamental wavelength at 1064 nm (RPP = Remaining Pump Power of the microchip laser @ 800 nm). The peak pump power at 1064 nm is 100 W.

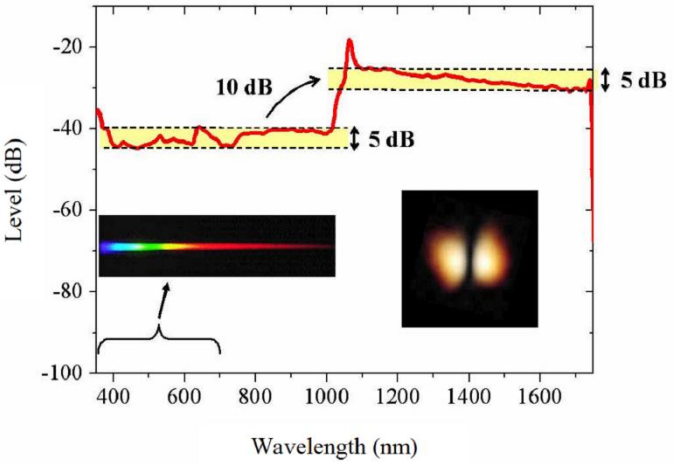

Fig. 4. Spectral broadening measured in visible and infrared ranges (peak pump power at 1064 nm: 6 kW). Inset: fiber output diffracted beam and far field transverse distribution (LP_{11} mode).

5. Analysis of the phenomenon

In order to analyze the experimental results shown on Fig. 4, we computed the parametric gain from the formalism initially developed by Stolen *et al.* in the case of double pumping near the ZDW of the fiber [12]. We applied this formalism to the case of two pump waves (1064 and 532 nm) positioned on both sides and far from the ZDW, for LP_{01} and LP_{11} modes.

#8215 - $15.00 USD
Received 19 July 2005; revised 1 September 2005; accepted 3 September 2005

The calculated parametric gain is extremely sensitive to the position of the ZDW of the considered transverse mode. When LP_{01} mode (ZDW = 870 nm) is considered, the parametric gain is mainly obtained between the two pump wavelengths. On the contrary, operating on LP_{11} mode (ZDW = 710 nm) permits to create new gain bands, particularly below the pump wavelength at 532 nm, i.e. in large normal dispersion regime. The shift of the ZDW towards shorter wavelengths makes possible phase matched nonlinear processes for visible spectral components and produces light in UV-blue range. Experimentally, the influence of the ZDW position is less significant than in numerical simulations but the experimental work demonstrates that the spectral position of the two pump waves is a crucial point in the spectrum build-up. So the position of the ZDW between the two pump wavelengths determines the shape of the spectrum generated in the fiber but also the conversion efficiency of the nonlinear process. In our case, operating on the second order mode of the fiber has led to a very large broadening, from the UV to the IR, with a low amount of power at 532 nm. In the case of SHG on the fundamental mode, the very low efficiency of this nonlinear process does not permit to induce MI and consequently does not create a large spectral broadening in the visible range.

It is clear that the propagation conditions of the generated second harmonic wave determine the phase matching conditions required for the SHG nonlinear process. This also determines the transverse mode of propagation of the supercontinuum in the visible range. In our case, the SHG is spontaneously created from LP_{01} mode towards LP_{11} mode. This surprising effect was already observed by Osterberg *et al.* [13] in a non microstructured optical fiber. The modal structure of the photoinduced second harmonic light in optical fibers depends on the IR intensity used to pump the material. It seems also that the core profile of the microstructured fiber plays a large role in the propagation of the 532 nm radiation.

The birefringence of the fiber is another important characteristic of the guide for SHG process, and we clearly observed its influence in our experiments. The orientation of the input beam polarization versus the neutral axes of the microstructured fiber permits us to excite LP_{11} mode either with horizontal polarization or with vertical polarization. This determines the polarization of the supercontinuum obtained at the output of the fiber. It is also possible to excite the two orthogonally polarized modes. In this case, these two structures propagate together in the fiber and the supercontinuum observed at the output end exhibits a ring-shaped transverse energy distribution ("white donut"). Nevertheless, the phase matching conditions of nonlinear processes are not identical for the two LP_{11} modes. The spectral width and shape of the generated continuum evolve with the polarization state of the input beam. The maximal enlargement of the spectrum corresponds in our case to a strictly vertically polarized excitation.

A final point is that it is obvious that the second ZDW at 1100 nm plays an important role in the spectral broadening, as it has already been demonstrated in other studies [14-15]. Indeed, the proximity of the pump wavelength at 1064 nm from this second ZDW should favor parametric processes. The change of dispersion sign between the two sides of the ZDW can allow nonlinear phase matched processes and lead in particular to degenerated four wave mixing processes. However, the efficiency of this phenomenon may be limited by the quasi bimodal propagation in this range of wavelength.

6. Conclusion

We have demonstrated ultra wide band supercontinuum generation in a highly nonlinear air-silica microstructured optical fiber, using for the first time SHG process in the fiber. The pump source is a simple subnanosecond microchip laser emitting at 1064 nm. The output beam is singlemode in the visible region and has its spectrum extended over the whole transparency window of silica (350-1750 nm). This spectral broadening is achieved thanks to a modulation instability process in which a wave at 532 nm is involved. This wavelength is created inside the fiber by second harmonic generation from the fundamental frequency of the pump laser.

#8215 - $15.00 USD Received 19 July 2005; revised 1 September 2005; accepted 3 September 2005

This experiment results in the design of a very compact and cost effective white light source, consequently easily usable in many applications. This technique is under patent pending with the French CNRS and opens new perspectives for multi-wavelength pumping of nonlinear microstructured optical fibers.

Acknowledgments

The authors thank ABX Diagnostics (HORIBA group) for financial support.

#8215 - $15.00 USD Received 19 July 2005; revised 1 September 2005; accepted 3 September 2005

Structured-Core GeO_2-Doped Photonic-Crystal Fibers for Parametric and Supercontinuum Generation

Alexis Labruyère, Philippe Leproux, Vincent Couderc, Vincent Tombelaine, Jens Kobelke, Kay Schuster, Hartmut Bartelt, Stéphane Hilaire, Guillaume Huss, and Gilles Mélin

***Abstract*—We demonstrate efficient broadband four-wave-mixing (FWM) generation at the particular frequency detuning of ∼150 THz from a 1064-nm sub-nanosecond laser pump in innovative structured-core germanium–oxide (GeO_2)-doped photonic crystal fibers (PCFs). Remarkably, the latter PCF has a small-diameter highly concentrated germanium rod in the core center that enables fine tuning of the FWM wavelengths. The generated anti-Stokes radiation at ∼700 nm is subsequently used as secondary pump for generating a bright visible supercontinuum in the fundamental mode from 370 nm to beyond 1750 nm, when splicing the GeO_2-doped PCF to a pure-silica PCF, whose zero-dispersion wavelength is set in-between the pump and anti-Stokes wavelengths, consistently with the standard dual-wavelength pumping scheme.**

***Index Terms*—Nonlinear propagation, optical fiber devices, optical frequency conversion.**

I. Introduction

WHITE-LIGHT supercontinuum (SC) sources emitting from the violet to the infrared (IR) range were successfully demonstrated using dual-wavelength (DW) pumping in photonic crystal fibers (PCFs) [1]–[6]. The future advances in fluorescence imaging and flow cytometry would then rely on extending the SC generation into the ultraviolet (UV) domain. In practice, when the DW pumping scheme is used, two laser pumps are simultaneously present in the near-IR and the visible domain, so that the nonlinear broadening of the continuum is mainly driven by cross-phase modulation (XPM) [7]. In general, the visible pump is generated from an infrared laser pump by frequency doubling [1], [2], or by four-wave-mixing (FWM) conversion into a visible anti-Stokes radiation [3]–[6]. In particular, SC can be generated in a cascade of two PCFs, FWM pump conversion being achieved in the first stage, and subsequently, DW pumping in the second one [5]. On the other hand, SC generation by single-wavelength CW pumping has been recently demonstrated using GeO_2-doped PCFs [8]. The presence of large quantities of GeO_2 greatly enhances the nonlinear response of the PCFs [9], [10]. In this context, GeO_2-doped PCFs could advantageously be used for improving FWM pump conversion in the first stage of DW pumping for SC generation. In general, the presence of GeO_2 strongly impacts the dispersion properties of an optical fiber. Indeed, zero-dispersion wavelength (ZDW) is considerably up-shifted, and consequently, in conventional GeO_2-doped fibers, only mixed-mode FWM is possible when pumping in the near-IR [9]. However, in GeO_2-doped PCFs, the dispersion curve can be tailored in such a way that the ZDW is sufficiently decreased to phase-match single-mode FWM [10]. Therefore, careful attention must be paid in the design of the GeO_2-doped PCFs for selecting FWM interacting modes [11], [12].

In this letter, we investigate FWM in a particular class of GeO_2-doped PCFs, referred to as structured-core GeO_2-doped PCFs, in which we demonstrate efficient broadband FWM conversion detuned by ∼150 THz from the 1064-nm sub-nanosecond (sub-ns) laser pump. These new PCFs have improved FWM efficiency by 10%–15% when compared to [5] thanks to a very high concentration in GeO_2 and provide an additional degree of freedom for phase-matching FWM by properly sizing the central doped rod. Indeed, we achieve the FWM in two different ways, either by single-mode or mixed-mode phase-matching in two different GeO_2-doped PCFs, respectively. In both cases, we obtained intense visible anti-Stokes radiation at ∼700 nm in the fundamental mode. The anti-Stokes radiation is subsequently used as secondary pump for generating a bright visible SC in the fundamental mode from 370 nm to beyond 1750 nm, when splicing the GeO_2-doped PCF to a conventional pure-silica PCF whose ZDW has been set in-between the pump and anti-Stokes wavelengths, consistently with the standard DW pumping scheme.

II. Four-Wave Mixing

We have used the two different structured-core GeO_2-doped PCFs, referred to as PCFs I and II, whose scanning electron microscope (SEM) pictures are represented in Fig. 1(a) and (b), respectively. PCFs I and II were fabricated by the Institute of Photonic Technology (IPHT) and *Draka*, respectively. Table I summarizes the PCF parameters. As a particularity, the core of these GeO_2-doped PCFs comprises two different regions, denoted as A and B, respectively. Region A refers to the central part of the core, in which GeO_2 concentration is high (36 mol%), while Region B covers the rest of the core where the GeO_2 vanishes. Consequently, the cores of PCFs I and II have refractive index profiles as depicted in Fig. 1(c) and (d), respectively.

Manuscript received April 09, 2010; revised May 21, 2010; accepted June 05, 2010. Date of publication June 14, 2010; date of current version July 23, 2010. This work was supported by the European Commission through the FP6 integrated project NextGenPCF.

A. Labruyère, P. Leproux, and V. Couderc are with the XLIM Research Institute, University of Limoges, 87060 Limoges, France (e-mail: alexis.labruyere@xlim.fr).

V. Tombelaine, S. Hilaire, and G. Huss are with Leukos, 87069 Limoges, France.

J. Kobelke, K. Schuster, and H. Bartelt are with the Institute of Photonic Technology (IPHT), 07745 Jena, Germany.

G. Mélin is with DRAKA, 91460 Marcoussis, France.

Color versions of one or more of the figures in this letter are available online at http://ieeexplore.ieee.org.

Digital Object Identifier 10.1109/LPT.2010.2052919

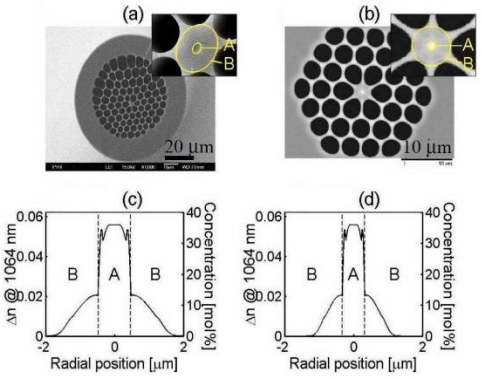

Fig. 1. (a) and (b) SEM pictures of PCF I and PCF II, respectively; (c) and (d) Refractive index difference (left axis) and GeO_2 concentration (right axis) of PCF I and PCF II, respectively. (a) PCF I, (b) PCF II, (c) PCF I, (d) PCF II.

TABLE I
PCF PARAMETERS

	Pitch [µm]	Air-hole diameter [µm]	Region A diameter [µm]	Region B diameter [µm]
PCF I	4.8	4.1	0.95	3.65
PCF II	3.65	3.35	0.65	3.25

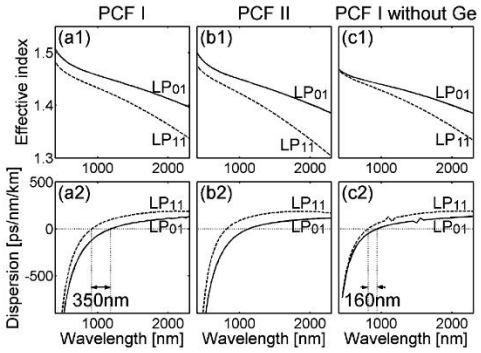

Fig. 2. (a1), (b1), and (c1) Calculated effective index curves; (a2), (b2), and (c2) calculated dispersion curves associated with LP_{01} (solid line) and LP11 (dashed line) modes for PCF I, PCF II, and PCF I without GeO_2, respectively.

Using a commercial mode solver based on the finite-element method, we have calculated the effective index curves, which are represented in Fig. 2(a1) and (b1) for linearly polarized LP_{01} (solid line) and LP_{11} (dashed line) modes in PCFs I and II, respectively. For comparison, the case of PCF I without GeO_2 is shown in Fig. 2(c1). The corresponding dispersion curves are represented in Fig. 2(a2), (b2), and (c2), respectively. In practice, the presence of GeO_2 mainly impacts the effective index and dispersion curves of the LP_{01} mode which mainly overlaps with the GeO_2-doped Region A, whereas the LP_{11} mode remains almost unchanged, as it propagates in the pure-silica

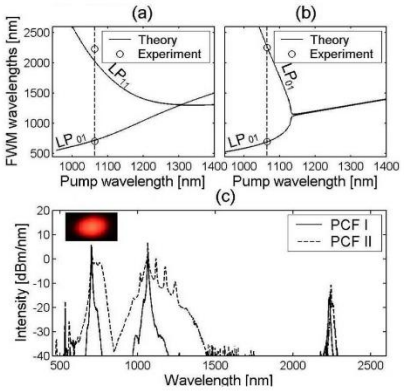

Fig. 3. (a) Mixed-mode phase-matching diagram in PCF I, and (b) single-mode phase-matching diagram in PCF II. (c) Output FWM spectra from 55 cm of PCF I (solid line) and from 55 cm of PCF II (dashed line). (a) PCF I; (b) PCF II.

Region B. Therefore, it is possible to tailor the effective indices of LP_{01} and LP_{11} modes almost independently. Then, the group velocity mismatch between these modes can be controlled to phasematch mixed-mode FWM. Alternatively, it is also possible to phase-match LP_{01} single-mode FWM. Indeed, LP_{01} mode is confined in the GeO_2-doped region at shorter wavelengths, while progressively expanding in the pure-silica region at longer wavelengths. By varying the diameter of the GeO_2-doped Region A, one can selectively tune LP_{01} effective indices at the Stokes and anti-Stokes wavelengths to phasematch single-mode FWM.

The two above-mentioned mechanisms for controlling FWM have been considered to design PCFs I and II for mixed-mode and single-mode FWM, respectively. Starting from an arbitrary air–silica cladding structure, the diameter of the GeO_2-doped region is tuned so that FWM is phase-matched at the particular frequency detuning of 150 THz. We used a 1064-nm Nd : YAG microchip laser delivering sub-ns pulses (peak power $\sim$10 kW). The single-mode FWM pump conversion involves fundamental LP_{01} mode only. This is achieved in 55 cm of PCF II, for which we have depicted the calculated phase-matching diagram in Fig. 3(b). The corresponding FWM spectrum is represented in Fig. 3(c) as the dashed line. The measured anti-Stokes and Stokes wavelengths are 704 and 2250 nm, in good agreement with the theory. The mixed-mode FWM phase-matching involving both LP_{01} and LP_{11} modes is observed in 55 cm of PCF I. The anti-Stokes and Stokes radiations are generated in the LP_{01} and LP_{11} modes, respectively. The calculated phase-matching diagram for PCF I is shown in Fig. 3(a), and FWM spectrum is represented in Fig. 3(c), as the solid line. The measured anti-Stokes and Stokes wavelengths are 710 and 2230 nm, which also agree pretty well with the predictions. Fig. 3(c) indicates that high conversion efficiency towards the anti-Stokes sideband can be achieved for both PCF I and II. Conversion efficiencies (P_{as}/P_p) of 46% and 39% are measured for PCF I and II, respectively, that represents 10% to 15% improvement with respect to [5].

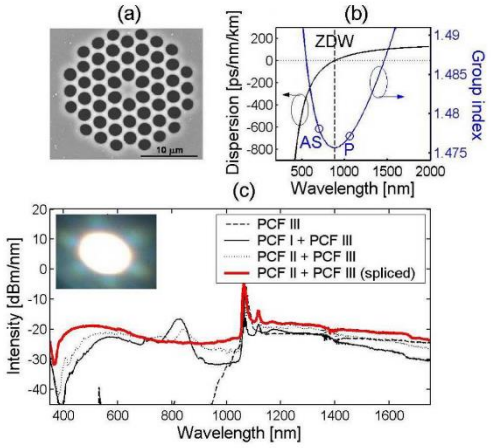

Fig. 4. (a) SEM picture of PCF III. (b) Dispersion and group index curves of PCF III. (c) Output continuum spectra from 10 m of the pure silica PCF III only (dotted line), 55 cm of Ge-doped PCF I butt-coupled with 10 m of PCF III (thin solid line), 55 cm of PCF II butt-coupled with 10 m of PCF III (thin dashed line), and 55 cm of PCF II spliced with 10 m of PCF III (thick solid line). (a) PCF III; (b) PCF III.

III. SC Generation

To illustrate FWM efficiency in GeO_2-doped PCFs, we have used the generated anti-Stokes radiation, as a secondary pump for generating a bright visible SC by DW pumping. Hence, the output of PCFs I and II was successively butt-coupled to 10 m of a pure-silica PCF, whose ZDW is set to ~890 nm. The latter is denoted as PCF III and represented in Fig. 4(a). Dispersion and group-index curves of PCF III are depicted in Fig. 4(b). Note that the lengths of PCFs I and II are limited to 55 cm, so as to prevent from undesirable spectral broadening in the first stage. The resulting output spectra are shown in Fig. 4(c) by the thin solid and dashed lines, respectively. These output spectra demonstrate visible SC generation down to 400 and 440 nm, respectively, through XPM of the infrared spectral components on the anti-Stokes radiation, consistently with the standard DW pumping scheme.

To improve the power coupling, the PCF II and the pure-silica PCF III were spliced together. A splice loss of 0.6 dB was achieved using a conventional arc fusion splicer. The overall output spectrum is represented as the thick solid line in Fig. 4(c), which shows an extension of the SC down to 370 nm. For comparison, we have plotted as the dotted line in Fig. 4(c), the output spectrum when the 1064-nm laser is directly injected into the pure silica PCF. In this case, an infrared SC is generated but its spectrum does not extend in the visible range. That confirms our hypothesis regarding the important role played by the anti-Stokes radiation for seeding visible SC generation.

IV. Conclusion

We have investigated FWM in a new class of PCFs, whose guiding region is structured by GeO_2-doping in a limited zone of the core. In these PCFs, we were able, either by single-mode or mixed-mode FWM, to generate a bright anti-Stokes sideband at ~700 nm on the fundamental mode when pumping with sub-ns pulses at 1064 nm. The later anti-Stokes sideband was used as a secondary pump to achieve SC generation down to 370 nm on the fundamental mode by double-wavelengths pumping in a pure silica fiber. The proposed method could be easily implemented to provide a low-cost, compact, and all-fibered white-light SC source.

References

[1] P. A. Champert, V. Couderc, P. Leproux, S. Février, V. Tombelaine, L. Labonté, P. Roy, C. Froehly, and P. Nérin, "White-light supercontinuum generation in normally dispersive optical fiber using original multi-wavelength pumping system," *Opt. Express*, vol. 12, pp. 4366–4371, 2004.

[2] E. Räikkönen, G. Genty, O. Kimmelma, M. Kaivola, K. P. Hansen, and S. C. Buchter, "Supercontinuum generation by nanosecond dual-wavelength pumping in microstructured optical fibers," *Opt. Express*, vol. 14, pp. 7914–7923, 2006.

[3] C. Lesvigne, V. Couderc, A. Tonello, P. Leproux, A. Barthélémy, S. Lacroix, F. Druon, P. Blandin, M. Hanna, and P. Georges, "Visible supercontinuum generation controlled by intermodal four-wave mixing in microstructured fiber," *Opt. Lett.*, vol. 32, pp. 2173–2175, 2007.

[4] W. J. Wadsworth, N. Joly, J. C. Knight, T. A. Birks, F. Biancalana, and P. S. J. Russell, "Supercontinuum and four-wave mixing with *Q*-switched pulses in endlessly single-mode photonic crystal fibres," *Opt. Express*, vol. 12, pp. 299–309, 2004.

[5] C. Xiong, Z. Chen, and W. J. Wadsworth, "Dual-wavelength-pumped supercontinuum generation in an all-fiber device," *J. Lightw. Technol.*, vol. 27, no. 11, pp. 1638–1643, Jun. 1, 2009.

[6] C. Xiong, A. Witkowska, S. G. Leon-Saval, T. A. Birks, and W. J. Wadsworth, "Enhanced visible continuum generation from a microchip 1064 nm laser," *Opt. Express*, vol. 14, pp. 6188–6193, 2006.

[7] G. P. Agrawal, *Nonlinear Fiber Optics*, 3rd ed. New York: Academic, 2001.

[8] Y. Li, F. Salisbury, Z. Zhu, T. Brown, P. Westbrook, K. Feder, and R. Windeler, "Interaction of supercontinuum and Raman solitons with microstructure fiber gratings," *Opt. Express*, vol. 13, pp. 998–1007, 2005.

[9] Y. P. Yatsenko, A. D. Pryamikov, V. M. Mashinsky, M. E. Likhachev, A. O. Mavritsky, and E. M. Dianov, "Four-wave mixing with large Stokes shifts in heavily Ge-doped silica fibers," *Opt. Lett.*, vol. 30, pp. 1932–1934, 2005.

[10] Y. P. Yatsenko, A. F. Kosolapov, A. E. Levchenko, S. L. Semjonov, and E. M. Dianov, "Broadband wavelength conversion in a germanosilicate-core photonic crystal fiber," *Opt. Lett.*, vol. 34, pp. 2581–2583, 2009.

[11] Y. P. Yatsenko and A. D. Pryamikov, "Parametric frequency conversion in photonic crystal fibres with germanosilicate core," *J. Opt. A, Pure Appl. Opt.*, vol. 9, pp. 716–722, 2007.

[12] A. Labruyère, V. Tombelaine, P. Leproux, V. Couderc, F. Gérôme, G. Humbert, J. Kobelke, K. Schuster, and H. Bartelt, "Intermodal four-wave mixing in structured-core photonic crystal fiber: Experimental results," in *Proc. Conf. Lasers and Electro-Optics (Optical Society Amer., 2009)*, Baltimore, MD, Paper CFS3.

Supercontinuum generation in a nonlinear Yb-doped, double-clad, microstructured fiber

Aude Roy, Philippe Leproux, Philippe Roy, Jean-Louis Auguste, and Vincent Couderc

Photonics Department, XLIM, 123 avenue Albert Thomas, 87060 Limoges Cedex, France

Received November 29, 2006; accepted November 29, 2006;
posted December 11, 2006 (Doc. ID 77575); published March 15, 2007

Supercontinuum is generated and enhanced by using a concept of fiber combining amplification and nonlinear properties. Amplification of pump pulses at 1062 nm in the nonlinear Yb-doped core of the fiber results simultaneously in an increase of the spectral power density level (average gain of 10 dB over the entire spectrum) and a spectral flattening in the visible range. © 2007 Optical Society of America

OCIS codes: 060.2320, 190.4370.

Supercontinuum (SC) generation has been widely studied these past many years. The first achievement of SC in an optical fiber was realized by Lin and Stolen in 1976,[1] leading to many experiments on spectral broadening in fibers. The advent of air–silica microstructured fibres in the Nineties provoked a revival in this research field mainly as a result of the shift down of the zero dispersion wavelength (ZDW) toward the visible domain. A fresh boost was given to visible continuum generation with the result of Ranka *et al.* in 2000.[2]

Currently, continuum generation consists of injecting high peak power into the small core of new-generation microstructured fibres. Among the latest improvements, the use of long tapers, fabricated by progressively decreasing the core size of the holey fibre during the drawing, has led to a decrease in the ZDW along the fiber and thus extension of spectral broadening to the ultraviolet.[3] In other work, a cavity laser configuration based on a double-clad, Er/Yb codoped fiber spliced with a highly nonlinear fibre was examined,[4] but the generated spectrum was limited to the 1300–1750 nm range. Generally speaking, the main parameter that limits SC generation is the quick decrease of the pump power along the propagation in the nonlinear fiber, which restricts the useful nonlinear interaction length. A way of compensating for this decrease is to inject more pump power into the fiber, but it would be distinctly more interesting to attain a regeneration of the power inside the fiber.

We propose here to include a gain medium in a nonlinear microstructured fiber to improve SC generation. First, the design of the fiber is presented and the main expected properties are listed. Then, fabrication and characterization of the first Yb^{3+}-doped, double-clad, microstructured fiber whose core is simultaneously nonlinear and amplifying are described. Thanks to this fiber, visible continuum generation is improved, particularly in terms of spectral power density (SPD) and flatness. Let us note that the association of gain and nonlinearity in an optical fiber can also lead to self-similar propagation of parabolic pulses[5] or wavelength tunability of a pulsed femtosecond source.[6]

The air–silica, microstructured fiber we aim for has to combine suitable nonlinear properties[2] and effective amplification. An efficient and compact nonlinear pumping scheme at 1064 nm is possible by using a pulsed microchip Nd:YAG laser and by shifting the ZDW of the fiber near the pump wavelength[7] or below.[8] Moreover, the core of the fiber is chosen birefringent in order to improve the phase-matching conditions of parametric effects at the origin of spectral broadening.[9] Furthermore, this core has to be doped with Yb^{3+} ions and a cladding pumping of these ions must be implemented. A high numerical aperture (NA) of the inner cladding (IC) is crucial in order to launch a significant level of multimode pump power and thus to ensure a high population inversion of the Yb^{3+} ions of the active core. This last point requires the use of an air outer cladding with a high air-filling factor. Taking into account all these design issues, an ideal fiber profile has been proposed and is shown in Fig. 1(a).

The choice of the value of the IC geometrical parameters (hole-to-hole pitch Λ and hole diameter d) is crucial for the SC build-up, since the air-filling factor d/Λ modifies the fiber ZDW position and consequently the dispersion regime at the pump wavelength. The calculation of the ZDW versus d/Λ is perfectly handled thanks to the use of numerical tools such as the finite element method (FEM). However, the present study is made more difficult by the d/Λ ratio's also having a strong influence on the multimode pump propagation in the IC. For this reason, the multimode guidance in the microstructured IC has been numerically studied by use of a three-dimensional fast Fourier transform beam propagation method (3D-FFT-BPM) algorithm,[10] which permits us to examine the multimode pump propagation inside the air-cladding structure[11] taking into account the power flow through silica bridges.[12]

Considering an incident pump beam at 975 nm, the multimode propagation in the IC has been computed over a 1 m length for different values of d/Λ ratio, the pitch being fixed at the value $\Lambda = 3.5$ μm. The transverse distribution of the input beam energy is spatially limited to the

0740-3224/07/040788-4/$15.00

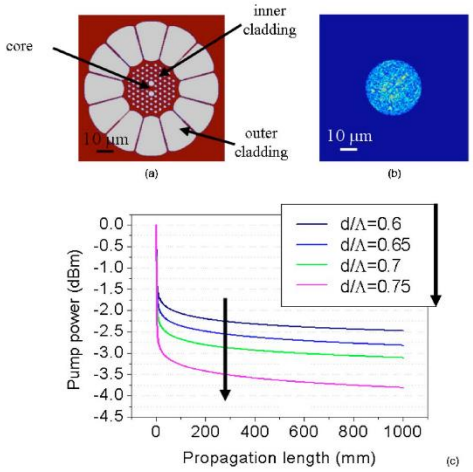

Fig. 1. (Color online) (a) Ideal profile of the proposed fiber. (b) Intensity distribution of the excitation field (BPM calculation). (c) Multimode pump power evolution versus propagation length (d, diameter of IC holes; Λ, IC hole-to-hole pitch, fixed at $\Lambda = 3.5$ μm).

IC area, as shown in Fig. 1(b). Its associated speckle pattern fills the entire wave vector space so as to excite all the guided modes of the IC.

The results obtained are plotted in Fig. 1(c) and show the longitudinal evolution of the pump power in the IC. The different curves have similar shapes with very similar slope evolutions, indicating that the influence of d/Λ on confinement losses is very weak. On the otherhand, the air-filling factor has a large impact on the rate of pump power launched into the IC. The higher d/Λ is, the less pump power is injected, mainly because of the decrease of the NA of the IC. As a result, after 1 m of propagation, the multimode pump power guided in the IC in the case $d/\Lambda = 0.75$ is ≈ 1.3 dB lower than in the case $d/\Lambda = 0.6$. This shows that the fiber structure proposed here is functional for a large range of air-filling factors, with a tolerable decrease of Yb^{3+} ion pumping efficiency for high d/Λ values. For the continuation of this study, we chose to favor the 975 nm pumping efficiency and consequently aimed to fabricate a fiber with geometrical parameters matching the case $d/\Lambda \approx 0.6$. Simultaneously, this case, resulting in a ZDW lower than 1 μm, allows us to pump the fiber nonlinear core in the anomalous dispersion regime by using a 1064 nm pulsed Nd:YAG laser.[8]

An Yb^{3+}-doped, double-clad, microstructured fiber whose scanning electron microscope (SEM) cross section is shown in Fig. 2, was then fabricated in our laboratory using the stack and draw method. This "hybrid" fiber consists of an elliptical core surrounded by two microstructured claddings. The rod that has been stacked to form the doped core is the central part of an Yb^{3+}-doped modified chemical-vapor deposition preform (1000 ppm). Its diameter in the final preform is very small (285 μm) and as a result the doped area in the fiber is ≈ 0.8 μm^2. The 32 μm diameter pure silica IC is made of a hexagonal arrangement of 1.7 μm diameter air holes with a pitch $\Lambda \approx 3.4$ μm, resulting in an air-filling factor close to 0.5.

The bridge width of the air-cladding structure surrounding the IC is $\approx$400 nm. The NA of the IC was also measured by plotting the pattern of radiation emerging from the fiber illuminated by white light. We obtained a high value of about 0.6, which foreshadows a high multimode pump power injection into the IC. Moreover, FEM was employed to calculate the chromatic dispersion curves of this fiber for the two polarization directions of LP_{01} and LP_{11} modes guided in the core (see Fig. 3). The ZDW of the fundamental mode is near 980 nm, which permits us to implement the nonlinear pumping scheme initially intended in spite of the slight geometrical discrepancies between the theoretical and fabricated fiber profiles. The LP_{01} effective area A_{eff} evolves from 8 to 12 μm^2 in the 400–1900 nm spectral range. The nonlinear coefficient $\gamma = 2\pi n_2/(\lambda A_{eff})$ evaluated using $n_2 = 2.6 \times 10^{-20}$ m^2/W is ≈ 14.4 $(W\,km)^{-1}$ at $\lambda = 1064$ nm.

A Q switched Nd:LSB microchip laser from Altechna Company (Model STA-01-1) delivering 1 ns pulses at 1062 nm (70 kHz repetition rate, 2.9 kW peak power) was used as pump source. These pulses are launched into the nonlinear core of a 10 m piece of hybrid fiber. Yb^{3+} ions are simultaneously excited through cladding pumping by

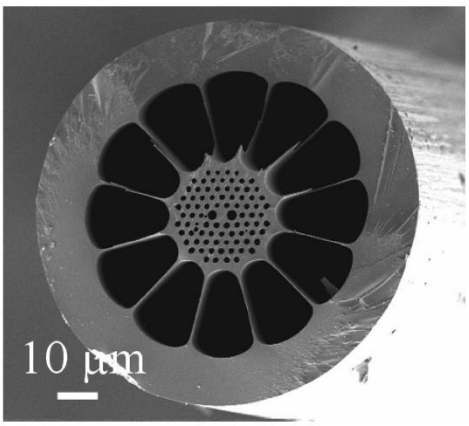

Fig. 2. SEM image of the fabricated fiber.

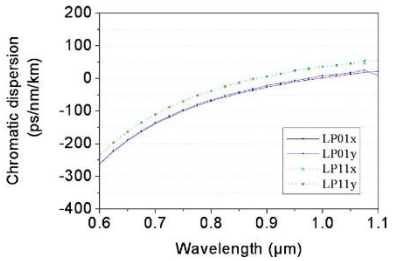

Fig. 3. (Color online) Chromatic dispersion curves of LP_{01} and LP_{11} modes (for the two polarization directions).

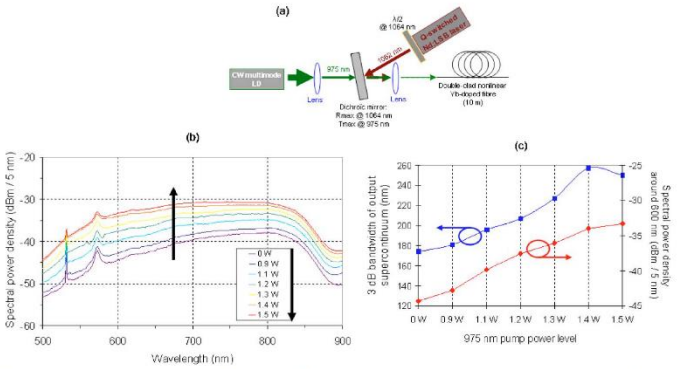

Fig. 4. (Color online) (a) Experimental setup. (b) SC measured for different 975 nm pump power levels. (c) Evolution of SC 3 dB bandwidth and SPD (measured around $\lambda = 600$ nm) versus 975 nm pump power.

a CW pigtailed multimode laser diode (100 μm core diameter, NA=0.22) emitting 5 W at 975 nm [experimental setup shown in Fig. 4(a)]. Thanks to the available gain around 1062 nm, the peak power of pulses propagating in the central core is maintained over a larger length of fiber, depending on the CW pump power level. The nonlinear conversion efficiency is thus significantly enhanced all along the fiber. SC output plotted in Fig. 4(b) was at the output end of the fiber in the 500–900 nm range, i.e., in a normal dispersion regime, for different CW pump power levels injected into the IC of the fiber.

These experimental results clearly demonstrate that the SPD regularly increases with the CW pump power over the entire spectral bandwidth. In particular, Fig. 4(c) shows the SPD around 600 nm versus the CW pump power and shows a gain of 11 dB for only 1.5 W injected into the IC. Moreover, the spectrum evolution toward a better flatness is noticeable in Fig. 4(b). This phenomenon is confirmed by the data of Fig. 4(c), which indicate a growth of the 3 dB bandwidth from 174 to 257 nm. Finally, the increase in the SPD is also observed in the infrared domain beyond the 1062 nm pump wavelength. Note that in all these experiments, visible and infrared continua were transversally single mode (LP_{01}).

Compared with SC sources using passive holey fibers,[7] the system proposed here does not exhibit better performance in terms of SPD and bandwidth because of several unfavorable experimental conditions: 70 kHz microchip laser with too low peak power, fiber ZDW distant from pump wavelength, and small Yb^{3+}-doped area. Nevertheless, the aim of this paper to demonstrate a principle for the improvement of SC generation was fulfilled. It is also pertinent to many biomedical applications, thanks to the high repetition rate of the microchip laser. The use of a more powerful pump laser and an optimized fiber should permit achievement of clearly superior performance. Furthermore, compared with highly nonlinear fibers having a very small core, the fiber presented here does not suffer constraint regarding core size. Indeed, it is possible to compensate for the increase of core size by the amplification of pump pulses inside the waveguide so as to maintain a high surface density of pump power. Using a larger core thus raises the damage threshold of the fiber input face. In our case ($A_{eff} \approx 10\ \mu m^2$ for LP_{01} mode at 1062 nm), this threshold was about four times higher than in a highly nonlinear microstructured fiber.

In conclusion, we have presented an important concept for SC generation based on a microstructured fiber, exhibiting simultaneously nonlinear and amplifying properties. This hybrid fiber was first designed with the help of BPM calculations, demonstrating on the one hand the weak influence of the air-filling factor of the IC on multimode pump confinement losses and on the other hand its high impact on the injection rate of multimode pump power. The fabrication of this nonlinear fiber allowed us to demonstrate an improvement in visible and infrared SC generation. Indeed, the simultaneous injection of 975 nm multimode CW pump power into the IC and of 1062 nm ns pulses into the core led to the regeneration of the pulse peak power all along the fiber. This distributed amplification of the pump pulses thus permitted us to maintain the nonlinear conversion efficiency over a larger length of fiber. As a result, a noticeable increase in the SC SPD (average gain $\approx$10 dB) and an improvement in spectrum flatness were demonstrated in the 500–900 nm range.

Corresponding author P. Leproux's e-mail address is leproux@xlim.fr.

REFERENCES

1. C. Lin and R. H. Stolen, "New nanosecond continuum for excited-state spectroscopy," Appl. Phys. Lett. **28**, 216–218 (1976).
2. J. K. Ranka, R. S. Windeler, and A. J. Stentz, "Optical properties of high-delta air–silica microstructure optical fibers," Opt. Lett. **25**, 796–798 (2000).
3. A. Kudlinski, A. K. George, J. C. Knight, J. C. Travers, A. B. Rulkov, S. V. Popov, and J. R. Taylor, "Zero-dispersion wavelength decreasing photonic crystal fibers for ultraviolet-extended supercontinuum generation," Opt. Express **14**, 5715–5722 (2006).
4. J. H. Lee, Y.-G. Man, S. B. Lee, and K. Kikuchi, "Continuous-wave supercontinuum generation from a simple ring cavity laser composed of double clad Er/Yb

codoped fiber and highly nonlinear optical fiber," presented at the OSA Conference on Lasers and Electro-Optics (CLEO) Long Beach, Calif., May 21–26, 2006, paper CMGG4.
5. V. I. Kruglov, A. C. Peacock, J. D. Harvey, and J. M. Dudley, "Self-similar propagation of high-power parabolic pulses in optical fiber amplifiers," Opt. Lett. **25**, 1753–1755 (2000).
6. J. H. V. Price, K. Furusawa, T. M. Monro, L. Lefort, and D. J. Richardson, "Tunable, femtosecond pulse source operating in the range 1.06–1.33 μm based on an Yb^{3+}-doped holey fiber amplifier," J. Opt. Soc. Am. B **19**, 1286–1294 (2002).
7. W. J. Wadsworth, N. Joly, J. C. Knight, T. A. Birks, F. Biancalana, and P. St. J. Russell, "Supercontinuum and four-wave mixing with Q-switched pulses in endlessly single-mode photonic crystal fibers," Opt. Express **12**, 299–309 (2004).
8. V. Tombelaine, C. Lesvigne, P. Leproux, L. Grossard, V. Couderc, J. L. Auguste, J. M. Blondy, G. Huss, and P. H. Pioger, "Ultra wide band supercontinuum generation in air-silica holey fibers by SHG-induced modulation instabilities," Opt. Express **13**, 7399–7404 (2005).
9. M. Lehtonen, G. Genty, H. Ludvigsen, and M. Kaivola, "Supercontinuum generation in a highly birefringent microstructured fiber," Appl. Phys. Lett. **82**, 2197–2199 (2003).
10. M. Frigo and S. G. Johnson, "The design and implementation of FFTW3," Proc. IEEE **93**, Special Issue on Program Generation, Optimization, and Platform Adaptation 216–231 (2005).
11. M. Åslund, J. Canning, S. D. Jackson, A. Teixeira, and K. Lyytikäinen, "Diffraction in air-clad fibers," Opt. Express **13**, 5227–5233 (2005).
12. N. A. Issa, "High numerical aperture in multimode microstructured optical fibers," Appl. Opt. **43**, 6191–6197 (2004).

Partie 2 - Développement de sources supercontinuum dédiées à des applications biomédicales

I. Contexte

Dans les années 2000, l'engouement pour les sources supercontinuum est suscité tant de par l'intérêt qu'elles présentent en optique non linéaire pour la richesse des mécanismes physiques mis en jeu, que du point de vue de leur fort potentiel applicatif dans des domaines très variés : télécommunications, métrologie, analyse de particules (au sens large), détection à distance, spectroscopie, imagerie, etc. A travers les différents développements d'architectures de sources supercontinuum présentées dans la **Partie 1**, je fais le constat d'une demande croissante de la part d'universitaires ou d'industriels qui recherchent des solutions laser à spectre large mais présentant des caractéristiques (temporelles, spatiales, spectrales, de puissance, etc.) propres à l'application sur laquelle ils travaillent. Mes activités de recherche se tournent ainsi progressivement vers la **conception de sources supercontinuum dédiées à des applications particulières, notamment dans le domaine biomédical, tout en conservant les éléments de positionnement précédemment introduits** (design de PCF originales et priorisation de la compacité/simplicité). Cette évolution thématique se concrétise réellement dans le cadre du **projet européen NextGenPCF** (2006-2010), dans lequel je suis en charge de coordonner les activités du WP3 « Biomedical applications » (voir ci-après, **Section II**). Par ailleurs, **la création de la start-up LEUKOS** en 2006 permet de faciliter et d'accélérer l'optimisation des sources supercontinuum dédiées aux applications dans la mesure où nos partenaires peuvent désormais tester des systèmes laser directement opérationnels sur leurs dispositifs applicatifs. Cet aspect sera un véritable atout dans mes activités de recherche qui s'étendront par la suite aux systèmes d'imagerie (voir **Partie 3**).

Dans cette seconde partie du manuscrit, nous présentons quatre problématiques d'applications biomédicales ayant donné lieu au développement de sources supercontinuum dédiées en collaboration avec les partenaires correspondants. Les applications concernées sont, dans l'ordre de numérotation des sections, la cytométrie en flux (**II**), la tomographie optique cohérente (OCT) (**III**), l'imagerie à travers un tissu épais (**IV**) et enfin la microspectroscopie CARS (**V**). La référence [44] donne une bonne synthèse de cet aspect de mes activités de recherche.

II. Source déclenchée pour la cytométrie en flux

Comme introduit ci-dessus, le projet européen NextGenPCF pose le cadre dans lequel je m'implique officiellement dans la conception de sources supercontinuum dédiées à des applications bien précises. Les données clés de cet imposant projet (une vingtaine de partenaires pour un coût total de 12,2 M€) sont récapitulées en **Figure 12**. Dans ce projet, je suis responsable du WP3 (10 partenaires impliqués), consacré aux applications biomédicales des PCF et en particulier à la thérapie photodynamique (PDT) et à la cytométrie en flux (**Figure 13**). En tant que partenaire (Université de Limoges), je suis en charge de proposer une architecture de source supercontinuum pour la cytométrie en flux, en collaboration avec les partenaires suivants :

- **Heraeus** (Allemagne), qui doit fournir les matériaux bruts (tubes, capillaires et barreaux de silice) pour la fabrication des PCF ;
- **IPHT** (Allemagne), qui doit fabriquer des échantillons de PCF non linéaires ;
- **Draka** (France), qui dans la continuité doit fabriquer des PCF de façon industrielle ;
- **Altechna** (Lituanie), chargé de développer une source de pompe de type microlaser ;
- **Multitel** (Belgique), chargé de développer une source de pompe de type laser à fibre ;
- **LEUKOS** (France), qui procèdera au prototypage de la source supercontinuum ;
- **Horiba Medical** (France), qui finalement intègrera le prototype de source supercontinuum dans un cytomètre en flux.

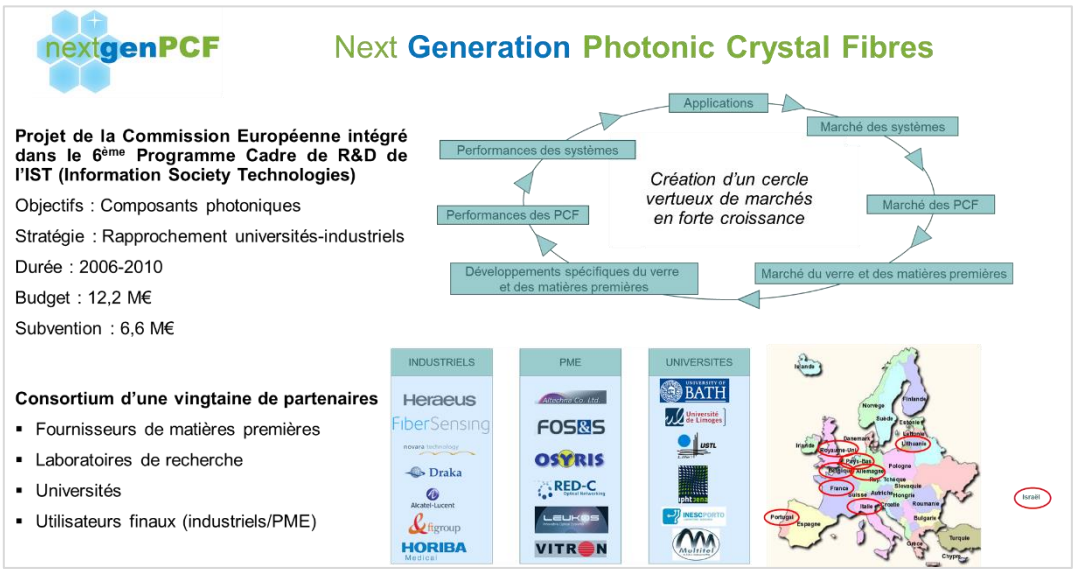

Figure 12 : Fiche d'identité du projet NextGenPCF.

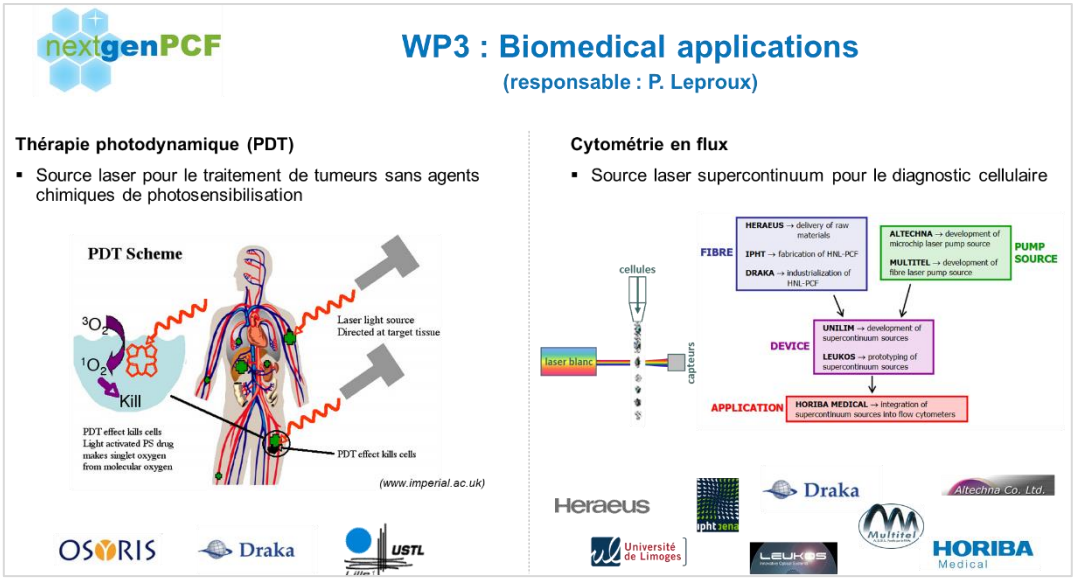

Figure 13 : Présentation du WP3 du projet NextGenPCF, consacré aux applications biomédicales des PCF.

Dans le domaine de la cytométrie en flux, la technologie supercontinuum représente une alternative très intéressante aux lasers multiples traditionnellement utilisés dans les approches multiparamétriques. L'étude de [Telford *et al.*, 2009] confirme ce fort potentiel mais fait également apparaître **des limitations en termes de densité spectrale de puissance aux longueurs d'onde visibles et surtout à cause du coût des systèmes** disponibles commercialement à l'époque (50-100 k€). Ces systèmes, testés dans l'étude, reposent sur l'utilisation d'un laser à fibre à blocage de modes (suivi d'un amplificateur à fibre) comme source de pompe de la PCF et délivrent généralement une puissance moyenne de quelques watts sur l'ensemble du spectre visible/infrarouge. Après avoir évalué plusieurs voies possibles dans le projet NextGenPCF, la solution que nous retenons finalement consiste à développer une source supercontinuum à faible coût (10-20 k€) et par voie de conséquence à faible puissance moyenne (< 6 mW), capable de délivrer des impulsions supercontinuum de façon synchronisée avec le passage des cellules dans le canal microfluidique (configuration "one cell-one shot" (OCOS), **Figure 14a**) [40]. **L'approche proposée repose sur l'utilisation d'un microlaser déclenché (*triggered microchip laser*)** comme source de pompe, dont la variation du délai de création d'impulsion (*pulse creation delay*) et de la gigue temporelle (*time jitter*) en fonction du taux de répétition (< 2 kHz) représente un aspect clé du système vis-à-vis de la précision dans le comptage des cellules (**Figure 14b**). En termes plus simples, un laser trop instable temporellement risque d'émettre l'impulsion optique trop tôt ou trop tard par rapport au passage de chaque cellule. La stabilité en amplitude pulse à pulse est une autre caractéristique clé de la solution proposée, **qui offre par ailleurs l'avantage de la compacité, d'une faible consommation électrique et d'un échauffement réduit**. Ces trois particularités font de ce type de source supercontinuum un très bon candidat pour l'intégration dans un cytomètre en flux.

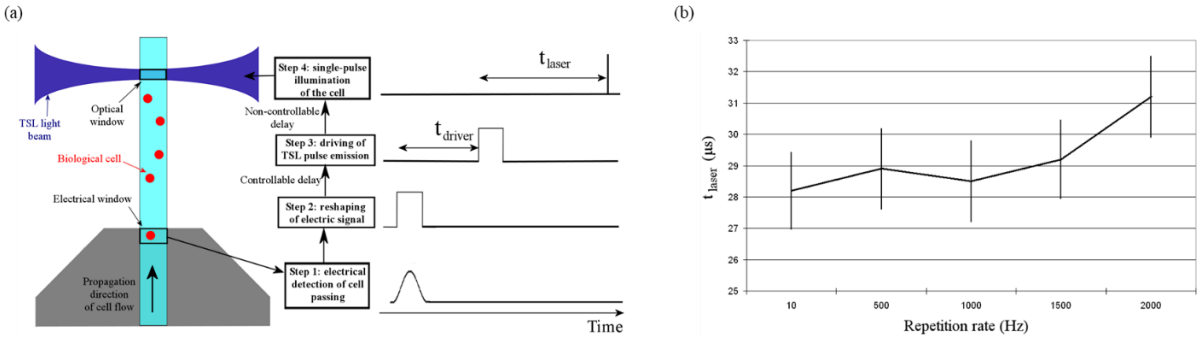

Figure 14 : (a) Principe de fonctionnement du cytomètre en flux en configuration "one cell-one shot" (OCOS). (b) Évolution du paramètre t_{laser} en fonction du taux de répétition de la source supercontinuum. t_{laser} est défini comme le temps entre le signal électrique de commande (*step 3*) et l'émission de l'impulsion laser (*step 4*). Les barres d'erreur représentent la gigue temporelle de la source supercontinuum. Figure adaptée à partir de [40].

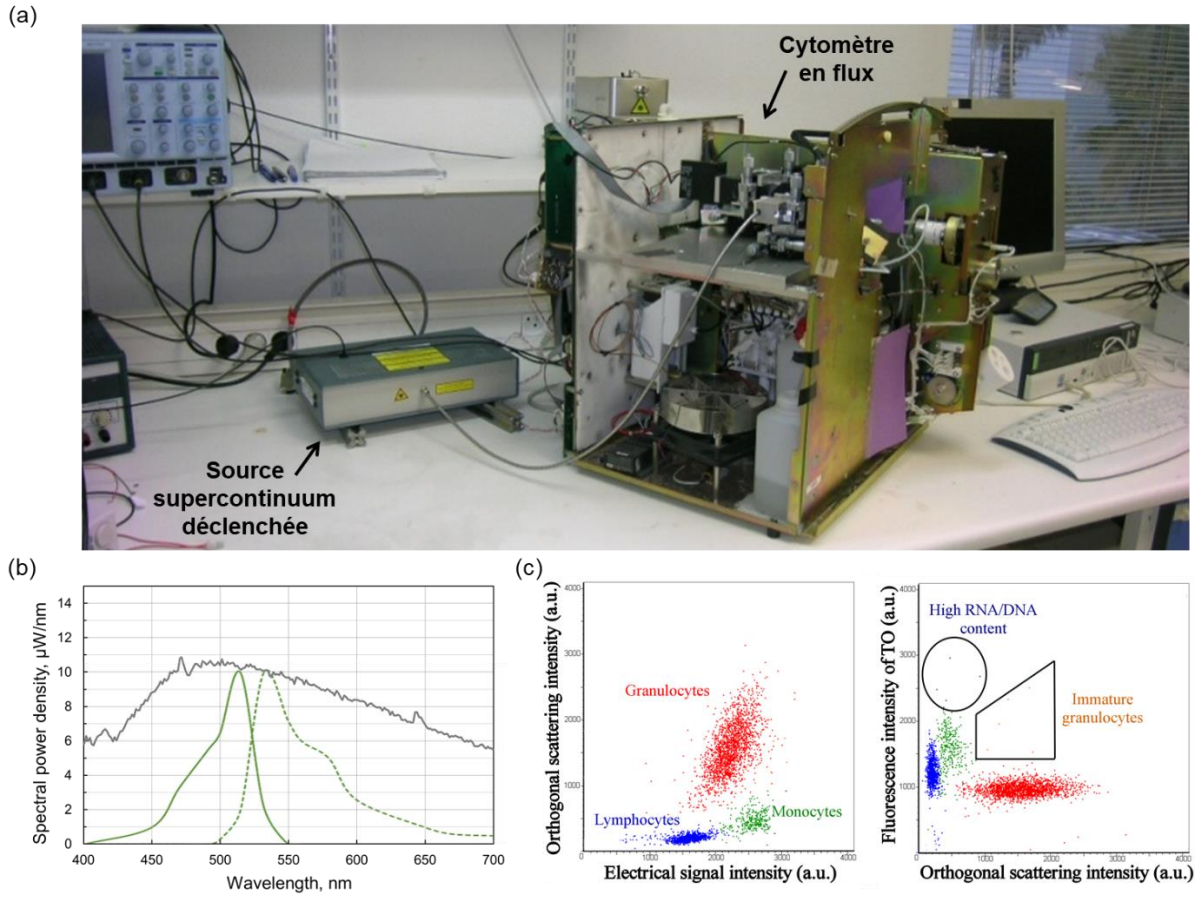

Figure 15 : (a) Photographie du système de cytométrie en flux avec excitation par le prototype de source supercontinuum déclenchée. (b) Spectres du supercontinuum (gris), d'absorption (vert) et d'émission (pointillés verts) du thiazole orange. (c) Analyse multiparamétrique (impédance, diffusion, fluorescence) de globules blancs périphériques humains en configuration OCOS sous illumination supercontinuum avec filtrage dans le bleu (482/35 nm).

Le prototype de source supercontinuum déclenchée a alors pu être testé sur une machine d'analyse hématologique en configuration OCOS (**Figure 15a**). Des mesures d'impédance, de diffusion et de fluorescence ont été réalisées sur des globules blancs périphériques humains, dont les acides nucléiques (ARN et ADN) ont été marqués au thiazole orange (TO) (voir les spectres du supercontinuum et d'absorption/émission du TO en **Figure 15b**). Les résultats finaux de l'analyse multiparamétrique ainsi effectuée sont présentés en **Figure 15c** et mettent en évidence une bonne discrimination des populations cellulaires (granulocytes, lymphocytes, monocytes). La preuve de principe de l'approche proposée est de ce fait démontrée. Néanmoins, afin d'amener la technologie à un niveau de maturité industriel, il faudrait améliorer les performances de la source supercontinuum, essentiellement en termes de stabilité temporelle et d'amplitude. Des solutions ont été proposées à cette fin, mais à ce jour et à notre connaissance, aucune d'entre elles n'est suffisamment convaincante pour un usage industriel.

Sur le plan de la couverture spectrale, la disponibilité de sources laser robustes et bas coût émettant dans l'ultraviolet (UV) est également un enjeu majeur en cytométrie en flux, du fait de l'intérêt que présentent nombre de fluorophores absorbant dans ce domaine spectral. Dans ce cadre, nous avons pu exploiter plus avant l'approche de FWM intermodal LP_{01}/LP_{11} décrite en **Partie 1, Section III** en l'étendant à la génération de supercontinuum dans l'UV-A. En effet, l'optimisation du profil de la PCF et de l'injection de la pompe a permis de démontrer un mécanisme de **FWM intermodal en cascade**, donnant lieu à la création de deux ondes anti-Stokes sur le mode LP_{11} jouant le rôle de pompes secondaires, l'une à 801 nm, l'autre à 643 nm (**Figure 16a**) [44]. Grâce à ces dernières, la génération de supercontinuum a pu couvrir la totalité de la bande des UV-A (315-400 nm).

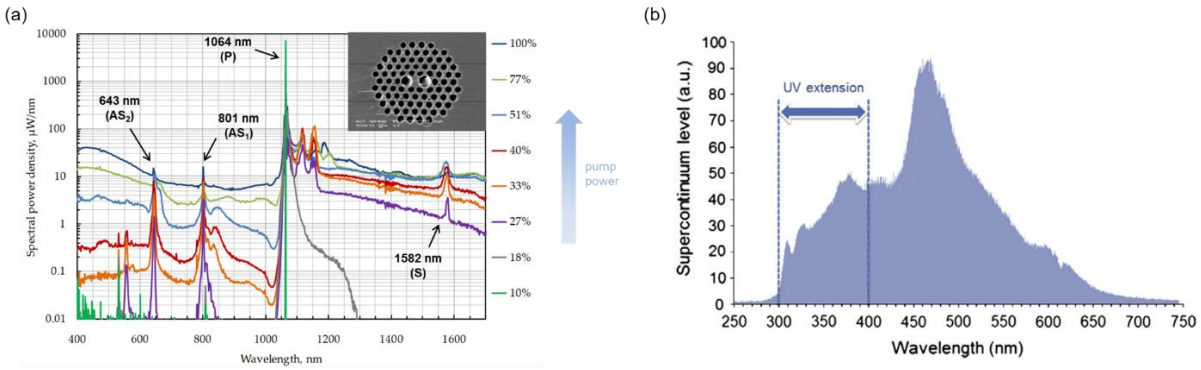

Figure 16 : Génération de supercontinuum assistée par FWM intermodal en cascade dans une PCF fortement biréfringente. (a) Construction du spectre en fonction de la puissance de pompe à 1064 nm (P). Visualisation de trois bandes latérales, correspondant respectivement à l'onde Stokes générée à 1582 nm (S), la première et la seconde ondes anti-Stokes générées à 801 nm (AS_1) et 643 nm (AS_2). Encart : image MEB de la fibre. (b) Mesure spécifique du supercontinuum dans le domaine UV/visible au maximum de puissance de pompe (100 %). La couverture spectrale de la bande 300-400 nm est mise en évidence. Figure adaptée à partir de [44].

III. Source optimisée pour la tomographie optique cohérente

A travers quelques collaborations informelles et avec le support de la société LEUKOS en termes d'intégration, j'ai eu l'occasion de travailler sur l'optimisation de sources supercontinuum visant à être utilisées comme sources d'illumination dans des expériences d'OCT. Ces travaux n'étant que ponctuels et ne s'inscrivant pas réellement dans le cadre de projets de recherche formalisés, je n'en présente ici qu'une courte synthèse par l'intermédiaire de la **Figure 17**. Celle-ci illustre **le besoin de profilage spatial et spectral des sources supercontinuum**.

L'aspect spatial concerne plus particulièrement l'OCT de type « plein champ » (FF-OCT pour *full-field optical coherence tomography*) [Wang *et al.*, 2022], pour laquelle il peut être intéressant d'utiliser une source optique (large bande) avec une forme particulière de distribution transversale d'énergie. La **Figure 17 (en haut à gauche)** montre une comparaison entre un faisceau monomode de type gaussien (profil conventionnel à la sortie d'une PCF) et un faisceau multimode de forme carrée après injection du supercontinuum dans une fibre optique adaptée (expérience réalisée en partenariat avec LEUKOS).

Sur le plan spectral, il est bien connu que les performances des systèmes OCT, notamment en termes de résolution axiale, dépendent de la longueur d'onde centrale, de la largeur spectrale et du profil spectral de la source d'illumination [Swanson *et al.*, 1992]. A cet égard, les sources supercontinuum sont naturellement des solutions attractives et, dans une certaine mesure, customisables grâce au choix du laser de pompe et du design de PCF [Humbert *et al.*, 2006 ; Aguirre *et al.*, 2006]. Dans notre cas, il a pu être démontré une résolution axiale de l'ordre du micromètre avec une source supercontinuum sub-nanoseconde cadencée à quelques dizaines de kHz [Yadav *et al.*, 2011 ; Heise *et al.*, 2012]. Correctement filtrée, cette source peut offrir un profil spectral de type gaussien (idéal pour l'OCT) avec une largeur nettement supérieure à celle d'une diode superluminescente (**Figure 17, en haut à droite**), conduisant à une forte amélioration de la résolution axiale.

Pour terminer cette courte section, nous présentons en **Figure 17** quelques exemples de résultats obtenus, dans différentes plages spectrales et sur différents types d'échantillons, par les partenaires avec lesquels j'ai collaboré sur l'optimisation de la source supercontinuum (intégrée dans chaque cas par la société LEUKOS). Dans le visible (500-600 nm), un système original d'OCT spectroscopique a permis d'enregistrer la signature, à la fois spatiale et spectrale, d'une solution d'éosine maintenue entre deux lamelles de microscope [23]. Dans deux fenêtres infrarouges différentes (625-1000 nm et 1360-1740 nm), la configuration SD-OCT (*spectral domain* OCT) a été appliquée, respectivement, à l'imagerie de la surface oculaire [Yadav *et al.*, 2011] et de l'ongle humains.

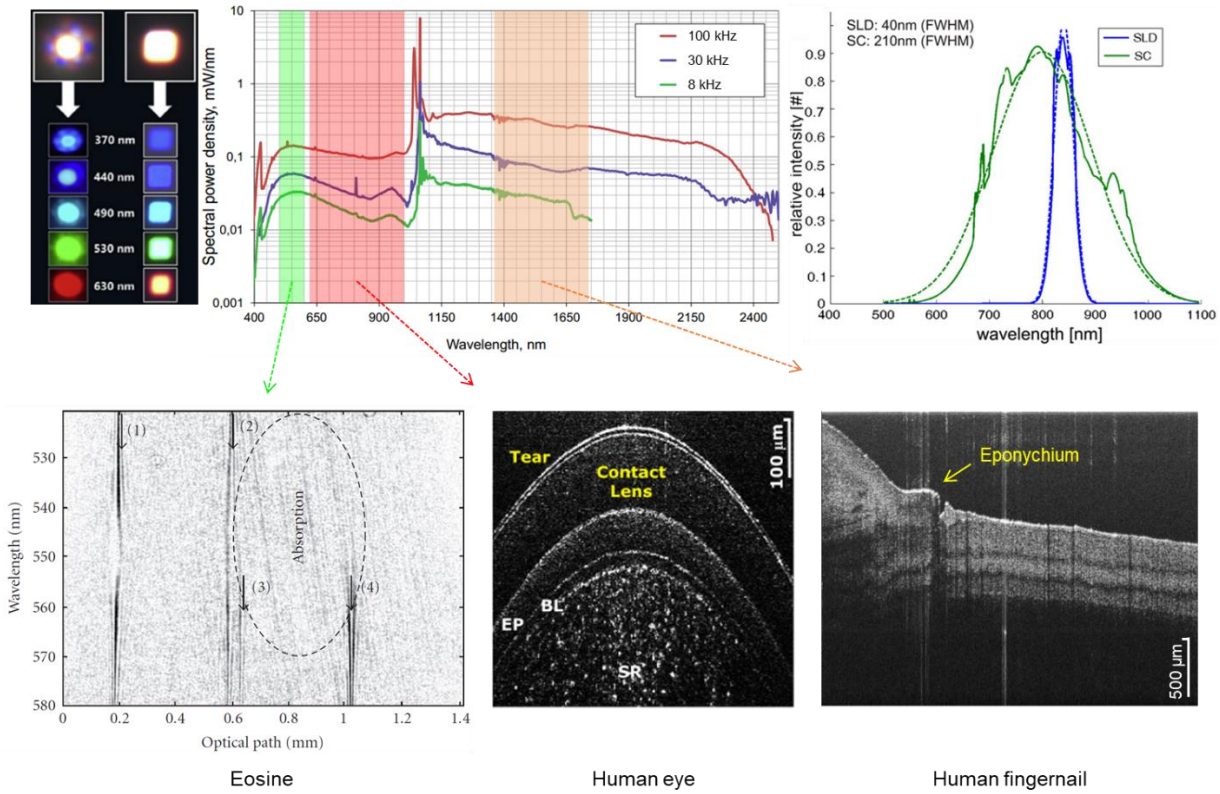

Figure 17 : Illustration de l'application des sources supercontinuum à la tomographie optique cohérente (OCT). **En haut à gauche, sur fond noir :** profilage spatial du faisceau pour l'OCT plein champ (à gauche, faisceau monomode de type gaussien ; à droite : faisceau multimode de forme carrée). **En haut au milieu :** exemples de spectres de sources supercontinuum sub-nanoseconde pour différents taux de répétition (mesures LEUKOS), appliquées à l'OCT par filtrage dans différentes plages spectrales (**en bas :** 500-600 nm, étude d'une solution d'éosine, *Université de Franche-Comté* ; 625-1000 nm : imagerie de la surface oculaire, *Université de Rochester, USA* ; 1360-1740 nm : imagerie de l'ongle, *Upper Austrian Research GmbH, Autriche*). **En haut à droite :** comparaison des spectres d'une diode superluminescente (SLD) et d'une source supercontinuum filtrée (SC) avec en pointillés l'approximation gaussienne correspondante. Figure construite à partir de [23] et de [Yadav *et al.*, 2011 ; Heise *et al.*, 2012].

IV. Emission dans les fenêtres biologiques pour l'imagerie à travers un tissu épais

Dans le cadre d'une collaboration ponctuelle avec le Pr. Alfano (*The City College of New York, USA*), j'ai travaillé sur un design de source supercontinuum permettant de maximiser la densité spectrale de puissance dans l'infrarouge, approximativement entre 1 et 2 µm. Cette plage spectrale contient en effet **deux fenêtres « biologiques », nommées II (1100-1350 nm) et III (1600-1870 nm)**, dans lesquelles la diffusion et l'absorption, limitées, autorisent un coefficient d'atténuation minimal [Sordillo *et al.*, 2014] (**Figure 18b**). Il est donc intéressant de pouvoir disposer de sources optiques à forte brillance dans ces fenêtres, telles que les sources supercontinnum.

La stratégie retenue consiste à pomper une fibre optique standard, de type « hautement non linéaire à dispersion décalée » (HNL-DSF), près de son zéro de dispersion avec un laser à fibre émettant à 1,55 µm (système commercial de diode laser amplifiée). Cette méthode permet d'obtenir un élargissement spectral (relativement) symétrique de part et d'autre de la pompe et offre ainsi une alternative plus simple et moins coûteuse à l'utilisation de PCF. Le supercontinuum présenté en **Figure 18c** a pu être généré, avec des impulsions de 40 ps, un taux de répétition de 6 MHz et une puissance moyenne totale d'environ 700 mW. La densité spectrale de puissance est supérieure à 200 µW/nm dans les fenêtres II et III. Comme précédemment, l'intégration du système a été réalisée par la société LEUKOS.

Ce rayonnement supercontinuum a été appliqué à l'imagerie à travers un milieu diffusant au moyen d'une simple expérience d'imagerie de transmission, dans laquelle trois fils de diamètres différents sont observés à travers un tissu biologique (poulet) d'épaisseur 7 mm (**Figure 18a**). Une comparaison avec une lampe incohérente (halogène) a été effectuée, mettant en évidence un contraste a priori supérieur dans le cas de l'illumination supercontinuum dans les fenêtres II et III (**Figure 18c**). Une étude plus complète a été menée afin de quantifier le contraste de l'image obtenue en fonction de l'épaisseur du tissu (de 2 à 10 mm) [52]. Celle-ci conclut à une supériorité de la source supercontinuum sur la lampe halogène dans la troisième fenêtre uniquement, mais des mesures complémentaires permettraient assurément d'aboutir à des conclusions plus consistantes. Également, il serait intéressant d'évaluer les potentialités des sources supercontinuum pour l'imagerie à travers un tissu épais dans la fenêtre IV (2100-2300 nm).

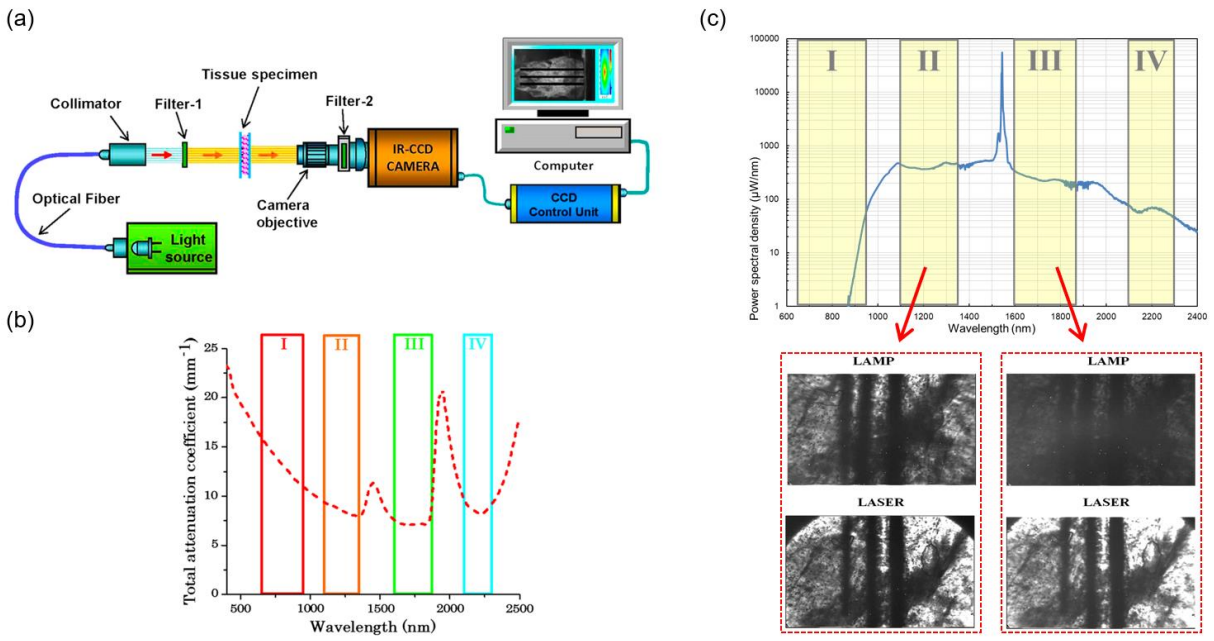

Figure 18 : Imagerie de tissu épais sous illumination supercontinuum. (a) Montage expérimental. (b) Évolution de l'atténuation d'un tissu biologique en fonction de la longueur d'onde, faisant apparaître quatre fenêtres optiques de travail. (c) Utilisation d'un rayonnement supercontinuum infrarouge (spectre tracé en bleu) pour l'imagerie dans les fenêtres II (1100-1350 nm) et III (1600-1870 nm) ; visualisation de trois fils de diamètres différents à travers un tissu d'épaisseur 7 mm avec une illumination par lampe halogène (LAMP) et par supercontinuum (LASER) (mesures réalisées par le groupe du Pr. Alfano, *The City College of New York, USA*). Figure (a,b) adaptée à partir de [Sordillo *et al.*, 2014].

V. Source à double sortie pour la microspectroscopie CARS

La micro(spectro)scopie CARS est une technique d'analyse et d'imagerie sans marquage, chimiquement sélective, d'échantillons biologiques ou chimiques. Elle repose sur l'exploitation du phénomène de diffusion Raman anti-Stokes cohérente, mécanisme non linéaire d'ordre trois faisant intervenir un FWM et mettant en jeu les niveaux d'énergie vibrationnels du milieu. A la suite de la publication de [Zumbusch *et al.*, 1999], démontrant un système de microscopie multiphotonique basé sur l'effet CARS, de nombreuses études sont parues sur l'application de cette technologie à l'imagerie biomédicale et, par voie de conséquence, sur le développement de sources laser adaptées.

Dans le cas particulier de la microspectroscopie CARS dite « multiplex », la combinaison d'un microscope et d'un spectroscope permet de cartographier spectralement l'échantillon : pour chaque point de mesure, un spectre CARS est acquis. Dans ce cas de figure, l'échantillon est excité simultanément par **une onde monochromatique, appelée onde de pompe**, et par **une onde large bande, appelée onde Stokes** (comprenant des longueurs d'onde supérieures à celle de la pompe). Ainsi, au début des années 2000, les systèmes laser faisant intervenir la génération d'un supercontinuum dans une PCF vont susciter beaucoup d'intérêt pour la microscopie CARS « large bande » [Kano & Hamaguchi, 2003 ; Paulsen *et al.*, 2003 ; Kee & Cicerone, 2004]. C'est dans ce contexte que se présente en 2007 une opportunité de collaboration avec le Pr. Kano de l'Université de Tokyo, Japon, associant notre savoir-faire en matière de génération de supercontinuum (et d'intégration de sources supercontinuum) à celui des collègues japonais dans le domaine de la microspectroscopie CARS. Nous présentons ci-dessous les principaux jalons de cette collaboration, toujours effective aujourd'hui.

(1) Dans un premier temps, nous avons démontré qu'il était possible et pertinent d'utiliser des sources supercontinuum sub-nanoseconde pour la microspectroscopie CARS. Cette preuve de principe a pu être obtenue dans le domaine visible au moyen d'un système à double pompage 532/1064 nm [19] (**Figures 19A, 19B, 19C, 19D**) et dans le domaine infrarouge au moyen d'un système à simple pompage à 1064 nm [24] (**Figures 19E, 19F, 19G**). **Dans le premier cas,** l'onde de pompe à 532 nm et un supercontinuum sur la plage 550-650 nm sont utilisés. La mesure du spectre (**Figure 19B**) fait apparaître la présence nette d'ondulations dues à l'effet SRS en régime de dispersion normal, le couplage de la pompe à 1064 nm dans la PCF étant insuffisant pour que la XPM soit prédominante (cas observé dans [10]). De même, le diagramme spectro-temporel (**Figure 19B**) témoigne de la présence importante de l'effet SRS à travers une forte déplétion de la partie centrale de l'impulsion de pompe à 532 nm, qui se répercute sur l'ensemble du supercontinuum côté Stokes (phénomène similaire observé dans [45]). Malgré ces conditions non optimales en termes de profil spectral et de recouvrement temporel pompe/Stokes, les spectres CARS de différents liquides purs ont pu être mesurés sur la plage 600-3200 cm^{-1} (**Figures 19C et 19D**), avec un temps d'exposition néanmoins long (de 10 s à 1 min). **Dans le second cas,** l'excitation de l'échantillon est réalisée avec l'onde de pompe à 1064 nm et un supercontinuum s'étendant de 1100 à 1700 nm, dont le profil spectral est très irrégulier (**Figure 19E**). Des spectres et des cartographies CARS d'une bille de polystyrène (**Figure 19F**) et de cellules de tabac BY2 (**Figure 19G**) ont pu être obtenus avec un temps d'exposition de quelques centaines de ms, le

rapport signal sur bruit restant cependant insuffisant dans la zone d'empreinte digitale pour les cellules BY2.

Ces résultats ont permis de montrer l'intérêt, pour la microspectroscopie CARS multiplex, d'utiliser des impulsions sub-nanoseconde plutôt que picoseconde [Petrov & Yakovlev, 2005] ou femtoseconde [Kano & Hamaguchi, 2005 ; Mitrokhin *et al.*, 2007]. D'une part, ce régime impulsionnel conduit à une **excellente résolution spectrale** du fait de la faible largeur de raie du microlaser de pompe (< 0,1 cm^{-1}). De ce fait, en pratique, cette résolution est limitée par celle du spectroscope. D'autre part, **le signal CARS peut être acquis en une seule mesure sur une large bande spectrale (> 2500 cm^{-1})** sans avoir à réajuster le retard entre les impulsions de pompe et Stokes. Ceci signifie que la dispersion de vitesse de groupe n'est pas critique pour le processus CARS lorsque le supercontinuum est généré avec des impulsions sub-nanoseconde, contrairement aux régimes picoseconde ou femtoseconde.

(2) Dans un second temps, en tenant compte des limites apparues lors de l'étape précédente, nous avons cherché à optimiser un certain nombre de caractéristiques :

- augmentation du taux de répétition du microlaser de pompe (passage de quelques kHz à > 30 kHz) et de la puissance moyenne/crête disponible sur chaque voie (> 300 mW au total) ;
- amélioration du profil spectral du supercontinuum et du recouvrement temporel pompe/Stokes en intervenant sur la PCF (profil, longueur, connectorisation), pompée à 1064 nm ;
- amélioration drastique de la stabilité en passant d'un dispositif de laboratoire (monté sur *breadboard*) à une source laser intégrée à double sortie (une sortie « pompe » en espace libre et une sortie « Stokes » fibrée), grâce au support de la société LEUKOS.

Cette nouvelle génération de source laser sub-nanoseconde pour la microspectroscopie CARS est illustrée par les **Figures 20A** et **20B**. La **Figure 20C** montre en outre comment cette source s'intègre dans le système de microspectroscopie. Afin d'en valider les performances, une cartographie de nématode *Caenorhabditis elegans* a été réalisée (**Figure 20D**) [36]. Le profil spectral obtenu avec un temps d'exposition de 100 ms se caractérise par un bon contraste vibrationnel à la fois dans les régions d'étirement CH (2800-3000 cm^{-1}) et d'empreinte digitale (1000-2000 cm^{-1}), **ce qui confirme l'efficacité du processus CARS multiplex sur une large bande**. Les images CARS obtenues pour différentes valeurs du décalage Raman (*i.e.*, pour différents modes vibrationnels) font apparaître de façon similaire les lipides insaturés stockés sous forme de gouttelettes lipidiques dans le nématode. Ceci corrobore le bon fonctionnement large bande et témoigne par ailleurs de la stabilité de la source. Enfin, le même type de source supercontinuum à double sortie a été utilisé par des collaborateurs du Max Plank Institute for Polymer Research, Allemagne, pour l'étude du tissu musculaire chez le rat [48]. La **Figure 20E**, extraite de cette étude, illustre l'intérêt que présente le régime sub-nanoseconde en termes de résolution spectrale à travers la mesure de spectres CARS « riches » sur la plage 2800-3100 cm^{-1}. Nous aborderons plus avant l'exploitation de cette bande dans la **Partie 3**.

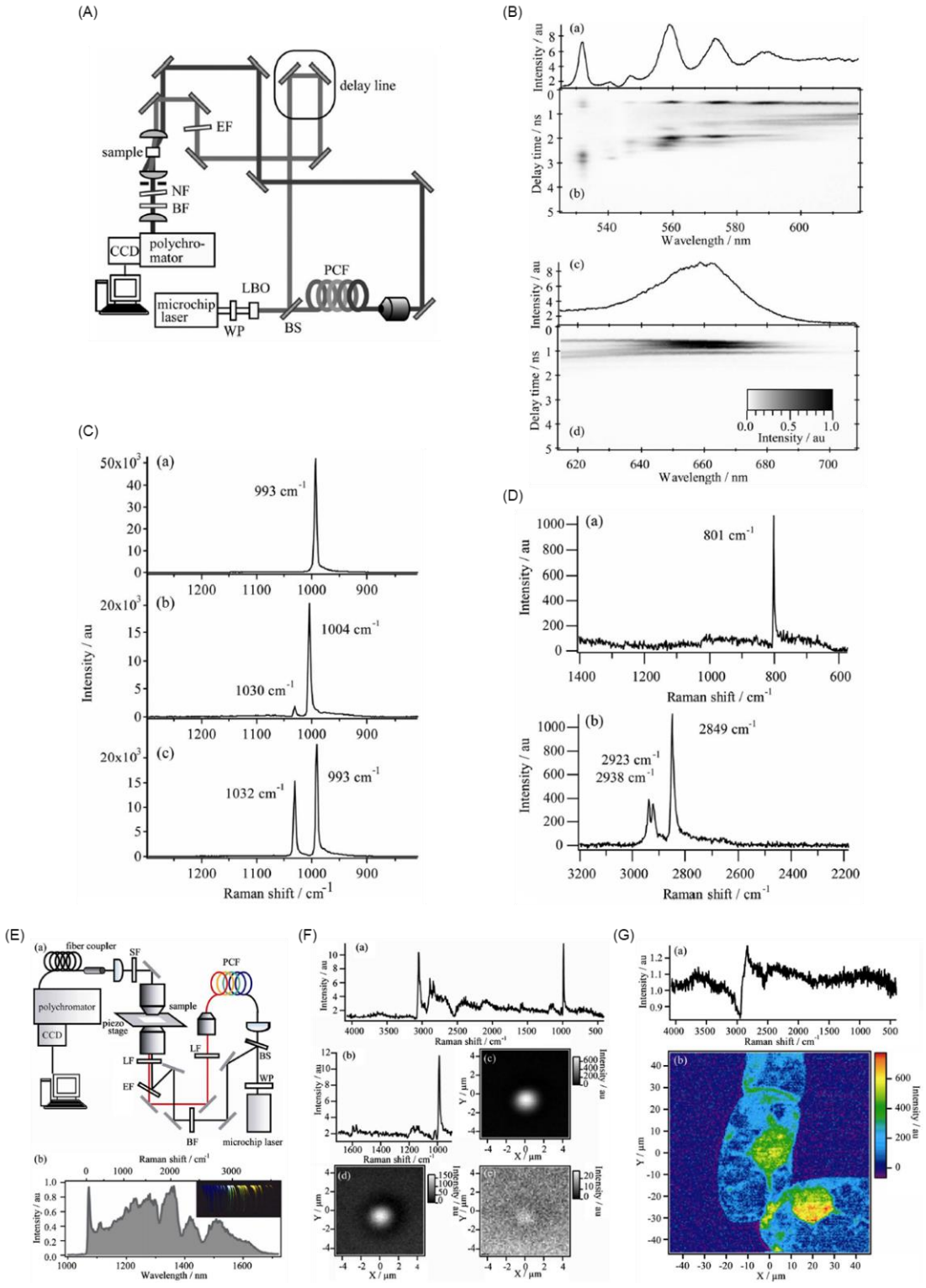

Figure 19 : Preuve de principe de l'application des sources supercontinuum sub-nanoseconde à la microspectroscopie CARS dans les domaines (A,B,C,D) visible et (E,F,G) infrarouge. **Dans le visible :** (A) montage expérimental, (B) profil spectral et diagramme spectro-temporel (mesuré avec une caméra à balayage) du supercontinuum Stokes, (C,D) spectres CARS (dans l'ordre) du benzène, du toluène, de la pyridine (t_{spec}=10 s) et du cyclohexane (t_{spec}=1 min). **Dans l'infrarouge :** (E) montage expérimental et profil spectral du supercontinuum Stokes, (F,G) spectres et images CARS d'une bille de polystyrène (t_{spec}=1 s, t_{pix}=100 ms) et de cellules de tabac BY2 (t_{spec}=300 ms, t_{pix}=300 ms). t_{spec} : temps d'exposition pour l'acquisition d'un spectre ; t_{pix} : temps d'exposition par pixel pour la réalisation d'une cartographie. Figure adaptée à partir de [19,24].

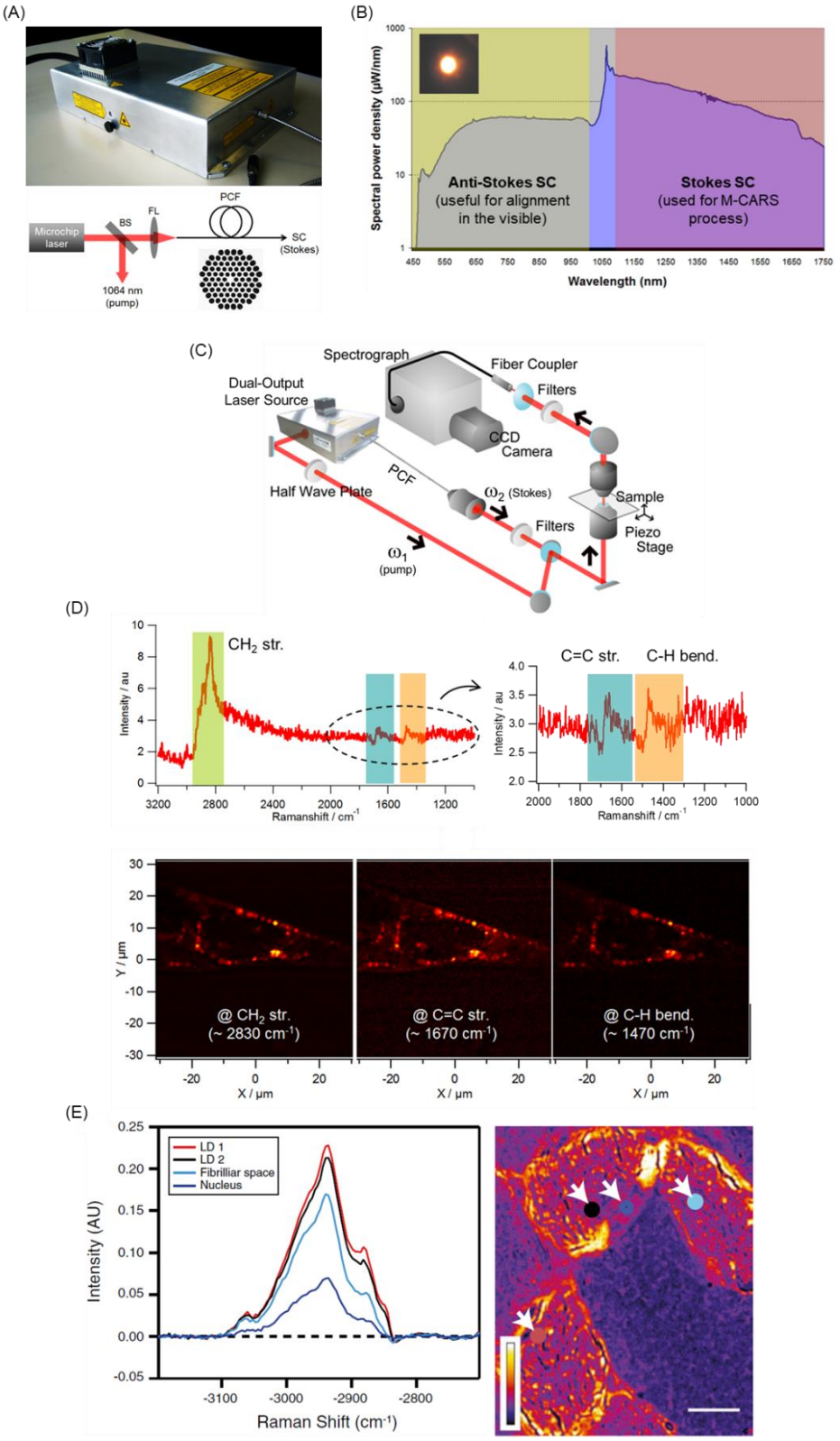

Figure 20 : Nouvelle génération de source laser sub-nanoseconde à double sortie pompe/supercontinuum pour la microspectroscopie CARS (~0,8 ns, 33 kHz, > 300 mW total). (A) Photographie et illustration du dispositif réalisé en collaboration avec LEUKOS. (B) Profil spectral de la sortie Stokes (supercontinuum). (C) Intégration de la source dans le système de microspectroscopie. (D) Spectres et images CARS de nématode *Caenorhabditis elegans* (t_{spec}=100 ms, t_{pix}=100 ms, 201px*201px). (E) Spectres et images CARS de tissu musculaire de rat (t_{spec}=1 s, t_{pix}=1 s, 81px*81px, barre d'échelle 20 µm). Figure adaptée à partir de [36,48].

Par la suite, dans le cadre de la collaboration franco-japonaise, cette génération de « source CARS » intégrée a permis aux collègues japonais de conduire un certain nombre d'études biologiques ayant donné lieu à des publications communes. En voici quelques exemples : imagerie multicolore résolue en temps d'une cellule de levure bourgeonnante (zygote de *Saccharomyces cerevisiae* et *Saccharomyces bayanus*) [32], imagerie multicolore du cheveu humain avec/sans traitement et analyse de la structure secondaire des protéines [37], imagerie moléculaire tétra-modale de cellules vivantes [38], imagerie spectrale multiplex et multimodale de la cornée de rat [55], imagerie multimodale de la rétine de rat [66]. Nous précisons que l'aspect multimodal (combinaison de la technique CARS avec d'autres modalités d'imagerie) sera traité dans la **Partie 3** de ce manuscrit.

(3) Plus récemment, nous avons proposé une nouvelle architecture de source CARS afin d'augmenter significativement le taux de répétition et diminuer la durée d'impulsion. L'objectif de ce travail est d'aboutir au meilleur compromis possible entre les régimes picoseconde (cadencé généralement à quelques dizaines de MHz) et (sub)nanoseconde (cadencé à quelques dizaines de kHz), en adéquation avec les besoins de l'application : réaliser des cartographies CARS d'échantillons biologiques (*i.e.*, potentiellement fragiles) le plus rapidement possible (et avec un rapport signal sur bruit convenable). **L'architecture introduite repose sur une configuration MOFA** (*master oscillator fiber amplifier*), comportant un oscillateur de type microlaser et un amplificateur à fibres dopées ytterbium (**Figure 21A**). Plus précisément, l'oscillateur est un microlaser à déclenchement passif constitué d'un cristal de Nd:YVO_4 collé à un absorbant saturable et pompé à 808 nm, délivrant à 1064 nm des impulsions de 85 ps à 0,82 MHz avec une polarisation linéaire. L'amplificateur à fibres comprend un préamplificateur et un booster utilisant respectivement une fibre dopée monomode et une fibre dopée à double gaine et large aire modale, toutes deux à maintien de polarisation afin de disposer d'une onde de pompe, après amplification, linéairement polarisée. Cette dernière est divisée en deux, une part servant de pompe pour le processus CARS et l'autre part étant injectée dans une PCF afin de générer un supercontinuum utilisé comme radiation Stokes. La puissance moyenne totale disponible en sortie des deux voies est d'environ 2 W. La **Figure 21B** montre le profil spectral du supercontinuum généré après collimation par un miroir parabolique hors axe (mesure non corrigée de la réponse du spectromètre) [70].

Combinée à un système de détection très performant, cette source a permis de cartographier des billes de polystyrène sur la plage 600-3600 cm^{-1} **avec un temps d'exposition par pixel record, inférieur à 1 ms** (0,8 ms, limité par le temps de lecture de la caméra CCD) [70]. Également, la source a été appliquée à l'imagerie CARS de cellules HeLa vivantes à différentes phases du cycle cellulaire. La **Figure 21C** présente les résultats obtenus dans le cas de la phase M (mitose, ou division cellulaire), mettant notamment en évidence la distribution des lipides, des protéines et des acides nucléiques. En particulier, la superposition de l'image CARS à 791 cm^{-1} (visualisation de l'ADN/ARN) et d'une image SHG (mettant en évidence le fuseau mitotique) illustre la capture des chromosomes par les fibres de ce fuseau (**Figure 21D**). Ici le temps d'exposition par pixel s'élevait à 50 ms, mais par la suite il a pu être réduit à 10 ms et même 1,8 ms lors de cartographies de cellules A549 vivantes [72].

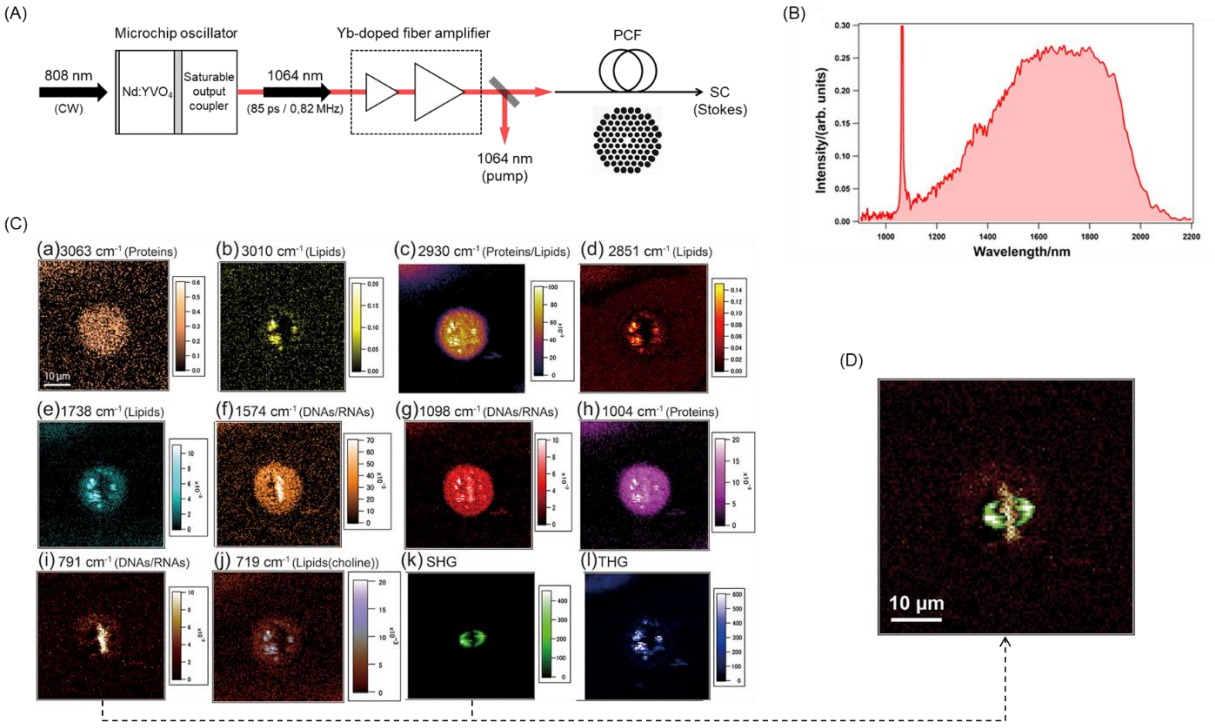

Figure 21 : Source laser sub-100-ps à architecture MOFA (*master oscillator fiber amplifier*) pour la microspectroscopie CARS rapide (85 ps, 0,82 MHz, ~2 W total). (A) Design de la source. (B) Profil spectral de la sortie supercontinuum Stokes (mesure non corrigée de la réponse du spectromètre). (C) Images CARS et SHG/THG de cellules HeLa vivantes en phase M (mitose) (t_{pix}=50 ms, 101px*101px). (D) Superposition de l'image CARS à 791 cm^{-1} et de l'image SHG, mettant en évidence la capture des chromosomes par les fibres du fuseau mitotique. SHG : *second harmonic generation* ; THG : *third harmonic generation*. Figure (B,C,D) adaptée à partir de [70].

(4) La toute dernière génération de source CARS que nous avons conçue repose sur une architecture à base de diode laser modulée et amplifiée, qui présente une meilleure stabilité et durée de vie que la solution précédente et permet de s'affranchir de la ligne à retard dans le système de microspectroscopie. Cette source étant développée dans le cadre de la mise au point d'un instrument complet de microscopie multimodale, nous l'introduirons en détails dans la **Partie 3**.

Synthèse Partie 2 avec indicateurs

Développement de sources supercontinuum dédiées à des applications biomédicales				
Articles	Communications internationales	Actes de congrès internationaux	Communications nationales	Brevets
41	28 dont 6 invitées	6	6	3

Mots clés

Design de source laser, cytométrie en flux, tomographie optique cohérente, imagerie à travers un tissu épais, microspectroscopie CARS

Points saillants / points forts

- Activité initiée et dynamisée grâce au projet européen NextGenPCF (~ 20 partenaires, 2006-2010)
- Optimisation de sources dédiées aux applications facilitée par la création de la start-up LEUKOS (tests réguliers de systèmes supercontinuum sur les dispositifs applicatifs des partenaires)
- Nombreuses valorisations en collaboration avec les partenaires, notamment autour de la microspectroscopie CARS

Collaborations principales

Horiba Medical (Montpellier), Horiba Scientific (Villeneuve-d'Ascq), FEMTO-ST (Besançon), Upper Austrian Research GmbH (Autriche), The City College of New York (USA), Universités de Tokyo/Tsukuba/Kyushu (Japon)

Contrats de recherche

Titre	**Type**	**Période**	**Rôle**	**Nombre de partenaires**	**Coût total**	**Financement XLIM**
Next Generation Photonic Crystal Fibres (NextGenPCF)	Projet intégré (IP) du programme FP6-IST	2006-2010	Partenaire et coordinateur du WP3 (10 partenaires)	20	12,2 M€	350 k€
Development of CARS micro-spectroscopy using compact	Projet bilatéral CNRS/JSPS	2008-2009	Responsable équipe française	2	N/A	20 k€

sub-nanosecond supercontinuum						
Développement d'un prototype de microscope CARS (SensiCARS)	Projet AVRUL-OSEO Détection Innovation Laboratoires (DIL)	2010-2012	Porteur	3	285 k€	50 k€
Development of novel molecular imaging method for visualization of functions of intravital lipids	Partenariat Hubert Curien (PHC) SAKURA	2012-2013	Responsable équipe française	2	N/A	12 k€
Study of chiral molecular fingerprint using an intense white light laser source in visible	Projet bilatéral CNRS/JSPS	2014-2015	Responsable équipe française	2	N/A	20 k€
TOTAL						**452 k€**

Publications majeures (insérées ci-après)

- *Compact supercontinuum sources and their biomedical applications*, A. Labruyère, A. Tonello, V. Couderc, G. Huss, **P. Leproux**, Optical Fiber Technology, vol. 18, no. 5, pp. 375-378, 2012 (référence [44] de la liste complète)
- *Flow cytometer based on triggered supercontinuum laser illumination*, N. Rongeat, **P. Leproux**, V. Couderc, P. Brunel, S. Ledroit, D. Cremien, S. Hilaire, G. Huss, P. Nérin, Cytometry Part A, vol. 81, no. 7, pp. 611-617, 2012 (référence [40] de la liste complète)
- *New opportunities offered by compact sub-nanosecond supercontinuum sources in ultrabroadband multiplex CARS microspectroscopy*, **P. Leproux**, V. Couderc, A. de Angelis, M. Okuno, H. Kano, H. Hamaguchi, Journal of Raman Spectroscopy, vol. 42, no. 10, pp. 1871-1874, 2011 (référence [36] de la liste complète)

Encadrement de thèses de doctorat

- **Nelly Rongeat**, « Utilisation de sources polychromes pour le diagnostic cytologique : application à l'hématologie » (2008-2011, **participation à l'encadrement**, directeur de thèse : Vincent Couderc)
- **Annalisa de Angelis**, « Electro-optical pump-probe system suitable for the investigation of electroporated biological cells » (2009-2012, **participation à l'encadrement**, directeur de thèse : Vincent Couderc)

Autres encadrements

- **Alexis Labruyère**, post-doctorant (2007-2010) dans le cadre du projet européen NextGenPCF
- **Kotaro Hiramatsu**, doctorant à l'Université de Tokyo, stage de 2 semaines à XLIM sur la génération de supercontinuum pour la microspectroscopie CARS (2014)
- **Guillaume Bascoul**, « Investigation of Multiplex-CARS microspectroscopy based on miniature laser source », stage 4^{e} année INSA Toulouse comprenant 1 mois au Japon (2009)

Publications majeures Partie 2

Optical Fiber Technology 18 (2012) 375–378

Contents lists available at SciVerse ScienceDirect

Optical Fiber Technology

www.elsevier.com/locate/yofte

Invited Papers

Compact supercontinuum sources and their biomedical applications

Alexis Labruyère [a], Alessandro Tonello [a], Vincent Couderc [a], Guillaume Huss [b], Philippe Leproux [a,b,*]

[a] Xlim Research Institute, UMR CNRS 7252, University of Limoges, 123 Av. Albert Thomas, 87060 Limoges Cedex, France
[b] Leukos Innovative Optical Systems, Ester Technopole, 1 Av. d'Ester, 87069 Limoges Cedex, France

ARTICLE INFO

Article history:
Available online 11 September 2012

Keywords:
Microchip laser
Photonic crystal fiber
Compact supercontinuum source
Biomedical applications
Flow cytometry
Multiplex CARS
Microspectroscopy
Optical coherence tomography

ABSTRACT

Recent developments of compact white-light supercontinuum laser sources are reviewed. Basically these sources make use of a sub-nanosecond microchip laser and a photonic crystal fiber, leading to spectral broadening in the ultraviolet, visible and infrared ranges. The applicability of such supercontinuum sources to the biomedical field is introduced, with the demonstration of promising results in flow cytometry, CARS microscopy and optical coherence tomography. Their attractive benefits in terms of size, robustness, stability and cost are highlighted.

1. Introduction

The process of supercontinuum generation in a photonic crystal fiber (PCF) is well-known for designing spatially coherent white-light sources, emitting light simultaneously in the ultraviolet (UV), visible and infrared (IR) ranges. In this context, the use of a microchip laser as the pump source of the PCF allows to engineer very compact supercontinuum systems, which thus become excellent candidates as illumination sources for many kinds of applications. In particular, numerous studies have already revealed the applicability and effectiveness of such sources in the biomedical field.

In this paper, we review several original methods for building a compact supercontinuum source, through the consideration of three basic applications: flow cytometry, CARS microscopy and optical coherence tomography (OCT). In each case, the key nonlinear process behind supercontinuum generation is highlighted and discussed, and the corresponding integrated solution, commercially available, is introduced.

2. Triggered, UV/visible, supercontinuum source for flow cytometry

2.1. Cascaded four-wave mixing for UV/visible spectral extension

So as to excite the fluorochromes that are commonly used in flow cytometry, the optical source has to cover the UV/visible part of the spectrum. For enhancing supercontinuum generation in this range, intermodal four-wave mixing (FWM) in a PCF can be used. Such principle has been previously demonstrated in a pure silica highly birefringent PCF [1], in a structured-core GeO_2-doped PCF [2] or even in a structured-core multicomponent glass PCF [3]. We show hereafter that the concept can be extended to cascaded FWM, thus increasing even more the conversion efficiency in the visible and UV.

As in Ref. [1], a Nd:YAG Q-switched microchip laser is coupled to a pure silica highly birefringent PCF. Here the geometrical parameters of the fiber (see inset of Fig. 1) are the following: $d \sim 2.7$ µm, $\Lambda \sim 3.35$ µm, resulting in an air-filling fraction of ~0.8. The evolution of the spectrum at the PCF output has been recorded as a function of the pump power, as exhibited in Fig. 1. It is noticeable in this graph that visible supercontinuum generation initiates from two distinct lines located at 801 nm and 643 nm respectively. These waves are generated through cascaded FWM. First, intermodal degenerate FWM gives birth to a Stokes wave at 1582 nm (S) on the LP_{01} mode and an anti-Stokes wave at 801 nm (AS_1) on the LP_{11} mode. Then, a second, non-degenerate FWM process takes place, mixing the pump (P), AS_1 and S waves, and a new anti-Stokes wave (AS_2), which appears at 643 nm on the LP_{11} mode. Therefore AS_1 and AS_2 act as secondary pumps that support frequency generation in the visible range. Finally the combination of cascaded FWM and cross-phase modulation (XPM) allows to increase the spectral power density in the blue[1]/UV and to enhance spectral broadening towards shorter

* Corresponding author at: Xlim Research Institute, UMR CNRS 7252, University of Limoges, 123 Av. Albert Thomas, 87060 Limoges Cedex, France.
E-mail address: philippe.leproux@xlim.fr (P. Leproux).

1068-5200/$ - see front matter © 2012 Elsevier Inc. All rights reserved.
http://dx.doi.org/10.1016/j.yofte.2012.08.003

[1] For interpretation of color in Fig. 2, the reader is referred to the web version of this article.

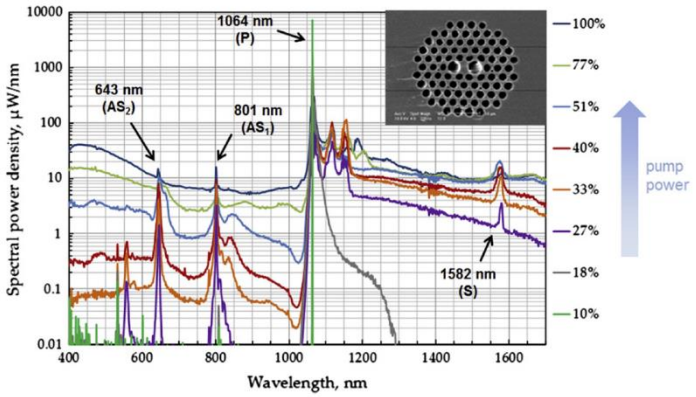

Fig. 1. Supercontinuum generation assisted by cascaded FWM in a PCF (spectrum building as a function of pump power). Four lines are clearly visualized, corresponding to the pump at 1064 nm (P), the Stokes wave generated at 1582 nm (S), the first and second anti-Stokes waves generated at 801 nm (AS_1) and 643 nm (AS_2) respectively. Inset: SEM image of the pure silica highly birefringent PCF ($d \sim 2.7$ µm, $\Lambda \sim 3.35$ µm).

wavelengths. To illustrate this last point, a specific measurement of the spectrum has been made in the UV/visible region (at maximum pump power), as plotted in Fig. 2. It is emphasized that the supercontinuum extends down to 300 nm, thus covering the whole UV-A range.

2.2. Specific beam profile

Considering the shape of the optical window in a flow cytometer, it is relevant to illuminate the flowing cells by a rectangular laser beam. Such configuration can be easily obtained by launching the supercontinuum PCF output beam into a highly-multimode rectangular-core optical fiber, followed by appropriate optics. In this case, the PCF modal content ($LP_{01} + LP_{11}$) is of no significance, since the propagation in the multimode fiber imposes a strong spatial incoherence at the output.

To enhance even more the spatial homogeneity of the illuminating beam, other profiles of fiber core can be utilized, especially the ones that may induce a chaotic propagation of the optical wave [4]. It is also noted that an alternate solution consists in directly generating the supercontinuum in a multimode fiber [5].

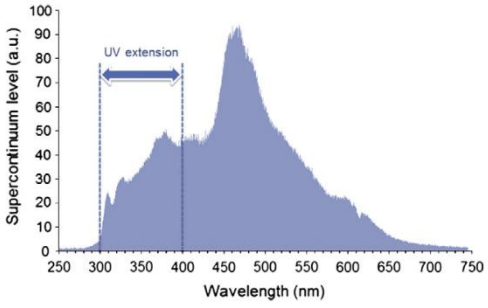

Fig. 2. Specific measurement of the supercontinuum in the UV/visible region (at maximum pump power). The UV extension in the (300–400 nm) range is highlighted.

2.3. Triggered laser emission

From now on, we consider the case of a flow cytometer which is working in the "one cell-one shot" (OCOS) configuration, i.e. each biological cell is irradiated by only one optical pulse. To realize this configuration, the supercontinuum laser emission has to be triggerable. This can be achieved by using a passively Q-switched Nd:YAG microchip laser (1064 nm/6 µJ/450 ps) with pulse-on-demand functionality as the pumping source of the PCF. Thence one key parameter of the system is the timing jitter of the microchip laser, which can be defined as the time uncertainty in the delivery of each optical pulse. Indeed, this timing jitter directly impacts the probability for an optical pulse to miss the corresponding biological cell (which makes the biological diagnosis less accurate). To date, a timing jitter value inferior to 2 µs is obtainable with a repetition rate ranging from 0 to 4 kHz. This value can be strongly reduced by optimizing the laser cavity design. In particular, a design based on a dual cavity has already been demonstrated [6].

2.4. Turn-key solution and results obtained

A compact supercontinuum source, specifically dedicated to flow cytometry, has been integrated by *Leukos Innovative Optical Systems*, as depicted in Fig. 3. This source offers UV/visible

Fig. 3. Turn-key supercontinuum source for flow cytometry.

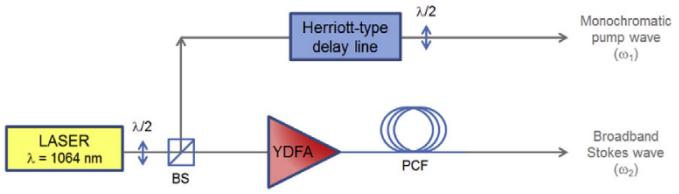

Fig. 4. Schematic of the dual-output laser source. $\lambda/2$: half-wave plate, BS: beam splitter, YDFA: ytterbium-doped fiber amplifier, PCF: photonic crystal fiber.

enhanced emission with pulse-on-demand functionality. It has already been successfully applied to flow cytometry in the case of hematological analysis, with the demonstration of the efficient discrimination of white blood cells [7].

The originality of this approach is underlined, in comparison with the usual technique, which uses a MHz/multi-watt supercontinuum source for bombarding the cell flow [8] (each cell being illuminated by many optical pulses). Here, thanks to the OCOS configuration, the laser average power is only in the mW range, which prevents from handling a high optical power in a flow cytometer. Additionally, it is attractive in terms of size and cost.

3. Dual-output, infrared, supercontinuum source for CARS microscopy

3.1. Need for two excitation waves

Multiplex coherent anti-Stokes Raman scattering (M-CARS) microspectroscopy is an effective method for investigating the dynamical behavior of living cells. It consists in simultaneously exciting several vibrational modes in the sample and consequently allows to get multicolor images of this sample. M-CARS can be efficiently implemented by using both a monochromatic pump wave (ω_1 frequency) and a broadband (supercontinuum) Stokes wave (ω_2 frequency) [9,10]. In this context, it is very helpful to develop a compact and turn-key laser source that can simultaneously emit the two required waves.

3.2. IR supercontinuum generation

The case of a 1064-nm monochromatic pump wave is considered here. Thus the spectral content of the broadband Stokes wave must extend roughly from 1100 to 2000 nm, so as to cover Raman shifts of few hundreds of cm^{-1} up to 4000 cm^{-1}.

The experimental setup for designing the dual-output laser source is schematically represented in Fig. 4. The beam coming from a Nd:YAG microchip laser (1064 nm/900 ps/75 kHz) is divided into two parts by means of a beam splitter (BS). On the pump arm, a Herriott-type delay line is used to synchronize the output pump and Stokes waves. On the Stokes arm, an ytterbium-doped fiber amplifier (YDFA) is inserted before the PCF to increase the peak and average power before generating the IR supercontinuum. The PCF has its zero-dispersion wavelength (ZDW) close to 1 μm, so that it is pumped in anomalous dispersion regime. Therefore the nonlinear process of spectral broadening during the propagation is mainly based on modulation instability (MI), soliton self-frequency shift (SSFS) and soliton collisions [11]. This allows us to generate longer IR wavelengths with constant power over one octave, as shown in the supercontinuum spectrum of Fig. 5. The spectral power density (SPD) is maintained superior to 700 μW/nm up to the 2-μm wavelength.

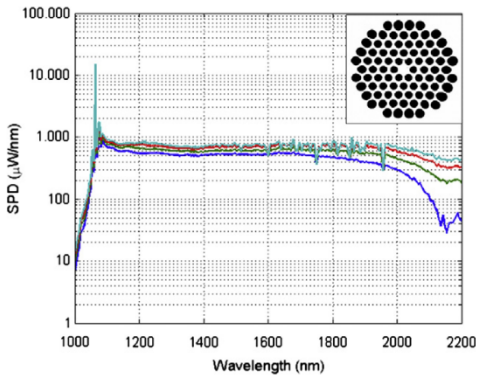

Fig. 5. IR supercontinuum generation in a PCF pumped in anomalous dispersion regime. The different curves have been recorded for different values of the peak power measured at the entrance of the PCF (blue: 5.8 kW, green: 7.7 kW, red: 9.7 kW, cyan: 11.6 kW). Inset: SEM image of the pure silica PCF (ZDW ~ 1 μm). (For interpretation of the references to color in this figure legend, the reader is referred to the web version of this article.)

3.3. Turn-key solution and results obtained

An integrated, compact, dual-output supercontinuum source, specifically dedicated to M-CARS microspectroscopy, is shown in Fig. 6. It offers both free-space monochromatic pump output and fibered broadband Stokes output. Such laser source has already been successfully applied to the imaging of tobacco cells [12], to the multicolor imaging of *Caenorhabditis elegans* nematode [13] and human hair [14], and moreover to the time-resolved multicolor imaging of yeast cells [15]. Its capability for operating multimodal imaging of living cells with CARS, SHG, THG and TSFG (second harmonic generation, third harmonic generation and third-order sum frequency generation) has been demonstrated as well [16]. The reader can also refer to the paper by Okuno et al. in the present special issue of *Optical Fiber Technology*. Finally, it is mentioned that Ref. [13] addresses the new opportunities offered by sub-nanosecond microchip-based supercontinuum sources in the CARS applications field, which appear as a disruptive and alternative technology to the widespread picosecond/femtosecond laser systems.

4. Polyvalent, visible/IR, supercontinuum source for optical coherence tomography

Here we succinctly introduce a polyvalent supercontinuum source, which can be applied to OCT in several spectral ranges (550 nm, 800 nm and 1550 nm windows). For this source, the spectral broadening in the PCF is based on the combination of many

Fig. 6. Turn-key, dual-output, supercontinuum source for CARS microscopy.

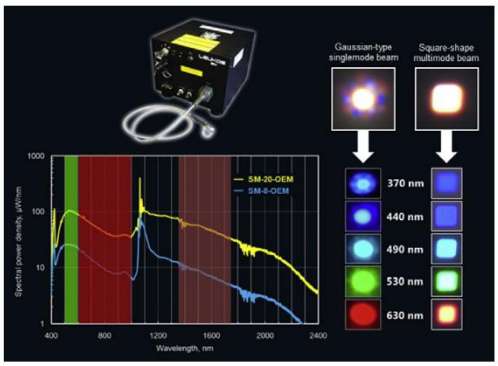

Fig. 7. Overview of a polyvalent, visible/IR, supercontinuum source and its applicability to OCT in several spectral ranges. Underlining of the possibility to spatially shape the output beam.

nonlinear processes (MI, SSFS, soliton collisions, parametric effects, XPM). Fig. 7 displays the typical spectrum that can be obtained, ranging from 400 to 2400 nm. As already mentioned in Section 2.2, the output beam can be shaped to better fit the needs of the application. For instance, spatially incoherent light can be required in the case of full-field OCT. In this case, a large-core multimode fiber can be spliced to the PCF to produce a highly-multimode beam of any shape. The example of a square-shape beam is illustrated in Fig. 7, in comparison with the usual Gaussian-type singlemode one.

For more details on the use of compact supercontinuum sources in the OCT field, the reader can refer to the papers by Froehly et al. and Heise et al. in the present special issue of *Optical Fiber Technology*.

5. Conclusion

We have reviewed recent developments and demonstrations of compact white-light supercontinuum laser sources. These sources are commonly based on the combination of an IR sub-nanosecond microchip laser (pulse duration < 1 ns) and a PCF, along which high peak power optical pulses are propagated in highly nonlinear regime. The spectral broadening obtained by this technique ranges from the UV/visible to the deep near IR. A strong increase of the supercontinuum spectral power density can be achieved by inserting a fiber amplifier between the pump laser and the PCF.

Such microchip-based white-light laser sources offer attractive benefits in terms of size, robustness, stability and cost. They also have great potential as illuminating sources for different kinds of applications. In particular, some promising results in the biomedical field have been introduced. These results relate to flow cytometry, CARS microscopy and OCT. They were obtained on different biological samples at different scales (cell, microorganism, tissue and organ).

All these results suggest interesting prospects regarding the use of compact supercontinuum sources intended for combining several modalities of cell imaging, counting and sorting.

References

[1] C. Lesvigne, V. Couderc, A. Tonello, P. Leproux, A. Barthélémy, S. Lacroix, F. Druon, P. Blandin, M. Hanna, P. Georges, Visible supercontinuum generation controlled by intermodal four-wave mixing in microstructured fiber, Opt. Lett. 32 (15) (2007) 2173–2175.
[2] A. Labruyère, P. Leproux, V. Couderc, V. Tombelaine, J. Kobelke, K. Schuster, H. Bartelt, S. Hilaire, G. Huss, G. Mélin, Structured-core GeO_2-doped photonic-crystal fibers for parametric and supercontinuum generation, IEEE Photon. Technol. Lett. 22 (16) (2010) 1259–1261.
[3] V. Tombelaine, A. Labruyère, J. Kobelke, K. Schuster, V. Reichel, P. Leproux, V. Couderc, R. Jamier, H. Bartelt, Nonlinear photonic crystal fiber with a structured multi-component glass core for four-wave mixing and supercontinuum generation, Opt. Express 17 (18) (2009) 15392–15401.
[4] P. Leproux, S. Février, V. Doya, P. Roy, D. Pagnoux, Modeling and optimization of double-clad fiber amplifiers using chaotic propagation of the pump, Opt. Fiber Technol. 7 (4) (2001) 324–339.
[5] F. Poletti, P. Horak, Dynamics of femtosecond supercontinuum generation in multimode fibers, Opt. Express 17 (8) (2009) 6134–6147.
[6] F. El Bassri, F. Doutre, N. Mothe, L. Jaffres, D. Pagnoux, V. Couderc, A. Jalocha, Hybrid Q-switched broadband laser source with low timing jitter, Opt. Express 20 (2) (2012) 1202–1212.
[7] N. Rongeat, P. Leproux, V. Couderc, P. Brunel, S. Ledroit, D. Cremien, S. Hilaire, G. Huss, P. Nérin, Flow cytometer based on triggered supercontinuum laser illumination, Cytometry Part A 81A (7) (2012) 611–617.
[8] W.G. Telford, F.V. Subach, V.V. Verkhusha, Supercontinuum white light lasers for flow cytometry, Cytometry Part A 75A (5) (2009) 450–459.
[9] H.N. Paulsen, K.M. Hilligse, J. Thøgersen, S.R. Keiding, J.J. Larsen, Coherent anti-Stokes Raman scattering microscopy with a photonic crystal fiber based light source, Opt. Lett. 28 (13) (2003) 1123–1125.
[10] T.W. Kee, M.T. Cicerone, Simple approach to one-laser, broadband coherent anti-Stokes Raman scattering microscopy, Opt. Lett. 29 (23) (2004) 2701–2703.
[11] M. Andreana, A. Labruyère, A. Tonello, S. Wabnitz, P. Leproux, V. Couderc, C. Duterte, A. Cserteg, A. Bertrand, Y. Hernandez, D. Giannone, S. Hilaire, G. Huss, Control of near-infrared supercontinuum bandwidth by adjusting pump pulse duration, Opt. Express 20 (10) (2012) 10750–10760.
[12] M. Okuno, H. Kano, P. Leproux, V. Couderc, H. Hamaguchi, Ultrabroadband multiplex CARS microspectroscopy and imaging using a subnanosecond supercontinuum light source in the deep near infrared, Opt. Lett. 33 (9) (2008) 923–925.
[13] P. Leproux, V. Couderc, A. De Angelis, M. Okuno, H. Kano, H. Hamaguchi, New opportunities offered by compact sub-nanosecond supercontinuum sources in ultra-broadband multiplex CARS microspectroscopy, J. Raman Spectrosc. 42 (10) (2011) 1871–1874.
[14] K. Bito, M. Okuno, H. Kano, S. Tokuhara, S. Naito, Y. Masukawa, P. Leproux, V. Couderc, H. Hamaguchi, Protein secondary structure imaging with ultrabroadband multiplex coherent anti-Stokes Raman scattering (CARS) microspectroscopy, J. Phys. Chem. B 116 (4) (2012) 1452–1457.
[15] M. Okuno, H. Kano, P. Leproux, V. Couderc, J.P.R. Day, M. Bonn, H. Hamaguchi, Quantitative CARS molecular fingerprinting of single living cells with the use of the maximum entropy method, Angew. Chem. Int. Ed. 49 (38) (2010) 6773–6777.
[16] H. Segawa, M. Okuno, H. Kano, P. Leproux, V. Couderc, H. Hamaguchi, Label-free tetra-modal molecular imaging of living cells with CARS, SHG, THG and TSFG (coherent anti-Stokes Raman scattering, second harmonic generation, third harmonic generation and third-order sum frequency generation), Opt. Express 20 (9) (2012) 9551–9557.

Cytometry
PART A
Journal of the International Society for Advancement of Cytometry

Flow Cytometer Based on Triggered Supercontinuum Laser Illumination

Nelly Rongeat,[1]* Philippe Leproux,[2] Vincent Couderc,[2] Patrick Brunel,[1] Sylvain Ledroit,[1] Didier Cremien,[1] Stéphane Hilaire,[3] Guillaume Huss,[3] Philippe Nérin[1]

[1]HORIBA Medical, Parc Euromédecine, 34000 Montpellier cedex 4, France

[2]Photonic Department, Université de Limoges, XLIM, 87060 Limoges cedex, France

[3]LEUKOS, Ester Technopole, 87069 Limoges cedex, France

Received 9 August 2011; Revision Received 3 April 2012; Accepted 4 April 2012

Grant sponsors: European Commission ("NextGenPCF" FP6 integrated project) and ANRT;

Additional Supporting Information (MIFlowCyt item location) may be found in the online version of this article.

*Correspondence to: Nelly Rongeat, Parc Euromédecine, rue du caducée, 34000 Montpellier cedex 4, France

Email: nelly.rongeat@horiba.com

Published online 9 May 2012 in Wiley Online Library (wileyonlinelibrary.com)

DOI: 10.1002/cyto.a.22065

Abstract

Multiple wavelength operation in a flow cytometer is an exciting way for cell analysis based on both fluorescence and optical scattering processing. For example, this multiparametric technique is currently used to differentiate blood cells subpopulations. The choice of excitation wavelengths matching fluorochrome spectra (it is currently the opposite) and the use of a broader range of fluorochromes can be made by taking advantage of a filtered supercontinuum white light source. In this study, we first wished to validate the use of a specific triggered supercontinuum laser in a flow cytometer based on white light scattering and electric sizing on human blood cells. Subsequently, to show the various advantages of this attractive system, using scattering effect, electrical detections, and fluorescence analysis, we realized cells sorting based on DNA/RNA stained by thiazole orange. Discrimination of white blood cells is efficiently demonstrated by using a triggered supercontinuum-based flow cytometer operating in a "one cell-one shot" configuration. The discriminated leukocyte populations are monocytes, lymphocytes, granulocytes, immature granulocytes, and cells having a high RNA content (monoblasts, lymphoblasts, and plasma cells). To the best of our knowledge, these results constitute the first practical demonstration of flow cytometry based on triggered supercontinuum illumination. This study is the starting point of a series of new experiments fully exploiting the spectral features of such a laser source. For example, the large flexibility in the choice of the excitation wavelength allows to use a larger number of fluorochromes and to excite them more efficiently. Moreover, this work opens up new research directions in the biophotonics field, such as the combination of coherent Raman spectroscopy and flow cytometry techniques. © 2012 International Society for Advancement of Cytometry

Key terms

blood cells; hematology analyzer; flow cytometry; nonlinear optics; supercontinuum white light laser; laser

Introduction

In cytometry devices, the use of multiple wavelength excitations (MWEs) represents a great advantage, especially for optical spectroscopic measurements. A few decades ago, MWE was realized using lamps based on QTH (Quartz Tungsten Halogen) or electric discharge in a gas (xenon- or mercury-type) (1,2). Unfortunately, many drawbacks inherent to the use of such light sources restrict the scale and range of biological analyses; in particular, the spatial coherence of these lamps is too weak for simultaneously measuring low angle light scattering, and the weak energy of the spectral density strongly limits fluorescence measurements. Subsequently, flow cytometry systems including a pulsed laser, such as a copper vapor laser or a semiconductor diode laser, have been proposed (3,4). These systems allow instantaneous illumination with higher intensity but with only one monochromatic radiation.

Multiple fluorescence measurements require the combination of several monochromatic lasers. In this context, new generation of cytometers can integrate up to

ISAC
International Society for Advancement of Cytometry

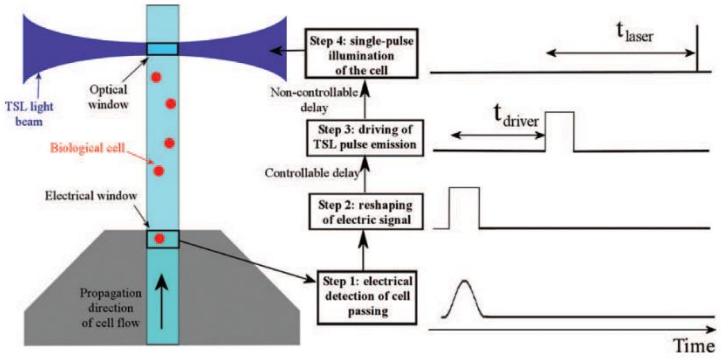

Figure 1. Principle of the flow cytometer in OCOS configuration.

six laser sources and allow the detection of 18 or more fluorescence signals (5–8). However, such MWE configuration requires a complex alignment of the optical system, reduces opto-mechanical stability and increases the cost of the system. The inability to tune the wavelengths to a specific value is also a limiting factor of these devices. Although new fluorochromes, including the FRET technology, enlarge the scope of multiple parameter analysis, limiting factors still exist, even if spectral compensations are used. Despite the recent diversification of monochromatic laser wavelengths (9), usual laser sources do not provide any flexibility to well-match the optimal excitation wavelength of any fluorochrome of interest. In addition, commercial lasers allow to excite only a small part of available fluorescent probes.

To overcome these drawbacks, the supercontinuum white-light laser (10,11) appears as an outstanding potential alternative (12). Once properly filtered, it can be suitable as an illumination source for any selected fluorochromes (for example Texas Red). Such broadband source can even be used to generate a set of spectral channels, thus allowing to simultaneously excite several fluorochromes. In addition, the replacement of several monochromatic lasers by a single light source may significantly improve the mechanical stability of the system and reduce optical alignment issues. Consequently, in the context of multiparametric flow cytometry, the use of supercontinuum sources is a promising approach both in terms of simplicity and quantity of information.

In this article, we introduce a new supercontinuum laser, specifically dedicated to flow cytometry. The implementation of this laser in a hematological analyzer is suggested with a novel "one cell-one shot" (OCOS) configuration, i.e., each biological cell is illuminated by a single optical pulse. To reach this aim, the laser emission is triggered according to the passing of the cells through a preliminary electrical measurement (13). We use a compact triggered supercontinuum laser (TSL), characterized by a low repetition rate (<2 kHz) and a low average power (<6 mW). This approach is fundamentally different from the usual one, which consists in several pulsed illuminations of biological cells (i.e., a lot of optical pulses for each cell) by means of a MHz/multi-watt supercontinuum source. It resolves the problem of handling high optical power in a flow cytometer (12) and is clearly advantageous in terms of size and cost (10–20 keuros).

Here, the TSL-based OCOS configuration is applied to the multiparametric analysis of human blood cells, including electrical sizing, orthogonal white light scattering, and fluorescence measurements. To the best of our knowledge, this is the first practical demonstration of using a TSL in a flow cytometer.

Materials and Methods

Experiment Overview

The general principle of the developed OCOS method is schematically depicted in Figure 1. First, the passing of a biological cell in the electrical window is detected through impedance measurement (Step 1). The produced electrical signal is then reshaped as a rectangular pulse (Step 2) to be used as electrical trigger. The emission of a laser pulse coming from the TSL is then obtained with a controllable time delay t_{driver} (Step 3). Finally, the laser pulse is effectively emitted after a given time (t_{laser}), and the biological cell is illuminated by this single laser pulse when passing through the optical window (step 4). Electrical and optical windows are separated by 210 μm.

Flow Sample and Specimen Description

Only healthy human peripheral bloods were used during the experiments. We punctured 4 mL blood sample in K3ETDA tubes (VACUETTE®). Then, 30 μL were mixed with 2 mL lytic reagent. Two different lytic reagents were tested to differentiate and to count white blood cells. In a first experiment, a reagent based on saponin (research-used Horiba ABX reagent) was used to demonstrate optical scattering and electrical sizing measurements. In a second experiment, to the same cell prep, thiazole orange (TO) dye was added (14) to stain the nucleic acid of leucocytes (RNA and DNA) and thus to operate fluorescence measurements. A total of 24 μL of

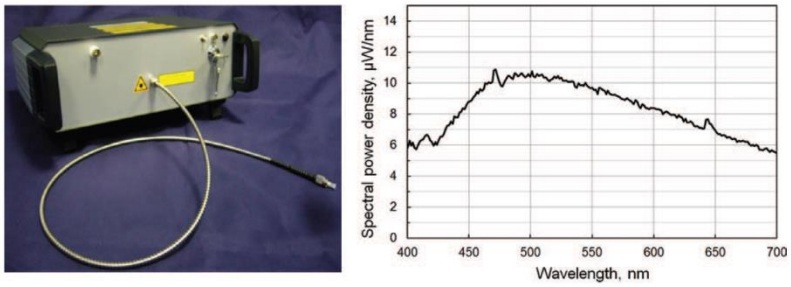

Figure 2. Picture of the compact TSL (left) and visible emission spectrum measured at 2 kHz repetition rate (right).

each dilution was carried to the flow chamber using hydrodynamic focusing. The flow rate was 5 m/s and the data collection was realized during 15 s.

Illumination Source

The illumination source, i.e., the supercontinuum laser [see picture in Fig. 2 (left)], is described hereafter. This laser system was built collectively by the authors and is now available as a commercial product from Leukos Company under "STM-4" reference. To operate the flow cytometer in OCOS configuration, the laser has to offer the functionality of external triggering by the electrical signal coming from the impedance measurement. Such TSL has been developed by combining specifically designed pump source and photonic crystal fiber (PCF). The pump source is a passively Q-switched Nd:YAG microchip laser operating at 1064 nm and delivering 6 μJ/450 ps pulses at a repetition rate ranging from 0 to 2 kHz. The 6-m-long PCF is based on a highly nonlinear air-silica microstructure with 2.5 μm average hole diameter and 4 μm hole-to-hole spacing. The pump energy is predominantly launched onto the fundamental guided mode of the structure (LP_{01} mode), having its zero-dispersion point located closely below the 1064 nm wavelength. A prominent spectral broadening is obtained on both sides of the pump by means of third-order nonlinear processes such as modulation instability, soliton propagation/interaction, four-wave mixing (FWM), and cross-phase modulation (XPM). The output supercontinuum ranges over more than two octaves from the blue/violet to the deep near infrared wavelengths (400–2000 nm), for any value of the repetition rate. At 2 kHz, the total visible/infrared average power is ~6 mW, and the spectral power density is primarily between 6 and 10 μW/nm in the visible range, as plotted in Figure 2 (right).

Laser Safety: Regarding laser safety, the TSL is classified as a Class IIIb laser product, against Class IV for ultrafast supercontinuum sources (12). In spite of the reduced average power, eyes protection is required.

Flow Cytometry

HORIBA Medical Pentra 60 instrument has been set-up and modified to integrate the specific supercontinuum laser source. This automatic hematology analyzer is based on flow cytometry principles using hydrodynamic focusing (15). The flow cell is coupled to a specific optical system as depicted in Figure 3. The flow of cells circulates in the perpendicular plane of the drawing. Before passing through the laser beam, biological cells pass through a microhole which is immersed in a liquid with a defined conductivity. Impedance modification between electrodes, placed on each side of the microaperture, reveals the presence of a cell and delivers information on its volume. The signal produced at the electrical gate drives the TSL using a specific electronic controller performing the following functions:

- electrical shaping of the trigger and restricting of the repetition rate (2 kHz maximum) to be compliant to supercontinuum requirements,
- acting as a delay line to adjust the time windowing between electrical and optical gates. This peculiar electronic function

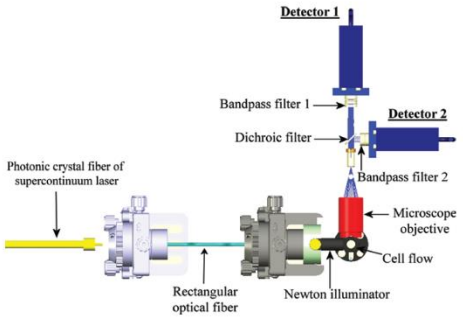

Figure 3. Optical system of hematology analyzer. The cell flow circulates in the perpendicular plane of this drawing. For experiment 1, operated under white-light supercontinuum illumination: side scattering is measured by detector 1; strictly no filter is used. For experiment 2, operated under blue supercontinuum illumination: dichroic filter is FF506-Di02 (Semrock), bandpass filter 1 is FF01-530/43 (Semrock), and TO fluorescence is measured by detector 1; bandpass filter 2 is FF01-482/35 (Semrock), side scattering is measured by detector 2.

permits accurate measurements and suppresses mechanical adjustment between the sensing regions, which is long and fastidious.

Thus, the controller operates the laser illumination when a blood cell crosses through the optical window. Thus, this precise driving of the TSL can be effective with OCOS configuration. The optical gate is created using a specific beam shaper (16). It is based on a 50 cm piece of multimode step index optical fiber having a rectangular cross section (RCS) 150 $\times$ 70 μm^2 core with 0.22 numerical aperture (NA). The output end of the PCF (NA $<$ 0.13 in the visible range) is placed nearly 50 μm front to the RCS fiber. The mismatch between NAs reduces the optical coupling efficiency down to 60%. The PCF end position is adjusted by means of micrometric translation stages so as to obtain the almost full illumination of the RCS fiber core. Therefore, a high number of transverse guided modes are excited in the RCS fiber, which acts as a spatial homogenizer producing a flat top illumination with a RCS. By this way, a polychromatic secondary optical source is available, with adequate brightness and beam profile. Afterwards, the light at the RCS fiber output end is imaged into the flow of cells. This optical illuminator, which chromatic and spherical aberrations have been corrected, produces a well-defined 97.7 $\times$ 45.6 μm^2 image intercepting the flow of cells. Cells are moving along the largest dimension of the optical gate to get a higher tolerance to laser time jitter as explained later.

A first experiment deals with full supercontinuum spectrum illumination without any spectral filtering in the setup. The orthogonal light scattered by the blood cells is collected with a high NA objective (NA = 0.8), for which sphero-chromatism have been minimized at 530 and 650 nm. To remove the stray light due to multiple reflection and refraction in the optical system, the orthogonal light is spatially filtered through a 500-μm-diameter pinhole. The cleaned light beam is directed toward an optical detector (detector 1 in Fig. 3) using a thin relay lens with 10 mm effective focal length.

A second experiment is dedicated to the measurement of scattering and fluorescence using blue illumination obtained using supercontinuum optical filtering. In this case, a bandpass filter (FF01-482/35, Semrock) is incorporated inside the illuminator where the light beam is collimated. A second detector (detector 2 in Fig. 3) is added to the setup and three filters: bandpass filter 1 (FF01-530/43), a dichroic filter (FF506-Di02), and bandpass filter 2 (FF01-482/35), all purchased from Semrock. TO fluorescence and orthogonal light scattering are measured by detectors 1 and 2. Absorption and emission spectra of TO dye are represented in Figure 4.

Detectors 1 and 2 are photomultiplier tubes (H9307, Hamamatsu Photonics).The PMT voltages are 590 V (SSC detector) and 600 V (fluorescence detector) for experiment with Thiazole Orange. The PMT signals are amplified using home made electronic amplifiers providing $\times$10 gain amplification with 100 kHz ($-$3 dB) bandwidth. SSC and fluorescence pulses are $\sim$1μs duration with 800 mV average amplitude. We used several steps to digitize and to store subsequent analysis: (1) analog processing and DSP (Digital Signal Processor)

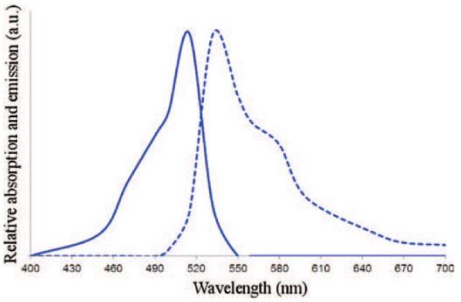

Figure 4. Absorption (line curve) and emission (dashed curve) spectra of Thiazole Orange (TO). [Color figure can be viewed in the online issue, which is available at wileyonlinelibrary.com.]

allow digitizing, (2) data are stored on the workstation as raw data, each pulse event being characterized by the pulse time arrival, the pulse amplitude, and the pulse width, and (3) data are processed to form in fcs format files. The acquisition time is 10 s and the average number of events collected is 7000.

Results

Laser Pulse-to-Pulse Temporal and Power Stability

For flow cytometry applications, TSL requires the setting of electro-optical parameters: spectrum extension, beam quality, spectral power density, total average power, long-term power drift, pulse-to-pulse power stability, and pulse-to-pulse temporal stability. The latter depends on two contributions, the pulse creation delay (PCD) and the temporal jitter (TJ):

- the PCD is the average time between electrical trigger and pulse light emission,
- the TJ expresses a random time due to statistical optical effects within the laser cavity.

Finally, the delay time t_{laser} (see Fig. 1) between trigger and cell illumination is comprised between law and high values as:

$$\mathrm{PCD} - \mathrm{TJ}/2 < t_{laser} < \mathrm{PCD} + \mathrm{TJ}/2 \qquad (1)$$

The PCD and the TJ were measured for the supercontinuum laser described previously as a function of the repetition rate and are plotted in Figure 5 (the TJ being depicted by error bars). The PCD ranges from 28.2 to 31.2 μs as the repetition rate varies from 10 Hz to 2 kHz. The TJ varies slightly from 2.5 to 2.6 μs. According to these results, the maximum variation of t_{laser} is 5.5 μs (32.5 $-$ 27) for a repetition rate ranging from 10 Hz to 2 kHz.

The pulse-to-pulse power stability of the laser source is another key feature in a flow cytometer. Here, it has been measured in two cases, i.e., without optical filtering of the supercontinuum and by using a blue filter (FF01-482/35, Semrock), the repetition rate being fixed to a specific value or ran-

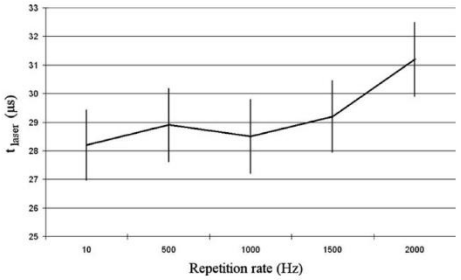

Figure 5. Evolution of t_{laser} parameter as a function of the laser repetition rate. t_{laser} is defined as the time between TSL driving and cell illumination. The error bars depict TJ (temporal jitter). Three repeats for each frequency are realized with 15 min of exposure time.

domly varied between 100 and 2000 Hz (Table 1). It can be observed that the maximum power variation is 6.8% for unfiltered TSL versus 11.2% with blue filtering. It has been recognized that intensity noise comes from optical nonlinear processes within the microstructured fiber (17). Such amplitude noise could be reduced by using a dedicated detector to measure the peak power of each laser pulse and by applying a correction factor during software postprocessing. Nevertheless, as demonstrated in the following experiments, this optical noise is acceptable to accurately measure scattering and fluorescence from stained leucocytes.

Side Scattering Under White-Light Supercontinuum Illumination

To obtain an effective OCOS demonstration, time windowing was optimized according to many others parameters among which are t_{driver}, t_{laser}, electrical and optical gate size/distance, cell velocity and its variation. The optimized system was first applied to the analysis of white blood cells through scattering measurements under white-light supercontinuum illumination.

Side (orthogonal) scattering coming from each cell after its interaction with the TSL light beam was detected and recorded. The results obtained are illustrated by the biparametric representation of Figure 6, where each dot represents one cell. The electrical signal allows to count cells and to determine their volume. The side scattering signal is a function of the cell lobularity and granularity (1). The discrimination of monocytes (5.9%), lymphocytes (32.4%), and granulocytes (60.6%) is then demonstrated, proving the effectiveness of our compact supercontinuum sources for hematological diagnostics in OCOS configuration. To the best of our knowledge, this is the first demonstration of flow cytometry based on triggered supercontinuum illumination.

Side Scattering and TO Fluorescence Under Blue Supercontinuum Illumination

To point out the attractiveness of our system, the TSL light beam was filtered in the blue range, allowing TO excitation. TO fluorescence, measured in the green range of wavelength, is correlated with the amount of nucleic acids (RNA and DNA). The multiparametric analysis of leukocytes was, therefore, conducted combining electrical, side scattering, and TO fluorescence signals. In Figure 7a, the side scattering intensity is plotted as a function of the electrical intensity. As previously, this cytogram displays the discrimination of monocytes (9.4%), lymphocytes (28.1%), and granulocytes (58.4%). Figure 7b exhibits the fluorescence versus scattering diagram. Immature granulocytes (0.16%) and cells with high RNA content (0.16%), which are monoblasts, lymphoblasts, and plasma cells, are visualized.

Discussion

A pulsed PCF-based supercontinuum optical source, synchronized with cell passing through an optical window, was coupled to a flow cytometry device for hematology purpose. The novelty of this system relies in the triggering mode, allowing cell by cell illumination and both qualitative and quantitative scattering and fluorescence measurements.

In comparison with solid-state lasers currently used in multicolor flow cytometers, microchip-based supercontinuum sources provides flexibility for multiple wavelength experiments by offering compactness and by reducing optical alignment constraints. The use of a supercontinuum as a programmable optical source considerably extends the field of multiple fluorescence measurements without the complexity of breakthrough technologies recently published (18). In addition, it is a cost-competitive approach, compared with the use of several monochromatic lasers, however, providing a significant quantity of biological information.

In comparison with supercontinuum technologies based on ultrafast pulsed lasers (10), the microchip laser technology allows a significant reduction of power consumption while producing super bright visible emission. Within the scope of our investigation, power and TJs are considered as the main cause of optical noise, and theoretical understanding and technical progress are needed to bring the technology to an industrial level. Despite these required improvements, the TSL used in our flow analyzer prototype made possible leukocyte differentiation and counting. The full discrimination of monocytes, lymphocytes,

Table 1. Pulse-to-pulse power variation of the TSL as a function of the repetition rate.

	REPETITION RATE (HZ)	100	500	1000	1500	2000	RANDOM
Pulse-to-pulse power variation (%)	Supercontinuum without filter	2.3	3.5	2.7	2.9	5.9	6.8
	Supercontinuum with blue filter	6.3	4.6	5.4	4.9	4.8	11.2

Measurements were made in two cases, i.e., without filtering the supercontinuum and by using a blue filter (FF01-482/35, Semrock). The repetition rate is fixed to a specific value or randomly varied between 100 and 2000 Hz.

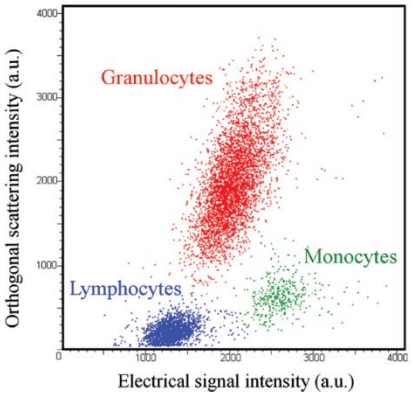

Figure 6. Biparametric analysis of human peripheral white blood cells using a TSL in OCOS configuration, operated under white-light supercontinuum illumination. Each dot stands for one cell. The electrical signal intensity (*x*-axis) is a function of the cell volume. The orthogonal scattering intensity (*y*-axis) is a function of the cell lobularity and granularity.

granulocytes, immature granulocytes, and high RNA content cells was demonstrated, by means of a multiparametric analysis using impedance, scattering and fluorescence signals.

The total energy received by biological cell is an important parameter to compare TSL technology, mode locked technology, and continuous wave (CW) laser. For TSL technology, the power density is about 10 μW/nm (in the visible range) for 0.45 ns pulse duration and 2 kHz repetition rate. Therefore, each pulse provides the total energy density of 5 nJ/nm. In a mode locked technology, the power density is about 1 mW/nm, whereas the pulse duration is 6 ps and the repetition frequency is 80 MHz (see http://www.fianium.com/pdf/whitelase-sc400.pdf). Therefore, each pulse provides the energy density of 10.5 pJ/nm. As the transit time is 3 μs (corresponding to a flow rate of 10 m/s and a beam size of 30 μm), each biological cell is illuminated with 240 light pulses. Therefore, the total energy density received by a biological cell is 2.5 nJ/nm. With TSL technology, the total energy density is twice higher than the one of mode locked technology (respectively, 5 nJ/nm and 2.5 nJ/nm). The only difference comes from the temporal distribution of the energy transmitted to the cell. In the TSL technology, this energy is provided by a single pulse illumination, whereas it is based on multiple pulse illuminations using mode locked operation. Also, in flow cytometry application, 20 mW CW laser is often used. Based on 3 μs transit time, laser beam provides 60 nJ of energy. This configuration can be reached by using 12 nm wavelength bandwidth using TSL technology, which is very acceptable for fluorescence applications.

In our research work, we did not consider the fluorescence saturation effects which depends on several other parameters such as laser intensity and chemical compounds used for staining cells (19,20).

We are currently investigating how electro-optical or acousto-optical (AOTF nC.TN, AA Opto Electronic Compagny) devices (21,22) can be combined with the supercontinuum technology so as to realize a fully programmable optical source for which one or several wavelengths are selected with adjustable energy. Such a programmable laser could be applied to cell diagnosis using several fluorochromes conjugated antibodies (6,7) with reduced spectral compensation (23), resulting in more accurate fluorescence measurements. The possibility to select multiple optical radiations with specific wavelength and intensity is an important improvement for single cell monitoring, allowing wider flexibility in multicolor flow cytometry applications. It is worth to note that using compact supercontinuum optical sources will open up new research avenues in biophotonic instrumentation, such as the implementation of coherent Raman spectroscopy or time-resolved fluorescence in flow cytometry devices.

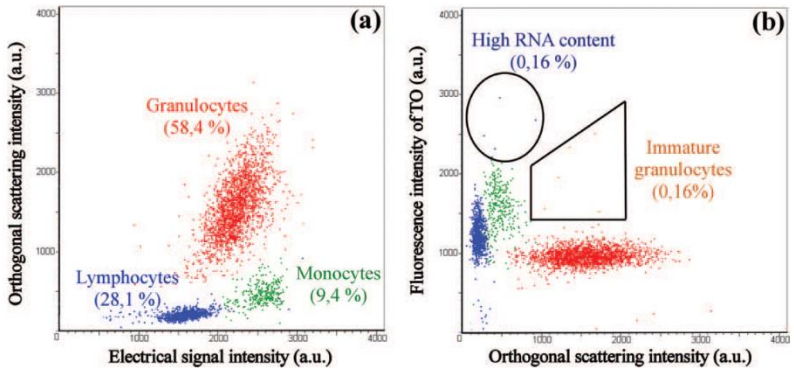

Figure 7. Multiparametric analysis of human peripheral white blood cells using a TSL in OCOS configuration, operated under blue supercontinuum illumination. Each dot stands for one cell. The number of events collected is 7000 on average. Representation (**a**): orthogonal scattering intensity versus electrical signal intensity. Representation (**b**): TO fluorescence intensity versus orthogonal scattering intensity.

Literature Cited

1. Shapiro HM. Practical Flow Cytometry, 2nd ed. New York: A. R. Liss; 1988.
2. De Grooth BG, Van Dam M, Swart NC, Willemsen A, Greve J. Multiple wavelength illumination in flow cytometry using a single arc lamp and a dispersing element. Cytometry 1987;8:445–452.
3. Taylor RH, Reid TA, Choi HY. System and method for a pulsed light source used in fluorescence detection. Patent WO 119277 (2006).
4. Wu TH, Gao L, Chen Y, Wei K, Chiou PY. Pulsed laser triggered high speed microfluidic switch. Appl Phys Lett 2008;93:144102–144104.
5. Craig FE, Foon KA. Flow cytometric immunophenotyping for hematologic neoplasms. J Am Soc Hematol 2008;111:3941–3967.
6. Faucher JL, Lacronique-Gazaille C, Frébet E, Trimoreau F, Donnard M, Bordessoule D, Lacombe F, Feuillard J. "6 markers/5 colors" extended white blood cell differential by flow cytometry. Cytometry Part A 2007;71A:934–944.
7. Arnoulet C, Béné MC, Durrieu F, Feuillard J, Fossat C, Husson B, Jouault H, Maynadié M, Lacombe F. Four- and five-color flow cytometry analysis of leukocyte differentiation pathways in normal bone marrow: A reference document based on a systematic approach by the GTLLF and GEIL. Cytometry Part B: Clin Cytometry 2010;78B:4–10.
8. Perfetto S, Chattopadhyay P, Roederer M. Seventeen-colour flow cytometry: Unraveling the immune system. Nat Rev Immunol 2004;4:648–655.
9. Kapoor V, Karpov V, Linton C, Subach FV, Verkhusha VV, Telford WG. Solid state yellow and orange lasers for flow cytometry. Cytometry Part A 2008;73A:570–577.
10. Dudley JM, Genty G, Coen S. Supercontinuum generation in photonic crystal fiber. Rev Mod Phys 2006;78:1135–1184.
11. Champert PA, Couderc V, Leproux P, Février S, Tombelaine V, Labonté L, Roy P, Froehly C, Nérin P. White-light supercontinuum generation in normally dispersive optical fiber using original multi-wavelength pumping system. Opt Express 2004;12:4366–4371.
12. Telford WG, Subach FV, Verkhusha VV. Supercontinuum white light lasers for flow cytometry. Cytometry Part A 2009;75A:450–459.
13. De Bisschop F. Electronic gating for particle/cell counting and sizing, DSP-operated. IEEE Trans Instrum Meas 2009;58:3159–3166.
14. Lefèvre D, Vériac S, Champseix H. Reagent and process for the identification and counting of biological cells. US Pat 7638290 (2009).
15. Spielman L, Goren SL. Improving resolution in Coulter counting by hydrodynamic focusing. J Colloid Interface Sci 1968;26:175–182.
16. Nérin P, Moreno P, Cremien D. Dispositif d'inspection d'un fluide par illumination uniforme au moyen d'un guide de lumière conforme. FR Pat 2878032 (2006).
17. Corwin KL, Newbury NR, Dudley JM, Coen S, Diddams SA, Washburn BR, Weber K, Windeler RS. Fundamental amplitude noise limitations to supercontinuum spectra generated in a microstructured fiber. Appl Phys B: Lasers Opt 2003;77:269–277.
18. Bendal SC, Simonds EF, Qiu P, Amir ED, Krutzik PO, Finck R, Bruggner RV, Melamed R, Trejo A, Ornatsky OI, et al. Single-cell mass cytometry of differential immune and drug responses across a human hematopoietic continuum. Science 2011;332:687–696.
19. van den Engh G, Farmer C. Photo-bleaching and photon saturation in flow cytometry. Cytometry 1992;13:669–677.
20. Doornbos R MP, de Grooth BG, Greve J. Experimental and model investigations of bleaching and saturation of fluorescence in flow cytometry. Cytometry 1997;29:204–214.
21. Rongeat N, Ledroit S, Chauvet L, Cremien D, Urankar A, Couderc V, Nérin P. Automatic cytometric device using multiple wavelength excitations. J Biomed Opt 2011;16. DOI: http://dx.doi.org/10.1117/1.3582162.
22. Rongeat N, Brunel P, Gineys J-P, Cremien D, Couderc V, Nérin P. Wavelength encoding technique for particle analyses in hematology analyzer. Opt Express 2011;19:14076–14082.
23. Roederer M. Spectral compensation for flow cytometry: Visualization artifacts, limitations, and caveats. Cytometry 2001;45:194–205.

Research Article

Journal of RAMAN SPECTROSCOPY

Received: 22 October 2010 Accepted: 18 April 2011 Published online in Wiley Online Library: 30 May 2011

(wileyonlinelibrary.com) DOI 10.1002/jrs.2995

New opportunities offered by compact sub-nanosecond supercontinuum sources in ultra-broadband multiplex CARS microspectroscopy†

P. Leproux,[a,b]* V. Couderc,[a] A. de Angelis,[a] M. Okuno,[c] H. Kano[c,d] and H. Hamaguchi[c]

We report, to the best of our knowledge, the first turn-key and compact dual-output sub-nanosecond supercontinuum source applicable to ultrabroadband multiplex coherent anti-Stokes Raman scattering microspectroscopy of biological samples. The light source design and the microspectroscopy setup are described in details. Easy multicolour imaging of *Caenorhabditis elegans* nematode is operated successfully and discussed. Copyright © 2011 John Wiley & Sons, Ltd.

Keywords: multiplex CARS; microspectroscopy; microchip laser; supercontinuum source; photonic crystal fibre

Introduction

Coherent anti-Stokes Raman scattering (CARS) microscopy is an efficient method for investigating the dynamical behaviour of living cells.[1–4] It is one of the most promising label-free techniques for chemical imaging with high vibrational selectivity and sensitivity. One of the key parameters for efficient biological imaging is the geometrical configuration. Tight focusing using a high numerical aperture (NA) objective is a well-established technique for CARS microscopy, since it permits both the relaxation of the phase matching condition and bringing high optical intensity into play.[5]

Besides, CARS microscopy offers only a monochromatic image at a given Raman shift, which is determined by the frequency difference between the pump and Stokes waves. On the contrary, multiplex CARS (M-CARS) microspectroscopy[6,7] allows the excitation of several vibrational modes simultaneously and consequently getting multicolour images. One effective way to implement M-CARS is to produce an ultra-broadband Stokes wave by generating a supercontinuum (SC) in a photonic crystal fibre (PCF).[8–10] In this context, the choice of the laser and the PCF design are the keys for efficient biological imaging. Whereas the method is typically based on the use of one or several picosecond or femtosecond pulsed lasers, sub-nanosecond excitation has been demonstrated more recently as a promising alternative to these usual solutions.[11–12]

Cars Advances Brought by Sub-Nanosecond Excitation

In the very recent past, ultra-broadband (>2000 cm^{-1}) sub-nanosecond M-CARS microspectroscopy has been successfully implemented by using a single, miniature microchip laser source combined with a PCF in the visible[11] and deep near-infrared (NIR)[12] ranges. This unusual microchip-based technological approach offers obvious benefits in terms of size, robustness, stability and cost compared to imaging systems using picosecond or femtosecond ultrafast lasers and/or optical parametric oscillators (OPOs).

Additionally, sub-nanosecond excitation (pulse duration <1 ns) allows easy multi-colour imaging thanks to the temporal superimposition of the pump and the broadband Stokes waves, which remains possible even for very different values of Raman shift. Practically, it means that a wide range of frequencies of molecular vibration can be detected without changing the delay time between the pump and the Stokes pulses. This low sensitivity to group-delay dispersion in the CARS process is characteristic of the sub-nanosecond regime and is a unique advantage over the picosecond or femtosecond regime. Thus it becomes uncomplicated to simultaneously get CARS images of a biological sample in both C–H stretching and fingerprint regions.

* *Correspondence to: P. Leproux, Institut de Recherche XLIM, UMR CNRS n° 6172, 123 Avenue Albert Thomas, 87060 Limoges Cedex, France. E-mail: philippe.leproux@xlim.fr*

† *This article is part of the Journal of Raman Spectroscopy special issue entitled "Proceedings of the 9th European Conference on Nonlinear Optical Spectroscopy (ECONOS), Bremen, Germany, June 21-23, 2010" edited by Peter Radi (PSI, Villigen, Switzerland) and Arnulf Materny (JacobsUniversity, Bremen, Germany).*

a *Institut de Recherche XLIM, UMR CNRS n° 6172, 87060 Limoges Cedex, France*

b *LEUKOS, ESTER Technopole, 87069 Limoges Cedex, France*

c *Department of Chemistry, School of Science, The University of Tokyo, Tokyo 113-0033, Japan*

d *Precursory Research for Embryonic Science and Technology (PRESTO), Japan Science and Technology Agency (JST), Saitama 332-0012, Japan*

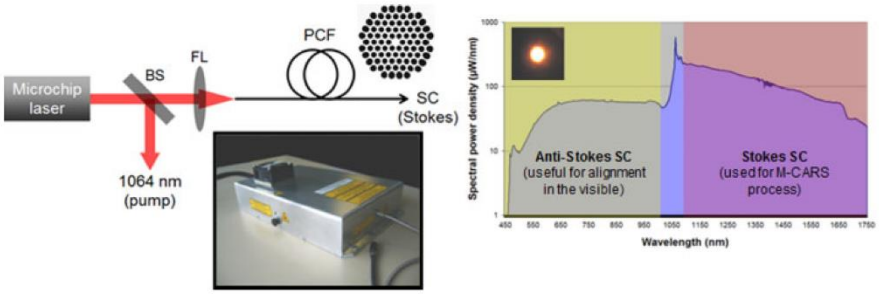

Figure 1. Schematic of the SC source (left) and output ultra-broadband spectrum (right). Inset: picture of the turnkey integrated prototype.

Finally, the sub-nanosecond temporal regime intrinsically provides a high spectral resolution (<0.1 cm^{-1}). Therefore a sub-nanosecond M-CARS device, based on a high-resolution spectroscope, is able to spot sharp vibrational resonances in the measured spectrum. In other words, the system combines the functionalities of ultra-broadband operation and high spectral resolution, which turns it into an ideal tool for biological imaging.

We report, to the best of our knowledge, the first compact sub-nanosecond SC source applied to ultra-broadband M-CARS microspectroscopy of biological samples. First, the light source design and the M-CARS setup are described. Then, multi-colour imaging of *Caenorhabditis elegans* is introduced and discussed.

Experimental

Novel SC source for M-CARS microspectroscopy

Here we describe the new laser system that is proposed as the illuminating source for implementing M-CARS microspectroscopy. As seen in Fig. 1 (left), the system is based on a passively Q-switched 1064 nm microchip laser. This compact laser delivers sub-nanosecond pulses (duration ~0.9 ns, peak power ~10 kW) at 33 kHz repetition rate, giving an average power of ~300 mW. A beam splitter (BS) is used to equally divide the laser beam into two parts. One part directly constitutes the pump radiation of the CARS process, whereas the other one is launched into a 6 m long piece of air–silica PCF through a focusing lens (FL). The latter exhibits a 2.5 μm average hole diameter and a 4 μm hole-to-hole spacing; the fundamental guided mode of the structure (LP_{01} mode) has its zero-dispersion point located closely below the 1064 nm pump wavelength. The relatively small fibre core and the high input pulse peak power induce strong third-order nonlinearities along the propagation in the PCF, resulting in broadband SC generation.[13] The main nonlinear processes responsible for spectral broadening towards longer (infrared) wavelengths, i.e. in the anomalous dispersion regime, are modulation instability, soliton formation, soliton self-frequency shift and soliton interaction. Frequency conversion towards shorter (visible) wavelengths is essentially due to four-wave mixing and cross-phase modulation. At the fibre output, spatially single-mode white laser emission is obtained with a spectral power density >100 μW/nm in the 1.05–1.4 μm range (fingerprint region) and >10 μW/nm in the 1.4–1.8 μm range (C–H stretching region) (Fig. 1 (right)). The infrared part of the SC is used as the broadband Stokes radiation of the M-CARS process. The visible part can be useful for easing the alignment procedure of the microscope, but it has to be filtered afterwards.

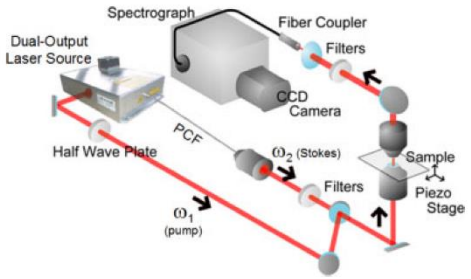

Figure 2. Schematic of the M-CARS experimental setup.

The whole laser system is integrated into a turnkey, compact and stable prototype with dual-output configuration. A picture of the final device is given in the inset of Fig. 1.

M-CARS setup

The M-CARS experimental setup is schematically depicted in Fig. 2A half-wave plate is used to rotate the linear polarisation of the pump wave. On the Stokes arm, the output beam of the PCF is collimated by a microscope objective, which then passes through several filters to eliminate anti-Stokes spectral components. After that, the pump and Stokes beams are recombined via a notch filter, directed towards a customised inverted microscope and tightly focused onto the sample with a high NA objective. The sample is held by a piezoelectric stage with <0.75 μm transverse and <4.5 μm axial resolution. Finally, the CARS signal is collected by another objective, filtered and fibre-guided towards an ensemble of spectrograph plus charge-coupled device (CCD) camera.

Results and Discussion

The nematode *Caenorhabditis elegans* is a known biological model of a multi-cellular organism. It is used for various studies such as generation, behaviour, ageing and intra-cellular signal transmission. In the present study, we have applied the M-CARS technique to visualise nematodes at the molecular level. The sample is a mutant called unc-119, which shows slow movement in comparison with native organisms. Before measurement, we exposed the sample specimens to the drug levamisole in order to suppress movement. Figure 3(a) shows a spectral profile of

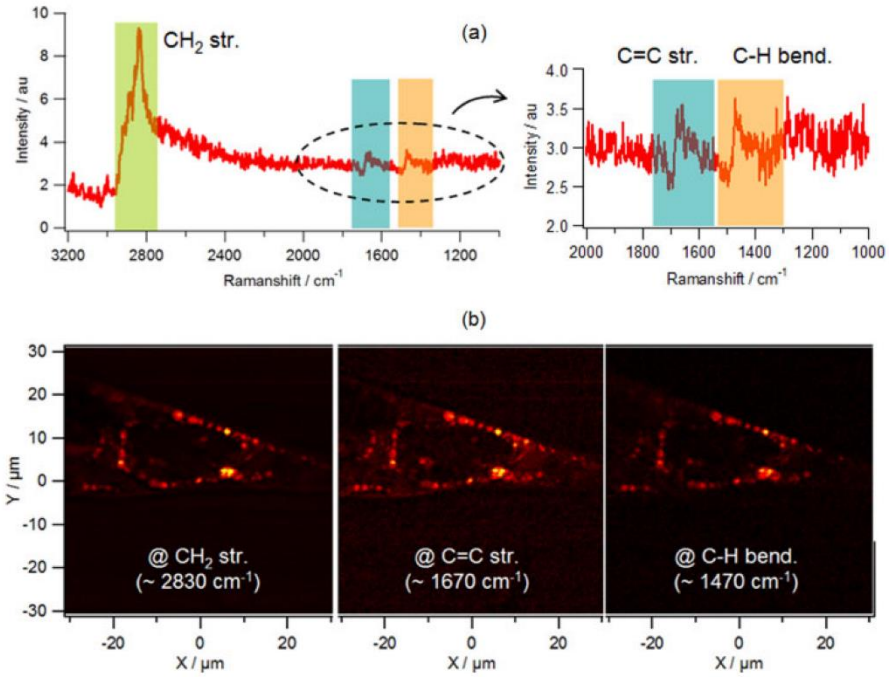

Figure 3. Spectral profile of M-CARS signal (a) and multi-colour imaging of *Caenorhabditis elegans* in both CH2 stretch and fingerprint regions (b). Exposure time is 100 ms/pixel. Image size is 201 pixel × 201 pixel.

the M-CARS signal. The exposure time is 100 ms. A strong signal is observed around 2830 cm^{-1} ($\lambda_{Stokes} \sim 1522$ nm), which corresponds to the CH_2 stretch vibrational mode. For this mode, the spectral power density of the Stokes radiation is 80 and 34 µW/nm before and after the filters, respectively. On the other hand, several dispersive patterns are observed in the fingerprint region. Based on the Raman shifts, the dispersive patterns at 1670 cm^{-1} ($\lambda_{Stokes} \sim 1294$ nm) and 1470 cm^{-1} ($\lambda_{Stokes} \sim 1261$ nm) are assigned to C=C stretch and C–H bend vibrational modes, respectively. At 1294 nm, the spectral power density of the Stokes radiation is 160 and 69 µW/nm before and after the filters, respectively. At 1261 nm, the spectral power density of the Stokes radiation is 175 and 75 µW/nm before and after the filters, respectively.

Finally, multi-colour imaging of *Caenorhabditis elegans* could be implemented in both the CH_2 stretch and fingerprint regions. Figure 3(b) shows each CARS image at the CH_2 stretch, C=C stretch and C–H bend vibrational modes. The image size is 201 pixels × 201 pixels. It should be noticed that all the images exhibit small spots inside the nematodes and are characterised by the same contrast. It means that they visualise the same molecular species. Taking into account the vibrational information, they originate from unsaturated lipids, which are stored as lipid droplets inside of the nematodes.

One of the main drawbacks of using our sub-nanosecond SC source for M-CARS microspectroscopy is the limited repetition rate (33 kHz), which makes the exposure time quite long. However, a new source with higher repetition rate has been developed recently, with the aim of performing video-rate imaging. Another drawback relates to the shot-by-shot fluctuations of the SC spectral profile. These fluctuations depend both on the stability of the 1064 nm microchip laser and on the nature of the nonlinear phenomena occurring in the PCF, which mainly are modulation instability and solitonic effects in the present case. In practice, the CARS signal is averaged according to the exposure time, with an impact on the contrast of the acquired image.

Conclusion

We have proposed and realised a new SC laser source for ultra-broadband M-CARS microspectroscopy. This source is designed to be of very compact configuration, based on the combination of a sub-nanosecond microchip laser and an air–silica PCF. Such configuration offers additional advantages regarding robustness, stability and cost. The applicability of the source to M-CARS microspectroscopy has been successfully demonstrated through the effortless multi-colour imaging of *Caenorhabditis elegans* in both the C–H stretch and fingerprint regions.

We emphasise that sub-nanosecond microchip-based SC sources embody a disruptive and alternative technology to the widespread picosecond or femtosecond laser systems. In this way, the results introduced here evidence that sub-nanosecond lasers offer really new opportunities in the CARS applications field. The applicability of these compact sources could be soon extended to other label-free or fluorescence imaging techniques, and ultimately to multi-modal imaging.

J. Raman Spectrosc. **2011**, *42*, 1871–1874

Acknowledgements

The authors wish to thank AVRUL/OSEO for financial support and LEUKOS company for technical support with the laser source development and integration. They also gratefully acknowledge J. Ukon (HORIBA, Ltd.) for assisting in the collaboration between the French and Japanese groups.

References

[1] M. D. Duncan, J. Reintjes, T. J. Manuccia, *Opt. Lett.* **1982**, *7*, 350.
[2] J. G. White, W. B. Amos, M. Fordham, *J. Cell Biol.* **1987**, *105*, 41.
[3] A. Zumbusch, G. R. Holtom, X. S. Xie, *Phys. Rev. Lett.* **1999**, *82*, 4142.
[4] M. Hashimoto, T. Araki, S. Kawata, *Opt. Lett.* **2000**, *24*, 1768.
[5] J. Cheng, X. S. Xie, *J. Phys. Chem. B* **2004**, *108*, 827.
[6] J. Cheng, A. Volkmer, L. D. Book, X. S. Xie, *J. Phys. Chem. B* **2002**, *106*, 8493.
[7] C. Otto, A. Voroshilov, S. G. Kruglik, J. Greve, *J. Raman Spectrosc.* **2001**, *32*, 495.
[8] T. W. Kee, M. T. Cicerone, *Opt. Lett.* **2004**, *29*, 2701.
[9] H. Kano, H. Hamaguchi, *Appl. Phys. Lett.* **2005**, *86*, 121113.
[10] E. R. Andresen, H. N. Paulsen, V. Birkedal, J. Thøgersen, S. R. Keiding, *J. Opt. Soc. Am. B* **2005**, *22*, 1934.
[11] M. Okuno, H. Kano, P. Leproux, V. Couderc, H. Hamaguchi, *Opt. Lett.* **2007**, *32*, 3050.
[12] M. Okuno, H. Kano, P. Leproux, V. Couderc, H. Hamaguchi, *Opt. Lett.* **2008**, *33*, 923.
[13] J. M. Dudley, G. Genty, S. Coen, *Rev. Mod. Phys.* **2006**, *78*, 1135.

Partie 3 - Microspectroscopie non linéaire multimodale sous excitation supercontinuum

I. Développement instrumental centré sur la microspectroscopie CARS

Cette thématique a débuté dans le cadre du projet ASTRID NEOSPRAM (« Nouveaux procédés de spectroscopie Raman pour l'analyse d'agents biologiques », 2014-2018), dont j'étais le coordinateur. NEOSPRAM se positionne dans le contexte de la détection rapide de la présence d'agents pathogènes (bactéries, virus, moisissures) dispersés dans l'air par un agresseur sur un théâtre d'opération. La voie proposée pour répondre à ce besoin avéré de la Défense consiste à intégrer une détection par spectroscopie Raman cohérente au sein d'un cytomètre en flux avec collecteur d'aérosol. Dans ce contexte, le but du projet NEOSPRAM était de « développer de nouveaux procédés de spectroscopie Raman non linéaire, compatibles avec les exigences de la cytométrie en flux à haut débit, permettant d'acquérir des spectres Raman d'agents biologiques avec une fréquence typique de l'ordre de quelques milliers de spectres par seconde, un rapport signal sur bruit, une résolution spectrale et une richesse compatibles avec leur classification au niveau de l'espèce ». La **Figure 22** présente l'organigramme technique du projet ainsi que l'architecture simplifiée d'une nouvelle source laser proposée pour mettre en œuvre les différents procédés de spectroscopie envisagés initialement. **NEOSPRAM s'articulait avec un autre projet ASTRID, SIBIRAM** (« Signature des agents biologiques par microspectroscopie Raman », LASIR-CSTB, coordonné par Ludovic Duponchel, Université de Lille), dont l'objectif était de démontrer la faisabilité de l'identification, au niveau de l'espèce, des microorganismes présents dans des prélèvements d'air et de comprendre les relations entre signatures spectrales et génotypes/phénotypes de ces microorganismes.

Le développement instrumental conduit dans le cadre de NEOSPRAM et de la thèse d'Erwan Capitaine (également financée par la DGA) est illustré en **Figure 23**. Notre stratégie a consisté à acquérir et modifier un microspectroscope Raman disponible sur le marché (LabRAM HR Evolution, HORIBA Scientific, France), afin de **disposer sur le même appareil de modalités d'analyse telles que Raman, CARS multiplex (modalité centrale) et génération d'harmoniques (SHG, THG), en détection à la fois *backward* et *forward***. Le microscope d'origine (ECLIPSE Ti, Nikon, Japon) étant de type inversé, la mise en place de la détection du signal *forward* a nécessité la modification de la partie haute du statif initial afin d'ajouter un objectif de collection, dont la position est réglable selon les trois dimensions. En ce qui concerne la partie laser, le système a été conçu pour fonctionner à partir d'une source émettant à 1064 nm, délivrant le rayonnement dit de pompe et servant également à générer un supercontinuum infrarouge Stokes dans une PCF, comme présenté dans la **Partie 2**. En effet, la source laser à sorties multiples dans le visible/UV (**Figure 22**), bien que construite et fonctionnelle dans le cadre de NEOSPRAM, n'a finalement pas été testée sur le système de microspectroscopie, la priorité ayant été donnée à l'excitation infrarouge par le consortium et la DGA.

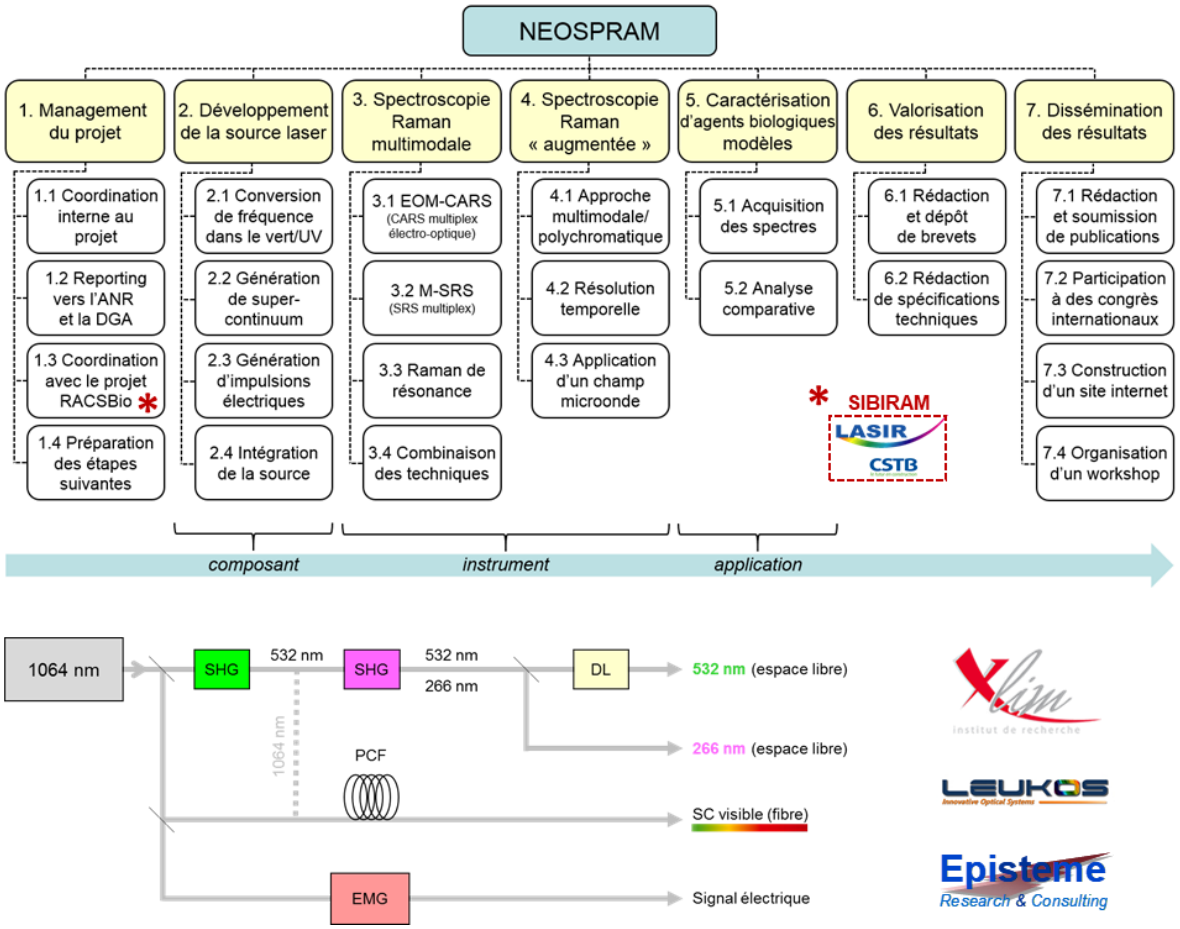

Figure 22 : Organigramme technique du projet NEOSPRAM et architecture simplifiée d'une nouvelle source laser proposée dans le cadre du projet (coordinateur : XLIM, partenaire : LEUKOS, sous-traitant : Episteme R&C). L'astérisque * met en évidence l'articulation entre les projets NEOSPRAM et SIBIRAM (coordinateur : LASIR-Université de Lille, partenaire : CSTB, Centre scientifique et technique du bâtiment) dans le cadre d'un projet plus global, RACSBio (« Raman-activated cell sorter for biosurveillance »).

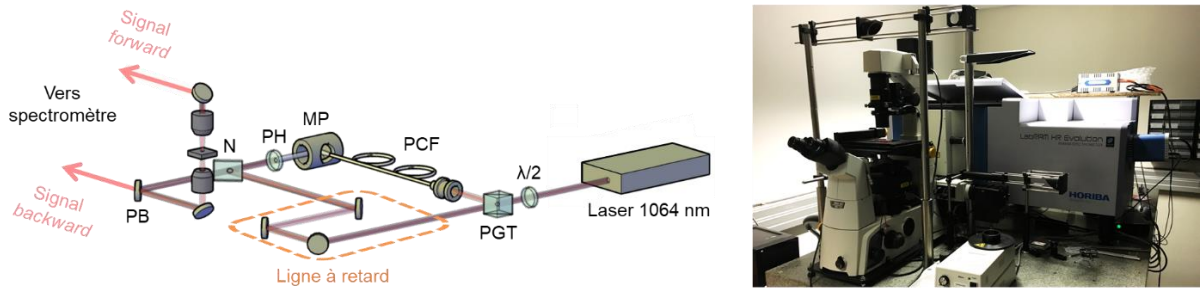

Figure 23 : Développement instrumental du projet NEOSPRAM. A gauche : représentation schématique de la partie laser et du microscope (PGT : polariseur de Glan-Taylor, MP : miroir parabolique, PH : filtre passe-haut, N : filtre notch, PB : filtre passe-bas). A droite : photographie du système complet de microspectroscopie (la partie laser se trouve derrière le spectroscope).

En complément du développement instrumental et en collaboration avec l'équipe du Pr. Kano, nous avons introduit une méthode électro-optique nommée **« electro-CARS »**, basée sur la combinaison de la spectroscopie CARS multiplex et de la stimulation de l'échantillon par application d'un champ électrique statique [63]. Cette méthode permet de discriminer le signal CARS résonant (*i.e.*, qui contient de l'information vibrationnelle) du bruit de fond non résonant (NRB pour *non-resonant background*), ce dernier représentant un inconvénient majeur de la spectroscopie CARS du fait des distorsions du signal qu'il engendre. L'expérience (**Figure 24a**) consiste à induire un phénomène d'orientation moléculaire dans le milieu grâce au champ électrique appliqué et à générer le signal CARS en contrôlant la direction de la polarisation optique par rapport à celle du champ électrique (et donc des liaisons chimiques des molécules). Alors, en fonction de l'angle entre le champ électrique et la polarisation optique, on observe une augmentation ou une diminution du rapport signal sur bruit, comme mis en évidence dans le cas des modes vibrationnels d'élongation symétrique/antisymétrique CH_2/CH_3 d'une solution de n-alkanes (**Figures 24b** et **24c**).

Cette expérience avec un type très simple de composé organique a permis de démontrer la preuve de principe de la méthode electro-CARS. Néanmoins, cette dernière n'a pas encore été testée sur des échantillons biologiques.

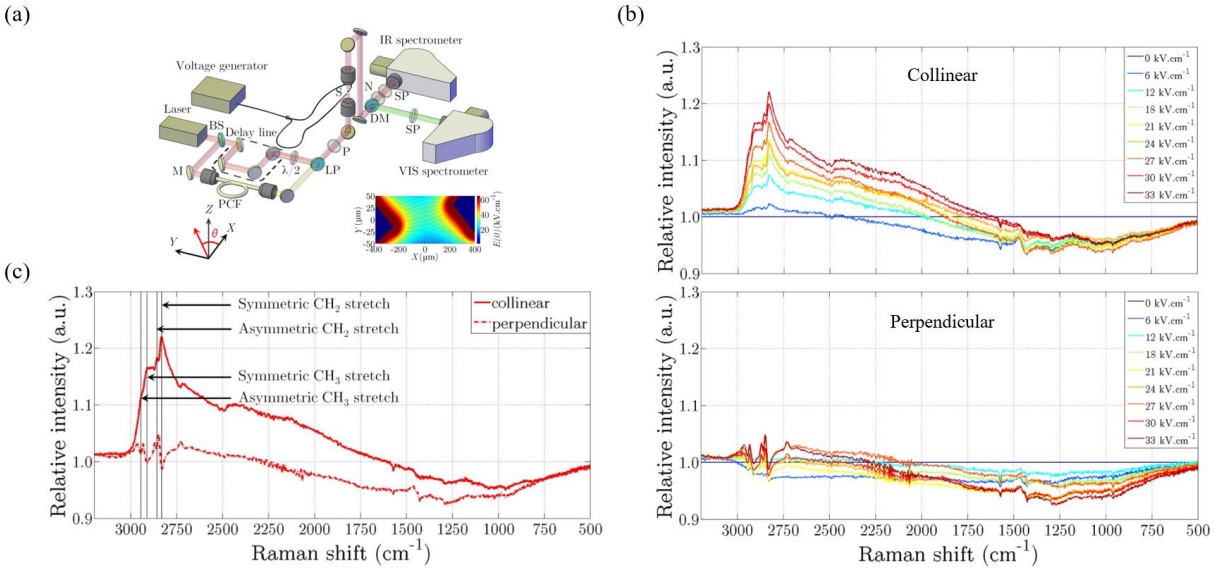

Figure 24 : Spectroscopie CARS multiplex sous stimulation par champ électrique statique (electro-CARS). (a) Montage expérimental (encart : distribution transversale du champ électrique entre les électrodes ; calcul réalisé avec COMSOL Multiphysics 4.5 pour une tension de 2400 V). (b) Évolution du spectre CARS d'une solution de n-alkanes en fonction de l'amplitude du champ électrique appliqué et pour deux orientations relatives entre les champs optique et électrique, correspondant aux configurations colinéaire et perpendiculaire (normalisation par le spectre mesuré en l'absence de champ électrique). (c) Comparaison entre les deux configurations pour la valeur maximale d'amplitude du champ électrique appliqué (33 kV/cm). Figure adaptée à partir de [63].

II. Application à l'imagerie d'échantillons biologiques sans marquage

Dans leur travail, les biologistes sont régulièrement amenés à visualiser les entités qu'ils étudient - les cellules - à l'échelle cellulaire ou tissulaire. Ces observations peuvent avoir de nombreuses motivations : suivi de cellules en culture, compréhension des mécanismes cellulaires/tissulaires associés à des changements d'état physiologique ou encore étude de l'organisation et de la composition des « organes » ou constituants de la cellule, appelés organites. **Ces opérations sont principalement faites à l'aide de microscopes optiques de fluorescence.** Pour cela, des molécules intrinsèquement fluorescentes ou marqueurs sont utilisées soit directement lorsqu'elles ont une affinité pour un constituant cellulaire précis (ex. : DAPI, BODIPY), soit couplées à un anticorps qui joue le rôle d'intermédiaire entre la molécule fluorescente et une biomolécule cible de la cellule. Une fois la cellule marquée, il est possible de détecter et d'acquérir la fluorescence émise pour visualiser la présence/localisation des différentes molécules. Cette méthode possède cependant des limites. Tout d'abord, il faut identifier des marqueurs compatibles avec l'organisme et/ou le mécanisme étudié. De plus, dans certains cas, les cellules doivent être fixées, c'est-à-dire figées chimiquement et donc « tuées » afin de conserver, dans le temps, leur état physiologique et leur morphologie. Enfin, le marquage nécessite plusieurs étapes de modification des cellules pour lier efficacement les molécules fluorescentes aux biomolécules cibles et ainsi permettre une acquisition de qualité. **Ces étapes altèrent irrémédiablement l'échantillon et peuvent biaiser la visualisation qui en est faite.**

Dans ce cadre, la microspectroscopie CARS est une alternative pertinente à la microscopie de fluorescence. En effet, reposant sur la mise en jeu de vibrations moléculaires au sein de l'échantillon, elle permet d'obtenir une information sur la composition chimique de ce dernier **sans nécessité de marquage préalable**. En mesurant le spectre CARS de l'échantillon en fonction de la position, une image dite hyperspectrale peut être acquise, le jeu de données correspondant se représentant sous la forme d'un hypercube. Il est alors possible, à partir de ce jeu de données, de reconstituer différentes images de l'échantillon correspondant aux différents constituants chimiques présents dans celui-ci. En fonction du type d'échantillon, il peut être intéressant de compléter l'analyse CARS par une ou plusieurs modalités non linéaires sans marquage, telles que la SHG, couramment utilisée pour révéler la présence de molécules non centrosymétriques (collagène, actomyosine, tubuline, etc.). Afin d'illustrer de façon plus large l'apport potentiel des **approches multimodales**, nous donnons en **Tableau 1** une synthèse des principales méthodes de micro(spectro)scopie optique pour la bio-imagerie, incluant pour chacune la nature de l'information chimique/biologique collectée.

Dans la suite de cette section, nous présentons les résultats majeurs, en matière de bio-imagerie sans marquage, obtenus au moyen du système de microspectroscopie « NEOSPRAM » et **en collaboration avec différent.e.s collègues biologistes** de l'Université de Limoges. Ces résultats portent sur l'étude (1) de coupes végétales (sapin de Douglas), (2) d'un prélèvement osseux (crâne de souris), (3) du cycle cellulaire (cellules HEK) et enfin (4) du métabolisme lipidique de cellules cancéreuses (HT29).

Nom	Acronyme/appellation	Type de signal mesuré	Information collectée
Microscopie confocale	**LCSM** (*laser confocal scanning microscopy*)	Fluorescence	**Structurelle et/ou fonctionnelle** (présence de molécules fluorescentes endogènes ou exogènes)
Microscopie multiphotonique	**TPEF** (*two-photon excitation microscopy*)		
	SHG (*second harmonic generation*)	Lumière générée à la fréquence double de l'excitation	**Structurelle** (présence de molécules non centrosymétriques telles que collagène, actomyosine, tubuline)
	THG (*third harmonic generation*)	Lumière générée à la fréquence triple de l'excitation	**Structurelle** (présence d'interfaces comme les membranes cellulaires)
Micro(spectro)scopie de diffusion Raman	**Raman**, **CARS** (*coherent anti-Stokes Raman scattering*), **SRS** (*stimulated Raman scattering*)	Vibrationnel	**Chimique => structurelle et/ou fonctionnelle** (caractérisation de la composition moléculaire)
Micro(spectro)scopie infrarouge à transformée de Fourier	**FTIR** (*Fourier-transform infrared spectroscopy*)	Vibrationnel	**Chimique => structurelle et/ou fonctionnelle** (caractérisation de la composition moléculaire)

Tableau 1 : Principales méthodes de micro(spectro)scopie optique pour la bio-imagerie.

A des fins de clarté, les résultats invoqués sont exposés ci-après sous forme de liste, avec pour chacun les éléments clés (conditions expérimentales et contexte scientifique). Des informations techniques complémentaires sont données dans les figures.

(1) Imagerie de coupes de sapin de Douglas (Figure 25)
Modalité : CARS multiplex [2500-3200 cm^{-1}]
Excitation : pompe 1064 nm / 1 ns / 20 kHz + supercontinuum infrarouge
Détection : *forward* | 50 ms/pixel
Contexte : thèses E. Capitaine et I. Plazanet
Collaborateur biologiste : **Guy Costa, PU, PEIRENE (maintenant LABCiS)**
Objectif : visualisation sans marquage des différents constituants de la paroi cellulaire du bois, tels que cellulose, lignine, polysaccharides, etc. (cible : coupes transversales de duramen, ou bois de cœur, de Douglas)

(2) Imagerie de l'os pariétal de la souris (Figure 26) [68]
Modalités : CARS multiplex [700-1200 cm^{-1}] et [2500-3200 cm^{-1}] + SHG à 532 nm
Excitation : pompe 1064 nm / 60 ps / 110 kHz + supercontinuum infrarouge
Détection : *backward* | 5 ms/pixel
Contexte : projet NEOSPRAM / thèse E. Capitaine
Collaboratrice biologiste : **Sylvia Bardet-Coste, MCF, XLIM**
Objectif : visualisation sans marquage des phases organique (fibres de collagène) et minérale (cristaux d'hydroxyapatite), ainsi que des cellules osseuses (ostéocytes)

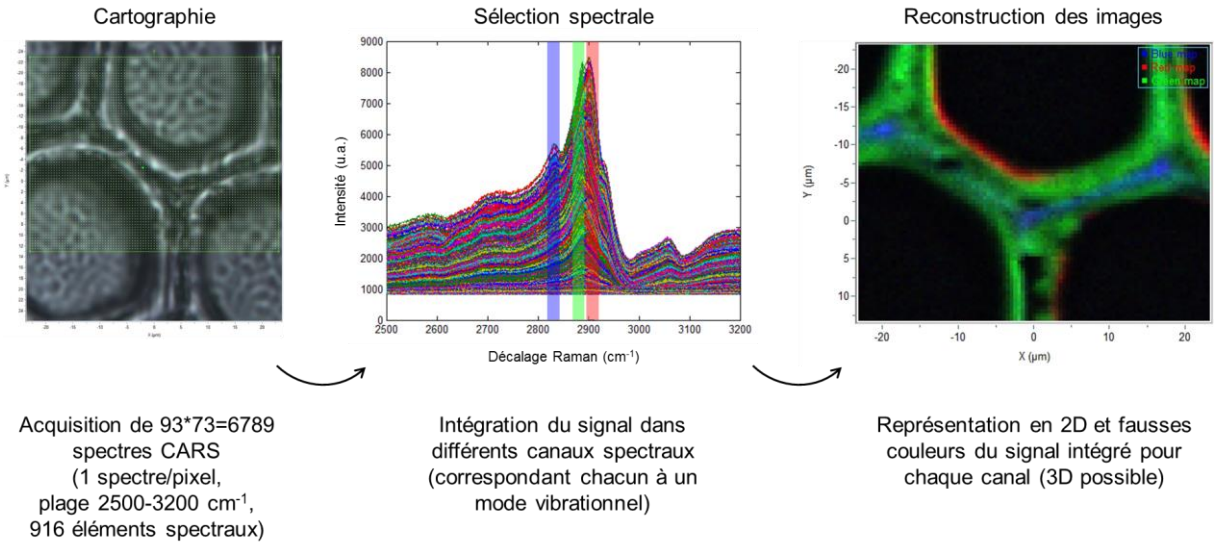

Figure 25 : Imagerie d'une coupe transversale de duramen de Douglas par microspectroscopie CARS. La figure illustre les différentes étapes permettant d'aboutir à l'obtention d'images chimiquement sélectives.

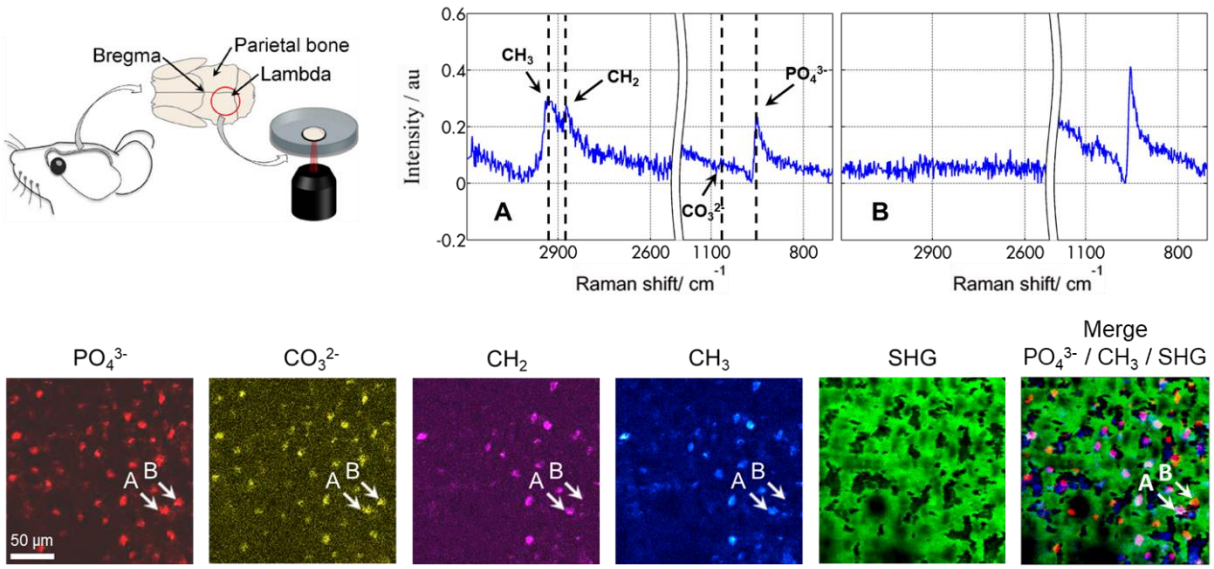

Figure 26 : Imagerie de l'os pariétal (os du crâne) de la souris par microspectroscopie CARS/SHG. En haut : spectres CARS bruts mesurés aux points A et B, mettant en évidence les modes vibrationnels des groupements PO_4^{3-} (961 cm^{-1}), CO_3^{2-} (1070 cm^{-1}), CH_2 (2878 cm^{-1}) et CH_3 (2950 cm^{-1}). En bas : images obtenues par dérivation des spectres bruts et intégration du signal pour chaque mode vibrationnel sur une bande de 20 cm^{-1} ; visualisation de l'hydroxyapatite (rouge/jaune), des ostéocytes (violet/bleu), de la matrice de collagène (vert) et des trois constituants superposés. Au point A, présence conjointe d'hydroxyapatite et d'un ostéocyte ; au point B : présence d'hydroxyapatite principalement. Figure adaptée à partir de [68].

(3) Étude du cycle cellulaire (Figure 27) [74]

Modalités : CARS multiplex [2500-3200 cm^{-1}] + transfluorescence plein champ (modalité de contrôle)

Excitation : pompe 1064 nm / 1 ns / 20 kHz + supercontinuum infrarouge

Détection : *forward* | 50 ms/pixel

Contexte : thèse T. Guerenne-Del Ben

Collaborateur biologiste : **Jean-Michel Petit, PU, PEIRENE (maintenant LABCiS)**

Objectif : visualisation sans marquage des différentes sous-phases de la mitose et comparaison aux images de fluorescence pour validation (cible : cellules HEK293, *human embryonic kidney* 293, fixées et marquées au DAPI)

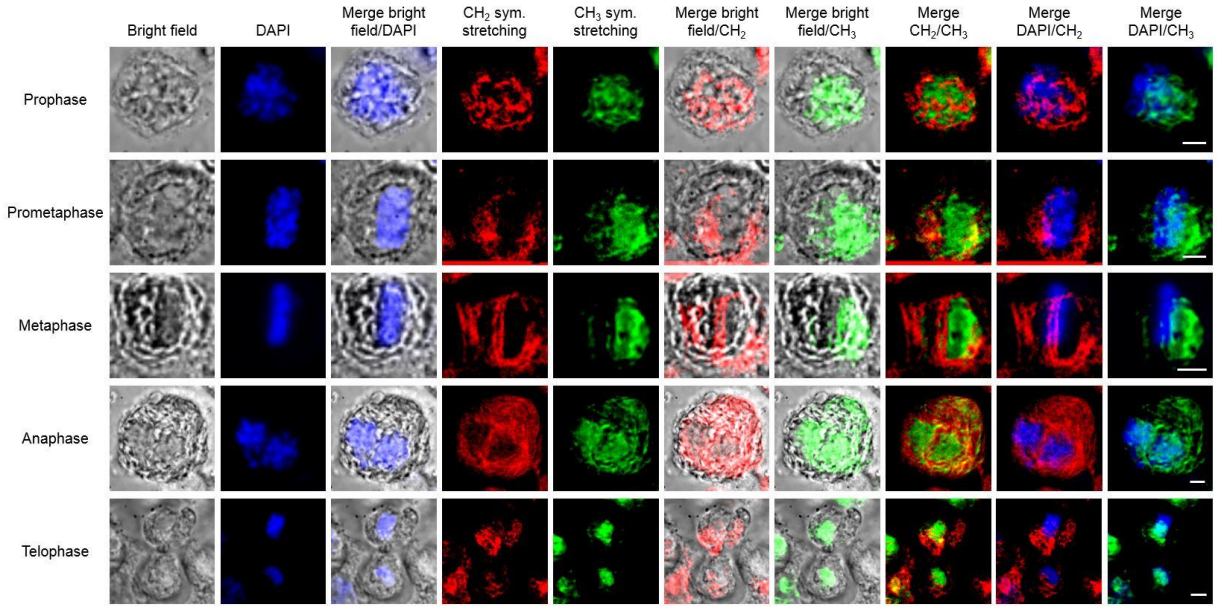

Figure 27 : Étude du cycle cellulaire (sous-phases de la mitose) par microspectroscopie CARS. La fluorescence du DAPI, qui met en évidence le noyau des cellules, est utilisée comme modalité de contrôle à des fins de validation. Les images CARS sont obtenues par intégration du signal pour les modes vibrationnels CH_2 (lipides) et CH_3 (protéines) après extraction de la partie vibrationnelle des spectres au moyen de la méthode de l'entropie maximale (MEM). Barre d'échelle : 5 µm. Figure extraite de [74].

(4) Étude du métabolisme lipidique de cellules cancéreuses (Figure 28) [78]

Modalités : CARS multiplex [2500-3200 cm^{-1}] + transfluorescence plein champ (modalité de contrôle)

Excitation : pompe 1064 nm / 1 ns / 20 kHz + supercontinuum infrarouge

Détection : *forward* | 50 ms/pixel

Contexte : thèse T. Guerenne-Del Ben

Collaborateur biologiste : **Jean-Michel Petit, PU, PEIRENE (maintenant LABCiS)**

Objectif : visualisation sans marquage de l'inactivation du récepteur TrkB par l'inhibiteur K252a à travers l'observation du métabolisme lipidique (cible : cellules HT29, lignée de cancer colorectal humain, vivantes et marquées au Hoechst 33342)

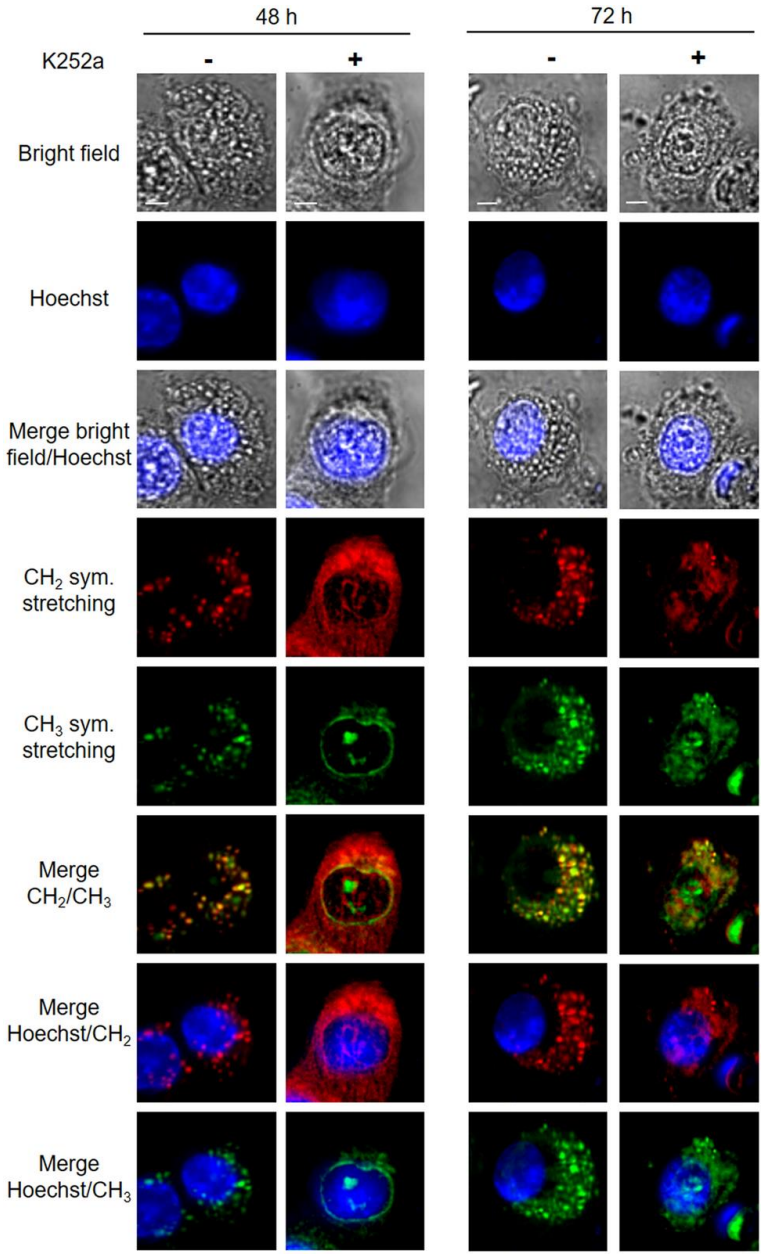

Figure 28 : Étude du métabolisme lipidique de cellules cancéreuses HT29 par microspectroscopie CARS. Les images CARS sont obtenues par intégration du signal pour les modes vibrationnels CH_2 (lipides) et CH_3 (protéines) après extraction de la partie vibrationnelle des spectres au moyen de la méthode de l'entropie maximale (MEM). Barre d'échelle : 5 µm. Figure extraite de [78].

En complément de ces résultats exploitant essentiellement la modalité CARS multiplex, nous avons eu l'occasion de démontrer les potentialités offertes par les sources supercontinuum compactes pour la microscopie multiphotonique *in vitro* et *in vivo* (modalités TPEF et SHG, voir **Tableau 1**) [59]. Dans ces travaux, seul le rayonnement supercontinuum est utilisé pour exciter sur une large bande spectrale des processus d'ordre deux (SHG) et trois (TPEF), indiquant la disponibilité d'une puissance crête compatible avec la mise en place de ces processus non linéaires. Il s'agit d'un aspect nouveau par rapport à la microspectroscopie CARS multiplex, dans laquelle l'échantillon est excité à la fois par l'onde Stokes supercontinuum et par une onde de

pompe monochromatique transportant une forte puissance crête. Par ailleurs, nos collaborateurs japonais ont pu explorer avec succès et à de multiples reprises les possibilités qu'offrent les sources CARS à double sortie pour implémenter plusieurs modalités non linéaires sur le même instrument, en particulier CARS, SHG, THG et TPEF [38,53,55,77,79,85]. Ainsi, l'ensemble de nos travaux suggère **le fort potentiel applicatif que présente la microspectroscopie multimodale sous excitation supercontinuum** (au sens large). A cet égard, nous terminons cette section en mentionnant le travail de synthèse intéressant de [Poudel & Kaminski, 2019], qui propose un état de l'art de l'utilisation des sources supercontinuum (fs, ps, ns et CW) pour les applications d'imagerie biomédicale.

III. Nouvelles approches de traitement et analyse de données hyperspectrales CARS

Dans ce qui a été présenté précédemment, les spectres CARS bruts sont généralement traités par la méthode de l'entropie maximale (MEM), qui permet d'en extraire l'information vibrationnelle (partie imaginaire de la susceptibilité non linéaire d'ordre 3) et ainsi d'obtenir des spectres équivalents - dans une certaine mesure - à ceux de la diffusion Raman spontanée [Vartiainen *et al.*, 2006]. La **Figure 29** illustre le principe de cette méthode. Une simple technique d'intégration du signal ou d'approximation gaussienne sur les bandes vibrationnelles d'intérêt est ensuite utilisée afin de reconstruire différentes images de l'échantillon. Comme dans le cas de la microspectroscopie Raman conventionnelle, **cette technique de traitement des données n'est généralement pas suffisamment performante** pour analyser des échantillons complexes (biologiques), dont les signatures vibrationnelles des différents constituants sont susceptibles de se recouvrir dans certaines bandes spectrales. Alors, avoir recours à des approches chimiométriques peut permettre de reconstruire des images plus spécifiques des constituants de l'échantillon.

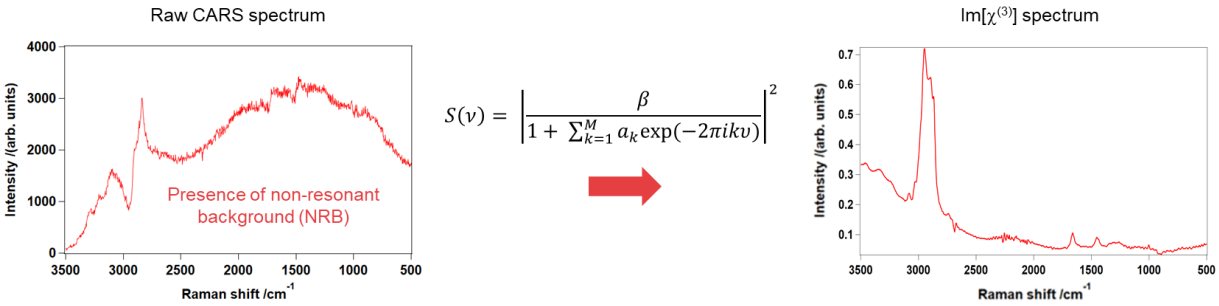

Figure 29 : Méthode de l'entropie maximale (MEM) appliquée à l'extraction du signal vibrationnel à partir d'un spectre CARS brut. La fonction S(ν) est le modèle utilisé pour ajuster chaque ligne dispersive CARS et retrouver la phase de la susceptibilité non linéaire $X^{(3)}$, dont la partie imaginaire fournit alors un spectre de type Raman conventionnel (comportant des pics ayant l'allure de fonctions lorentziennes). La MEM ne nécessite pas d'information *a priori* sur les modes vibrationnels pouvant exister dans l'échantillon. La méthode est décrite en détails dans [Vartiainen *et al.*, 2006].

Pour répondre à cette problématique de traitement/analyse des données hyperspectrales CARS, je co-porte un projet transdisciplinaire dans le cadre du flagship « Promoting health with

advanced diagnostics and therapies » du Labex Σ-LIM (2020-2025), en collaboration avec les chercheurs de l'axe ASALI (Synthèse et analyse d'images) d'XLIM et de l'équipe « Biomatériaux » de l'IRCER. L'aspect applicatif du projet sur les dispositifs biocéramiques étant traité dans la section suivante, nous nous concentrons ici sur la partie traitement/analyse de données, qui a été initiée dans le cadre de la thèse de Damien Boildieu, soutenue en décembre 2022. Une contribution majeure de cette thèse consiste en une **nouvelle approche d'imagerie/segmentation cellulaire CARS avec analyse de données non supervisée** [84]. D'une part, il s'agit d'exploiter la technique dite de résolution de courbes multivariées (MCR pour *multivariate curve resolution*) [De Juan *et al.*, 2014], dans laquelle le jeu de données est décomposé de manière itérative comme le produit d'une matrice de concentrations C et d'une matrice de spectres S^T ; d'autre part, la méthode (également itérative) de Chan-Sandberg-Vese (CSV) [Chan *et al.*, 2000] est utilisée comme contrainte de segmentation dans l'algorithme MCR (**Figure 30**). Alors, l'approche proposée permet d'extraire K composants, pour chacun desquels sont disponibles une carte de concentration ou image (reconstruite à partir de C, avec ou sans segmentation) et un spectre (issu de S^T). En termes mathématiques, les K spectres constituent une base de dimension réduite et les K images correspondent à la projection du jeu de données initial sur ces spectres.

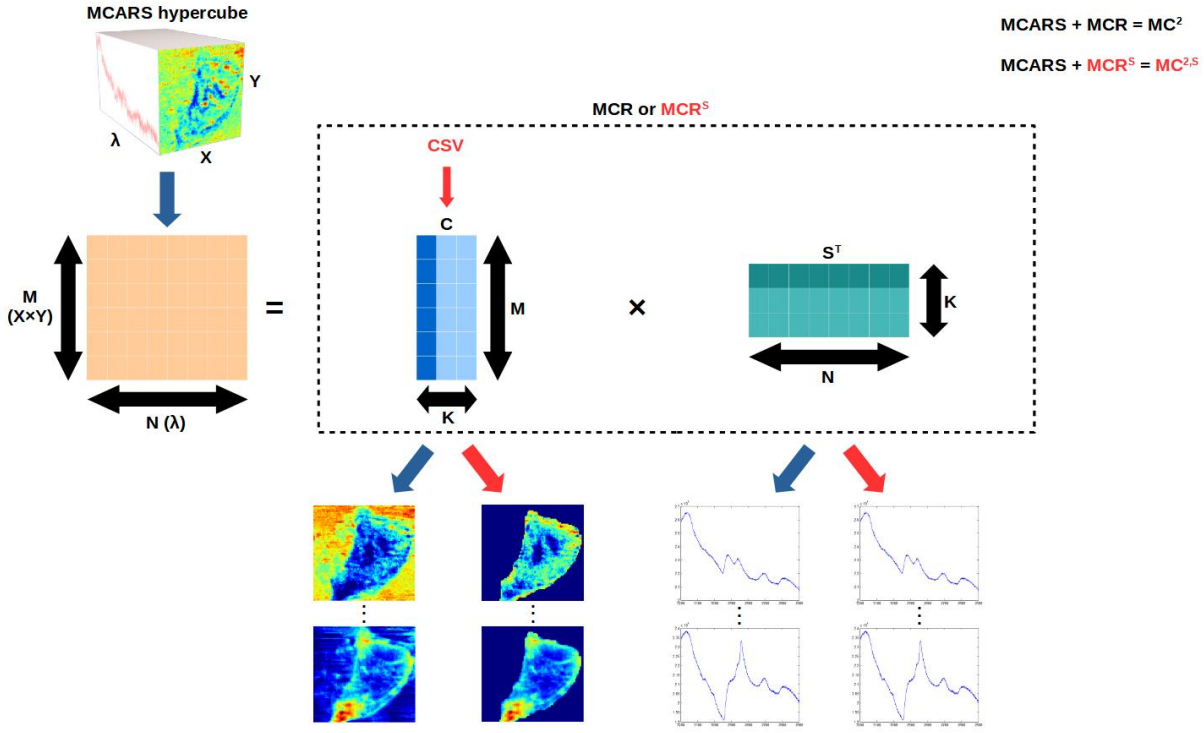

Figure 30 : Analyse de données hyperspectrales CARS par résolution de courbes multivariées (MCR) pour l'imagerie (méthode MC^2) et la segmentation (méthode $MC^{2,S}$) cellulaire. Le jeu de données CARS est linéarisé (M spectres contenant chacun N éléments spectraux), puis l'algorithme MCR (sans segmentation) ou MCR^S (avec segmentation) est appliqué pour calculer les matrices de concentration C (de dimension M*K) et de spectres S^T (de dimension K*N) de manière itérative ; finalement, une image (segmentée dans le cas de la MCR^S) et un spectre sont extraits pour chacun des K composants. L'acronyme CSV désigne la méthode de Chan-Sandberg-Vese, qui est utilisée comme contrainte de segmentation dans l'algorithme MCR^S. Figure extraite de [84].

Dans un premier temps, l'approche a été appliquée sans contrainte de segmentation (MC^2) à l'imagerie cellulaire, en revisitant l'analyse des nombreux jeux de données acquis durant la thèse de biologie cellulaire de Tiffany Guerenne-Del Ben. L'analyse d'une cellule HEK293 fixée en interphase a permis de valider la méthode MC^2 à la fois en termes d'imagerie chimiquement sélective (**Figure 31A**) et de spectroscopie (**Figures 31B et 31C**). Notamment, on observe **une très bonne discrimination des lipides** (cytoplasme et membrane plasmique, composant #3), **des protéines** (noyau/nucléoles, composant #2) **et de l'eau** (milieu extracellulaire, composants #1 et #4). La robustesse de la méthode a ensuite été évaluée en analysant, de manière non supervisée, des cellules dans différents états physiologiques et situations expérimentales (**Figures 31D, 31E, 31F, 31G**). Cette étude a mis en évidence une très bonne stabilité de l'approche. Nous soulignons le fait que ces résultats sont obtenus en travaillant uniquement dans la bande 2500-3200 cm^{-1}, c'est-à-dire en s'affranchissant de la région dite d'empreinte digitale (ou moléculaire). Ceci s'explique par l'utilisation combinée d'une excitation laser en régime (sub)nanoseconde et d'un spectroscope à haute résolution (~ 0,8 cm^{-1}), qui permet de capter puis de traiter/analyser numériquement **une information vibrationnelle riche bien que sur une plage spectrale limitée** (en termes de nombres d'onde et de types de modes vibrationnels). Enfin, concernant la détermination du nombre de composants K employé dans l'algorithme MCR (dimension de l'espace de projection), nous avons introduit l'utilisation du *lack-of-fit* (LOF) afin d'évaluer numériquement (i.e., objectivement) la qualité de la décomposition MCR en fonction de la valeur de K. Nous ne développons pas ce point autour de la dimensionnalité ici, mais les détails sont disponibles aux sections 2.4 et 4.1 de [84].

Dans un second temps, le jeu de données correspondant à la cellule HEK293 de la **Figure 31A** a été traité par l'algorithme MCR^S (méthode globale $MC^{2,S}$), dans lequel est appliquée la contrainte de segmentation CSV. La **Figure 32** présente les résultats ainsi obtenus, avec comme référence ceux issus de l'approche sans segmentation. On constate, pour chaque composant extrait, une nette délimitation de la cellule par rapport à son environnement, **ce qui valide l'effet de segmentation escompté**. En outre, lorsque la contrainte CSV est utilisée, la résolution MCR est resserrée sur la région intracellulaire, résultant en une extraction plus précise du contenu aqueux à l'intérieur de la cellule (composants #1 et #4). Une forte contribution est notamment visualisée au niveau de la périphérie interne de la cellule (particulièrement visible dans le cas du composant #4). Au-delà de l'observation de l'eau intracellulaire, la méthode $MC^{2,S}$ serait intéressante pour l'étude d'éléments majoritairement présents dans l'environnement de la cellule.

Finalement, les méthodes MC^2 et $MC^{2,S}$ ont été appliquées à l'analyse sans marquage d'amas cellulaires de différentes tailles (**Figure 33**). Les résultats obtenus témoignent d'une excellente reproductibilité par rapport à ceux décrits précédemment. A savoir, les composants #1 et #4 révèlent la distribution du contenu aqueux, le composant #2 est associé aux noyaux/nucléoles, et le composant #3, majoritairement cytoplasmique, met ici en évidence une structure périnucléaire probablement constituée de membranes intracellulaires appartenant au réticulum endoplasmique. La méthode $MC^{2,S}$ permet de raffiner l'analyse des structures à l'intérieur des amas et fournit une meilleure visualisation de l'eau dans l'espace intercellulaire. Une étude plus

approfondie des composants #1 et #4 pourrait permettre de discriminer l'état des molécules d'eau, qui peuvent être libres ou bien liées à des macromolécules.

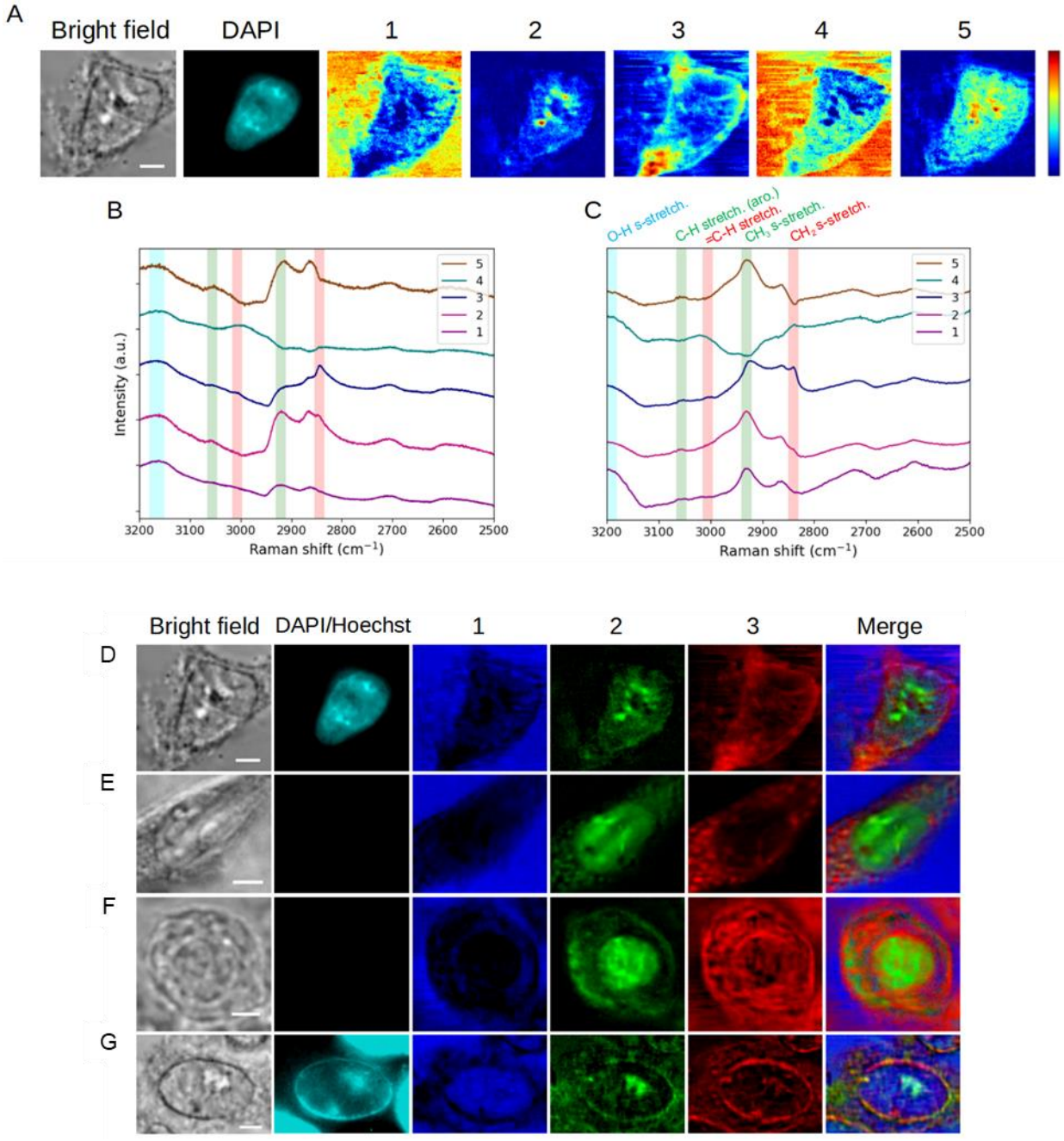

Figure 31 : Application de la méthode MC^2 à l'imagerie cellulaire. (A) Images en champ clair et de fluorescence, et cartes de concentration (K=5) obtenues pour une cellule HEK293 fixée en interphase et marquée au DAPI. (B) Spectres extraits correspondants. (C) Spectres de type Raman après traitement MEM, avec mise en évidence des modes vibrationnels associés majoritairement (en rouge) aux lipides, (en vert) aux protéines et (en bleu) à l'eau. Les barres verticales de (C) ont été reportées en (B) en tenant compte du décalage spectral existant entre les données CARS brutes et après traitement MEM. Représentation en fausses couleurs des cartes de concentration #1, #2 et #3 obtenues pour (D,E) des cellules fixées en interphase, (F) une cellule fixée en mitose et (G) une cellule vivante en interphase. Barre d'échelle : 5 µm. Figure adaptée à partir de [84].

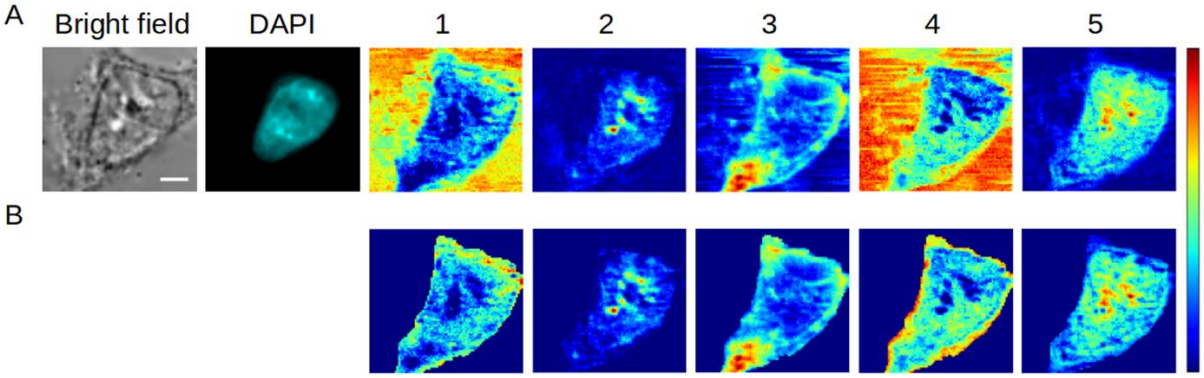

Figure 32 : Cartes de concentration d'une cellule HEK293 obtenues par application des méthodes (A) MC^2 et (B) $MC^{2,S}$. Figure adaptée à partir de [84].

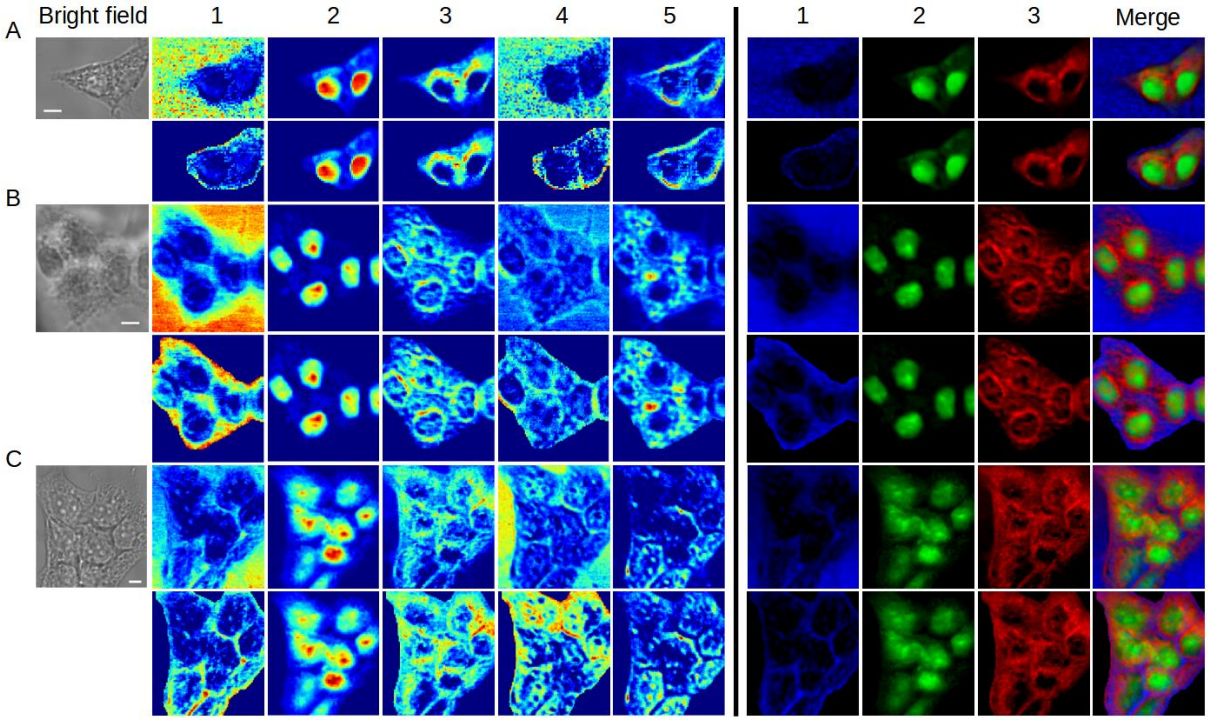

Figure 33 : Application des méthodes MC^2 et $MC^{2,S}$ à l'analyse sans marquage d'amas de cellules (fixées). Amas de (A) 2 cellules, (B) 5 cellules et (C) 8 cellules. Pour chaque amas, les cartes de concentration obtenues par les méthodes MC^2 et $MC^{2,S}$ sont représentées en première et seconde lignes, respectivement, en utilisant deux palettes de couleurs différentes. Barre d'échelle : 5 µm. Figure extraite de [84].

Dans la continuité des travaux précédents, nous avons également pu éprouver l'algorithme MCR sur des données hyperspectrales CARS massives issues de mesures sur des coupes de cerveau de souris, réalisées par nos partenaires japonais en collaboration avec l'*International Institute for Integrative Sleep Medicine* (IIIS). Les dimensions des jeux de données correspondant à ces mesures (pour les champs les plus larges) sont de l'ordre de 700px*600px, avec environ 1340 éléments spectraux sur la plage 400-4000 cm^{-1}. Pour cette raison, le traitement des données est exécuté sur

une machine disposant d'une grande quantité de mémoire vive (384 Go) et appartenant à l'axe ASALI d'XLIM. Les résultats obtenus permettent de démontrer une méthode d'imagerie moléculaire sans marquage du cerveau de souris aux échelles macroscopique et microscopique (**Figure 34**). Par exemple, à l'échelle macroscopique, il est possible de visualiser avec précision les lipides distribués dans la substance blanche, riche en fibres neuronales. A l'échelle microscopique, dans le cortex et l'hippocampe, des cellules riches en lipides ou bien riches en eau peuvent être mises en évidence. Ainsi, il est envisageable de construire un **atlas moléculaire du cerveau murin avec une résolution unicellulaire**, sans avoir recours à un marquage préalable de l'échantillon.

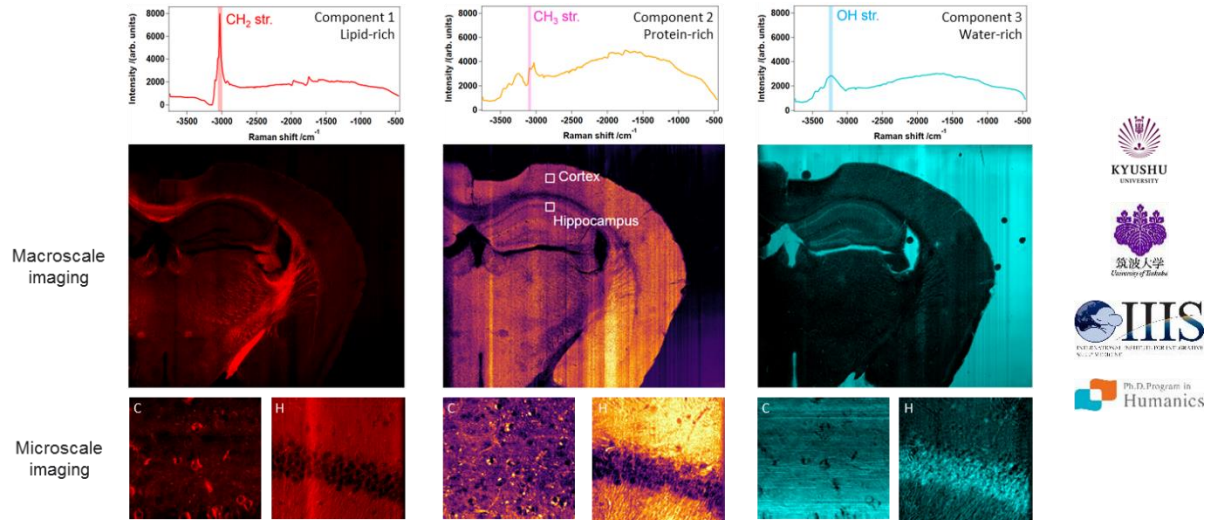

Figure 34 : Analyse de données hyperspectrales CARS massives pour l'imagerie moléculaire sans marquage du cerveau de souris aux échelles macroscopique et microscopique. Figure adaptée à partir de [AC_25].

En conclusion, l'approche multivariée que nous avons proposée est applicable à une grande variété de données hyperspectrales CARS et permet d'en réaliser l'analyse **non supervisée**, avec ou sans segmentation. A ce titre, le fait de pouvoir exploiter les données brutes (sans prétraitement*, sans appliquer la MEM) est une stratégie intéressante, d'autant plus qu'elle permet de limiter la perte d'information. Cependant, l'interprétation des spectres CARS extraits, dans ce cas, peut être complexe à effectuer, notamment lorsque le niveau de signal vibrationnel est faible par rapport au NRB (typiquement, dans la région d'empreinte digitale). Cette interprétation nécessite d'ailleurs l'intervention d'un expert, ce qui limite le développement des applications biomédicales de la microspectroscopie CARS. Dans ce contexte, **l'exploration d'approches basées sur l'intelligence artificielle** a été initiée durant la thèse de D. Boildieu et s'inscrit dans mon projet de recherche actuel, qui fait l'objet de la section suivante.

* Sauf retrait des raies cosmiques dans le cas de l'étude du cerveau de souris.

IV. Mise en place d'une chaîne complète pour l'étude d'un dispositif biocéramique

L'état de l'art de la microspectroscopie CARS multiplex (éventuellement agrémentée de modalités complémentaires) fait apparaître deux aspects majeurs qui en limitent le déploiement dans le domaine de la bio-imagerie. D'une part, l'instrumentation photonique associée n'est pas suffisamment mûre pour que des études biologiques complètes et fiables puissent être menées : le design expérimental actuel, fortement lié à l'architecture de la source laser (pompe + Stokes) utilisée, comporte un certain nombre de réglages induisant de la variabilité dans le signal CARS mesuré (même si ces réglages sont réalisés par un expert). D'autre part, les solutions actuelles de traitement/analyse des données acquises ne sont pas assez performantes en termes de sélectivité chimique, d'interprétabilité et de rapidité/portabilité. Nous proposons de relever ces défis en nous positionnant dans un cadre global de **développement d'une chaîne complète d'acquisition, de traitement et d'analyse automatique de données hyperspectrales CARS (+ autres modalités) massives**. Cette stratégie est mise en œuvre à travers l'articulation de trois projets collaboratifs (MIMU, DEEP'NCARS et BELENOS, voir **Figure 35**) cofinancés par le Labex Σ-LIM et la Région Nouvelle-Aquitaine, impliquant les équipes XLIM-Photonique (Limoges), XLIM-ASALI (Poitiers), IRCER-Biomatériaux, le Centre technologique ALPhANOV, l'entreprise LEUKOS et le CHU de Limoges. Nous présentons ci-après de façon synthétique les activités réalisées ou prévues dans chacun de ces projets.

Dans le projet MIMU (« Microscope pour l'imagerie multimodale », 2020-2024, coordination LEUKOS), **un nouveau design de système complet de microspectroscopie** CARS a été proposé et développé en collaboration étroite avec ALPhANOV et LEUKOS. En particulier, dans la continuité des travaux portant sur la configuration MOFA avec microlaser et amplificateur à fibres (**Partie 2, Section V, Point 3**), une nouvelle génération de source CARS à double sortie a été conçue. Son architecture à base de diode laser modulée et amplifiée (50 ps / 1 MHz) permet de disposer de deux sorties fibrées et collimatées délivrant des trains d'impulsions pompe et Stokes (supercontinuum) stables et synchronisés. Cette dernière propriété conduit à supprimer la ligne à retard du schéma expérimental, ce qui représente une avancée importante en termes de simplification du système tout en conservant deux voies indépendantes (possibilité de réglage de la puissance sur chaque voie, indispensable pour les applications visées). Nous avons alors étendu l'effort de simplification à l'ensemble du dispositif, que nous avons par ailleurs construit autour de trois blocs (laser, microscope, spectroscope) connectés par des fibres optiques et compatibles avec les modes de détection *backward* et *forward*. Ce design modulaire permet de modifier un ou plusieurs blocs, par exemple le spectroscope, en fonction des applications visées. De plus, toutes les sources mécaniques de variabilité du signal ont été supprimées, à l'exception du condenseur collectant le signal *forward* et dont la hauteur dépend de la position axiale du point de focalisation. Enfin, un logiciel optimisé pour piloter l'ensemble des appareils et acquérir rapidement une grande quantité de données est en cours de développement ; nous travaillons également sur son ergonomie afin de faciliter la prise en main de la technologie CARS par tout utilisateur. L'ajout de modalités supplémentaires (SHG, TPEF) au système fait aussi partie de la feuille de route du projet MIMU, dans sa dernière phase.

Dans le projet DEEP'NCARS (« Méthodes d'apprentissage profond pour l'analyse de données CARS hyperspectrales massives », 2023-2026, coordination XLIM, doctorant(e) en cours de recrutement), nous proposons d'intégrer la modélisation complète du phénomène physique mis en jeu dans la génération du signal vibrationnel hyperspectral, afin d'obtenir une extraction de signatures chimiques/biologiques de qualité supérieure. Bien sûr, cette analyse plus fine engendre une complexité accrue dans la conception de l'algorithme de traitement des données, un défi majeur qui ne trouve actuellement pas de solution convaincante au sein de la communauté. **Le projet s'appuie sur le développement de techniques issues de l'analyse multivariée et de l'intelligence artificielle** afin d'exploiter au mieux les données collectées par le dispositif photonique du projet MIMU (*data mining* ou fouille de données). D'un point de vue méthodologique, il s'agit d'une part de reformuler la décomposition par approche multivariée en intégrant les spécificités des spectres CARS, et d'autre part de développer plus avant la structure de type **autoencodeur**, n'ayant pas encore pu être utilisée de manière optimale dans ce cadre précis[†]. A travers les deux blocs de projection (encodeur) et de reconstruction (décodeur) composant l'autoencodeur, il s'agit de définir une stratégie permettant d'identifier, sous forme d'images, les différents composants de l'échantillon observé et par ailleurs les signatures spectrales associées. Ce problème est complexe, c'est pourquoi une structure de complexité adaptative est requise pour le résoudre. Un autre jalon scientifique du projet DEEP'NCARS concerne le choix de la **fonction dite de coût**, correspondant à l'erreur de reconstruction, et que l'on cherche à minimiser durant l'apprentissage des paramètres des réseaux de neurones. Nous chercherons notamment à exploiter les caractéristiques du capteur et de l'information recherchée pour guider la conception de cette fonction et ainsi permettre l'intégration d'apriori dans le modèle d'intelligence artificielle. Entre autres, l'intégration de l'information spatiale est envisagée à travers l'utilisation de structures dites **super-pixels**, qui regroupent des pixels à la fois connexes spatialement et similaires spectralement sans contrainte sur la géométrie des groupes formés (approche associée à des réseaux de neurones sur graphe).

Finalement, **le projet BELENOS** (« Biomatériau hybride céramique-cellules humaines, élaboré par fabrication additive et bio-impression 3D couplées, pour des applications en chirurgie réparatrice osseuse », 2022-2025, coordination IRCER) apporte le cadre applicatif dans lequel sont développées les approches de microscopie multimodale. Ce projet ambitionne de faire la preuve de concept d'un **dispositif hybride implantable innovant qui permette d'améliorer le traitement de pathologies osseuses** dans le contexte de médecines régénératives, notamment en chirurgie orthopédique ou maxillo-faciale. Ce dispositif stimulera la formation de nouveaux tissus, ouvrant ainsi la voie vers la restauration de grandes pertes de substance osseuse. La démarche de BELENOS consiste à s'appuyer sur la ponction et l'utilisation de cellules de la moelle osseuse, grâce à l'intervention du CHU de Limoges dans le projet, pour favoriser la réparation tissulaire. Ainsi, le dispositif hybride sera constitué d'une matrice céramique phosphocalcique poreuse fonctionnalisée par les précurseurs biologiques contenus naturellement dans la moelle osseuse. Dans cet objectif, des technologies de fabrication additive et de bio-impression 3D seront mises en œuvre à l'IRCER pour l'élaboration du dispositif. La caractérisation de ses performances

[†] De premiers travaux sur l'utilisation d'un autoencodeur pour la MCR ont été réalisés durant la thèse de D. Boildieu.

biologiques sera réalisée dans un cadre d'imagerie multimodale, à la fois à travers une approche conventionnelle de microscopie de fluorescence (immunofluorescence) et par microspectroscopie vibrationnelle CARS (instrumentation développée dans le projet MIMU). Les données acquises par les deux techniques seront alors analysées de façon croisée ou globale au moyen de méthodes numériques conçues essentiellement dans le projet DEEP'NCARS. L'objectif est de pouvoir étudier finement les phénomènes se produisant à l'interface entre le matériau céramique et les cellules vivantes lors de la régénération osseuse. Dans le cadre de BELENOS, la thèse de Souad Hamraoui a débuté fin 2022 ; un(e) post-doctorant(e) est également en cours de recrutement.

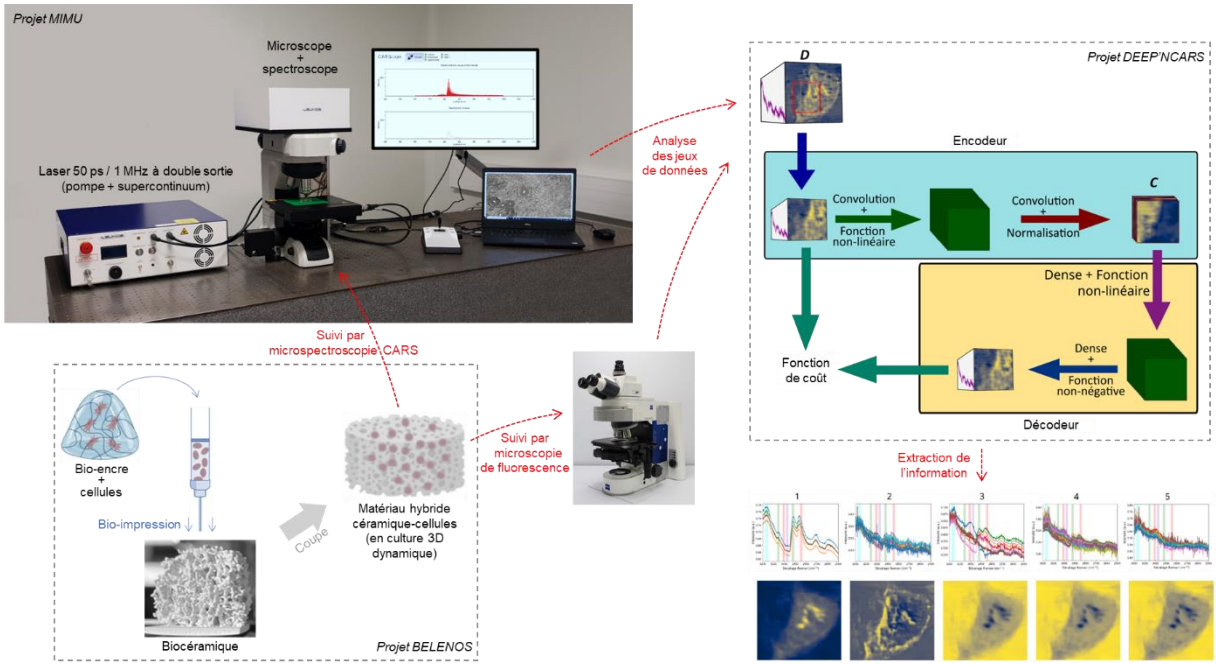

Figure 35 : Développement d'une chaîne complète d'acquisition, de traitement et d'analyse automatique de données hyperspectrales CARS (+ autres modalités) massives, dans le cadre de l'articulation de trois projets collaboratifs cofinancés par le Labex Σ-LIM et la Région Nouvelle-Aquitaine. **MIMU** (2020-2024) : « Microscope pour l'imagerie multimodale » ; **DEEP'NCARS** (2023-2026) : « Méthodes d'apprentissage profond pour l'analyse de données CARS hyperspectrales massives » ; **BELENOS** (2022-2025) : « Biomatériau hybride céramique-cellules humaines, élaboré par fabrication additive et bio-impression 3D couplées, pour des applications en chirurgie réparatrice osseuse ». Ces projets réunissent un consortium pluridisciplinaire : XLIM-Photonique (Limoges), XLIM-ASALI (Poitiers), IRCER-Biomatériaux, ALPhANOV, LEUKOS, CHU Limoges.

Synthèse partie 3 avec indicateurs

Microspectroscopie non linéaire multimodale sous excitation supercontinuum				
Articles	Communications internationales	Actes de congrès internationaux	Communications nationales	Brevets
9	18 dont 4 invitées	8	4	1

Mots clés

Microspectroscopie CARS, (bio)imagerie multimodale, développement instrumental, analyse de données, apprentissage profond, données hyperspectrales, données massives

Points saillants / points forts

- Développement au sein d'XLIM d'un système de microspectroscopie CARS dans le cadre du projet ASTRID NEOSPRAM (2014-2018)
- Application à l'imagerie d'échantillons biologiques sans marquage (en particulier, utilisation intensive du système comme méthode de routine par T. Guerenne-Del Ben tout au long de sa thèse de biologie cellulaire, 2016-2019)
- Mise en place de nouvelles collaborations dans le cadre du Labex Σ-LIM sur les aspects « analyse de données » avec l'axe ASALI d'XLIM et « application à la chirurgie réparatrice osseuse » avec l'équipe Biomatériaux de l'IRCER et le CHU de Limoges

Collaborations principales

XLIM-ASALI (Poitiers), IRCER-Biomatériaux (Limoges), LABCiS (Limoges), E2Lim (Limoges), ISM (Talence), LASIRE (Villeneuve-d'Ascq), Universités de Tsukuba/Kyushu (Japon), ALPhANOV (Talence)

Contrats de recherche

Titre	**Type**	**Période**	**Rôle**	**Nombre de partenaires**	**Coût total**	**Financement XLIM**
Nouveaux procédés de spectroscopie Raman pour l'analyse d'agents	Projet ASTRID (financement DGA, gestion ANR)	2014-2018	Coordinateur	2	856 k€	241 k€

biologiques (NEOSPRAM)						
Étude de nouveaux procédés de spectroscopie Raman : application à la cytométrie en flux	Bourse de thèse DGA	2014-2017	Responsable scientifique	N/A	N/A	120 k€
Towards coherent Raman endomicroscopy for brain tissue imaging (ENDOCRAM)	Projet international de coopération scientifique (PICS) CNRS	2015-2017	Responsable scientifique	2	N/A	21 k€
Nouveaux matériaux pour les sources laser supercontinuum appliquées à la bio-imagerie (NEMATUUM)	Projet Région NA (AAP ESR)	2017-2021	Coordinateur	6	618 k€	312 k€ (+ 49 k€ Labex)
Microscope pour l'Imagerie Multimodale (µMu)	Projet Région NA (R&D portée par des entreprises)	2020-2024	Partenaire et responsable scientifique « Imagerie multimodale »	3	973 k€	115 k€
Biomatériau hybride céramique-cellules humaines, élaboré par fabrication additive et bioimpression 3D couplées, pour des applications en chirurgie réparatrice osseuse (BELENOS)	Projet Région NA (AAP ESR)	2022-2025	Partenaire	4	174 k€	87 k€ (+ 87 k€ Labex)
Dynamique des microplastiques dans l'environ-nement par µspectroscopie CARS (DYNAPLAST)	Projet MITI CNRS (Programme Interne Blanc)	2022-2023	Porteur	3	N/A	32 k€
Development of functional molecular imaging method by coherent Raman	Partenariat Hubert Curien (PHC) SAKURA	2023-2024	Responsable équipe française	2	N/A	12 k€

spectroscopy using a white-light laser source						
Méthodes d'apprentissage profond pour l'analyse de données CARS hyperspectrales massives - Application à la bioimagerie (Deep'nCars)	Projet Région NA (AAP ESR)	2023-2026	Coordinateur	3	117 k€	58,5 k€ (+ 58,5 k€ MESR)
TOTAL						**1 193 k€**

Publications majeures (insérées ci-après)

- *Fast epi-detected broadband multiplex CARS and SHG imaging of mouse skull cells*, E. Capitaine, N. Ould Moussa, C. Louot, S. M. Bardet, H. Kano, L. Duponchel, P. Lévêque, V. Couderc, **P. Leproux**, Biomedical Optics Express, vol. 9, no. 1, pp. 245-253, 2018 (référence [68] de la liste complète)
- *Coherent anti-Stokes Raman scattering cell imaging and segmentation with unsupervised data analysis*, D. Boildieu, T. Guerenne-Del Ben, L. Duponchel, V. Sol, J. M. Petit, E. Champion, H. Kano, D. Helbert, A. Magnaudeix, **P. Leproux**, P. Carré, Frontiers in Cell and Developmental Biology, vol. 10, 933897, 2022 (référence [84] de la liste complète)

Encadrement de thèses de doctorat

- **Erwan Capitaine**, « Nouveaux procédés de microspectroscopie Raman cohérent à bande ultralarge » (2014-2017, **codirection**, directeur de thèse : Vincent Couderc)
- **Tiffany Guerenne-Del Ben**, « La microspectroscopie CARS appliquée au suivi de l'activation d'un récepteur associé à la cancérogenèse » (2016-2019, **codirection**, directeur de thèse : Jean-Michel Petit)
- **Alice Lemarquand**, « Rhéologie ultrasonore et spectroscopie CARS pour la caractérisation multi-échelle d'explants de peau » (2017-2020, **participation à l'encadrement**, directeur de thèse : Stéphane Serfaty, CY Paris Cergy Université)
- **Zakaniaina Rajaofara**, « Non-linéarité optique au sein des matériaux oxydes inorganiques (tellurites, borophosphate de niobium) et d'échantillons biologiques » (2018-2021, **codirection**, directeur de thèse : Vincent Couderc)
- **Sahar Wehbi**, « Imagerie multimodale assistée par champ électrique pulsé » (2018-2021, **codirection**, directeur de thèse : Vincent Couderc)
- **Damien Boildieu**, « Méthodes de résolution de courbes multivariées pour la microspectroscopie CARS » (2019-2022, **codirection**, directeur de thèse : Philippe Carré)

- **Souad Hamraoui**, « Biomatériau hybride céramique-cellules humaines, élaboré par fabrication additive et bioimpression 3D, pour des applications en chirurgie réparatrice osseuse » (2022-2025, **codirection**, directeur de thèse : Éric Champion)

Autres encadrements

- **Nawel Ould Moussa**, post-doctorante (2016-2017) dans le cadre du projet ASTRID NEOSPRAM
- **Zakaniaina Rajaofara**, post-doctorant (2021-2022) dans le cadre du projet Région INTENSIVE

Publications majeures Partie 3

Research Article | Vol. 9, No. 1 | 1 Jan 2018 | BIOMEDICAL OPTICS EXPRESS 245
Biomedical Optics EXPRESS

Fast epi-detected broadband multiplex CARS and SHG imaging of mouse skull cells

ERWAN CAPITAINE,[1,6] NAWEL OULD MOUSSA,[1] CHRISTOPHE LOUOT,[1] SYLVIA M. BARDET,[1] HIDEAKI KANO,[2,3,4], LUDOVIC DUPONCHEL,[5] PHILIPPE LÉVÊQUE,[1] VINCENT COUDERC,[1] AND PHILIPPE LEPROUX[1,*]

[1]*XLIM UMR 7252, CNRS-Université de Limoges, 123 avenue Albert Thomas, 87060 Limoges Cedex, France*
[2]*Department of Applied Physics, Graduate School of Pure and Applied Sciences, University of Tsukuba, 1-1-1 Tennodai, Tsukuba, Ibaraki, 305-8573, Japan*
[3]*Institute of Applied Physics, University of Tsukuba, 1-1-1 Tennodai, Tsukuba, Ibaraki, 305-8573, Japan*
[4]*Tsukuba Research Center for Interdisciplinary Materials Science (TIMS), University of Tsukuba, 1-1-1 Tennodai, Tsukuba, Ibaraki, 305-8571, Japan*
[5]*LASIR UMR 8516, CNRS-Université Lille 1, Sciences et Technologies, 59655 Villeneuve d'Ascq Cedex, France*
[6]*erwan.capitaine@xlim.fr*
[*]*philippe.leproux@xlim.fr*

Abstract: We present a bimodal imaging system able to obtain epi-detected mutiplex coherent anti-Stokes Raman scattering (M-CARS) and second harmonic generation (SHG) signals coming from biological samples. We studied a fragment of mouse parietal bone and could detect broadband anti-Stokes and SHG responses originating from bone cells and collagen respectively. In addition we compared two post-processing methods to retrieve the imaginary part of the third-order nonlinear susceptibility related to the spontaneous Raman scattering.

OCIS codes: (300.6230) Spectroscopy, coherent anti-Stokes Raman scattering; (180.4315) Nonlinear microscopy; (170.3880) Medical and biological imaging.

References and links

1. L. L. McManus, G. A. Burke, M. M. McCafferty, P. O'Hare, M. Modreanu, A. R. Boyd, and B. J. Meenan, "Raman spectroscopic monitoring of the osteogenic differentiation of human mesenchymal stem cells," Analyst **136**, 2471 (2011).
2. B. Blum, O. Bar-Nur, T. Golan-Lev, and N. Benvenisty, "The anti-apoptotic gene survivin contributes to teratoma formation by human embryonic stem cells," Nat. Biotechnol. **27**, 281 (2009).
3. A. Downes, R. Mouras, P. Bagnaninchi, and A. Elfick, "Raman spectroscopy and CARS microscopy of stem cells and their derivatives," J. Raman Spectrosc. **42**, 1864–1870 (2011).
4. E. Gentleman, R. J. Swain, N. D. Evans, S. Boonrungsiman, G. Jell, M. D. Ball, T. A. V. Shean, M. L. Oyen, A. Porter, and M. M. Stevens, "Comparative materials differences revealed in engineered bone as a function of cell-specific differentiation," Nat. Mater. **8**, 763–770 (2009).
5. H. K. Chiang, F.-Y. Peng, S.-C. Hung, and Y.-C. Feng, "In situ Raman spectroscopic monitoring of hydroxyapatite as human mesenchymal stem cells differentiate into osteoblasts," J. Raman Spectrosc. **40**, 546–549 (2009).
6. Y. J. Lee, S. L. Vega, P. J. Patel, K. A. Aamer, P. V. Moghe, and M. T. Cicerone, "Quantitative, Label-Free Characterization of Stem Cell Differentiation at the Single-Cell Level by Broadband Coherent Anti-Stokes Raman Scattering Microscopy," Tissue Eng. Part C Methods **20**, 562–569 (2014).
7. A. D. Hofemeier, H. Hachmeister, C. Pilger, M. Schürmann, J. F. W. Greiner, L. Nolte, H. Sudhoff, C. Kaltschmidt, T. Huser, and B. Kaltschmidt, "Label-free nonlinear optical microscopy detects early markers for osteogenic differentiation of human stem cells," Sci. Rep. **6**, 26716 (2016).
8. A. Volkmer, J.-X. Cheng, and X. Sunney Xie, "Vibrational Imaging with High Sensitivity via Epidetected Coherent Anti-Stokes Raman Scattering Microscopy," Phys. Rev. Lett. **87**, 023901 (2001).
9. J.-x. Cheng, A. Volkmer, L. D. Book, and X. S. Xie, "An Epi-Detected Coherent Anti-Stokes Raman Scattering (E-CARS) Microscope with High Spectral Resolution and High Sensitivity," J. Phys. Chem. B **105**, 1277–1280 (2001).

#307240 https://doi.org/10.1364/BOE.9.000245
Journal © 2018 Received 15 Sep 2017; revised 30 Nov 2017; accepted 8 Dec 2017; published 18 Dec 2017

Biomedical Optics EXPRESS

10. Z. Wang, W. Zheng, C.-Y. S. Hsu, and Z. Huang, "Epi-detected quadruple-modal nonlinear optical microscopy for label-free imaging of the tooth," Appl. Phys. Lett. **106**, 033701 (2015).
11. A. Lukic, S. Dochow, H. Bae, G. Matz, I. Latka, B. Messerschmidt, M. Schmitt, and J. Popp, "Endoscopic fiber probe for nonlinear spectroscopic imaging," Optica **4**, 496–501 (2017).
12. M. Müller and J. M. Schins, "Imaging the thermodynamic state of lipid membranes with multiplex CARS microscopy," J. Phys. Chem. B **106**, 3715–3723 (2002).
13. G. W. H. Wurpel, J. M. Schins, and M. Müller, "Chemical specificity in three-dimensional imaging with multiplex coherent anti-Stokes Raman scattering microscopy," Opt. Lett. **27**, 1093–1095 (2002).
14. M. Okuno, H. Kano, P. Leproux, V. Couderc, and H.-O. Hamaguchi, "Ultrabroadband multiplex CARS microspectroscopy and imaging using a subnanosecond supercontinuum light source in the deep near infrared," Opt. Lett. **33**, 923 (2008).
15. C. M. Hartshorn, Y. J. Lee, C. H. Camp, Z. Liu, J. Heddleston, N. Canfield, T. A. Rhodes, A. R. Hight Walker, P. J. Marsac, and M. T. Cicerone, "Multicomponent chemical imaging of pharmaceutical solid dosage forms with broadband CARS microscopy," Anal. Chem. **85**, 8102–8111 (2013).
16. H. Segawa, M. Okuno, H. Kano, P. Leproux, V. Couderc, and H.-o. Hamaguchi, "Label-free tetra-modal molecular imaging of living cells with CARS, SHG, THG and TSFG (coherent anti-Stokes Raman scattering, second harmonic generation, third harmonic generation and third-order sum frequency generation)," Opt. Express **20**, 9551 (2012).
17. H. Segawa, Y. Kaji, P. Leproux, V. Couderc, T. Ozawa, T. Oshika, and H. Kano, "Multimodal and multiplex spectral imaging of rat cornea ex vivo using a white-light laser source," J. Biophotonics **8**, 705–713 (2015).
18. E. Capitaine, N. Ould Moussa, C. Louot, C. Lefort, D. Pagnoux, J.-R. Duclère, J. F. Kaneyasu, H. Kano, L. Duponchel, V. Couderc, and P. Leproux, "Coherent anti-Stokes Raman scattering under electric field stimulation," Phys. Rev. B **94**, 245136 (2016).
19. A. Awonusi, M. D. Morris, and M. M. J. Tecklenburg, "Carbonate Assignment and Calibration in the Raman Spectrum of Apatite," Calcif. Tissue Int. **81**, 46–52 (2007).
20. G. S. Mandair and M. D. Morris, "Contributions of Raman spectroscopy to the understanding of bone strength," Bonekey Rep. **4** (2015).
21. G. Zhang, D. J. Moore, C. R. Flach, and R. Mendelsohn, "Vibrational microscopy and imaging of skin: from single cells to intact tissue," Anal. Bioanal. Chem. **387**, 1591–1599 (2007).
22. I. R. Hill and I. W. Levin, "Vibrational spectra and carbon–hydrogen stretching mode assignments for a series of n-alkyl carboxylic acids," J. Chem. Phys. **70**, 842–851 (1979).
23. B. G. Saar, C. W. Freudiger, J. Reichman, C. M. Stanley, G. R. Holtom, and X. S. Xie, "Video-rate molecular imaging in vivo with stimulated Raman scattering," Science **330**, 1368–1370 (2010).
24. E. M. Vartiainen, H. A. Rinia, M. Müller, and M. Bonn, "Direct extraction of Raman line-shapes from congested CARS spectra," Opt. Express **14**, 3622 (2006).
25. A. Savitzky and M. J. Golay, "Smoothing and differentiation of data by simplified least squares procedures," Anal. Chem. **36**, 1627–1639 (1964).
26. P. Deladurantaye, A. Paquet, C. Paré, H. Zheng, M. Doucet, D. Gay, M. Poirier, J.-F. Cormier, O. Mermut, B. C. Wilson, and E. J. Seibel, "Advances in engineering of high contrast CARS imaging endoscopes," Opt. Express **22**, 25053–25064 (2014).

1. Introduction

The use of non-destructive, non-invasive and label-free methods is particularly interesting to realize medical diagnosis of diseases or to develop tissue engineering and regenerative medicine [1]. In bone tissue engineering, the discrimination of different cellular pools is crucial prior to the application of any clinical treatment [2,3]. In this context spontaneous Raman [1,3–5] and coherent anti-Stokes Raman scattering (CARS) [3,6,7] spectroscopies have proven that they could distinguish progenitor cells by detecting specific molecular vibrations.

To obtain a CARS signal, the difference between the optical frequencies of a pump and a Stokes laser beam, $\omega_p - \omega_S$, has to match the vibrational frequency of a molecule. The use of a third beam as a probe wave can then, by four-wave mixing, lead to the generation of anti-Stokes signal both emitted in the forward and the backward directions. Usually, the role of the probe is given to the pump beam so that the frequency of the anti-Stokes wave is $\omega_{aS} = 2\omega_p - \omega_S$. In most cases, CARS imaging is implemented in forward configuration where the anti-Stokes photons are collected after going through the whole thickness of the sample. The use of microscope objectives with high numerical aperture permits the phase matching condition to be always fulfilled. On the other hand, in epi-configuration the wave vector mismatch is more important [8]. Therefore, the signal coming from objects larger than the anti-Stokes wavelength is less or

Biomedical Optics EXPRESS

not collected due to destructive interferences. Consequently, epi-detection seems to be more suitable for living cells monitoring because the solvent does not participate in the generation of backward signal [9]. Furthermore, in this case, the implementation of the experimental setup is facilitated and the study of *in vivo* samples become possible. Epi-CARS analysis of biological objects has been demonstrated by measuring single-frequency anti-Stokes wave [10, 11], but the simultaneous acquisition of different anti-Stokes wavelengths has not been achieved to our knowledge. To achieve multicolor epi-CARS, a supercontinuum radiation can be used as a broadband Stokes wave. In this manner, a broad anti-Stokes spectrum covering the fingerprint and the CH vibration regions can be instantaneously acquired. This system is well established in the forward configuration and called multiplex CARS (M-CARS) [12–14]. One publication introduces its implementation in epi-detection but it was only applied to the study of a mineral sample with long pixel dwell time [15]. In addition to the vibrational signal, second harmonic generation (SHG) from the pump beam, due to the presence of non-centrosymmetric components in the sample such as type I collagen fibrils, can also be acquired [16–18]. Thereby, CARS and SHG detection can provide rich and complementary molecular information.

We propose here a bimodal system, with epi-detected M-CARS and SHG, applicable to biological tissues. To demonstrate the ability of our setup, we study biopsies from mouse skull bone. We measure CARS spectra from 700 cm^{-1} to 3200 cm^{-1} with a spectral resolution of 2 cm^{-1} and a short pixel dwell time of 5 ms. Maps of typical vibrations of skull bone cells and SHG signal coming from collagen fibrils are obtained. We then compare qualitatively two algorithms that can extract the resonant signal from raw CARS data and we evaluate their respective post-processing time. Finally we compare our results with two-photon fluorescence images obtained on similar biopsies with different staining methods in order to confirm the presence of skull bone cells.

2. Materials and methods

The schematic of the epi-detected M-CARS and SHG system is presented in Fig.1. We use a laser source (Spark Lasers, Sirius series, 1064 nm, 60 ps, 110 kHz, linearly polarized) to generate the pump radiation. By using a half-wave plate and a Glan-Taylor polarizer (GTP), a part of the pump is directed into a photonic crystal fiber (PCF) to generate an infrared supercontinuum Stokes wave from 600 nm to 1650 nm. To compensate for the difference of optical length between the pump and the Stokes beams and, thus, to assure their temporal overlapping, a delay-line is set on the path of the pump. A long-pass filter at 1050 nm (Thorlabs, FEL1050) is used on the Stokes beam to suppress wavelengths that could be confused with anti-Stokes signals. The two beams are then spatially combined by mean of a notch dichroic mirror (Semrock, NFD01-1064-25x36) which can reflect the pump in the direction of propagation of the Stokes. Then, the beams travel together toward a dichroic short-pass mirror at 1000 nm (Thorlabs, DMSP1000R) that reflects them toward a microscope objective (Olympus, UPlanSApo 60x, N.A. = 1.2, water immersion) that focuses them onto the sample. The backscattered signal, collimated by the objective, is transmitted by the short-pass filter in the direction of a spectrometer (Horiba, LabRam Evolution). A notch filter at 1064 nm (Thorlabs, NF1064-44) is set to suppress the remaining pump signal. The different anti-Stokes wavelengths are then diffracted by a grating (Horiba, 520 29, 600 $gr.mm^{-1}$) and spanned on the CCD camera (Horiba, Synapse).

The use of animals has received the approval of the local Ethical and Animal Care Committee (registration number 15-2015-15, MoNaPulse and CRAMpON). All animal cares and experimental procedures were conducted in conformity with the French legislation n° 2013-118 1st February 2013 in accordance with European Community guidelines (directive 2010/63/UE for the Care and Use of Laboratory Animals). 12-week-old wild-type (no label), SwissTg(CAG-EGFP)1Osb (ubiquitous GFP expression) and B6.CgTg(Col1a1*2.3GFP)1Rowe/J (GFP in the osteogenic lineage) mice were dissected immediately following euthanasia. Cranium bone was removed

Biomedical Optics EXPRESS

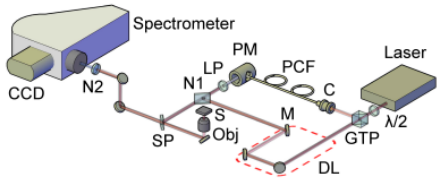

Fig. 1. Experimental setup of the epi-detected M-CARS and SHG imaging system (C: laser coupler; CCD: CCD camera; DL: delay line (delimited by the red dashed line); LP: long-pass filter; M: mirror; N1: notch dichroic mirror; N2: notch filter; Obj: objective; PCF: photonic crystal fiber; GTP: Glan-Taylor polarizer; PM: parabolic mirror; S: sample; SP: short-pass filter; $\lambda/2$: half-wave plate).

from the parietal region with a dental drill as illustrated in Fig. 2. One label-free fragment was counterstained with 50 µM Rhodamine B (R6626, Sigma-Aldricht, λ_{em} 627 nm) for 10 min. For two-photon fluorescence measurements we used an upright multiphoton microscope (Olympus, BX61WI/FV1200MPE) coupled with a tunable femtosecond Ti:Sapphire laser (Coherent, Chameleon Ultra II) via 25x immersion objective (Olympus, XLPLN25XWMP, N.A. = 1.05).

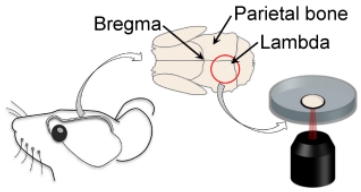

Fig. 2. Schematic representation of the mouse parietal bone area studied in the experiment. The bregma and the lambda are both classical anatomical landmarks located on the midline of the outer surface of the skull, that are often used as reference points for stereotaxic surgery in this region. The bregma and the lambda are indeed the meeting point respectively between frontal and parietal bones, and between parietal and occipital bones. Here the cranium bone was extracted from the parietal region, down left from the lambda, as highlighted by the red circle.

3. Results and discussion

Using our CARS setup, we mapped an area of 260 µm × 260 µm with a 1 µm-step of the wild mouse parietal bone. The lateral resolution was 540 nm (FWHM). Because the grating and the CCD camera used could not collect the entire anti-Stokes spectrum and SHG response without loss of spectral resolution, we split the measurement into three sets of acquisitions: from 700 cm^{-1} to 1200 cm^{-1} (5 ms per spectrum); from 2500 cm^{-1} to 3200 cm^{-1} (5 ms per spectrum); and from 510 nm to 555 nm (1 ms per spectrum). For each point of the mapping, two accumulations were made to avoid random spikes in spectra due to cosmic rays.

In Fig. 3 are presented typical raw CARS spectra obtained at two different acquisition points in the fingerprint (700-1200 cm^{-1}) and CH (2500-3200 cm^{-1}) vibrational regions. In the fingerprint region of Figs. 3(a) and 3(b), typical dispersive profiles with maxima at 950 cm^{-1} and 1061 cm^{-1} demonstrate the presence of two vibrational modes. In the CH region the dispersive lines with maxima at 2869 cm^{-1} and 2932 cm^{-1}, only present in Fig. 3(b), attest to the presence of two

Biomedical Optics EXPRESS

other vibrational modes. The frequency of all these maxima does not exactly match the frequency of the corresponding spontaneous Raman band. As a matter of fact, due to the dispersive aspect of the CARS spectra, the frequency of the peaks is shifted in the low-energy direction. In Table 1, we list the vibrational modes for the different CARS peaks of Fig. 3, including the corresponding Raman shifts and associated molecule types.

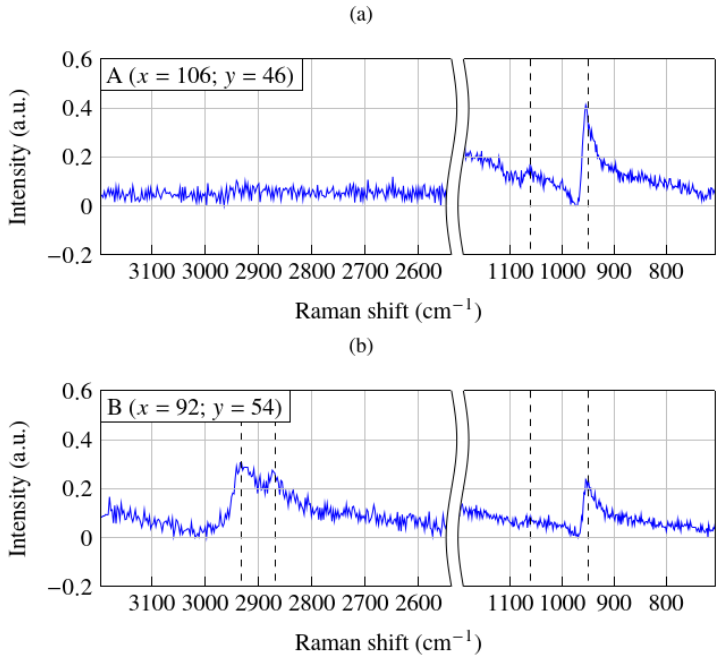

Fig. 3. Typical raw CARS spectra of mouse parietal bone for fingerprint and CH vibrational domains at two different points of acquisition ((a) and (b)). The spectra acquisition position in µm is given in the insets. The pump and Stokes average power at the sample is 66 mW and 4 mW, respectively.

It appears that PO_4^{3-} symmetric stretching and CO in plane stretching of CO_3^{2-} characterize the presence of apatite crystals with phosphate and carbonate content [5, 7, 19, 20]. CH_2 asymmetric stretching indicates the presence of lipids [21]. CH_3 symmetric stretching, which besides is coupled to overtone of asymmetric deformation [22], points out proteins [23].

We used two types of post-treatment methods to suppress the non-resonant background (NRB) from the CARS spectra. We first used an algorithm based on the Maximum Entropy Method (MEM) [24] in order to retrieve the imaginary part of the third order nonlinear susceptibility $\chi^{(3)}$ involved in the four-wave mixing. It is this physical variable that carries the vibrational information, for it is directly comparable to the first order susceptibility $\chi^{(1)}$ of the spontaneous Raman scattering. The second method utilizes a Savitzky-Golay filter [25] (second order polynomial fit with a 21-point window) to obtain the first order derivative of the CARS spectra with respect to the Raman shift. We consider that the NRB, varying slowly with the Raman shift, would present a weak participation to the derivative in comparison with the sharp variations of CARS peaks. Furthermore we computed in Fig. 4 the difference $\Delta\omega$ between the positions of theoretical spontaneous Raman and CARS peaks (blue curve) according to the spectral half-width of the Raman peak (Γ) from 1 cm^{-1} to 200 cm^{-1}. We also computed the difference between the positions

Table 1. Band assignment for CARS spectra of mouse cranial bone

CARS peak maximum (cm^{-1})	Raman shift (cm^{-1})	Assignment	Comment	Reference(s)
950	961	PO_4^{3-} symmetric stretching	Phosphate	[5, 7, 19, 20]
1061	1070	CO_3^{2-} symmetric stretching (enveloping PO_4^{3-} asymmetric stretching)	Carbonate (primarily)	[5, 19, 20]
2869	2878	CH_2 asymmetric stretching	Lipids	[21]
		Overtone of asymmetric deformation in Fermi resonance with CH_3 symmetric stretching	Proteins	[22]
2932	2950	CH_3 symmetric stretching	Proteins (primarily)	[23]

of the Raman peak and the derivative of the CARS peak (red curve). We can see that, compared to the position of a CARS peak, the position of its derivative is closer to the one of the Raman peak with a small increase of $\Delta\omega$ with Γ. This indicates that we can use the derivative of a CARS peak to retrieve the position of the corresponding Raman line with good precision.

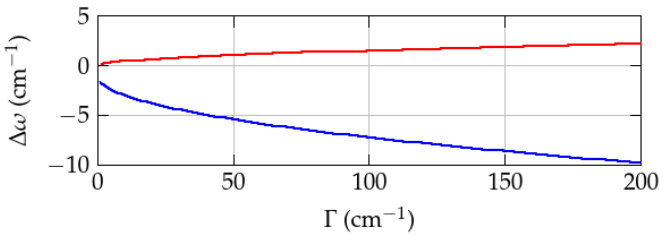

Fig. 4. Evolution of the difference $\Delta\omega$ between the positions of a Raman peak and a CARS peak maximum (blue curve) and between a Raman peak and the derivative of a CARS peak maximum (red curve) according to Γ, the spectral half-width of the Raman peak.

The measured CARS spectra presented before have been processed using the two methods. The resulting spectra are plotted in Fig. 5. We observe that in both cases the dispersive profile of the CARS peaks has disappeared but the spectral features carrying the vibrational information have remained. This correction of the dispersive aspect is highlighted by the shifting of each CARS peak towards the Raman shifts presented in the literature. The two methods provided almost the same maxima positions: 961 cm^{-1}, 1070 cm^{-1}, 2878 cm^{-1} and 2950 cm^{-1} for PO_4^{3-} symmetric, CO in plane of CO_3^{2-} stretching modes and the CH_2 asymmetric and CH_3 symmetric stretching modes respectively. We also noted that the post-processing time of the derivative algorithm was shorter than that of the MEM algorithm: 25 ms per spectrum instead of 1 s per spectrum.

We then produced normalized intensity maps integrated over a bandwidth of 20 cm^{-1} for these four vibrational modes. To do so, we used both the spectra extracted with the MEM algorithm and the derivative spectra. By computing the standard-deviation and mean of each map, we found

Biomedical Optics EXPRESS

that the contrast was the same for the MEM and derivative algorithms. However a better signal to noise ratio of the maps was observed when using the derivative method. The intensity maps of PO_4^{3-}, CO_3^{2-}, CH_2 and CH_3 stretching modes obtained with the derivative method are displayed in Fig. 6, as well as the SHG intensity map.

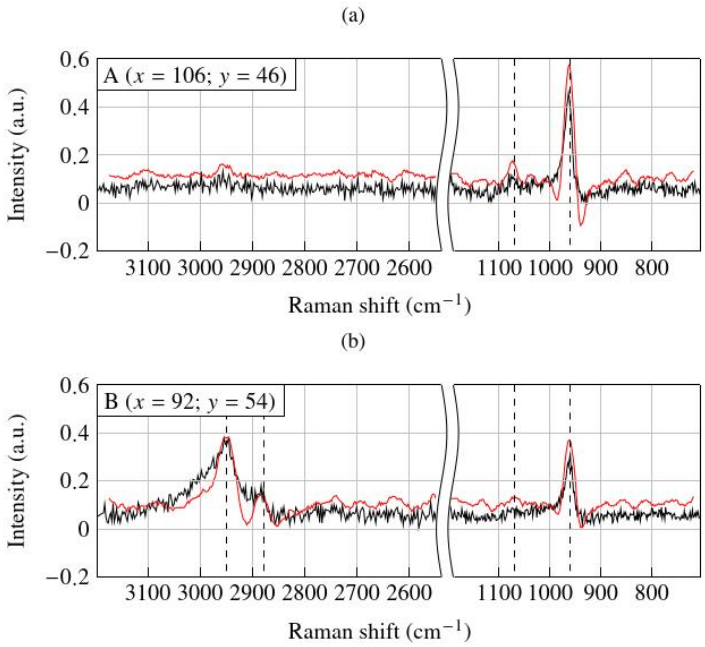

Fig. 5. Normalized and baseline corrected imaginary part of $\chi^{(3)}$ extracted with MEM algorithm (black curve) and normalized derivative of the typical raw CARS spectra (red curve) for fingerprint and CH vibrational domains at two different points of acquisition ((a) and (b)).

We merged three of those maps (PO_4^{3-} at 961 cm^{-1} in red, CH_3 at 2950 cm^{-1} in blue, SHG in green) into a single image, as depicted Fig. 7(a). In this image, the red and blue clusters represent hydroxyapatite and proteins signal respectively. Thus these clusters would indicate the presence of bone cells embedded in a fibrous collagen matrix, the latter coinciding with the SHG signal in green.

To confirm this hypothesis, two-photon fluorescence intensity mapping of the same type of sample with different labels was realized. Thanks to the resulting maps we can observe the characteristic features of indeterminate cells labelled with GFP and Rhodamine (Figs. 7(b) and 7(c)); and osteogenic cells labelled with GFP (Fig. 7(d)). In Fig. 7(b) the SHG signal originating from collagen is also plotted. This allows us to compare the previous M-CARS/SHG map with a reference measurement. The two images show a similarity between the size, shape and density of hydroxyapatite/proteins clusters on one hand (Fig. 7(a)), and of GFP labeled cells on the other hand (Fig. 7(b)). As well, the clusters and the cells both appear as embedded objects in the collagen matrix. We can thus affirm that the hydroxyapatite and proteins M-CARS signals originate from mouse bone cells. This highlights the relevance of epi-detected M-CARS for tracking biological cells in a complex environment.

Finally we calculated the number of cells from each of the five maps, i.e., from the two PO_4^{3-} /

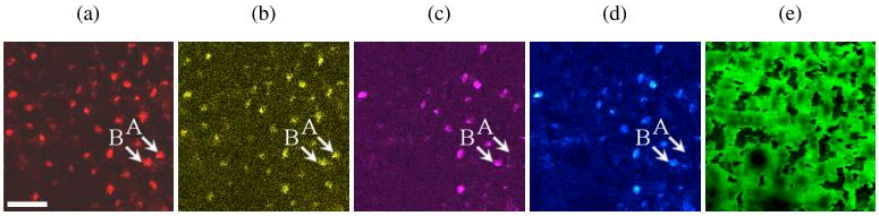

Fig. 6. Intensity maps of a mouse parietal bone fragment obtained from CARS spectra derivatives for (a) PO_4^{3-}, (b) CO_3^{2-}, (c) CH_2, (d) CH_3 stretching modes (integrated over a bandwidth of 20 cm^{-1} around 961 cm^{-1}, 1070 cm^{-1}, 2878 cm^{-1} and 2950 cm^{-1} respectively) and (e) corresponding SHG image. Scale bar: 50 µm. The arrows in (a-b) and (c-d) indicate the acquisition position of the spectra displayed Figs. 3(a)-5(a) and 3(b)-5(b) respectively.

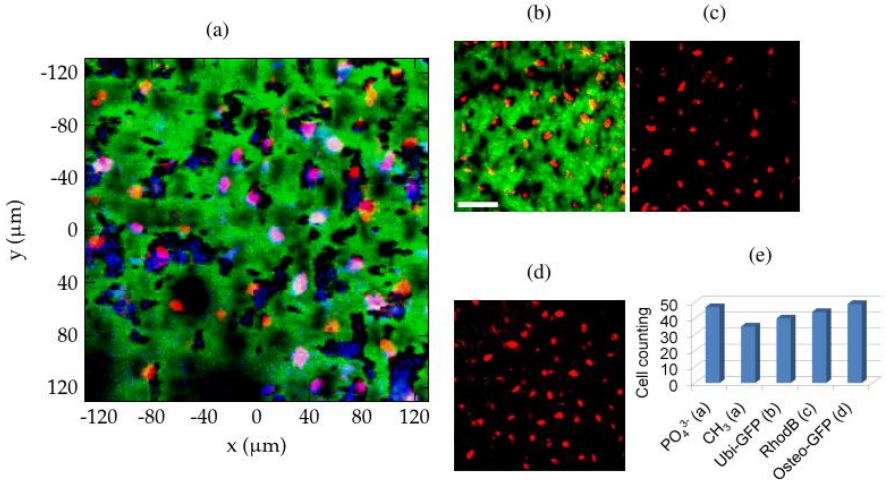

Fig. 7. Intensity maps of a mouse parietal bone fragment obtained from (a) CARS spectra derivatives of PO_4^{3-} symmetric stretching (red) and CH_3 stretching (blue) modes, two-photon fluorescence of (b) GFP labeled cells (red), (c) counterstained cells with Rhodamine B (red) and (d) GFP labeled osteogenic cells (red). In (a) and (b) the SHG signal is shown in green. Scale bar: 50 µm. (e) Population density of the cells in the different maps.

CH_3 vibrational intensity maps and from the three fluorescence intensity maps. The resulting cell counting is plotted in the histogram of Fig. 7(e). At this stage, the variability in population density between the different modalities cannot be assigned to any specific chemico-biological assumption, because it would require a full biology protocol for making quantitative cell counting. However the difference of population density between PO_4^{3-} and CH_3 modalities relates to the only-partial colocalization of hydroxyapatite crystals and proteins, which is also confirmed by the colorimetric variations in Fig. 7(a). This confirms the potential of M-CARS as a rich, label-free and chemically-selective imaging method for studying biological systems.

Biomedical Optics EXPRESS

4. Conclusion

We have demonstrated that the epi-detection of M-CARS and SHG signals coming from mouse bone cells was possible at low average power and short pixel dwell time (5 ms and 1 ms, respectively). The repartition maps of PO_4^{3-} symmetric stretching and CH_3 stretching vibrational modes could clearly reveal the presence of mineralized hydroxyapatite and proteins, respectively, and permitted the identification of bone cells. This study shows the potential of the multiplex configuration in the promising domain of CARS endoscopy [26]. Furthermore, we have proved that the use of the derivative of CARS spectra was as effective as the MEM for retrieving Raman lines, with high vibrational contrast. The derivative method also demonstrated shorter post-processing time. This represents an interesting track towards real-time processing of multiplex CARS data. Finally, we have illustrated that, because the width of the CARS spectrum is crucial for calculating the derivative, broadband M-CARS measurements are highly compatible with this post-processing method.

Funding

Direction Générale de l'Armement; Agence Nationale de la Recherche (ANR-14-ASTR-0014); Région du Limousin.

Acknowledgments

We wish to acknowledge the support of French defense agency (Direction Générale de l'Armement) and of French research agency (Agence Nationale de la Recherche) through the NEOSPRAM project.

This research was partly conducted in the scope of LEA-EBAM, a European Associated Laboratory titled "Pulsed Electric Fields Applications in Biology and Medicine".

Disclosures

The authors declare that there are no conflicts of interest related to this article.

frontiers | Frontiers in Cell and Developmental Biology

TYPE Original Research
PUBLISHED 16 August 2022
DOI 10.3389/fcell.2022.933897

OPEN ACCESS

EDITED BY
Zhichao Fan,
UCONN Health, United States

REVIEWED BY
Rongrong Liu,
Northwestern University, United States
Ilhan Candan,
Dicle University, Turkey

*CORRESPONDENCE
Philippe Leproux,
philippe.leproux@xlim.fr

SPECIALTY SECTION
This article was submitted to Cellular Biochemistry,
a section of the journal
Frontiers in Cell and Developmental Biology

RECEIVED 01 May 2022
ACCEPTED 11 July 2022
PUBLISHED 16 August 2022

CITATION
Boildieu D, Guerenne-Del Ben T, Duponchel L, Sol V, Petit J-M, Champion É, Kano H, Helbert D, Magnaudeix A, Leproux P and Carré P (2022), Coherent anti-Stokes Raman scattering cell imaging and segmentation with unsupervised data analysis.
Front. Cell Dev. Biol. 10:933897.
doi: 10.3389/fcell.2022.933897

Coherent anti-Stokes Raman scattering cell imaging and segmentation with unsupervised data analysis

Damien Boildieu[1,2], Tiffany Guerenne-Del Ben[3], Ludovic Duponchel[4], Vincent Sol[3], Jean-Michel Petit[3], Éric Champion[5], Hideaki Kano[6], David Helbert[2], Amandine Magnaudeix[5], Philippe Leproux[1]* and Philippe Carré[2]

[1]University of Limoges, CNRS, XLIM, UMR 7252, Limoges, France, [2]University of Poitiers, CNRS, XLIM, UMR 7252, Poitiers, France, [3]University of Limoges, PEIRENE, UR 22722, Limoges, France, [4]University of Lille, CNRS, UMR 8516, LASIRE - Laboratoire de Spectroscopie Pour Les Interactions, La Réactivité et L'Environnement, Lille, France, [5]University of Limoges, CNRS, Institut de Recherche sur Les Céramiques, UMR 7315, Limoges, France, [6]Department of Chemistry, Faculty of Science, Kyushu University, Fukuoka, Japan

Coherent Raman imaging has been extensively applied to live-cell imaging in the last 2 decades, allowing to probe the intracellular lipid, protein, nucleic acid, and water content with a high-acquisition rate and sensitivity. In this context, multiplex coherent anti-Stokes Raman scattering (MCARS) microspectroscopy using sub-nanosecond laser pulses is now recognized as a mature and straightforward technology for label-free bioimaging, offering the high spectral resolution of conventional Raman spectroscopy with reduced acquisition time. Here, we introduce the combination of the MCARS imaging technique with unsupervised data analysis based on multivariate curve resolution (MCR). The MCR process is implemented under the classical signal non-negativity constraint and, even more originally, under a new spatial constraint based on cell segmentation. We thus introduce a new methodology for hyperspectral cell imaging and segmentation, based on a simple, unsupervised workflow without any spectrum-to-spectrum phase retrieval computation. We first assess the robustness of our approach by considering cells of different types, namely, from the human HEK293 and murine C2C12 lines. To evaluate its applicability over a broader range, we then study HEK293 cells in different physiological states and experimental situations. Specifically, we compare an interphasic cell with a mitotic (prophase) one. We also present a comparison between a fixed cell and a living cell, in order to visualize the potential changes induced by the fixation protocol in cellular architecture. Next, with the aim of assessing more precisely the sensitivity of our approach, we study HEK293 living cells overexpressing tropomyosin-related kinase B (TrkB), a cancer-related membrane receptor, depending on the presence of its ligand, brain-derived neurotrophic factor (BDNF). Finally, the segmentation capability of the approach is evaluated in the case of a single cell and also by considering cell clusters of various sizes.

KEYWORDS

cell imaging, cell segmentation, coherent anti-Stokes Raman scattering, unsupervised data analysis, coherent Raman imaging, label-free imaging, supercontinuum, multivariate curve resolution

1 Introduction

In the context of label-free cell imaging, vibrational spectroscopic approaches have proven their effectiveness to visualize the cellular content and processes (Matthäus et al., 2008; Klein et al., 2012; Palonpon et al., 2013; Smith et al., 2016). As chemically selective techniques, they can provide both structural and functional information from the sample. Among these techniques, coherent anti-Stokes Raman scattering (CARS) and stimulated Raman scattering (SRS) have been extensively applied to live-cell imaging in the last 2 decades (Zumbusch et al., 1999; Freudiger et al., 2008; Cheng and Xie, 2015). More specifically, both methods have been successfully used to probe the intracellular lipid, protein, nucleic acid, and water content with a high-acquisition rate and sensitivity.

In this context, multiplex CARS (MCARS) microspectroscopy (Kee and Cicerone, 2004; Kano and Hamaguchi, 2005) is a powerful technology for extracting rich vibrational information from biological samples. It is based on the excitation of the sample by two laser beams, namely, the monochromatic pump (ω_p frequency) and the broadband Stokes (ω_S frequency) beam. When the difference ω_p - ω_S matches the vibration frequency of a vibrational mode, a resonant CARS signal is generated at the frequency $2\omega_p$ - ω_S, that is, at a wavelength lower than that of the pump laser, preventing any fluorescence background in the measured MCARS spectrum. This is a considerable advantage for this technique because conventional Raman often presents a fluorescence that completely masks the vibrational signal, especially in biology. However, it is well-known that MCARS is affected by the presence of a so-called non-resonant background (NRB), which is inherent to its physical mechanism. In this regard, phase retrieval approaches like the maximum entropy method (MEM) and time-domain Kramers–Kronig (TDKK) are generally used to extract the pure vibrational signal and to recover conventional Raman-like spectra (Cicerone et al., 2012). These spectra are then more easily interpretable and allow generating high-contrast images from the identified Raman bands. More recently, phase extraction from MCARS spectra was investigated by using a deep learning approach, based on the concept of supervised methods and using a long short-term memory network (LSTM) architecture (Houhou et al., 2020). Another study introduced a workflow for fast Raman signal extraction, denoising, error correction, and the applicability of this workflow to machine learning (Camp et al., 2020).

On the other hand, chemometric methods as principal component analysis (PCA) or multivariate curve resolution (MCR) are widely used in spectroscopy-based data analysis (Pisapia et al., 2018; Ghaffari et al., 2019; Amigo, 2020). They consist of an unsupervised, statistical multivariate exploration of the collected data, being considered as established approaches, especially in the field of Raman microspectroscopy. PCA's purpose is to project data into a subspace, allowing to decorrelate the measurements and to maximize the variance of projections. Thus, PCA facilitates the observation of the relevant information of the dataset. Following this concept of projection of a multicomponent signal into subspaces, MCR is an iterative matrix decomposition method. It decomposes the considered dataset by means of its projection into a subspace guided by different constraints (for instance, non-negativity constraint). This is a definite advantage because this signal unmixing approach allows us to find contributions in the sample that are far more easily interpreted than those obtained from PCA. Specifically, the MCR approach decomposes the initial dataset into a matrix of "pure concentration profiles" and a matrix of "pure spectral profiles," providing a concentration map (quantitative information) and the associated spectrum (qualitative information) of each contribution within the investigated sample. For example, the algorithm allows, in a context of chemical analysis, to extract the "pure" chemical species of the sample (De Juan and Tauler, 2021).

To date, MCR has never been applied to the analysis of MCARS hyperspectral datasets. The only work that could come close to such an approach was published by Zhang et al., 2013, with idea to extract images of major components in breast cancer cells using SRS. In this case, the multivariate exploration involved a spectral stack of only ~80 SRS images, and representative spectra of lipid droplets, nuclei, and culture medium were used at the initial estimation step (supervised method). Regarding CARS data processing in the context of cell imaging, few studies report on the use of chemometric methods within the proposed workflow, including PCA (Parekh et al., 2010; Pohling et al., 2011; Lee et al., 2014), singular value decomposition (SVD) (Masia et al., 2013), or hierarchical cluster analysis (HCA) (El Mashtoly et al., 2014). These studies aim at performing an unsupervised quantitative chemical analysis of an unknown biological sample and/or a classification of cells or subcellular organelles. Overall, they rely on relatively complex data analysis pipelines, including a heavy spectrum-to-spectrum phase retrieval step, which limit their dissemination into the biomedical field. A more recent work focused on using PCA and k-means clustering to perform a comparison between CARS and SRS in the context of tissue imaging (Bocklitz et al., 2018). Based on all these works, it is

evident that an MCR-based approach should be able to bring a new look on MCARS data by generating less biased cell images while facilitating the interpretation of the extracted chemical and biological information. Moreover, such approach would be all the more powerful as it could take both the spectral and spatial dimensions of the dataset into account, and the sole spectra being usually exploited in the field.

Today, MCARS microspectroscopy using a dual-output sub-nanosecond laser source is recognized as a mature and straightforward technology for bioimaging, offering the high spectral resolution of conventional Raman spectroscopy with reduced acquisition time (Kano et al., 2019; Kaneta et al., 2021). We have recently demonstrated its efficiency for cell cycle studies (Guerenne-Del Ben et al., 2019) or cancer cells characterization (Guerenne-Del Ben et al., 2020). In the proposed study, we naturally combine the potential of both this imaging technique and the MCR source separation method under the classical signal non-negativity constraint and, even more originally, under a new spatial constraint based on cell segmentation. We thus introduce a new approach of MCARS hyperspectral cell imaging and segmentation, based on a simple workflow, without any phase retrieval computation, for data acquisition, chemical analysis, and visualization.

The imaging capability of this approach is first described using a MCARS dataset obtained from a fixed human embryonic kidney 293 (HEK293) cell in the interphase of the cell cycle (G_1/S). This cell is subsequently used as the "reference" cell. Second, we compare the results obtained for the reference HEK293 cell with those obtained for a premyoblastic cell from the C2C12 murine line under similar conditions (*i.e.*, fixed during the interphase of the cell cycle). This comparison allows us to assess the robustness of our approach by considering two very different cell types. To evaluate its applicability over a broader range, we then study HEK293 cells in different physiological states and experimental situations (Guerenne-Del Ben et al., 2019; Guerenne-Del Ben et al., 2020). For this purpose, we compare the results of the reference (interphasic) cell to those obtained from another cell in mitosis (prophase), during which important nuclear and cytoplasmic rearrangements occur. We also present a comparison between the reference (fixed) cell and a living cell, in order to visualize the potential changes induced by the fixation protocol in cellular architecture. Next, with the aim of assessing more specifically the sensitivity of our approach, we study HEK293 living cells overexpressing tropomyosin-related kinase B (TrkB), a cancer-related membrane receptor, depending on the presence of its ligand, brain-derived neurotrophic factor (BDNF). Finally, the application of the segmentation constraint in the MCR framework is introduced and discussed in the case of the single reference cell. Then, the segmentation capability of the approach is evaluated by considering cell clusters of various sizes.

2 Materials and methods

2.1 Cell samples preparation

The datasets of HEK293 cells used in this study were obtained from cell samples prepared by T. Guerenne-Del Ben, according to the protocols described in Guerenne-Del Ben et al., 2019 and Guerenne-Del Ben et al., 2020. HEK293 cell line was provided by Pr. F. Lalloue, CAPTuR, UMR INSERM 1308, Faculty of Medicine, University of Limoges, France. HEK293 cells were non-modified or overexpressing the TrkB receptor.

Non-modified HEK293 cells were routinely cultured in a complete medium consisting in high-glucose (4.5 g/L) DMEM (Gibco), supplemented with 10% (v/v) fetal calf serum (Eurobio), 1 µg/ml amphotericin B (Gibco), 100 units/ml penicillin, and 100 µg/ml streptomycin (Gibco) in an incubator heated at 37°C under 5% CO_2 humidified atmosphere. HEK293 cells overexpressing TrkB were cultured in a complete medium supplemented with 750 µg/ml geneticin (G418, Roth). C2C12 cell line (ATCC, Manassas, VA, United States) was cultured in DMEM supplemented with L-glutamine, 10% (v/v) fetal calf serum, 50 units/mL penicillin, and 50 µg/ml streptomycin.

For MCARS analysis, the cells were seeded at a density of 8,750 cells/cm^2 on 18-mm glass coverslips in 12-well plates for 48 h.

For the synchronization of non-modified HEK293 cells (study of the cell cycle), a first blocking with thymidine was performed for 18 h. Then for obtaining G_1/S or mitotic cells, after a release phase in complete medium of, respectively, 9 and 4 h, the cells were exposed to either 2-mM thymidine (double block procedure) for 17 h or 100 ng/ml nocodazole (Sigma-Aldrich) during 12 h before being replaced in fresh complete medium (for more details, refer to Guerenne-Del Ben et al., 2019). When a fixation was performed, the cells were washed three times in DPBS (Gibco), immersed in 4% paraformaldehyde (PFA) for 10 min at room temperature, and washed again three times in DPBS. A subset of living cells was labeled with the nuclear dye Hoechst 33342 (ThermoFisher) at 10 µg/ml for 15 min and room temperature before being rinsed in DPBS.In addition, a subset of fixed cells was labeled with the nuclear dye DAPI (4′,6-diamidino-2-phenylindole, Sigma-Aldrich) at 1 µg/ml for 5 min.

HEK293 cells overexpressing TrkB were cultured in the presence of recombinant human BDNF (Peprotech) at a final concentration of 75 ng/ml, or its solvent (DPBS), for 72 h. Cell nuclei were then stained with Hoechst 33342 as described earlier.

Glass coverslips with living or fixed cells were mounted on a microscope slide in DPBS and sealed with nail polish.

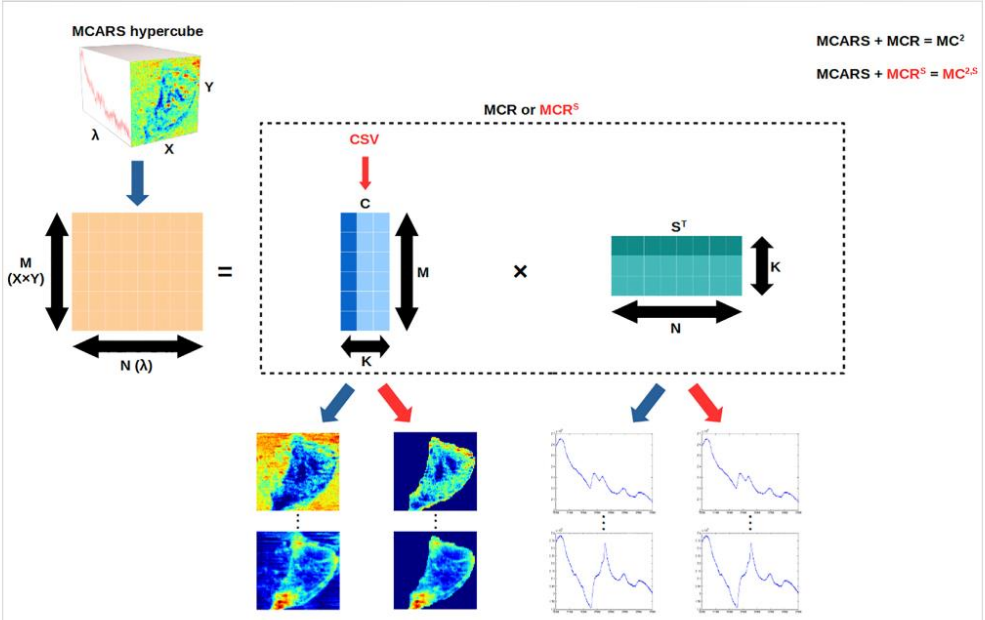

FIGURE 1
MC^2 and $MC^{2,S}$ frameworks. MCARS data are linearized, and then MCR or MCR^S is applied to compute the concentration $M \times K$-matrix C and the spectra $K \times N$-matrix S^T iteratively. Finally, an image (reconstructed from C; segmented in the case of MCR^S) and a spectrum (stored in S^T) are available for each of the K extracted components. CSV stands for the Chan–Sandberg–Vese method, which is used as a segmentation constraint in MCR^S.

2.2 MCARS microspectroscopy and fluorescence imaging

The MCARS microspectroscope and associated experimental conditions are described in Guerenne-Del Ben et al., 2019. In brief, the MCARS setup is based on a passively Q-switched microchip laser (Horus Laser, 1,064 nm, 1 ns, 20 kHz), a photonic crystal fiber for generating the broadband infrared Stokes wave, focusing (Olympus, UPlanSApo 60x, N.A. = 1.2, water immersion) and collecting (Nikon, S Plan Fluor ELWD 60x, N.A. = 0.7) microscope objectives, and a spectrometer (Horiba, LabRam HR Evolution). CARS spectra were acquired from 2,500 to 3,200 cm^{-1} with ~0.8 cm^{-1} spectral resolution, 50 ms pixel dwell time, and 300 nm lateral step for cross-sectional mapping. The lateral and axial resolutions were ~300 nm and ~2 µm, respectively. The laser power of the pump and Stokes radiations at the sample position was 55 and 9 mW, respectively, for which no morphological change of cells was observed during the experiments.

Fluorescence imaging was realized on the same system by using a halogen light source, appropriate excitation and emission filters, and a dedicated CCD camera (Thorlabs, 1500M-GE).

2.3 Maximum entropy method

As we have seen in the introduction, CARS spectra suffer from the presence of NRB that greatly distorts the acquired spectra and therefore the images that are extracted afterward. For the purpose of spectroscopic validation of our approach, we used the MEM algorithm from Vartiainen et al. (2006) as a reference method to extract the imaginary part of the third order non-linear susceptibility ($\mathrm{Im}\{\chi^{(3)}\}$) and thus obtain conventional Raman-like spectra. The implementation of MEM was performed using MATLAB software (R2018b, MathWorks).

2.4 Multivariate curve resolution

MCARS datasets were analyzed using MCR (De Juan et al., 2014). MCR is a signal unmixing method, which aims at finding the K components of a multicomponent signal. The data matrix D, which contains M measures for N Raman shifts, is decomposed into two matrices, as depicted in Figure 1: the concentration $M \times K$-matrix C, including the K component

concentration maps along its columns (corresponding to the projection of the initial data), and the spectra $K \times N$-matrix S^T, including the K component spectra along its rows (corresponding to the projection basis). More formally, the model is defined as follows:

$$D = CS^T + E, \tag{1}$$

where E being the error matrix, containing data not represented by the basis and expected to be noise or irrelevant information. In the case of chemical mixture analysis, $c_{i,j}$ is the concentration of compound j for measuring (i.e. pixel) i and row j of S^T, which is the characteristic spectrum of this compound.

In order to evaluate the quality of the MCR decomposition according to the value of K, the so-called lack-of-fit (LOF) was used:

$$LOF = \frac{\sum_{i,j} e_{i,j}^2}{\sum_{i,j} d_{i,j}^2}, \tag{2}$$

where $e_{i,j}$ and $d_{i,j}$ being elements of row i and column j of matrices E and D, respectively. The LOF corresponds to the ratio between the data contained in E (i.e., not expressed by the model) and those contained in the experimental dataset. Based on the variation of the LOF as a function of K for the datasets used in our study, the number of components was set to $K = 5$. This choice will be investigated later in the Discussion.

Even if MCR allows us to explore complex signals, this approach nevertheless presents what is called ambiguities, meaning that different pairs of C and S^T matrices can be acceptable solutions. In this context, applying constraints to C and S^T during MCR calculation allows reducing these ambiguities and the number of possible solutions, in order to potentially converge toward a unique decomposition. Two of the most common constraints are non-negativity and normalization. The non-negativity constraint ensures to have only positive values for all elements of C and/or S^T matrices, while the normalization constraint implies that the sum of all values of each row or column of C and/or S^T is equal to one. Obviously, constraints have to be selected according to the acquisition method, the study subject, and the intrinsic nature of the data. In this study, we applied the non-negativity constraint to the concentration matrix C and to the spectra matrix S^T, while the normalization constraint was only applied to each row (i.e., measure) of the concentration matrix.

One way to solve the MCR problem is to use an alternating regression algorithm to compute C and S^T. Here, we used the common "alternating least squares" (ALS) algorithm, the method being then called MCR-ALS. Moreover, we applied the non-negativity constraint within the decomposition process by using non-negative least squares (NNLS) (Lawson and Hanson, 1974). Practically, these results are a three-step process: first, the C matrix is computed by NNLS, then it is normalized and, in turn, the S matrix is computed by NNLS. This process is then repeated until convergence. Furthermore, we used the SIMPLISMA algorithm (Windig and Guilment, 1991) for computing the initial S matrix of the iterative process.

We implemented the whole MCR-ALS workflow in Python language, based on the freely available "pyMCR" package (Camp, 2019). In the following sections, the combination of MCARS acquisition and MCR data analysis (with the two classical constraints) will be denoted as MC^2 (Figure 1).

2.5 New cell segmentation constraint (MCR^S)

To extract cells from their environment and refine the intracellular analysis, we have developed in this work a new spatial constraint to be applied to the concentration matrix C, additionally to the previous constraints in the MCR framework. Specifically, we applied a segmentation constraint based on the Chan–Sandberg–Vese (CSV) method (Chan et al., 2000), which has already shown its ability to segment biological cells (Dufour et al., 2005; Maška et al., 2013). With the use of this additional spatial constraint, the framework will be denoted as MCR^S and the whole approach as $MC^{2,S}$ in this work (Figure 1).

The CSV method is an iterative segmentation method based on active contours. It consists of splitting the given image into two regions, using an energy-dependent model. The goal of the algorithm is to minimize the fitting energy between the model and the input image I:

$$\underset{c_1,c_2,\mathfrak{C}}{arg\,min}\, F(c_1, c_2, \mathfrak{C}) \tag{3}$$

with $F(c_1, c_2, \mathfrak{C}) = \mu \cdot Length(\mathfrak{C}) + \nu \cdot Area(inside(\mathfrak{C})) + \lambda_1 \int_{x,yeinside(\mathfrak{C})} ||I(x,y) - c_1||^2 dxdy + \lambda_2 \int_{x,yeoutside(\mathfrak{C})} ||I(x,y) - c_2||^2 dxdy,$

where $\mathfrak{C}$ is the border between the two regions, and c_1 and c_2 are the region averages. This equation is solved using a partial differential equation. The method requires the following parameters to be defined:

1) "Length penalty" μ (to be set between 0 and 1) regularizes the length of $\mathfrak{C}$. It is the most important parameter to tune (Getreuer, 2012). A small value leads to define the border of the cells with potentially a high level of detail, while a large one generates a smoother boundary. Here, we use $\mu = 0.35$. The rationale behind this choice is stated in Section 3 (more specifically, in the sub-section entitled "Comparison between MC^2 and $MC^{2,S}$ methods applied to the reference cell";
2) "Area penalty" ν tunes the penalty ($\nu > 0$) or reward ($\nu < 0$) to be applied to the area inside $\mathfrak{C}$ during minimization. As we do not have any *a priori* on the size of cells in the acquisition window, ν is set to zero;
3) "Fit weights" λ_1 and λ_2 allow to control deviation from the original image in terms of pixel intensity for areas inside and

outside $\mathfrak{C}$, respectively. We use $\lambda_1 = \lambda_2 = 1$ in order to not to penalize one area against the other;

4) "Time step" Δt is the discretization step used to solve the partial differential equation. A small value gives better results with increased computation time, while a large value can lead to convergence problems. We use the default value $\Delta t = 0.5$ (Getreuer, 2012).

The new algorithm corresponding to one iteration of MCR^S is the following:

1) compute C using NNLS;
2) refold C into K images of size $X \times Y$ (consistently with the initial dataset);
3) apply the CSV method to these images in order to compute a segmentation mask;
4) use the mask to set concentration values outside $\mathfrak{C}$ to zero;
5) unfold segmented images in order to retrieve a (spatially) constrained C matrix;
6) apply the normalization constraint to C;
7) compute S using NNLS.

The addition of the segmentation constraint to the MCR-ALS framework was also implemented in Python.

2.6 Projection onto reference spectra

In the case of living HEK293 cells overexpressing TrkB cancer-related protein, a particular approach was used to compare cells that were incubated with or without BDNF. First, the MC^2 approach was applied to a cell that was incubated without BDNF, considering the spectra of the extracted components as reference spectra. Then, the MCARS dataset of a second cell, incubated with BDNF, was projected onto the basis of reference spectra by using the NNLS regression algorithm. The resulting concentration matrix was then normalized, as previously. With this approach, we could visualize the spatial distribution of the same components in both cells, comparatively.

2.7 Statistical analysis of cell segmentation

In order to generate the ground truth masks, bright-field images of the cells were opened within NIH ImageJ software (https://imagej.nih.gov/ij/) and manually segmented using the "Polygons selection" tool. The comparison between ground truth and MC^{2,S} masks, and the calculation of Dice similarity coefficients were realized by using "imshowpair" and "dice" functions in MATLAB software (R2018b, MathWorks).

The statistical analysis of Dice coefficients was performed using PAST software (O. Hammer, D.A.T. Harper, P.D. Ryan, PAST: paleontological statistics software package for education and data analysis, Palaeontol. Electron. 4 (2001) 1–9). After having tested the normality of the values using a Shapiro–Wilk test, a one-way analysis of variance (ANOVA) was performed and followed by a Tukey's multiple comparison test. Differences were considered significant for $p < 0.05$.

3 Results

3.1 Spectroscopic validation of the approach

We first applied the MC^2 approach to the analysis of a fixed, DAPI-stained, interphase HEK293 cell. Figure 2A displays the bright-field and fluorescence images, as well as the five concentration maps, while the corresponding component spectra are plotted in Figure 2B. In order to validate the spectroscopic features observed on these extracted spectra (as expected for conventional raw MCARS spectra), they were processed by the MEM algorithm so as to extract the corresponding conventional Raman-like spectra (Figure 2C). We have highlighted in Figure 2C the vibrational modes that are most relevant for cell analysis in this spectral range, namely, CH_2 symmetric (2,845 cm^{-1}) and = C-H (3,005 cm^{-1}) stretching, mainly associated to lipids (red vertical bars), CH_3 symmetric (2,930 cm^{-1}) and C-H aromatic (3,056 cm^{-1}) stretching, mainly associated to proteins (green vertical bars), and O-H symmetric stretching (3,200 cm^{-1}) of water (blue vertical bar). It is reminded that no vibrational signature of DAPI is expected in the high wavenumber (C-H stretching) region (Krause et al., 2007).

It appears from Figure 2C that components #1 and #4 are characterized by a high water content, concomitantly with the presence of proteins (for component #1) and lipids (for component #4). Components #2 and #5 are clearly dominated by the protein content but differ from each other by the lipid content (weak in component #2 and absent in component #5). Last, component #3 stands out by a strong lipid content, together with proteins. Therefore, from the spectroscopic viewpoint, the chemical species behind these components exhibit five different proportions of lipids, proteins, and water. This spectroscopic and chemical information of a given spectral contribution can then be related to the associated concentration map in order to observe the spatial distributions and biochemically investigate the intra- and extracellular contents.

In the following, we perform such biochemical study by simply using the spectral contributions extracted by the MC^2 approach, that is, without phase retrieval computation by the MEM. To this aim, we have replicated and slightly shifted the vertical bars of Figure 2C onto Figure 2B, taking into account the spectral shift of peaks that occurs between raw CARS spectra and MEM-processed ones (Freudiger et al., 2008; Capitaine et al., 2018). In that respect and in a first approach, the spectroscopic

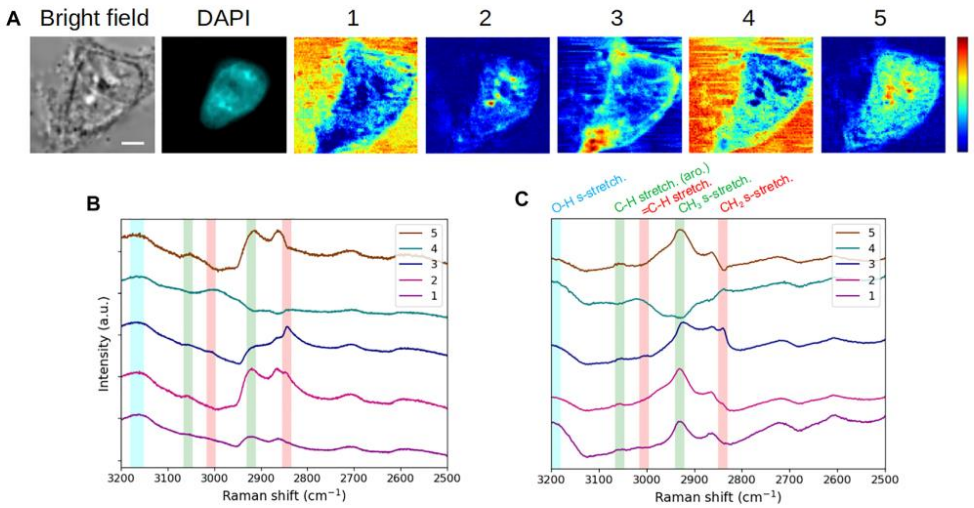

FIGURE 2
Application and spectroscopic validation of the MC² approach for the analysis of a fixed interphase HEK293 cell. **(A)** Bright-field and fluorescence images and concentration maps obtained for the five computed components. The scale bar corresponds to 5 µm and applies to all images. **(B)** Spectra extracted for these five components. **(C)** Raman-like spectra after MEM processing, with the following vibrational modes highlighted: CH_2 symmetric (2,845 cm^{-1}) and = C-H (3,005 cm^{-1}) stretching mainly associated to lipids (red vertical bars), CH_3 symmetric (2,930 cm^{-1}) and C-H aromatic (3,056 cm^{-1}) stretching mainly associated to proteins (green vertical bars), and O-H symmetric stretching (3,200 cm^{-1}) of water (blue vertical bar). Vertical bars were replicated into **(B)**, taking into account the peak spectral shift that occurs between raw CARS and MEM-processed data. After fixation, the cell was stained with DAPI.

analysis can be made from the MC² spectra by appreciating the presence of CARS peaks in the different spectral channels indicated by the vertical bars. A more thorough interpretation is to consider the significance (mathematically, the slope and the amplitude) of the dispersive lines associated to these peaks. This is particularly useful when the CARS peak is not apparent, due to an insufficient ratio between vibrationally resonant and non-resonant contributions, as in the case of CH_3 symmetric stretching for spectral contribution #3 (Figure 2B).

Finally, the fixed interphasic HEK293 cell observed in Figure 2 will be considered as the reference cell throughout the rest of this work. As a supplemental validation of our approach, we also applied MCR to the reference cell dataset after a prior step of MEM processing, taking into account the impact of the NRB spectrum source (here, the raw MCARS spectrum of the solvent) and of the baseline detrending (corresponding to the dark noise/background related to the spectrometer). Supplementary Figure S1 shows the evolution of the final outputs, according to these different processing steps. In this figure, the results obtained in the last case (NRB normalization combined with background subtraction) can thus be compared with MC² results (first row). From the spectral point of view, we stress the obvious quality difference of $\mathrm{Im}\{\chi^{(3)}\}$ spectra plotted in Figure 2C (MEM applied to the five spectra extracted by MCR) and Supplementary Figure S1 (MCR applied to all spectra first processed by MEM). Moreover, the $\mathrm{Im}\{\chi^{(3)}\}$ spectra of Figure 2C demonstrate that MCR performs well with non-linear CARS intensity, since both the spectral shape and the exhibited vibrational information are consistent with Raman-like spectra and with the images of Figure 2A, respectively.

3.2 Comparative analysis of fixed cells in interphase (G_1/S)

In this part of the work, we assessed the robustness of the MC² method by comparatively analyzing the HEK293 reference cell and a C2C12 interphasic unstained cell. Figure 3 shows the extractions obtained on these 2 cells. It should be noted that two separate MCR analyses were conducted on these two datasets.

When considering the concentration maps of the reference cell (Figure 3A), it is clear that components #1 and #4 (dominated by a high-water content, as already explained before) are mainly

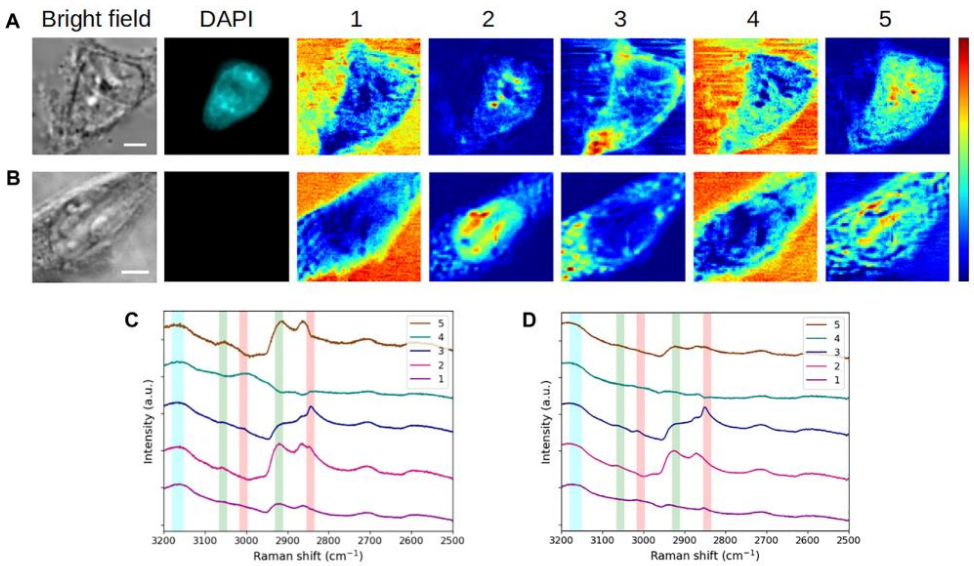

FIGURE 3
Comparative analysis of fixed **(A,C)** HEK293 and **(B,D)** C2C12 cells in interphase (G_1/S). **(A,B)** Bright-field and fluorescence images and concentration maps obtained for the five computed components. The scale bar corresponds to 5 µm. **(C,D)** Spectra corresponding to **(A,B)**, respectively. Vertical bars highlight the presence of lipids (red), proteins (green), and water (blue). After fixation, the HEK293 cell was stained with DAPI.

related to the aqueous extracellular environment. From a spatial point of view, component #2 is localized at the nucleus as depicted by its round shape, overlapping with DAPI staining. The high-concentration spots highlight specific areas that can reasonably be attributed to nucleoli in relation to DAPI staining together with bright-field images. Nucleoli are active nuclear subcompartments whose one of the main functions is to be the site for the initial steps of ribosome biogenesis. This implies the presence of proteins linked to the transcription machinery and post-transcriptional modifications by small nucleolar ribonucleoproteins in the dense fibrillary component. The rRNA assembly with the ribosomal proteins then occurs in the granular component of the nucleolus (Pederson, 2011). This is thus in agreement with the high protein content emerging in spectral profile #2 (Figure 3C). Regarding component #3, it is concentrated in an area corresponding to the plasma membrane (or its very close periphery) and it is found in the cytoplasm as well. This is in line with the chemical species highlighted by the associated spectrum, that is, a lipid-rich content with the presence of proteins. Finally, component #5, which corresponds to a high protein content and an absence of lipids, is located throughout cell nucleus and cytoplasm, with a higher concentration in the nucleus and near nucleoli.

Overall, the extracted spectra of HEK293 and C2C12 cells (Figures 3C,D, respectively) exhibit a reasonable stability when they are observed pairwise for each component (except for component #5, which will be examined later). Accordingly, the concentration maps (Figures 3A,B) reveal a comparable spatial distribution of the signal between both cells for the first four components. Hence, with a high-water content, components #1 and #4 highlight the extracellular milieu. The observations made for component #2 in the case of the reference cell are applicable to the second cell, that is, a high protein content (with more or less lipids) emphasizes the nucleus and nucleoli (visible in bright-field for both cells). Regarding component #3 (lipid-rich content with the presence of proteins), the distribution of the signal in the cytoplasm of the C2C12 cell is more or less punctiform, suggesting that the related cytoplasmic structures correspond to lipid droplets. Lipid droplets are organelles consisting in a phospholipid monolayer surrounding a core composed of neutral lipids. They are well described in C2C12 premyoblastic cells (Billecke et al., 2015; Ichimura et al., 2015), and their abundance in myoblast cytoplasm was recently associated with a facilitated (induced) differentiation into myotubes (Tan et al., 2021). Moreover, in both cells, a portion of component #3 appears to surround the

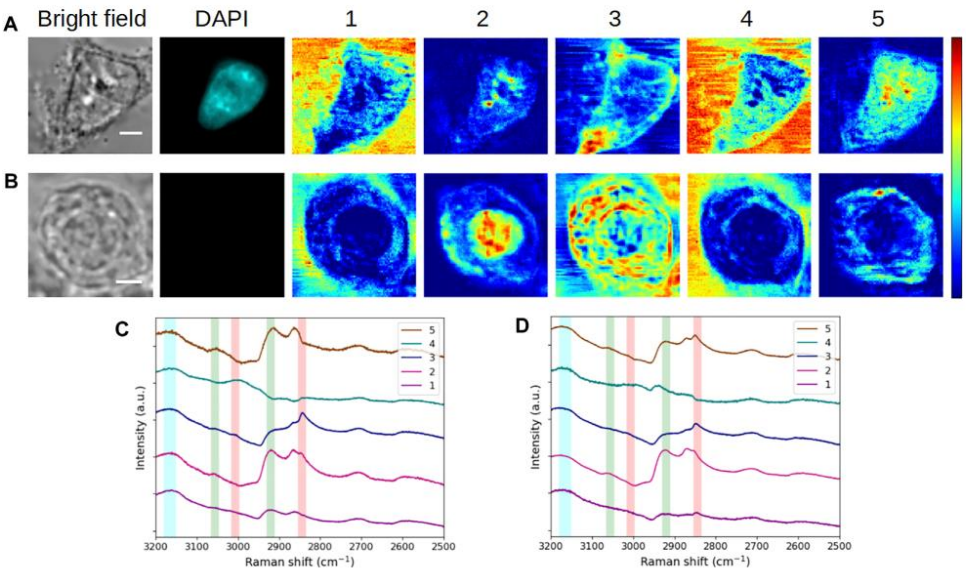

FIGURE 4
Comparative analysis of fixed HEK293 cells in **(A,C)** interphase (G_1/S) and **(B,D)** mitosis (prophase). **(A,B)** Bright-field and fluorescence images and concentration maps obtained for the five computed components. The scale bar corresponds to 5 µm. **(C,D)** Spectra corresponding to **(A,B)**, respectively. Vertical bars highlight the presence of lipids (red), proteins (green), and water (blue). After fixation, the interphase cell was stained with DAPI.

nuclear structure and could be related to the nuclear envelope. For all these reasons, component #3 seems to relate to cellular membrane constituents such as phospholipids.

In the case of component #5, a variability is observed between both cells. For the reference HEK293 cell, this component represents a pure protein content in the cytoplasm and, more abundantly, in the nucleus, which is difficult to assign to a particular cellular compartment. For the C2C12 cell, spectrum #5 (Figure 3D) reveals a mixed content of proteins, lipids, and water. In the corresponding concentration map (Figure 3B), the signal is less diffuse and more reticular than for the HEK293 cell. This would suggest that endoplasmic reticulum (ER) is highlighted, assuming that lateral resolution is not sufficient to resolve individual ER layers and that the seeming presence of signal in the nucleus is due to positioning the focal plane at the nucleus periphery. However, further experiments would be necessary to support this assertion, including the specific labeling and fluorescence imaging of the ER. Anyhow, in both cases, the concentration map of component #5 is complementary to the other four maps. Regarding the variability of the spatial distribution between HEK293 and C2C12 cells, it can be hypothesized that component #5 is specific to the cell line, given that the cells studied here belong to distinct types with very different physiological functions.

3.3 Comparative analysis of fixed cells in interphase (G_1/S) and mitosis (prophase)

Next, we compared the reference interphasic cell with an HEK293 unstained cell that was fixed in mitosis (prophase), as displayed in Figure 4. As previously, MCR analyses were performed separately.

Again, it is interesting to see that a certain stability is maintained at the spectral level between both cells for components #1–#4. Accordingly, in the concentration maps of the mitotic cell (Figure 4B), the extracellular environment is disclosed by components #1 and #4. Component #2 (high protein content) shows a strong and rather homogeneous signal at the place of nucleus, in agreement with the nuclear rearrangements occurring during prophase. The observed intensity variations can be correlated with the level of chromatin condensation. The concentration map of component #3 (lipid-rich content with proteins) highlights concentric structures looking like

membranes, the outermost layer corresponding to the plasma membrane. During mitosis, a major rearrangement of membrane structures takes place and is essential for the completion of a proper cell division leading to fully functional daughter cells (recently reviewed in Carlton et al., 2020). The fractionation of some of the organelles such as the ER and the Golgi apparatus, disassembled during late prophase (or prometaphase), leads to a new membrane organization with a modification of the protein/lipid ratio in the resulting membranes. Notably, an important part of the membrane components is bound to the plasma membrane. It is interesting to note that the concentric lamellar signal observed in concentration map #3 suggests such an organization, which would be consistent with the division state of the studied cell, visually estimated in prophase to late prophase.

Regarding component #5, we notice a divergence in the spectra and concentration maps corresponding to the interphasic and mitotic cells, respectively. We can assign this divergence to the different physiological states of the cells. In the case of the mitotic cell, the extracted spectrum displays a mixed protein-lipid content and the resulting concentration map exhibits a specific, polarized, and intracellular structure in the cytoplasm. As seen in Supplementary Figure S2A, this structure (plotted in green here) is entangled with component #3 (plotted in red). The same trend is visualized for another (late) prophase cell (Supplementary Figure S2B), with an even more distinct polarization of component #5. These observations would suggest that this component might be linked to the mitotic spindle of the cells. The results obtained for an early-metaphase cell (Supplementary Figure S2C) consolidate this hypothesis, as well.

3.4 Comparative analysis of interphase (G_1/S) fixed and living cells

Cell fixation prior to *in situ* labeling and/or the use of several imaging methods have non-negligible effects on cell structure. These effects differ according to the fixation reagent. For example, formaldehyde, routinely used, can react with numerous functional groups of macromolecules, especially inducing protein or protein-DNA cross-linking (Hoffman et al., 2015). The consequences of fixation from a chemical standpoint are accompanied by the alteration of cell mechanical properties, which were investigated in Kim et al. (2017) by means of atomic force microscopy and scanning ion conductance microscopy. For their part, Hobro and Smith (2017) could use Raman spectroscopic imaging and PCA to evaluate several fixation methods. In this context, we sought to assess our approach for the study of cell alterations induced by fixation. In that way, Figure 5 presents the concentration maps and the associated spectra, resulting from the application of the MC^2 method to the reference cell (Figures 5A,C), fixed with PFA, and a living HEK293 cell (Figures 5B,D).

First, some common features persist when comparing the concentration maps of the 2 cells. Components #1 and #4, dominated by the water content, again points out here the extracellular environment. Nucleoli visualization is still found in component #2, while component #3 discloses membrane structures. However, we can notice some obvious differences between both cells, which are described later.

In the living cell, component #1 highlights not only the extracellular milieu but also the nucleus, which is visible for neighbor cells in the field of view, as well. In addition to the nucleus, the cytoplasm is shown by component #4, which is spectrally characterized by the combined presence of water and lipids. Interestingly, this component spotlights the border of the nucleus and the nucleoli as low-signal areas, indicating that water and lipids are not found together in these areas (the sole lipids being expected at the nuclear envelope and non-expected in the nucleoli). Overall, the presence of the intracellular aqueous content is not observed for the fixed cell. This would be consistent with a loss of cellular content due to the fixation that may induce shrinkage, especially when performed at room temperature.

In the case of component #2, besides nucleoli, the border of the nucleus (the nuclear envelope) is highlighted in the living cell, in agreement with bright-field and Hoechst 33342 fluorescence images. A further investigation of spectrum #2 brings out some vibrational information in the channel plotted in violet (Figure 5D). This contribution is assigned to CH_3 antisymmetric stretching in the 2,960–2,980 cm^{-1} range (Matthews et al., 2010). In Supplementary Figure S3, we have compared the spectra of component #2 obtained for all fixed and living cells considered so far, including both raw and MEM-processed spectra. This figure displays a stronger contribution of the interphase living HEK293 cell in the highlighted 2,960–2,980 cm^{-1} channel. Following Lu et al., 2015, this contribution can be attributed to DNA in live cells and can thus be associated with a structure linked to the nuclear envelope in the present case (Figure 5B, map #2). Indeed, during interphase, heterochromatin binds indirectly to the nuclear envelope by means of proteins involved in tethering chromatin. The absence of such a perinuclear signal in the fixed cell (Figure 5A, map #2) would be consistent with the chemical mechanism of action related to cell fixation with PFA.

Regarding component #3, in the living cell, the cytoplasm and the nuclear border clearly appear. Taking into account the combined presence of lipids/proteins and the reticular aspect of the signal in the cytoplasm, one can suggest that the revealed structures correspond to the nuclear envelope in contiguity with the rough ER. This assumption is supported by the weak contribution of CH_3 antisymmetric stretching to component #3 (Figure 5D, spectrum #3, violet channel), which is assigned to ribosomal RNA in the cytoplasm (Lu et al., 2015). Finally, component #5, dominated by proteins and exempt from lipids, discloses the inner border of the nuclear envelope, likely

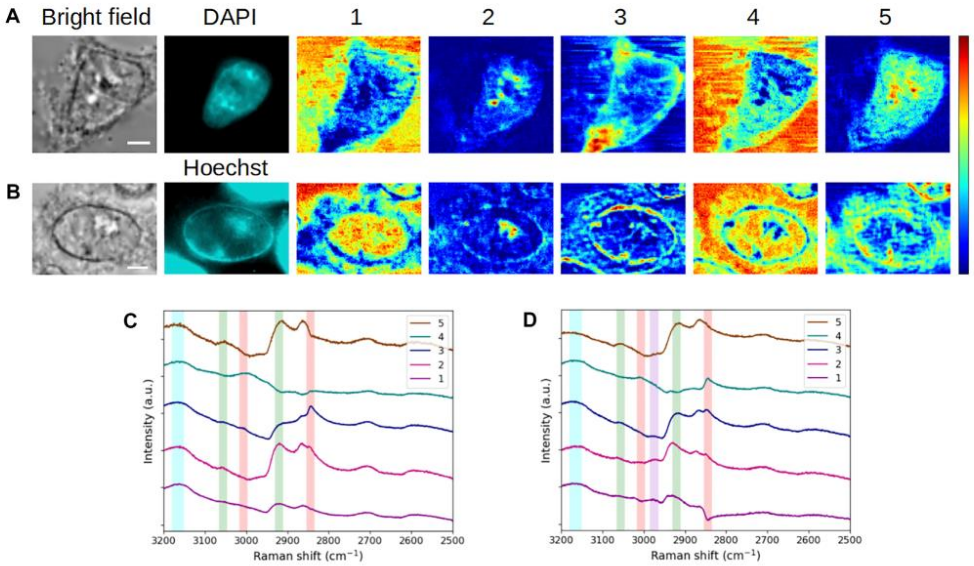

FIGURE 5
Comparative analysis of interphase **(A,C)** fixed and **(B,D)** living HEK293 cells. **(A, B)** Bright-field and fluorescence images and concentration maps obtained for the five computed components. The scale bar corresponds to 5 µm. **(C, D)** Spectra corresponding to **(A, B)**, respectively. Vertical bars highlight the presence of lipids (red), proteins (green), DNA/RNA (violet), and water (blue). The fixed and living cells were stained with DAPI and Hoechst 33342, respectively.

corresponding to the nuclear lamina and the cytoplasm, likely due to the presence of resident soluble proteins in the latter. The absence of lipids in this component results in a "double ring" signal, localized on both sides of the nuclear envelope.

In order to illustrate the potential of the MC^2 approach for single-cell imaging, Figure 6 summarizes the results obtained with HEK293 and C2C12 cells in the different physiological states (fixed interphase, fixed mitotic, and living interphase cells). In this figure, we plotted the concentration maps of components #1, #2, and #3 from Figures 2A, 3, 4, 5B in false colors, specifically in blue, green, and red, respectively. The merge column shows the overlay of these three maps, illustrating the complementarity of the extracted components under each biological condition. Moreover, an easier comparative analysis of all results can be made from Figure 6.

For a further validation of our approach, the workflow of Supplementary Figure S1 (NRB normalization + background subtraction + MEM + MCR) was applied to the four cells of Figure 6. Output maps and spectra are available in Supplementary Figures S4 and S5. Generally speaking, combining MEM and MCR leads to more noisy images and spectra, due to additional processing steps and thus potential loss of information. In Supplementary Figure S4, the parallel representation of "MCR" and "MEM + MCR" results allows to validate our new approach, especially by comparing the high-protein and high-lipid content channels (second and third columns, in each case). However, even if our approach is workable and concentration maps are quite similar in this figure, we draw attention to the fact that, rigorously, the method is not expected to be quantitative since the raw CARS signal is not proportional to the concentration.

3.5 Analysis of living cells overexpressing TrkB and treated or not with brain-derived neurotrophic factor

Last, we evaluated the robustness and the applicability of the MC^2 method for detecting changes in cells where a variable was introduced. For this purpose, we analyzed the datasets of two living HEK293 cells overexpressing the TrkB receptor at a basal level or activated by the introduction of its ligand, BDNF, in the culture medium for 72 h (Figure 7). In this case, we used the spectra calculated for the non-treated cell (Figure 7C) as a reference, and then we projected both datasets onto this base to construct the concentration maps of the non-treated (Figure 7A) and TrkB-activated (Figure 7B) cells. In addition,

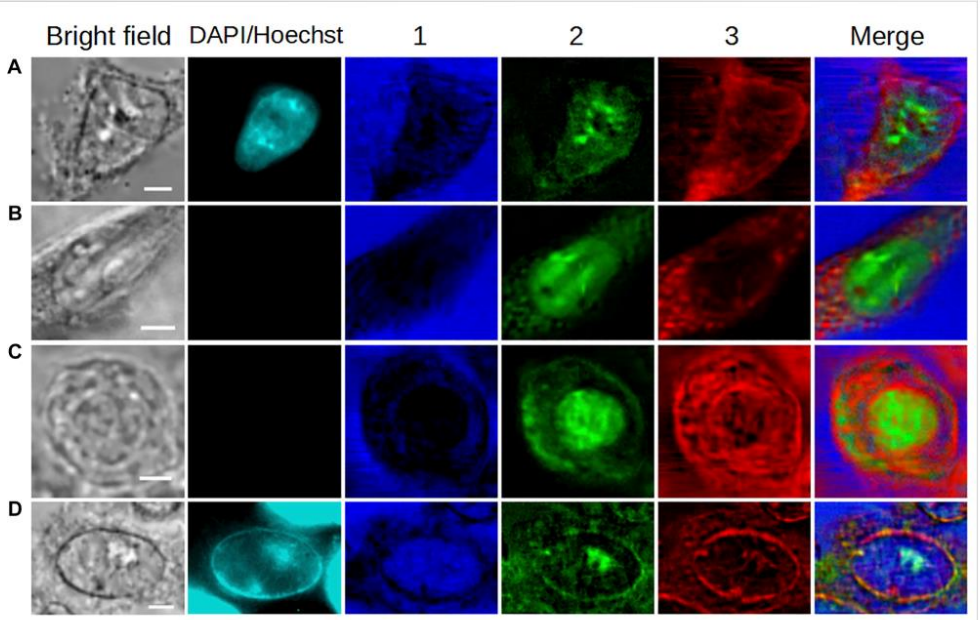

FIGURE 6
Overview of the application of the MC^2 approach to single-cell imaging in different cases. **(A,B)** Fixed interphase cells. **(C)** Fixed mitotic cell. **(D)** Living interphase cell. Images in 1,2, and 3 are the concentration maps of components #1, #2, and #3 extracted from Figures 2A, 3, 4, 5B, respectively, and plotted in false blue/green/red colors. The scale bar corresponds to 5 µm.

both cells can be visualized in false colors for components #1–3, as displayed in Figure 7D.

As an initial investigation, the information contained in components #1–3 is rather similar to that of the previously studied living HEK293 cell. Specifically, in both cells, some water appears in the nucleus (except the nucleoli), the nucleoli, and the nuclear border are highlighted, as well as the lipid content in the cytoplasm. As previously, the DNA contribution is found in spectrum #2, as confirmed in Supplementary Figure S2 (green spectra). Concerning component #3, given the punctiform distribution of the corresponding intracytoplasmic signal and considering the shape of spectrum #3, it is stressed that this component exhibits lipid droplets in both cells. Thereupon, the apparent larger accumulation of lipid droplets in the TrkB-activated cell would be related to a modification of the lipid metabolism, as suggested by Guerenne-Del Ben et al., 2020. Further than this work, here the comparative study of the non-treated and treated cells is substantially facilitated by the great complementarity between components #1–3. In the case of component #4, the obvious increase of high-intensity spots in the second cell may also correlate with the alteration of the lipid metabolism.

Finally, for component #5, the signal is distributed throughout the nucleus and the cytoplasm of both cells, but a more reticular structure is observed in the non-treated one. In both cases, an intense spot is visible in the nucleus, partially overlapping with nucleoli and low-water content areas. Another feature is the presence of the signal, in the TrkB-activated cell, at the place of the plasma membrane. Yet, proteins constitute the main vibrational signature in spectrum #5, which furthermore differs from other spectra by the complete lack of contribution in the water region. Then, this high protein content near the plasma membrane may reflect the consequences of cell exposure to the growth factor, and particularly the activation of TrkB by BDNF at the cell surface. At this step, it is more difficult to interpret the intracellular content revealed by component #5.

3.6 Comparison between MC^2 and MC^{2,S} methods applied to the reference cell

We have seen in the previous sections that the MC^2 approach allows to extract interesting biological information from the MCARS spectra. Nevertheless, we should not forget that only

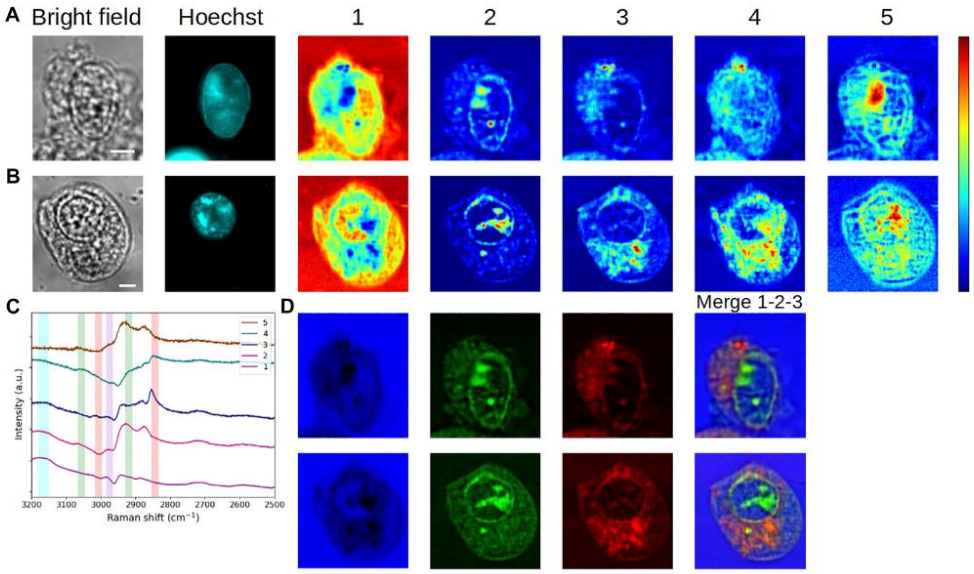

FIGURE 7
Analysis of living cells overexpressing TrkB cancer-related protein, in the presence or absence of its ligand BDNF. Application of the MC^2 approach to the analysis of a cell that was incubated without BDNF, with its **(A)** concentration maps and **(C)** corresponding spectra, considered as reference spectra. Vertical bars highlight the presence of lipids (red), proteins (green), DNA/RNA (violet), and water (blue). **(B)** Concentration maps of a cell that was incubated with BDNF, obtained by the projection of its dataset onto the reference spectra. **(D)** False-color images corresponding to concentration maps #1 (blue), #2 (green), and #3 (red). Both cells were incubated without/with BDNF during 72 h and stained with Hoechst 33342. The scale bar corresponds to 5 µm.

the spectral data were exploited to generate these maps and that the spatial information was not exploited in this approach. We thus developed the MC^{2,S} method in order to take into account simultaneously the spectral and spatial dimensions, to refine the extraction of components and to perform cell segmentation.

As mentioned in Section 2, the length penalty μ is an important parameter to set (between 0 and 1) in the MC^{2,S} approach. Several values of μ were tested for the reference cell, as illustrated in Supplementary Figure S6. We could then study the evolution of the cell contour according to μ variation, for each of the five components extracted by MCR^S. Small values of μ lead to cropping the bottom-left part of the cell, particularly in the case of components #1 and #5 (arrow heads, Supplementary Figure S6). From μ = 0.35, this bottom-left curve becomes comparable to what is observed without using the segmentation constraint. Higher values of μ induce an oversegmentation, visible for components #1, #3, and #4 on the upper side of the cell (full arrows, Supplementary Figure S6). For these reasons, we set the value of μ to 0.35.

Then, to appreciate the impact of the addition of the segmentation constraint to the MCR framework, both MC^2 and MC^{2,S} methods were applied to the reference cell. The results are shown in Figures 8A,C and in Figures 8B,D, respectively.

The vibrational modes of each extracted spectrum were not modified by the introduction of the segmentation constraint, though some noise appeared on the spectral profiles. Regarding concentration maps, the value added by the new constraint is undeniable since the cell is clearly delimited from the background under these new conditions. In addition, the improved contrast within the cell allows a better rendering of intracellular structures. The most obvious changes are observed in concentration maps #1 and #4. In these maps, the extracellular milieu was initially the main contributing element. By using the segmentation constraint in the MCR process, the resolution is tightened on the intracellular area, resulting in a more accurate extraction of the aqueous content inside the cell. As a consequence, the main contributions in concentration maps #1 and #4 now appear in the inner periphery of the plasma membrane (this is particularly true for component #4) and, secondarily, in the nucleus and cytoplasm. Beyond the investigation of intracellular water, MC^{2,S} would be of interest for the study of elements that are prominent in the cell environment.

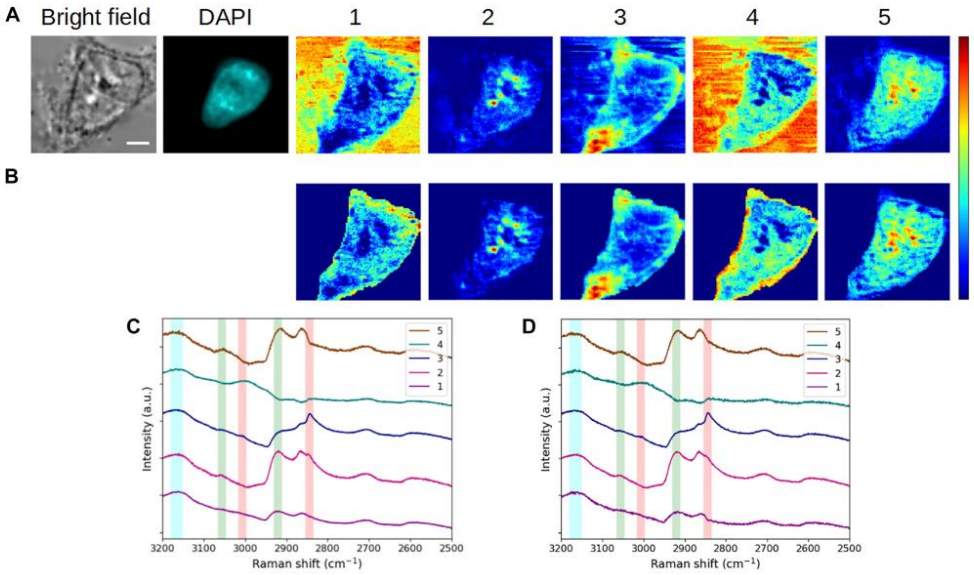

FIGURE 8
Analysis of a fixed HEK293 cell in interphase (G_1/S) without or with segmentation. Concentration maps and corresponding spectra obtained by means of **(A, C)** MC^2 and **(B, D)** $MC^{2,S}$ approaches. The scale bar corresponds to 5 µm. Vertical bars in **(C, D)** highlight the presence of lipids (red), proteins (green), and water (blue). After fixation, the cell was stained with DAPI.

3.7 Application of MC^2 and $MC^{2,S}$ methods to the analysis of cell clusters

Three different unlabeled, fixed, HEK293 cell clusters were analyzed to assess the robustness of MC^2 and $MC^{2,S}$ methods and their applicability to more complex situations (Figure 9). The corresponding spectra are given in Supplementary Figures S7–S9.

When looking at the concentration maps obtained by the MC^2 approach, we can notice a good reproducibility in the extraction of components for each cell cluster, with respect to previous results.Specifically, components #1 and #4 reveal the extracellular environment. Component #2 is associated with nuclei/nucleoli. Component #3 is mostly cytoplasmic and highlights a perinuclear structure (obvious in 2-cell and 5-cell clusters), probably made up of intracellular membranes belonging to the ER. Component #5 allows to visualize other cytoplasmic elements distributed asymmetrically within the cells.

The application of the $MC^{2,S}$ method provides the suitable segmentation of each cell cluster and a better visualization of intracluster structures. This benefit is noticeable in the false color representation of concentration maps #1, #2, and #3. In particular, it is interesting to see the presence of water in the intercellular space (5-cell and 8-cell clusters) and on the periphery of the clusters. Of course, the study of aqueous content would be supplemented by taking component #4 into account and by investigating the contribution of vibrational modes reflecting the presence of other chemical species. The $MC^{2,S}$ approach would thus be of interest to determine the state of water, namely, free water or water hydrating macromolecules.

3.8 Statistical analysis of cell segmentation

The accuracy of the segmentation included in the $MC^{2,S}$ analysis was evaluated by calculating the Dice similarity coefficients that are well recognized as a valuable metrics (Hermsen et al., 2019; Eelbode et al., 2020). Dice coefficients estimate the spatial overlap between the ground truth, corresponding in our case to a manual segmentation made by a cell biologist, and the segmentation mask generated by the $MC^{2,S}$ method. They are defined by DC (Ground truth, $MC^{2,S}$ segmentation) = 2 (|Ground truth|∩|$MC^{2,S}$ segmentation|)/(|Ground truth|+|$MC^{2,S}$ segmentation|), where ∩ is the

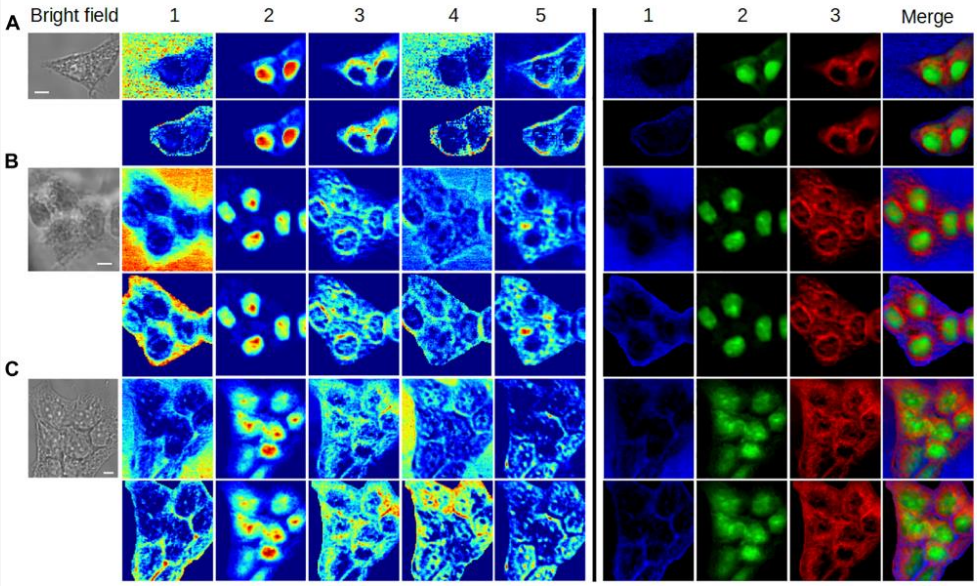

FIGURE 9
Application of MC^2 and $MC^{2,S}$ approaches to the analysis of cell clusters. **(A)** 2-cell cluster, **(B)** 5-cell cluster, and **(C)** 8-cell cluster. For each cluster, the concentration maps computed by MC^2 and $MC^{2,S}$ are plotted in first and second rows, respectively, using two different colormaps. The scale bar corresponds to 5 µm. The corresponding spectra are available in Supplementary Material.

intersection. Dice coefficients are comprised between 0 and 1, 0 being a total absence of overlapping, and 1 a total overlap between manual and automatic segmentations. We calculated the Dice coefficients for a total of 18 comparisons that correspond to cells or clusters included in Guerenne-Del Ben et al., 2019 and to unpublished results obtained in the context of the cited work. These comparisons were classified according to four categories, as shown in Supplementary Figure S10 (interphase fixed cells), Supplementary Figure S11 (mitosis fixed cells), Supplementary Figure S12 (interphase living cells), and Supplementary Figure S13 (fixed cell clusters).

Overall mean of Dice coefficients was 0.86 ± 0.07. In light of this result, $MC^{2,S}$ segmentation can be considered of good quality, all the more so as manual segmentation from bright-field images is a source of error and CARS measurement differs from bright-field by its optical sectioning capability (causing lateral shift and/or size modification between both modalities, as seen in several cases). Finally, we plotted in Figure 10 the calculated Dice coefficients, according to the physiological state of the cells. Following the p-value analysis of these data ($p > 0.05$), no significant difference was observed between the different cell categories, highlighting the robustness of the proposed method toward the cell morphology.

4 Discussion

4.1 Determination of the number of components used in multivariate curve resolution

Here, we discuss the strategy that we adopted to set the number of components to $K = 5$.

From the signal analysis point of view, we consider that the analyzed MCARS hypercube is created by various sources of information, each of them having an internal structure that can be exploited. There are many methods in the literature for solving this source separation problem. A first family of methods relies on stochastic assumptions, the main approach in this field being PCA. The latter consists in diagonalizing the covariance matrix to build a projection basis and thus decorrelate the data (specifically, the second-order moments). A second family of methods aims at providing the sparsest approximation, allowing to reconstruct the initial dataset as best as possible. A typical example is the matching pursuit (Shi et al., 2013). We position our approach in this second family of methods. As previously mentioned, in the case of MCR, the C matrix can be interpreted as the projection of original data onto a new vector basis defined by S^T, which contains K rows (i.e., K

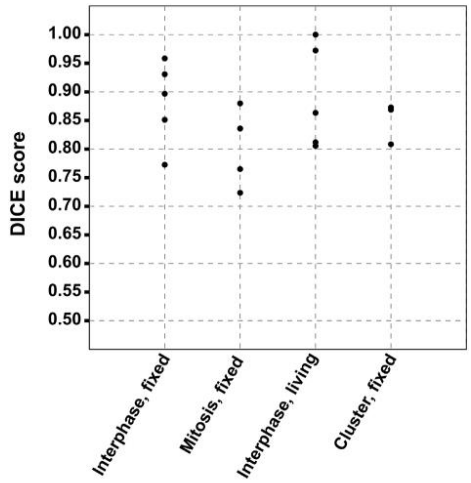

FIGURE 10
Dice coefficients according to the physiological state of the cells. The similarity was calculated between the ground truth, corresponding to the manual segmentation from bright-field images and the segmentation mask generated by the $MC^{2,5}$ method.

TABLE 1 LOF evolution according to the number of components. First row is the number of components K extracted by MCR, second row is the LOF mean μ_{LOF} (in percent), and third row is the LOF standard deviation σ_{LOF} (in percent). The corresponding curve is given in Supplementary Figure S7.

K	1	2	3	4	5	6	7	8	9	10	11	12	13	14	15
μ_{LOF} (%)	0.481	0.369	0.262	0.243	**0.214**	0.202	0.20	0.192	0.193	0.189	0.186	0.186	0.186	0.175	0.175
σ_{LOF} (%)	0.771	0.592	0.463	0.443	**0.373**	0.361	0.365	0.356	0.363	0.362	0.355	0.354	0.355	0.327	0.327

The "elbow" points are underlined, and the selected value is in bold.

components). Whichever method is chosen, a difficult question is to estimate the size of the projection space ensuring the selection of the informative components from the analyzed signal.

For the PCA approach, most of the estimators work exclusively from the eigenvalues of the covariance matrix. It is usual to use a screen test, which consists in detecting the existence of a significant decay in the eigenvalues diagram for determining the rank (the number of eigenvectors to retain). In practice, this method is not always reliable because of its subjectivity. Another method is to use the approximation error to determine the best choice of the number of components: during the iterative construction of the projection basis, the Euclidean norm of the approximation error is used in the stopping criterion. In the case of a linear transformation like conventional PCA, these two methods of rank selection are actually equivalent.

For the MCR approach, it is common practice to determine the dimension of the projection space by studying the eigenvalues of the covariance matrix—by means of PCA—before the MCR computation. However, in our case, we focus on building the best approximation of the initial dataset. Therefore, we introduce the use of the LOF to evaluate the quality of the MCR decomposition according to the value of K. In this context, the LOF mean and standard deviation, μ_{LOF} and σ_{LOF}, respectively, were calculated for the whole group of datasets considered in the present work. The elbow method (Thorndike, 1953) was then applied to determine the best value of K. Table 1 shows μ_{LOF} and σ_{LOF} with K varying from 1 to 15. The corresponding curve is plotted in Supplementary Figure S14. According to the elbow method, we derive $4 \leq K \leq 6$ with $0.243 \geq \mu_{LOF} \geq 0.202$ and $0.443 \geq \sigma_{LOF} \geq 0.361$. Given that $K = 5$ provides new information compared to $K = 4$, whereas $K = 6$ only brings redundancy, and the number of components is set to $K = 5$. As a comparison, by applying the criterion of decay of the eigenvalues, we obtain $K = 2$, which is clearly insufficient in view of the information effectively contained in the datasets. Thus, we suggest that our strategy is appropriate to realize the unsupervised exploration of the different cell samples.

4.2 Robustness and relevance of the MC² method for label-free cell imaging

For all the cells considered in this study, except those overexpressing TrkB, the first four MCR components are remarkably stable, highlighting cell common constituents (in both spectra and maps) and allowing a consistent comparison between the samples. Component #5 appears to be more specific to each studied individual condition and contains information related to this specificity, namely, cell type, step of the cell cycle, and (patho) physiological or metabolic status. In this sense, component #5 is highly relevant and confirms the capability of the MC² method to extract peculiar information. However, as this component is specific, a direct comparison of different cells (regarding component #5) is not sufficient for a reliable analysis. Hence, the use of MC² on a reference cell/condition and the subsequent projection of data obtained with different cells/conditions onto the reference spectra is particularly useful. This kind of data relativization is commonly used in biology, for example in metabolic activity assays, or for representing qRT-PCR data (ΔΔCT method). The choice of the reference cell/condition is then crucial, and modifying this choice allows to carry out a systematic and deeper analysis, considering the specificity of component #5. Of course, this approach is applicable to all components extracted by MCR. Furthermore, it is stressed that it is valid when only a unique variable is introduced in the experimental context (e.g. pharmacological treatment, ligand binding, *etc.*), as in the case of living cells overexpressing TrkB and treated or not with BDNF.

In view of the overall results presented in this work, the MC² method shows its great potential in label-free cell imaging. First, the observations made here are consistent with the previous ones using largely the same datasets (Guerenne-Del Ben et al., 2019; Guerenne-Del Ben et al., 2020). Beyond that, we could make more accurate analyses and comparisons of experimental situations, thanks to the superior unmixing of cell constituents and the extraction of additional contributions. For instance, when comparing cells in different stages of the cell cycle, it was possible to propose a better estimation of the mitotic subphase (from late prophase/prometaphase to metaphase). New information came also from the comparison of the living cell with the fixed one regarding the loss of cellular content due to the fixation. Yet, the reader should note that these findings are based on the study of individual cells to establish a proof-of-concept, and that they cannot, at this step, be generalized to cell populations.

4.3 Refinement of intracellular/intracluster analysis by the addition of a segmentation constraint (MC^{2,S} method)

As displayed in Figure 8 for the reference cell, the MC^{2,S} method performs a good extraction of the cell from its environment and improves the image contrast within the cell, allowing to refine the intracellular analysis. The use of the segmentation constraint makes the LOF increase from 0.165 to 55.6% in this case, expressing that a major part of data (the extracellular milieu) was removed. Therefore, MC^{2,S} can be of particular interest for studying intracellular events linked to a component that is in abundance in the extracellular milieu. The aqueous content, associated with components #1 and #4, is a perfect illustration of this perspective, as seen in the corresponding concentration maps (Figure 8B). In that respect, it is worth noting that the study of "biological water" can raise different view angles and interests, depending on the involved disciplinary field (interestingly outlined in Jungwirth, 2015). Anyhow, we stress that the detailed knowledge of the water state and distribution in cellular compartments would have a high (patho) physiological relevance. Moreover, several optical approaches were recently introduced for intra/extracellular water imaging, based on MCARS (Nuriya et al., 2019), stimulated Raman excited fluorescence (Shi et al., 2019), or fluorescence lifetime measurement (Rao et al., 2019). In this context, we suggest that the MC^{2,S} approach could significantly contribute to the field by taking into account both spatial and spectral dimensions from data acquisition to numerical processing. Obviously, our approach can be extended to the O-H stretching and fingerprint regions, as we already demonstrated ultra-multiplex CARS with 500–4,000 cm^{-1} coverage in previous works (Kano et al., 2019; Nuriya et al., 2019; Kaneta et al., 2021).

Finally, the potentialities offered by the MC^{2,S} method are confirmed in the case of cell clusters, whatever number of cells is considered. Here, the extraction of information is refined inside the cluster and, in particular, the water content can be clearly visualized between the cells forming the cluster. These results show that the MC^{2,S} method is also applicable to the study of biological tissues.

To conclude, this work establishes MC^{2,S} as a new methodology for MCARS hyperspectral cell imaging and segmentation, based on a simple, unsupervised workflow without any spectrum-to-spectrum phase retrieval computation. Such easy-to-use methodology, combined with the constant simplification of MCARS instrumentation, should substantially participate in disseminating coherent Raman technologies into the biomedical field.

Data availability statement

Publicly available datasets were analyzed in this study. This data can be found here: https://gitlab.xlim.fr/datacart/mc2s.

Author contributions

TG-DB prepared the samples. PL developed the custom-made MCARS system. TG-DB and PL performed the experiments. LD performed a preliminary chemometric exploration of experimental data. DB designed and implemented the numerical methods, processed all experimental data, and performed the analysis, under the supervision of DH, PC, PL, and AM. PL and AM interpreted the results. DB, PL, AM, DH, and PC wrote the manuscript; LD, J-MP, VS, ÉC, and HK reviewed it. All authors provided critical input and helped shape the research.

Funding

We acknowledge French government support managed by the National Research Agency under the Investments for the Future program, with the reference ANR-10-LABX-0074–01 Sigma-LIM.

Conflict of interest

The authors declare that the research was conducted in the absence of any commercial or financial relationships that could be construed as a potential conflict of interest.

Publisher's note

Supplementary material

The Supplementary Material for this article can be found online at: https://www.frontiersin.org/articles/10.3389/fcell.2022.933897/full#supplementary-material

References

Amigo, J. M. (2020). *Hyperspectral imaging*. Elsevier Vol. 32. Available at: https://www.sciencedirect.com/bookseries/data-handling-in-science-and-technology/vol/32.

Billecke, N., Bosma, M., Rock, W., Fleissner, F., Best, G., Schrauwen, P., et al. (2015). Perilipin 5 mediated lipid droplet remodelling revealed by coherent Raman imaging. *Integr. Biol.* 7, 467–476. doi:10.1039/c4ib00271g

Bocklitz, T., Meyer, T., Schmitt, M., Rimke, I., Hoffmann, F., von Eggeling, F., et al. (2018). Invited Article: Comparison of hyperspectral coherent Raman scattering microscopies for biomedical applications. *APL Photonics* 3, 092404. doi:10.1063/1.5030159

Camp, C. H., Jr., Bender, J. S., and Lee, Y. J. (2020). Real-time and high-throughput Raman signal extraction and processing in CARS hyperspectral imaging. *Opt. Express* 28, 20422–20437. doi:10.1364/OE.397606

Camp, C. H., Jr. (2019). pyMCR: A Python library for multivariate curve resolution analysis with alternating regression (MCR-AR). *J. Res. Natl. Inst. Stand. Technol.* 124, 1–10. doi:10.6028/jres.124.018

Capitaine, E., Ould Moussa, N., Louot, C., Bardet, S. M., Kano, H., Duponchel, L., et al. (2018). Fast epi-detected broadband multiplex CARS and SHG imaging of mouse skull cells. *Biomed. Opt. Express* 9, 245–253. doi:10.1364/BOE.9.000245

Carlton, J. G., Jones, H., and Eggert, U. S. (2020). Membrane and organelle dynamics during cell division. *Nat. Rev. Mol. Cell Biol.* 21, 151–166. doi:10.1038/s41580-019-0208-1

Chan, T. F., Sandberg, B. Y., and Vese, L. A. (2000). Active contours without edges for vector-valued images. *J. Vis. Commun. Image Represent.* 11, 130–141. doi:10.1006/jvci.1999.0442

Cheng, J. X., and Xie, X. S. (2015). Vibrational spectroscopic imaging of living systems: An emerging platform for biology and medicine. *Science* 350, aaa8870. doi:10.1126/science.aaa8870

Cicerone, M. T., Aamer, K. A., Lee, Y. J., and Vartiainen, E. (2012). Maximum entropy and time-domain Kramers-Kronig phase retrieval approaches are functionally equivalent for CARS microspectroscopy. *J. Raman Spectrosc.* 43, 637–643. doi:10.1002/jrs.3169

De Juan, A., Jaumot, J., and Tauler, R. (2014). Multivariate Curve Resolution (MCR). Solving the mixture analysis problem. *Anal. Methods* 6, 4964–4976. doi:10.1039/c4ay00571f

De Juan, A., and Tauler, R. (2021). Multivariate curve resolution: 50 years addressing the mixture analysis problem - a review. *Anal. Chim. Acta* 1145, 59–78. doi:10.1016/j.aca.2020.10.051

Dufour, A., Shinin, V., Tajbakhsh, S., Guillén-Aghion, N., Olivo-Marin, J. C., Zimmer, C., et al. (2005). Segmenting and tracking fluorescent cells in dynamic 3-D microscopy with coupled active surfaces. *IEEE Trans. Image Process.* 14, 1396–1410. doi:10.1109/tip.2005.852790

Eelbode, T., Bertels, J., Berman, M., Vandermeulen, D., Maes, F., Bisschops, R., et al. (2020). Optimization for medical image segmentation: theory and practice when evaluating with dice score or jaccard index. *IEEE Trans. Med. Imaging* 39, 3679–3690. doi:10.1109/TMI.2020.3002417

El-Mashtoly, S. F., Niedieker, D., Petersen, D., Krauss, S. D., Freier, E., Maghnouj, A., et al. (2014). Automated identification of subcellular organelles by coherent anti-Stokes Raman scattering. *Biophys. J.* 106, 1910–1920. doi:10.1016/j.bpj.2014.03.025

Freudiger, C. W., Min, W., Saar, B. G., Lu, S., Holtom, G. R., He, C., et al. (2008). Label-free biomedical imaging with high sensitivity by stimulated Raman scattering microscopy. *Science* 322, 1857–1861. doi:10.1126/science.1165758

Getreuer, P. (2012). Chan-Vese segmentation. *Image Process. Line* 2, 214–224. doi:10.5201/ipol.2012.g-cv

Ghaffari, M., Chateigner-Boutin, A. L., Guillon, F., Devaux, M. F., Abdollahi, H., Duponchel, L., et al. (2019). Multi-excitation hyperspectral autofluorescence imaging for the exploration of biological samples. *Anal. Chim. Acta* 1062, 47–59. doi:10.1016/j.aca.2019.03.003

Guerenne-Del Ben, T., Couderc, V., Duponchel, L., Sol, V., Leproux, P., and Petit, J. M. (2020). Multiplex coherent anti-Stokes Raman scattering microspectroscopy detection of lipid droplets in cancer cells expressing TrkB. *Sci. Rep.* 10, 16749. doi:10.1038/s41598-020-74021-z

Guerenne-Del Ben, T., Rajaofara, Z., Couderc, V., Sol, V., Kano, H., Leproux, P., et al. (2019). Multiplex coherent anti-Stokes Raman scattering highlights state of chromatin condensation in CH region. *Sci. Rep.* 9, 13862. doi:10.1038/s41598-019-50453-0

Hermsen, M., de Bel, T., den Boer, M., Steenbergen, E. J., Kers, J., Florquin, S., et al. (2019). Deep learning-based histopathologic assessment of kidney tissue. *J. Am. Soc. Nephrol.* 30, 1968–1979. doi:10.1681/ASN.2019020144

Hobro, A. J., and Smith, N. I. (2017). An evaluation of fixation methods: Spatial and compositional cellular changes observed by Raman imaging. *Vib. Spectrosc.* 91, 31–45. doi:10.1016/j.vibspec.2016.10.012

Hoffman, E. A., Frey, B. L., Smith, L. M., and Auble, D. T. (2015). Formaldehyde crosslinking: a tool for the study of chromatin complexes. *J. Biol. Chem.* 290, 26404–26411. doi:10.1074/jbc.R115.651679

Houhou, R., Barman, P., Schmitt, M., Meyer, T., Popp, J., Bocklitz, T., et al. (2020). Deep learning as phase retrieval tool for CARS spectra. *Opt. Express* 28, 21002–21024. doi:10.1364/OE.390413

Ichimura, T., Chiu, L., Fujita, K., Machiyama, H., Kawata, S., Watanabe, T. M., et al. (2015). Visualizing the appearance and disappearance of the attractor of differentiation using Raman spectral imaging. *Sci. Rep.* 5, 11358. doi:10.1038/srep11358

Jungwirth, P. (2015). Biological water or rather water in biology? *J. Phys. Chem. Lett.* 6, 2449–2451. doi:10.1021/acs.jpclett.5b01143

Kaneta, D., Goto, M., Hagihara, M., Leproux, P., Couderc, V., Egawa, M., et al. (2021). Visualizing intra-medulla lipids in human hair using ultra-multiplex CARS, SHG, and THG microscopy. *Analyst* 146, 1163–1168. doi:10.1039/d0an01880e

Kano, H., and Hamaguchi, H. (2005). Ultrabroadband (> 2500 cm^{-1}) multiplex coherent anti-Stokes Raman scattering microspectroscopy using a supercontinuum generated from a photonic crystal fiber. *Appl. Phys. Lett.* 86, 121113. doi:10.1063/1.1883714

Kano, H., Maruyama, T., Kano, J., Oka, Y., Kaneta, D., Guerenne, T., et al. (2019). Ultra-multiplex CARS spectroscopic imaging with 1-millisecond pixel dwell time. *OSA Contin.* 2, 1693. doi:10.1364/OSAC.2.001693

Kee, T. W., and Cicerone, M. T. (2004). Simple approach to one-laser, broadband coherent anti-Stokes Raman scattering microscopy. *Opt. Lett.* 29, 2701–2703. doi:10.1364/OL.29.002701

Kim, S. O., Kim, J., Okajima, T., and Cho, N. J. (2017). Mechanical properties of paraformaldehyde-treated individual cells investigated by atomic force microscopy and scanning ion conductance microscopy. *Nano Converg.* 4, 5. doi:10.1186/s40580-017-0099-9

Klein, K., Gigler, A. M., Aschenbrenner, T., Monetti, R., Bunk, W., Jamitzky, F., et al. (2012). Label-free live-cell imaging with confocal Raman microscopy. *Biophys. J.* 102, 360–368. doi:10.1016/j.bpj.2011.12.027

Krause, M., Radt, B., Rösch, P., and Popp, J. (2007). The investigation of single bacteria by means of fluorescence staining and Raman spectroscopy. *J. Raman Spectrosc.* 38, 369–372. doi:10.1002/jrs.1721

Lawson, C. L., and Hanson, R. J. (1974). *Solving least squares problems*. New York: Prentice-Hall.

Lee, Y. J., Vega, S. L., Patel, P. J., Aamer, K. A., Moghe, P. V., Cicerone, M. T., et al. (2014). Quantitative, label-free characterization of stem cell differentiation at the single-cell level by broadband coherent anti-Stokes Raman scattering microscopy. *Tissue Eng. Part C Methods* 20, 562–569. doi:10.1089/ten.TEC.2013.0472

Lu, F. K., Basu, S., Igras, V., Hoang, M. P., Ji, M., Fu, D., et al. (2015). Label-free DNA imaging *in vivo* with stimulated Raman scattering microscopy. *Proc. Natl. Acad. Sci. U. S. A.* 112, 11624–11629. doi:10.1073/pnas.1515121112

Masia, F., Glen, A., Stephens, P., Borri, P., and Langbein, W. (2013). Quantitative chemical imaging and unsupervised analysis using hyperspectral coherent anti-Stokes Raman scattering microscopy. *Anal. Chem.* 85, 10820–10828. doi:10.1021/ac402303g

Maška, M., Daněk, O., Garasa, S., Rouzaut, A., Muñoz-Barrutia, A., Ortiz-de-Solorzano, C., et al. (2013). Segmentation and shape tracking of whole fluorescent cells based on the Chan-Vese model. *IEEE Trans. Med. Imaging* 32, 995–1006. doi:10.1109/TMI.2013.2243463

Matthäus, C., Bird, B., Miljković, M., Chernenko, T., Romeo, M., Diem, M., et al. (2008). Chapter 10: Infrared and Raman microscopy in cell biology. *Methods Cell Biol.* 89, 275–308. doi:10.1016/S0091-679X(08)00610-9

Matthews, Q., Jirasek, A., Lum, J., Duan, X., and Brolo, A. G. (2010). Variability in Raman spectra of single human tumor cells cultured *in vitro*: correlation with cell cycle and culture confluency. *Appl. Spectrosc.* 64, 871–887. doi:10.1366/000370210792080966

Nuriya, M., Yoneyama, H., Takahashi, K., Leproux, P., Couderc, V., Yasui, M., et al. (2019). Characterization of intra/extracellular water states probed by ultrabroadband multiplex coherent anti-Stokes Raman scattering (CARS) spectroscopic imaging. *J. Phys. Chem. A* 123, 3928–3934. doi:10.1021/acs.jpca.9b03018

Palonpon, A., Ando, J., Yamakoshi, H., Dodo, K., Sodeoka, M., Kawata, S., et al. (2013). Raman and SERS microscopy for molecular imaging of live cells. *Nat. Protoc.* 8, 677–692. doi:10.1038/nprot.2013.030

Parekh, S. H., Lee, Y. J., Aamer, K. A., and Cicerone, M. T. (2010). Label-free cellular imaging by broadband coherent anti-Stokes Raman scattering microscopy. *Biophys. J.* 99, 2695–2704. doi:10.1016/j.bpj.2010.08.009

Pederson, T. (2011). The nucleolus. *Cold Spring Harb. Perspect. Biol.* 3, a000638. doi:10.1101/cshperspect.a000638

Pisapia, C., Jamme, F., Duponchel, L., and Ménez, B. (2018). Tracking hidden organic carbon in rocks using chemometrics and hyperspectral imaging. *Sci. Rep.* 8, 2396. doi:10.1038/s41598-018-20890-4

Pohling, C., Buckup, T., and Motzkus, M. (2011). Hyperspectral data processing for chemoselective multiplex coherent anti-Stokes Raman scattering microscopy of unknown samples. *J. Biomed. Opt.* 16, 021105. doi:10.1117/1.3533309

Rao, C., Verma, N. C., and Nandi, C. K. (2019). Unveiling the hydrogen bonding network of intracellular water by fluorescence lifetime imaging microscopy. *J. Phys. Chem. C* 123, 2673–2677. doi:10.1021/acs.jpcc.8b12439

Shi, L., Hu, F., and Min, W. (2019). Optical mapping of biological water in single live cells by stimulated Raman excited fluorescence microscopy. *Nat. Commun.* 10, 4764. doi:10.1038/s41467-019-12708-2

Shi, Z., Tang, W., Duren, Z., and Jiang, Z. (2013). Subspace matching pursuit for sparse unmixing of hyperspectral data. *IEEE Trans. Geosci. Remote Sens.* 52, 3256–3274. doi:10.1109/TGRS.2013.2272076

Smith, R., Wright, K. L., and Ashton, L. (2016). Raman spectroscopy: an evolving technique for live cell studies. *Analyst* 141, 3590–3600. doi:10.1039/C6AN00152A

Tan, Y., Jin, Y., Zhao, P., Wu, J., and Ren, Z. (2021). Lipid droplets contribute myogenic differentiation in C2C12 by promoting the remodeling of the acstin-filament. *Cell Death Dis.* 12, 1102. doi:10.1038/s41419-021-04273-8

Thorndike, R. L. (1953). Who belongs in the family? *Psychometrika* 18, 267–276. doi:10.1007/BF02289263

Vartiainen, E. M., Rinia, H. A., Müller, M., and Bonn, M. (2006). Direct extraction of Raman line-shapes from congested CARS spectra. *Opt. Express* 14, 3622–3630. doi:10.1364/OE.14.003622

Windig, W., and Guilment, J. (1991). Interactive self-modeling mixture analysis. *Anal. Chem.* 63, 1425–1432. doi:10.1021/ac00014a016

Zhang, D., Wang, P., Slipchenko, M. N., Ben-Amotz, D., Weiner, A. M., Cheng, J. X., et al. (2013). Quantitative vibrational imaging by hyperspectral stimulated Raman scattering microscopy and multivariate curve resolution analysis. *Anal. Chem.* 85, 98–106. doi:10.1021/ac3019119

Zumbusch, A., Holtom, G. R., and Xie, X. S. (1999). Three-dimensional vibrational imaging by coherent anti-Stokes Raman scattering. *Phys. Rev. Lett.* 82, 4142–4145. doi:10.1103/PhysRevLett.82.4142

Conclusion et perspectives

Mes activités sur le développement de sources supercontinuum ont démarré au début des années 2000, période à laquelle le fort dynamisme autour des PCF a apporté un renouveau majeur au domaine de la génération de supercontinuum. Dans ce contexte compétitif, notre positionnement à XLIM a consisté d'une part à concevoir et fabriquer nos propres PCF afin d'exploiter des mécanismes non linéaires originaux, et d'autre part à privilégier la compacité et la simplicité des systèmes en utilisant majoritairement des microlasers sub-nanoseconde comme sources de pompe. Ce positionnement nous a amenés à introduire de nouveaux schémas non linéaires pour la génération de supercontinuum, dont les plus marquants concernent l'utilisation d'une **double excitation 532/1064 nm** et l'exploitation d'un effet de **mélange à quatre ondes intermodal**. Ces deux approches ont alors permis d'obtenir des spectres à très large bande dans l'infrarouge et le visible, en couvrant notamment la région du bleu/ultraviolet, particulièrement utile pour exciter certains fluorophores d'intérêt en biologie. Également, afin de répondre à la problématique de montée en puissance des sources supercontinuum, nous avons proposé de **combiner amplification et élargissement spectral** grâce à l'utilisation d'une PCF à cœur dopé ytterbium et à double gaine microstructurée. Au-delà de la démonstration expérimentale de l'effet recherché (augmentation de la densité spectrale de puissance du supercontinuum avec la puissance de pompe multimode injectée dans la fibre), ce type de PCF présente un intérêt, d'un point de vue plus fondamental, pour l'étude de la propagation guidée non linéaire de l'onde de pompe en présence de gain terre rare.

Ces travaux autour du développement d'architectures de sources supercontinuum m'ont rapidement amené à m'intéresser aux aspects applicatifs de ces sources, notamment dans le domaine biomédical. A travers différents projets dont NextGenPCF (projet européen intégré, 2006-2010) et avec le support privilégié de la start-up Leukos (créée en 2006), j'ai pu collaborer de façon régulière avec des partenaires académiques et industriels afin de concevoir **des sources supercontinuum compactes dédiées à des applications particulières**. Les résultats les plus saillants obtenus dans ce cadre portent sur l'utilisation d'une source supercontinuum déclenchée dans un cytomètre en flux et sur le design et l'application de différentes générations de sources supercontinuum à double sortie à la microspectroscopie CARS. Dans ce dernier cas, j'ai initié en 2007 **une collaboration avec l'équipe japonaise du Pr. Kano** (université de Tokyo et par la suite universités de Tsukuba et Kyushu). Cette collaboration, toujours très active aujourd'hui, a donné lieu à de nombreux échanges de chercheurs (étudiants en master, doctorants, permanents) et à de multiples publications communes (40+ articles).

Dans la continuité de nos travaux avec le Japon, j'ai ensuite proposé de **développer au sein même d'XLIM une activité allant des sources supercontinuum jusqu'aux systèmes d'imagerie**. Pour maximiser les chances de succès de ce projet, je me suis appuyé sur le savoir-faire complémentaire, acquis auprès de nos partenaires japonais, en matière de microspectroscopie optique non linéaire. Un premier développement instrumental a été réalisé dans le cadre du projet ASTRID NEOSPRAM (2014-2018), consistant en l'implémentation de la modalité CARS multiplex

sur un appareil de microspectroscopie Raman commercial. Le système mis au point a alors permis de démontrer à XLIM l'imagerie multimodale de divers échantillons biologiques sans marquage. En particulier, le dispositif a pu être exploité de façon intensive et avec succès tout au long d'une thèse de biologie cellulaire, qui a ainsi permis de valider la méthode d'imagerie CARS proposée. A la suite de ces travaux, **le Labex Σ-LIM (2020-2025) a constitué un cadre favorable pour construire un projet plus large et pérenne** en associant des compétences supplémentaires autour de l'analyse de données et de l'intelligence artificielle (XLIM-ASALI), ainsi que des applications en chirurgie réparatrice osseuse (IRCER-Biomatériaux et CHU de Limoges), tout en conservant des relations étroites avec nos partenaires japonais. Nous avons dans ce projet l'ambition de mettre en place, dans les années à venir, **une chaîne complète d'imagerie multimodale**, *i.e.*, couvrant l'acquisition, le traitement, l'analyse et la visualisation (automatiques) des données. Cette ambition est notamment nourrie par les premiers résultats, très positifs, que nous avons pu obtenir dans le périmètre de ce nouveau consortium, pluridisciplinaire et international. S'agissant de la collaboration France-Japon, nous projetons de la poursuivre, après le PHC Sakura en cours (2023-2024), sous la forme d'un IRP (*International Research Project*) impliquant l'ensemble des partenaires.

Notre stratégie consiste enfin à renforcer ce consortium par la présence d'acteurs complémentaires comme le Centre technologique ALPhANOV et l'entreprise LEUKOS. En collaboration avec ces derniers, nous avons d'ores et déjà développé une **nouvelle version de système complet de microspectroscopie CARS**, basée sur un design modulaire et une nouvelle génération de source supercontinuum à double sortie. Ce système a été validé par différents tests de cartographie sur des échantillons variés tels que tissu adipeux, coupes végétales ou encore microplastiques. Sur ce dernier point, pour lequel un projet est en cours avec le laboratoire E2Lim (DYNAPLAST, « Dynamique des microplastiques dans l'environnement par µspectroscopie CARS », financement MITI CNRS), la rapidité de mesure déjà démontrée par le système permet d'entrevoir des perspectives intéressantes en termes d'applications dans le domaine des géosciences environnementales. Concernant la caractérisation de cibles végétales, un projet collaboratif financé par la Région Nouvelle-Aquitaine (WOODSCOPE) démarrera prochainement, visant à développer un démonstrateur d'imagerie CARS/p-SHG permettant d'effectuer sur le terrain l'analyse chimique et structurale du matériau bois (collaborations supplémentaires LABCiS et ISM). Ce projet se positionne ainsi dans un contexte de montée en TRL de nos approches de microspectroscopie multimodale sous excitation supercontinuum.

Au-delà de ces perspectives en matière d'applications, les avancées majeures dans le design instrumental et l'analyse de données devraient permettre, dans les années à venir, d'une part, de faciliter la mise en œuvre de nouveaux concepts de spectroscopie Raman cohérente (e.g., exploitation simultanée des signaux *backward* et *forward*), et d'autre part, de tirer davantage profit de la multimodalité.

Bibliographie

Aguirre, A., Nishizawa, N., Fujimoto, J., Seitz, W., Lederer, M. and Kopf, D., "Continuum generation in a novel photonic crystal fiber for ultrahigh resolution optical coherence tomography at 800 nm and 1300 nm," Opt. Express 14, 1145-1160 (2006)

Alfano, R. R. and Shapiro, S. L., "Emission in the region 4000 to 7000 Å via four-photon coupling in glass," Phys. Rev. Lett. 24, 584 (1970)

Avdokhin, A. V., Popov, S. V. and Taylor, J. R., "Continuous-wave, high-power, Raman continuum generation in holey fibers," Opt. Lett. 28, 1353-1355 (2003)

Chan, T. F., Sandberg, B. Y. and Vese, L. A., "Active contours without edges for vector-valued images," J. Vis. Commun. Image Represent. 11, 130-141 (2000)

Chernikov, S. V., Zhu, Y., Taylor, J. R. and Gapontsev, V. P., "Supercontinuum self-Q-switched ytterbium fiber laser," Opt. Lett. 22, 298-300 (1997)

Coen, S., Chau, A. H., Leonhardt, R., Harvey, J. D., Knight, J. C., Wadsworth, W. J. and Russell, P. St. J., "White-light supercontinuum generation with 60-ps pump pulses in a photonic crystal fiber," Opt. Lett. 26, 1356-1358 (2001)

Coen, S., Chau, A. H., Leonhardt, R., Harvey, J. D., Knight, J. C., Wadsworth, W. J. and Russell, P. St. J., "Supercontinuum generation by stimulated Raman scattering and parametric four-wave mixing in photonic crystal fibers," J. Opt. Soc. Am. B 19, 753-764 (2002)

De Juan, A., Jaumot, J. and Tauler, R., "Multivariate Curve Resolution (MCR). Solving the mixture analysis problem," Anal. Methods 6, 4964-4976 (2014)

De La Fuente, R., Barthelemy, A. and Froehly, C., "Spatial-soliton-induced guided waves in a homogeneous nonlinear Kerr medium," Opt. Lett. 16, 793-795 (1991)

Dudley, J. M. and Coen, S., "Coherence properties of supercontinuum spectra generated in photonic crystal and tapered optical fibers," Opt. Lett. 27, 1180-1182 (2002)

Gaeta, A. L., "Nonlinear propagation and continuum generation in microstructured optical fibers," Opt. Lett. 27, 924-926 (2002)

Heise, B., Schausberger, S. E., Häuser, S., Plank, B., Salaberger, D., Leiss-Holzinger, E. and Stifter, D., "Full-field optical coherence microscopy with a sub-nanosecond supercontinuum light source for material research," Opt. Fiber Technol. 18, 403-410 (2012)

Herrmann, J., Griebner, U., Zhavoronkov, N., Husakou, A., Nickel, D., Knight, J. C., Wadsworth, W. J., Russell, P. St. J. and Korn, G., "Experimental evidence for supercontinuum generation by fission of higher-order solitons in photonic fibers," Phys. Rev. Lett. 88, 173901 (2002)

Hilligsøe, K. M., Vestergaard Andersen, T., Nørgaard Paulsen, H., Nielsen, C. K., Mølmer, K., Keiding, S., Kristiansen, R., Hansen, K. P. and Larsen, J. J., "Supercontinuum generation in a photonic crystal fiber with two zero dispersion wavelengths," Opt. Express 12, 1045-1054 (2004)

Humbert, G., Wadsworth, W., Leon-Saval, S., Knight, J., Birks, T., Russell, P. St. J., Lederer, M., Kopf, D., Wiesauer, K., Breuer, E. and Stifter, D., "Supercontinuum generation system for optical coherence tomography based on tapered photonic crystal fibre," Opt. Express. 14, 1596-1603 (2006)

Ilev, I., Kumagai, H., Toyoda, K. and Koprinkov, I., "Highly efficient wideband continuum generation in a single-mode optical fiber by powerful broadband laser pumping," Appl. Opt. 35, 2548-2553 (1996)

Kano, H. and Hamaguchi, H., "Characterization of a supercontinuum generated from a photonic crystal fiber and its application to coherent Raman spectroscopy," Opt. Lett. 28, 2360-2362 (2003)

Kano, H. and Hamaguchi, H., "Ultrabroadband (>2500cm−1) multiplex coherent anti-Stokes Raman scattering microspectroscopy using a supercontinuum generated from a photonic crystal fiber," Appl. Phys. Lett. 86, 121113 (2005)

Kee, T. W. and Cicerone, M. T., "Simple approach to one-laser, broadband coherent anti-Stokes Raman scattering microscopy," Opt. Lett. 29, 2701-2703 (2004)

Knight, J. C., Birks, T. A., Russell, P. St. J. and Atkin, D. M., "All-silica single-mode optical fiber with photonic crystal cladding," Opt. Lett. 21, 1547-1549 (1996)

Kudlinski, A. and Mussot, A., "Visible cw-pumped supercontinuum," Opt. Lett. 33, 2407-2409 (2008)

Leon-Saval, S. G., Birks, T. A., Wadsworth, W. J., Russell, P. St. J. and Mason, M. W., "Supercontinuum generation in submicron fibre waveguides," Opt. Express 12, 2864-2869 (2004)

Mitrokhin, V. P., Fedotov, A. B., Ivanov, A. A., Alfimov, M. V. and Zheltikov, A. M., "Coherent anti-Stokes Raman scattering microspectroscopy of silicon components with a photonic-crystal fiber frequency shifter," Opt. Lett. 32, 3471-3473 (2007)

Paulsen, H. N., Hilligse, K. M., Thøgersen, J., Keiding, S. R. and Larsen, J. J., "Coherent anti-Stokes Raman scattering microscopy with a photonic crystal fiber based light source," Opt. Lett. 28, 1123-1125 (2003)

Petrov, G. I. and Yakovlev, V. V., "Enhancing red-shifted white-light continuum generation in optical fibers for applications in nonlinear Raman microscopy," Opt. Express 13, 1299-1306 (2005)

Poudel, C. and Kaminski, C. F., "Supercontinuum radiation in fluorescence microscopy and biomedical imaging applications," J. Opt. Soc. Am. B 36, A139-A153 (2019)

Price, J. H. V., Furusawa, K., Monro, T. M., Lefort, L. and Richardson, D. J., "Tunable, femtosecond pulse source operating in the range 1.06-1.33 µm based on an Yb^{3+}-doped holey fiber amplifier," J. Opt. Soc. Am. B 19, 1286-1294 (2002)

Provino, L., Dudley, J. M., Maillotte, H., Grossard, N., Windeler, R. S. and Eggleton, B. J., "Compact broadband continuum source based on microchip laser pumped microstructured fibre," Electron. Lett. 37, 558-560 (2001)

Ranka, J., Windeler, R. and Stentz, A., "Visible continuum generation in air-silica microstructure optical fibers with anomalous dispersion at 800 nm," Opt. Lett. 25, 25-27 (2000)

Sordillo, L. A., Pu, Y., Pratavieira, S., Budansky, Y. and Alfano, R. R., "Deep optical imaging of tissue using the second and third near-infrared spectral windows," J. Biomed. Opt. 19, 056004 (2014)

Swanson, E. A., Huang, D., Hee, M. R., Fujimoto, J. G., Lin, C. P. and Puliafito, C. A., "High-speed optical coherence domain reflectometry," Opt. Lett. 17, 151-153 (1992)

Telford, W. G., Subach, F. V. and Verkhusha, V. V., "Supercontinuum white light lasers for flow cytometry," Cytometry A 75, 450-459 (2009)

Travers, J. C., Popov, S. V. and Taylor, J. R., "Extended blue supercontinuum generation in cascaded holey fibers," Opt. Lett. 30, 3132-3134 (2005)

Travers, J. C., Rulkov, A. B., Cumberland, B. A., Popov, S. V. and Taylor, J. R., "Visible supercontinuum generation in photonic crystal fibers with a 400 W continuous wave fiber laser," Opt. Express 16, 14435-14447 (2008)

Vartiainen, E. M., Rinia, H. A., Müller, M. and Bonn, M., "Direct extraction of Raman line-shapes from congested CARS spectra," Opt. Express 14, 3622-3630 (2006)

Wadsworth, W. J., Joly, N., Knight, J. C., Birks, T. A., Biancalana, F. and Russell, P. St. J., "Supercontinuum and four-wave mixing with Q-switched pulses in endlessly single-mode photonic crystal fibres," Opt. Express 12, 299-309 (2004)

Wang, L., Fu, R., Xu, C. and Xu, M., "Methods and applications of full-field optical coherence tomography: a review," J. Biomed. Opt. 27, 050901 (2022)

Yadav, R., Lee, K. S., Rolland, J. P., Zavislan, J. M., Aquavella, J. V. and Yoon, G., "Micrometer axial resolution OCT for corneal imaging," Biomed. Opt. Express 2, 3037-3046 (2011)

Zumbusch, A., Holtom, G. R. and Xie, X. S., "Three-dimensional vibrational imaging by coherent anti-Stokes Raman scattering," Phys. Rev. Lett. 82, 4142 (1999)

Liste des publications

[1] *Theoretical and experimental study of loss at splices between standard single-mode fibres and Er-doped fibres versus direction*
P. Leproux, P. Roy, D. Pagnoux, B. Kerrinckx, J. Marcou
Optics Communications, vol. 174, pp. 419-425, 2000

[2] *Analysis of the bandpass filtering behaviour of a single-mode depressed-core-index photonic-band-gap fibre*
F. Brechet, **P. Leproux**, P. Roy, J. Marcou and D. Pagnoux
Electronics Letters, vol. 36, no. 10, pp. 870-872, 2000

[3] *Modeling and optimization of double clad fiber amplifiers using chaotic propagation of the pump*
P. Leproux, S. Fevrier, V. Doya, P. Roy, D. Pagnoux
Optical Fiber Technology, vol. 7, no. 4, pp. 324-339, 2001

[4] *Influence of mode orientations on power transfer at misaligned fibre connections*
C. Simos, **P. Leproux**, P. Di Bin, P. Facq
Journal of Optics A : Pure and Applied Optics, vol. 4, no. 1, pp. 8-15, 2002

[5] *Experimental study of pump power absorption along rare-earth-doped double clad optical fibres*
P. Leproux, V. Doya, P. Roy, D. Pagnoux, F. Mortessagne, O. Legrand
Optics Communications, vol. 218, pp. 249-254, 2003

[6] *Very large effective area singlemode photonic bandgap fibre*
S. Février, P. Viale, F. Gérôme, **P. Leproux**, P. Roy, J.-M. Blondy, B. Dussardier, G. Monnom
Electronics Letters, vol. 39, no. 17, pp.1240-1242, 2003

[7] *White-light supercontinuum generation in normally dispersive optical fiber using original multi-wavelength pumping system*
P. A. Champert, V. Couderc, **P. Leproux**, S. Février, V. Tombelaine, L. Labonté, P. Roy, C. Froehly, P. Nérin
Optics Express, vol. 12, no. 19, pp. 4366-4371, 2004

[8] *Spatial filtering efficiency of single-mode optical fibers for stellar interferometry applications: phenomenological and numerical study*
G. Huss, **P. Leproux**, F. Reynaud, V. Doya
Optics Communications, vol. 244, pp. 209-217, 2005

[9] *Ultra wide band supercontinuum generation in air-silica holey fibers by SHG-induced modulation instabilities*
V. Tombelaine, C. Lesvigne, **P. Leproux**, L. Grossard, V. Couderc, J. L. Auguste, J. M. Blondy, G. Huss, P. H. Pioger
Optics Express, vol. 13, no. 19, pp. 7399-7404, 2005

[10] *Raman cascade suppression by using wide band parametric conversion in large normal dispersion regime*
V. Couderc, **P. Leproux**, V. Tombelaine, L. Grossard, A. Barthélémy
Optics Express, vol. 13, no. 21, pp. 8584-8590, 2005

[11] *Photonic crystal fibres for lasers and amplifiers*
P. Roy, **P. Leproux**, S. Février, D. Pagnoux, J. L. Auguste, J. M. Blondy, S. Hilaire, L. Lavoute, R. Jamier, A. Desfarges-Berthelemot, V. Kermène, C. Restoin
Comptes rendus de l'Académie des Sciences, 2006

[12] *Modal properties of solid-core photonic bandgap fibers*
P. Viale, S. Février, **P. Leproux**, Y. Jaouën, A. F. Obaton
Photonics and Nanostructures – Fundamentals and Applications, vol. 4, pp. 116-122, 2006

[13] *Stable mode-locked operation of a low repetition rate diode-pumped Nd:GdVO4 laser by combining quadratic polarisation switching and a semiconductor saturable absorber mirror*
C. Gerhard, F. Druon, P. Georges, V. Couderc, **P. Leproux**
Optics Express, vol. 14, no. 16, pp. 7093-7098, 2006

[14] *Visible supercontinuum generation in holey fibers by dual-wavelength subnanosecond pumping*
V. Tombelaine, **P. Leproux**, V. Couderc, A. Barthélémy
Photonics Technology Letters, vol. 18, no. 23, pp. 2466-2468, 2006

[15] *Compact subnanosecond wide band laser source for biological applications*
M. Laroche, **P. Leproux**, V. Couderc, C. Lesvigne, H. Gilles, S. Girard
Applied Physics B, vol. 86, no. 4, pp. 601-604, 2007

[16] *Supercontinuum generation in a nonlinear Yb-doped double-clad microstructured fibre*
A. Roy, **P. Leproux**, P. Roy, J. L. Auguste, V. Couderc
Journal of the Optical Society of America B, vol. 24, no. 4, pp. 788-791, 2007

[17] *Visible supercontinuum generation controlled by intermodal four-wave mixing in micro-structured fibre*
C. Lesvigne, V. Couderc, A. Tonello, **P. Leproux**, A. Barthélémy, S. Lacroix, F. Druon, P. Blandin, M. Hanna, P. Georges
Optics Letters, vol. 32, no. 15, pp. 2173-2175, 2007

[18] *High spectral power density supercontinuum generation in a nonlinear fiber amplifier*
P. H. Pioger, V. Couderc, **P. Leproux**, P. A. Champert
Optics Express, vol. 15, no. 18, pp. 11358-11363, 2007

[19] *Ultrabroadband (>2000 cm−1) multiplex coherent anti-Stokes Raman scattering spectroscopy using a subnanosecond supercontinuum light source*
M. Okuno, H. Kano, **P. Leproux**, V. Couderc, H. Hamaguchi
Optics Letters, vol. 32, no. 20, pp. 3050-3052, 2007

[20] *Q-switched Yb-doped nonlinear microstructured fiber laser for the emission of broadband spectrum*
A. Roy, M. Laroche, P. Roy, **P. Leproux**, J. L. Auguste
Optics Letters, vol. 32, no. 22, pp. 3299-3301, 2007

[21] *Broadband ultrafast spectroscopy using a photonic crystal fiber: application to the photophysics of malachite green*
J. Léonard, N. Lecong, J. -P. Likforman, O. Crégut, S. Haacke, P. Viale, **P. Leproux**, V. Couderc
Optics Express, vol. 15, no. 24, pp. 16124-16129, 2007

[22] *Microstructured fibers with highly nonlinear materials*
K. Schuster, J. Kobelke, S. Grimm, A. Schwuchow, J. Kirchhof, H. Bartelt, A. Gebhardt, **P. Leproux**, V. Couderc, W. Urbanczyk
Optical and Quantum Electronics, published online first, 2007

[23] *Spectroscopic OCT by grating based temporal correlation coupled to optical spectral analysis*
L. Froehly, M. Ouadour, L. Furfaro, P. Sandoz, **P. Leproux**, G. Huss, V. Couderc
International Journal of Biomedical Imaging, ID 752340, 2008

[24] *Ultrabroadband multiplex CARS microspectroscopy and imaging using a subnanosecond supercontinuum light source in the deep near infrared*
M. Okuno, H. Kano, **P. Leproux**, V. Couderc, H. -o. Hamaguchi
Optics Letters, vol. 33, no. 9, pp. 923-925, 2008

[25] *Optical poling in germanium-doped microstructured optical fiber for visible supercontinuum generation*
V. Tombelaine, C. Buy-Lesvigne, **P. Leproux**, V. Couderc, G. Mélin
Optics Letters, vol. 33, no. 17, pp. 2011-2013, 2008

[26] *Picosecond polarized supercontinuum generation controlled by intermodal four-wave mixing for fluorescence lifetime imaging microscopy*
P. Blandin, F. Druon, M. Hanna, S. Lévêque-Fort, C. Lesvigne, V. Couderc, **P. Leproux**, A. Tonello, P. Georges
Optics Express, vol. 16, no. 23, pp. 18844-18849, 2008

[27] *BPM-Numerical Study of Microstructured Fiber with High Difference Index Profile*
L. Lavoute, A. Roy, **P. Leproux**, P. Roy, E. Suran
Journal of Lightwave Technology, vol. 26, no. 18, pp. 3261-3268, 2008

[28] *Controlling intermodal four-wave mixing from the design of microstructured optical fibers*
A. Labruyere, A. Martin, **P. Leproux**, V. Couderc, A. Tonello, N. Traynor
Optics Express, vol. 16, no. 26, pp. 21997-22002, 2008

[29] *Nonlinear photonic crystal fiber with a structured multi-component glass core for four-wave mixing and supercontinuum generation*
V. Tombelaine, A. Labruyère, J. Kobelke, K. Schuster, V. Reichel, **P. Leproux**, V. Couderc, R. Jamier, H. Bartelt
Optics Express, vol. 17, no. 18, pp. 15392-15401, 2009

[30] *Unprecedented Raman cascading and four-wave mixing from second harmonic generation in optical fiber*
V. Couderc, A. Tonello, C. Buy-Lesvigne, **P. Leproux**, L. Grossard
Optics Letters, vol. 35, no. 2, pp. 145-147, 2010

[31] *Highly germanium and lanthanum modified silica based glasses in microstructured optical fibers for nonlinear applications*
J. Kobelke, K. Schuster, D. Litzkendorf , A. Schwuchow, J. Kirchhof, V. Tombelaine, H. Bartelt, **P. Leproux**, V. Couderc, A. Labruyere, R. Jamier
Optical Materials, vol. 32, no. 9, pp. 1002-1006, 2010

[32] *Quantitative CARS molecular fingerprinting of single living cells with the use of the maximum entropy method*
M. Okuno, H. Kano, **P. Leproux**, V. Couderc, J. P. R. Day, M. Bonn, H. Hamaguchi
Angewandte Chemie International Edition, vol. 49, no. 38, pp. 6773-6777, 2010

[33] A. Labruyère, **P. Leproux**, V. Couderc, V. Tombelaine, J. Kobelke, K. Schuster, H. Bartelt, S. Hilaire, G. Huss, G. Mélin
Photonics Technology Letters, vol. 22, no. 16, pp. 1259-1261, 2010

[34] *Nonlinear pulse reshaping with highly birefringent photonic crystal fiber for OCDMA receivers*
I. Fsaifes, S. Cordette, A. Tonello, V. Couderc, C. Lepers, C. Ware, **P. Leproux**, C. Buy-Lesvigne
Photonics Technology Letters, vol. 22, no. 18, pp. 1367-1369, 2010

[35] *Blue-extended sub-nanosecond supercontinuum generation in simply designed nonlinear microstructured optical fibers*
D. Ghosh, S. Roy, M. Pal, **P. Leproux**, P. Viale, V. Tombelaine, S. K. Bhadra
Journal of Lightwave Technology, vol. 29, no. 2, pp. 146-152, 2011

[36] *New opportunities offered by compact sub-nanosecond supercontinuum sources in ultrabroadband multiplex CARS microspectroscopy*
P. Leproux, V. Couderc, A. de Angelis, M. Okuno, H. Kano, H. Hamaguchi
Journal of Raman Spectroscopy, vol. 42, no. 10, pp. 1871-1874, 2011

[37] *Protein secondary structure imaging with ultrabroadband multiplex coherent anti-Stokes Raman scattering (CARS) microspectroscopy*
K. Bito, M. Okuno, H. Kano, S. Tokuhara, S. Naito, Y. Masukawa, **P. Leproux**, V. Couderc, H. Hamaguchi
The Journal of Physical Chemistry B, vol. 116, no. 4, pp. 1452-1457, 2012

[38] *Label-free tetra-modal molecular imaging of living cells with CARS, SHG, THG and TSFG (coherent anti-Stokes Raman scattering, second harmonic generation, third harmonic generation and third-order sum frequency generation)*
H. Segawa, M. Okuno, H. Kano, **P. Leproux**, V. Couderc, H. Hamaguchi
Optics Express, vol. 20, no. 9, pp. 9551-9557, 2012

[39] *Control of near-infrared supercontinuum bandwidth by adjusting pump pulse duration*
M. Andreana, A. Labruyère, A. Tonello, S. Wabnitz, **P. Leproux**, V. Couderc, C. Duterte, A. Cserteg, A. Bertrand, Y. Hernandez, D. Giannone, S. Hilaire, G. Huss
Optics Express, vol. 20, no. 10, pp. 10750-10760, 2012

[40] *Flow cytometer based on triggered supercontinuum laser illumination*
N. Rongeat, **P. Leproux**, V. Couderc, P. Brunel, S. Ledroit, D. Cremien, S. Hilaire, G. Huss, P. Nérin
Cytometry Part A, vol. 81, no. 7, pp. 611-617, 2012

[41] *Observation of Raman optical activity by heterodyne-detected polarization-resolved coherent anti-Stokes Raman scattering*
K. Hiramatsu, M. Okuno, H. Kano, **P. Leproux**, V. Couderc, H. Hamaguchi
Physical Review Letters, vol. 109, no. 8, 083901, 2012

[42] *Quantitative coherent anti-Stokes Raman scattering microspectroscopy using a nanosecond supercontinuum light source*
M. Okuno, H. Kano, **P. Leproux**, V. Couderc, H. Hamaguchi
Optical Fiber Technology, vol. 18, no. 5, pp. 388-393, 2012

[43] Second and third order susceptibilities mixing for supercontinuum generation and shaping
F. Baronio, M. Conforti, C. De Angelis, D. Modotto, S. Wabnitz, M. Andreana, A. Tonello, **P. Leproux**, V. Couderc
Optical Fiber Technology, vol. 18, no. 5, pp. 283-289, 2012

[44] *Compact supercontinuum sources and their biomedical applications*
A. Labruyère, A. Tonello, V. Couderc, G. Huss, **P. Leproux**
Optical Fiber Technology, vol. 18, no. 5, pp. 375-378, 2012

[45] *Time-frequency resolved analysis of a nanosecond supercontinuum source dedicated to multiplex CARS application*
A. De Angelis, A. Labruyère, V. Couderc, **P. Leproux**, A. Tonello, H. Segawa, M. Okuno, H. Kano, D. Arnaud-Cormos, P. Lévèque, H. Hamaguchi
Optics Express, vol. 20, no. 28, pp. 29705-29716, 2012

[46] *Three-pulse multiplex coherent anti-Stokes/Stokes Raman scattering (CARS/CSRS) microspectroscopy using a white-light laser source*
K. Bito, M. Okuno, H. Kano, **P. Leproux**, V. Couderc, H. Hamaguchi
Chemical Physics, vol. 419, pp. 156-162, 2013

[47] *Frequency-dissymmetric parametric sideband generation in a microstructured fiber*
M. Barbier, **P. Leproux**, P. Roy, P. Delaye
Journal of the Optical Society of America B, vol. 30, no. 11, pp. 2889-2897, 2013

[48] *Chemical imaging of lipid droplets in muscle tissues using hyperspectral coherent Raman microscopy*
N. Billecke, G. Rago, M. Bosma, G. Eijkel, A. Gemmink, **P. Leproux**, G. Huss, P. Schrauwen, M. K. C. Hesselink, M. Bonn, S. H. Parekh
Histochemistry and Cell Biology, vol. 141, no. 3, pp. 263-273, 2014

[49] *Surfactant uptake dynamics in mammalian cells elucidated with quantitative coherent anti-Stokes Raman scattering microspectroscopy*
M. Okuno, H. Kano, K. Fujii, K. Bito, S. Naito, **P. Leproux**, V. Couderc, H. Hamaguchi
Plos One, vol. 9, no. 4, e93401, 2014

[50] *Electronically resonant third-order sum frequency generation spectroscopy using a nanosecond white-light supercontinuum*
H. Segawa, N. Fukutake, **P. Leproux**, V. Couderc, T. Ozawa, H. Kano
Optics Express, vol. 22, no. 9, pp. 10416-10429, 2014

[51] *Linear and nonlinear Raman microspectroscopy: History, instrumentation, and applications*
H. Kano, H. Segawa, **P. Leproux**, V. Couderc
Optical Review, vol. 21, no. 6, pp. 752-761, 2014

[52] *Near-infrared supercontinuum laser beam source in the second and third near-infrared optical windows used to image more deeply through thick tissue as compared with images from a lamp source*
L. A. Sordillo, L. Lindwasser, Y. Budansky, **P. Leproux**, R. R. Alfano
Journal of Biomedical Optics, vol. 20, no. 3, 030501, 2015

[53] *Multimodal Imaging of Living Cells with Multiplex Coherent Anti-stokes Raman Scattering (CARS), Third-order Sum Frequency Generation (TSFG) and Two-photon Excitation Fluorescence (TPEF) Using a Nanosecond White-light Laser Source*
H. Segawa, M. Okuno, **P. Leproux**, V. Couderc, T. Ozawa, H. Kano
Analytical Sciences, vol. 31, no. 4, pp. 299-305, 2015

[54] *Efficiency of dispersive wave generation in dual concentric core microstructured fiber*
D. Modotto, M. Andreana, K. Krupa, G. Manili, U. Minoni, A. Tonello, V. Couderc, A. Barthélémy, A. Labruyère, B. M. Shalaby, **P. Leproux**, S. Wabnitz, A. B. Aceves
Journal of the Optical Society of America B, vol. 32, no. 8, pp. 1676-1685, 2015

[55] *Multimodal and multiplex spectral imaging of rat cornea ex vivo using a white-light laser source*
H. Segawa, Y. Kaji, **P. Leproux**, V. Couderc, T. Ozawa, T. Oshika, H. Kano
Journal of Biophotonics, vol. 8, no. 9, pp. 705-713, 2015

[56] *Raman optical activity spectroscopy by visible-excited coherent anti-Stokes Raman scattering*
K. Hiramatsu, **P. Leproux**, V. Couderc, T. Nagata, H. Kano
Optics Letters, vol. 40, no. 17, pp. 4170-4173, 2015

[57] *Hyperspectral coherent Raman imaging–principle, theory, instrumentation, and applications to life sciences*
H. Kano, H. Segawa, M. Okuno, **P. Leproux**, V. Couderc
Journal of Raman Spectroscopy, vol. 47, no. 1, pp. 116-123, 2016

[58] *Supercontinuum generation in an ytterbium-doped photonic crystal fiber for CARS spectroscopy*
C. Louot, B. M. Shalaby, E. Capitaine, S. Hilaire, **P. Leproux**, D. Pagnoux, V. Couderc
IEEE Photonics Technology Letters, vol. 28, no. 19, pp. 2011-2014, 2016

[59] *Multicolor multiphoton microscopy based on a nanosecond supercontinuum laser source*
C. Lefort, R. P. O'Connor, V. Blanquet, L. Magnol, H. Kano, V. Tombelaine, P. Lévêque, V. Couderc, **P. Leproux**
Journal of Biophotonics, vol. 9, no. 7, pp. 709-714, 2016

[60] *Dynamical study of the water penetration process into a cellulose acetate film studied by coherent anti-Stokes Raman scattering (CARS) microspectroscopy*
R. Fujisawa, T. Ohno, J. F. Kaneyasu, **P. Leproux**, V. Couderc, H. Kita, H. Kano
Chemical Physics Letters, vol. 655, pp. 86-90, 2016

[61] *Spectro-temporal shaping of supercontinuum for subnanosecond time-coded M-CARS spectroscopy*
B. M. Shalaby, C. Louot, E. Capitaine, K. Krupa, A. Labruyère, A. Tonello, D. Pagnoux, **P. Leproux**, V. Couderc
Optics Letters, vol. 41, no. 21, pp. 5007-5010, 2016

[62] *Spatiotemporal characterization of supercontinuum extending from the visible to the mid-infrared in a multimode graded-index optical fiber*
K. Krupa, C. Louot, V. Couderc, M. Fabert, R. Guénard, B. M. Shalaby, A. Tonello, D. Pagnoux, **P. Leproux**, A. Bendahmane, R. Dupiol, G. Millot, S. Wabnitz
Optics Letters, vol. 41, no. 24, pp. 5785-5788, 2016

[63] *Coherent anti-Stokes Raman scattering under electric field stimulation*
E. Capitaine, N. Ould Moussa, C. Louot, C. Lefort, D. Pagnoux, J. R. Duclère, J. F. Kaneyasu, H. Kano, L. Duponchel, V. Couderc, **P. Leproux**
Physical Review B, vol. 94, no. 24, 245136, 2016

[64] *Identification of intracellular squalene in living algae, Aurantiochytrium mangrovei with hyper-spectral coherent anti-Stokes Raman microscopy using a sub-nanosecond supercontinuum laser source*
K. Ishitsuka, M. Koide, M. Yoshida, H. Segawa, **P. Leproux**, V. Couderc, M. M. Watanabe, H. Kano
Journal of Raman Spectroscopy, vol. 48, no. 1, pp. 8-15, 2017

[65] *Effect of a stretching procedure on the penetration process of water into a cellulose acetate film by coherent anti-Stokes Raman scattering (CARS) microspectroscopy*
R. Fujisawa, T. Ohno, **P. Leproux**, V. Couderc, K. Fukusaka, H. Kita, H. Kano
Chemistry Letters, vol. 46, no. 1, pp. 92-94, 2017

[66] *SHG-specificity of cellular Rootletin filaments enables naive imaging with universal conservation*
T. Akiyama, A. Inoko, Y. Kaji, S. Yonemura, K. Kakiguchi, H. Segawa, K. Ishitsuka, M. Yoshida, O. Numata, **P. Leproux**, V. Couderc, T. Oshika, H. Kano
Scientific Reports, vol. 7, no. 1, pp. 1-12, 2017

[67] *Effect of a waterproofing agent on the penetration process of water into a cellulose acetate film by time-resolved coherent anti-Stokes Raman scattering (CARS) microspectroscopy*
R. Fujisawa, T. Ohno, **P. Leproux**, V. Couderc, K. Fukusaka, H. Kita, H. Kano
Chemistry Letters, vol. 46, no. 6, pp. 833-836, 2017

[68] *Fast epi-detected broadband multiplex CARS and SHG imaging of mouse skull cells*
E. Capitaine, N. Ould Moussa, C. Louot, S. M. Bardet, H. Kano, L. Duponchel, P. Lévêque, V. Couderc, **P. Leproux**
Biomedical Optics Express, vol. 9, no. 1, pp. 245-253, 2018

[69] *Ultrabroadband multiplex coherent anti-Stokes Raman scattering (CARS) microspectroscopy using a CCD camera with an InGaAs image intensifier*
R. Fujisawa, T. Iwamura, **P. Leproux**, V. Couderc, H. Okada, H. Kano
Chemistry Letters, vol. 47, no. 6, pp. 704-707, 2018

[70] *CARS molecular fingerprinting using sub-100-ps microchip laser source with fiber amplifier (invited article)*
H. Yoneyama, K. Sudo, **P. Leproux**, V. Couderc, A. Inoko, H. Kano
APL Photonics, vol. 3, no. 9, 092408, 2018

[71] *Characterization of intra/extracellular water states probed by ultrabroadband multiplex coherent anti-stokes Raman scattering (CARS) spectroscopic imaging*
M. Nuriya, H. Yoneyama, K. Takahashi, **P. Leproux**, V. Couderc, M. Yasui, H. Kano
The Journal of Physical Chemistry A, vol. 123, no. 17, pp. 3928-3934, 2019

[72] *Ultra-multiplex CARS spectroscopic imaging with 1-millisecond pixel dwell time*
H. Kano, T. Maruyama, J. Kano, Y. Oka, D. Kaneta, T. Guerenne, **P. Leproux**, V. Couderc, M. Noguchi
OSA Continuum, vol. 2, no. 5, pp. 1693-1705, 2019

[73] *Spatial beam self-cleaning and supercontinuum generation with Yb-doped multimode graded-index fiber taper based on accelerating self-imaging and dissipative landscape*
A. Niang, T. Mansuryan, K. Krupa, A. Tonello, M. Fabert, **P. Leproux**, D. Modotto, O. N. Egorova, A. E. Levchenko, D. S. Lipatov, S. L. Semjonov, G. Millot, V. Couderc, S. Wabnitz
Optics Express, vol. 27, no. 17, pp. 24018-24028, 2019

[74] *Multiplex coherent anti-Stokes Raman scattering highlights state of chromatin condensation in CH region*
T. Guerenne-Del Ben, Z. Rajaofara, V. Couderc, V. Sol, H. Kano, **P. Leproux**, J. M. Petit
Scientific Reports, vol. 9, no. 1, pp. 1-10, 2019

[75] *Measurement of the third order nonlinear susceptibility of paratellurite single crystal using multiplex CARS*
Z. Rajaofara, **P. Leproux**, E. Capitaine, H. Kano, T. Hayakawa, P. Thomas, J. R. Duclère, V. Couderc
AIP Advances, vol. 9, no. 10, 105301, 2019

[76] *Photo-induced meta-stable polar conformations in polystyrene microspheres revealed by time-resolved SHG microscopy*
K. Makihara, D. Kaneta, T. Iwamura, A. Sugita, **P. Leproux**, V. Couderc, H. Kano
Applied Physics Express, vol. 13, no. 5, 052003, 2020

[77] *Multimodal nonlinear optical imaging of Caenorhabditis elegans with multiplex coherent anti-Stokes Raman scattering, third-harmonic generation, second-harmonic generation, and two-photon excitation fluorescence*
S. Miyazaki, **P. Leproux**, V. Couderc, Y. Hayashi, H. Kano
Applied Physics Express, vol. 13, no. 7, 072002, 2020

[78] *Multiplex coherent anti-Stokes Raman scattering microspectroscopy detection of lipid droplets in cancer cells expressing TrkB*
T. Guerenne-Del Ben, V. Couderc, L. Duponchel, V. Sol, **P. Leproux**, J. M. Petit
Scientific Reports, vol. 10, no. 1, pp. 1-12, 2020

[79] *Visualizing intra-medulla lipids in human hair using ultra-multiplex CARS, SHG, and THG microscopy*
D. Kaneta, M. Goto, M. Hagihara, **P. Leproux**, V. Couderc, M. Egawa, H. Kano
Analyst, vol. 146, no. 4, pp. 1163-1168, 2021

[80] *Visualization of water concentration distribution in human skin by ultra-multiplex coherent anti-Stokes Raman scattering (CARS) microscopy*
D. Kaneta, M. Kimura, **P. Leproux**, V. Couderc, M. Goto, M. Egawa, H. Kano
Applied Physics Express, vol. 14, no. 4, 042010, 2021

[81] *Visualization of intracellular lipid metabolism in brown adipocytes by time-lapse ultra-multiplex CARS microspectroscopy with an onstage incubator*
Y. Takei, R. Hirai, A. Fukuda, S. Miyazaki, R. Shimada, Y. Okamatsu-Ogura, M. Saito, **P. Leproux**, K. Hisatake, H. Kano
The Journal of Chemical Physics, vol. 155, no. 12, 125102, 2021

[82] *Mapping the second and third order nonlinear susceptibilities in a thermally poled microimprinted niobium borophosphate glass*
Z. Rajaofara, **P. Leproux**, M. Dussauze, A. Tonello, V. Rodriguez, L. Karam, H. Kano, J. R. Duclère, V. Couderc
Optical Materials Express, vol. 11, no. 10, pp. 3411-3420, 2021

[83] *Label-free detection of polysulfides and glycogen of Cyanidium caldarium using ultra-multiplex coherent anti-Stokes Raman scattering microspectroscopy*
Y. Oka, M. Yoshida, A. Minoda, **P. Leproux**, M. M. Watanabe, H. Kano
Journal of Raman Spectroscopy, vol. 52, no. 12, pp. 2572-2580, 2021

[84] *Coherent anti-Stokes Raman scattering cell imaging and segmentation with unsupervised data analysis*
D. Boildieu, T. Guerenne-Del Ben, L. Duponchel, V. Sol, J. M. Petit, E. Champion, H. Kano, D. Helbert, A. Magnaudeix, **P. Leproux**, P. Carré
Frontiers in Cell and Developmental Biology, vol. 10, 933897, 2022

[85] *Label-free visualization of cellular response to molecularly targeted agents using multiplex coherent anti-Stokes Raman scattering and third harmonic generation microscopy*
Y. Oka, L.T. W. Shen, T. Mori, T. Iwamura, **P. Leproux**, S. Matsusaka, H. Kano
Applied Physics Express, vol. 15, no. 10, 102001, 2022

[86] *Label-free identification of spore-forming bacteria using ultrabroadband multiplex coherent anti-Stokes Raman scattering microspectroscopy*
K. Tanaka, R. Oketani, T. Terada, **P. Leproux**, Y. Morono, H. Kano
The Journal of Physical Chemistry B, vol. 127, no. 9, pp. 1940-1946, 2023

[87] *Backward multiplex coherent anti-Stokes Raman (CARS) spectroscopic imaging with electron-multiplying CCD (EM-CCD) camera*
Y. Murakami, M. Yoshimura, W. J. N. Klement, A. Oda, R. Sakamoto, M. Yakabe, A. Matsumoto, R. Oketani, **P. Leproux**, J. Ikenouchi, W. R. Browne, H. Kano
Optics Continuum, vol. 2, no. 9, pp. 2044-2054, 2023

Annexe 1 : liste des conférences invitées

[CI_1] *Original holey fibres and nonlinear schemes for supercontinuum generation*
P. Leproux, V. Couderc, P. Roy, C. Lesvigne, A. Roy, V. Tombelaine, J. L. Auguste, J. M. Blondy
Optics and Optoelectronics (SPIE), Prague, Czech Republic, paper 6588-06, 2007

[CI_2] *Microstructured fibres and applications*
P. Roy, L. Lavoute, S. Février, J. L. Auguste, J. M. Blondy, D. Gaponov, M. Devautour, A. Roy, **P. Leproux**, L. Bigot, G. Bouwmans, V. Pureur
CLEO/Europe-IQEC, Munich, Germany, paper CJ5-3-THU, 2007

[CI_3] *Phase matched and phase unmatched second harmonic generation in optical fibres*
V. Couderc, C. Lesvigne, **P. Leproux**, V. Tombelaine, G. Mélin, A. Fleureau, S. Lempereur, A. Galkovsky
IEEE LEOS, 20th annual meeting, Lake Buena Vista, Florida, 2007

[CI_4] *Continuum source and adaptive spectral selection for nonlinear imaging system and fluorescence analysis*
V. Couderc, D. Bouyge, A. Crunteanu, **P. Leproux**, P. Blondy, M. Okuno, H. Kano, H. Hamaguchi
Optical Complex Systems, Cannes, France, session H, 2008

[CI_5] *Recent developments in microstructured optical fibres and optical fibre glasses*
J. M. Blondy, F. Gérôme, J. L. Auguste, C. Restoin, G. Humbert, P. Roy, **P. Leproux**, S. Février
Optical Fibre Sensors, Perth, Australia, 2008

[CI_6] *Active optical fibers: new design and alternative method of fabrication*
P. Roy, M. Devautour, L. Lavoute, S. Février, G. Humbert, **P. Leproux**, A. Roy, R. Jamier, F. Gérôme, K. Schuster, J. Kobelke, S. Grimm, C. Pedrido, F. Sandoz
Photonics, New Delhi, India, session WE2, 2008

[CI_7] *Microstructured fibers with high lanthanum oxide glass core for nonlinear applications*
J. Kobelke, K. Schuster, D. Litzkendorf, A. Schwuchow, J. Kirchhof, H. Bartelt, V. Tombelaine, **P. Leproux**, V. Couderc, A. Labruyère
Optics + Optoelectronics (SPIE), Prague, Czech Republic, paper 7357-1, 2009

[CI_8] *New biomedical opportunities offered by compact sub-nanosecond supercontinuum sources*
P. Leproux, V. Couderc, A. Labruyère, M. Andreana, A. de Angelis
Photonics, Guwahati, India, session M1B, 2010

[CI_9] *Sub-nanosecond fibre-based supercontinuum sources and their biomedical applications*
P. Leproux, V. Couderc, G. Huss
International Laser Physics Workshop (LPHYS'11), Sarajevo, Bosnia and Herzegovina, Seminar 8.5, paper 8.5.1, 2011

[CI_10] *Compact white-light lasers and their biomedical applications*
P. Leproux, V. Couderc, G. Huss, V. Tombelaine
CDAMOP, New Delhi, India, Session 6, paper L12, 2011

[CI_11] *The promise of compact supercontinuum for biomedicine*
P. Leproux, V. Couderc, C. Lefort
Strategies in Biophotonics, Boston, USA, 2014

[CI_12] *Compact supercontinuum sources for biomedical applications*
P. Leproux, V. Couderc, C. Lefort
SPIE BiOS, San Francisco, CA, USA, paper PW15B-BO206-41, 2015

[CI_13] *CARS molecular fingerprinting using a sub-nanosecond supercontinuum light source*
H. Kano, T. Akiyama, A. Inoko, T. Kobayashi, **P. Leproux**, V. Couderc, Y. Kaji, T. Oshika
SPIE BiOS, San Francisco, CA, USA, paper 10498-59, 2018

[CI_14] *CARS microscopy under supercontinuum illumination and electric field stimulation*
P. Leproux, H. Kano
SciX Conference (FACSS), Atlanta, GA, USA, Session 18RAM09, paper 505, 2018

[CI_15] *Impact of periodic self-imaging on the nonlinear propagation in GRIN multimode fibers*
T. Mansuryan, K. Krupa, A. Niang, E. Deliancourt, A. Tonello, **P. Leproux**, M. Fabert, J. L. Auguste, A. Desfarges-Berthelemot, V. Kermene, A. Barthelemy, U. Minoni, D. Modotto, G. Millot, S. Wabnitz, V. Couderc
PIERS, Rome, Italy, Session 3A9, 2019

[CI_16] *Recent advances in cell and tissue imaging by multiplex CARS microspectroscopy*
P. Leproux, D. Boildieu, Z. Rajaofara, D. Helbert, A. Magnaudeix, E. Champion, P. Carré, H. Kano
International conference on Laser Applications in Life Science (LALS), Nancy, France, Session 4, paper 6, 2022

[CI_17] *Multiplex CARS microspectroscopy: advances in instrumentation, data analysis and applications*
P. Leproux
International Conference on Advanced Applied Raman Spectroscopy (RamanFest), Paris, France, 2023

Annexe 2 : liste des actes de congrès

[AC_1] *Theoretical and experimental study of light propagation into novel fibers designed for the management of the chromatic dispersion*
J. Marcou, D. Pagnoux, F. Brechet, **P. Leproux**, P. Roy, A. Peyrilloux
Photonics (SPIE), Calcutta, India, 2000

[AC_2] *Numerical simulations on spatial filtering efficiency with optical fibers and integrated optics components*
P. Leproux, V. Weber, I. Schanen-Duport, P. Haguenauer, V. Doya, F. Reynaud, P. Benech, J.-E. Broquin, P. Kern
Interferometry for Optical Astronomy II (SPIE), Hawaï, USA, 2002

[AC_3] *Microstructured fibers for sensing applications*
D. Pagnoux, S. Février, **P. Leproux**, M. C. Phan Huy, A. Pryamikov, P. Viale, V. Tombelaine, V. Couderc, P. Roy, J. L. Auguste, J. M. Blondy, G. Laffont, V. Dewinter-Marty, P. Ferdinand, B. Dussardier, W. Blanc
International Conference on Optical Fibre Sensors (SPIE), Bruges, Belgium, paper WS1-2 (workshop), 2005

[AC_4] *Finite-element analysis of properties in real and idealized Photonic Crystal Fibres, application to supercontinuum generation*
F. Gérôme, P. Viale, V. Tombelaine, **P. Leproux**, J. L. Auguste, S. Février, J. M. Blondy, V. Couderc
Femlab Conference, Paris, France, 2005

[AC_5] *Real-time optical coherence spectro-tomography: proof of principle*
L. Froehly, G. Petitjean, M. Ouadour, P. Sandoz, T. Gharbi, **P. Leproux**, G. Huss, V. Couderc
Photonics Europe (SPIE), Strasbourg, France, 2006

[AC_6] *Near-UV supercontinua generated in photonic crystal fibers for femtosecond spectroscopy*
J. Léonard, N. Lecong, J.-P. Likforman, O.Crégut, **P. Leproux**, V. Couderc, S. Haacke
Photonics Europe (SPIE), Strasbourg, France, 2006

[AC_7] *Original holey fibres and nonlinear schemes for supercontinuum generation*
P. Leproux, V. Couderc, P. Roy, C. Lesvigne, A. Roy, V. Tombelaine, J. L. Auguste, J. M. Blondy
Optics and Optoelectronics (SPIE), Prague, Czech Republic, paper 6588-06 (invited), 2007

[AC_8] *Supercontinuum generation in a highly birefringent photonic crystal fibre seeded by a low-repetition rate picosecond infrared laser*
P. Blandin, F. Druon, M. Hanna, P. Georges, S. Lévêque-Fort, C. Lesvigne, V. Couderc, **P. Leproux**
Optics and Optoelectronics (SPIE), Prague, Czech Republic, paper 6588-07, 2007

[AC_9] *Methods for visible supercontinuum generation in doped/undoped holey fibres*
P. Leproux, C. Buy-Lesvigne, V. Tombelaine, V. Couderc, J. L. Auguste, J. M. Blondy, G. Mélin, K. Schuster, J. Kobelke, H. Bartelt
Photonics Europe (SPIE), Strasbourg, France, paper 6990-6, 2008

[AC_10] *Second harmonic generation in Ge-doped silica holey fibres and supercontinuum generation*
V. Tombelaine, C. Buy-Lesvigne, V. Couderc, **P. Leproux**, G. Mélin, K. Schuster, J. Kobelke, H. Bartelt
Photonics Europe (SPIE), Strasbourg, France, paper 6990-22, 2008

[AC_11] *Recent developments in microstructured optical fibres and optical fibre glasses*
J. M. Blondy, F. Gérôme, J. L. Auguste, C. Restoin, G. Humbert, P. Roy, **P. Leproux**, S. Février
Optical Fibre Sensors, Perth, Australia, invited paper, 2008

[AC_12] *Microstructured fibers with high lanthanum oxide glass core for nonlinear applications*
J. Kobelke, K. Schuster, D. Litzkendorf, A. Schwuchow, J. Kirchhof, H. Bartelt, V. Tombelaine, **P. Leproux**, V. Couderc, A. Labruyère
Optics + Optoelectronics (SPIE), Prague, Czech Republic, paper 7357-1 (invited), 2009

[AC_13] *Adjustable supercontinuum laser source with low coherence length and low timing jitter*
M. Andreana, A. Bertrand, Y. Hernandez, **P. Leproux**, V. Couderc, S. Hilaire, G. Huss, D. Giannone, A. Tonello, A. Labruyère, N. Rongeat, P. Nérin
Photonics Europe (SPIE), Brussels, Belgium, paper 7714-1, 2010

[AC_14] *A novel electro-optical pump-probe system for bioelectromagnetic investigations*
A. De Angelis, V. Couderc, **P. Leproux**, A. Labruyère, A. Tonello, S. El Amari, D. Arnaud-Cormos, P. Leveque
SPIE Proceedings Volume 8487, Novel Optical Systems Design and Optimization XV; 84870M, 2012

[AC_15] *Imaging microfractures and other abnormalities of bone using a supercontinuum laser source with wavelengths in the four NIR optical windows*
L. A. Sordillo, P. P. Sordillo M.D., Y. Budansky, **P. Leproux**, R. R. Alfano
SPIE Proceedings Volume 9303, Photonic Therapeutics and Diagnostics XI; 93033Y, 2015

[AC_16] *Imaging of tissue using a NIR supercontinuum laser light source with wavelengths in the second and third NIR optical windows*
L. A. Sordillo, L. Lindwasser, Y. Budansky, **P. Leproux**, R. R. Alfano
SPIE Proceedings Volume 9319, Optical Tomography and Spectroscopy of Tissue XI; 93191Y, 2015

[AC_17] *All-normal dispersion supercontinuum generation in the near-infrared by Raman conversion in standard optical fiber*
C. Louot, E. Capitaine, B. M. Shalaby, K. Krupa, A. Tonello, D. Pagnoux, C. Lefort, **P. Leproux**, V. Couderc
SPIE Proceedings Volume 9731, Nonlinear Frequency Generation and Conversion: Materials, Devices, and Applications XV; 97310M, 2016

[AC_18] *Nanosecond coherent anti-Stokes Raman scattering for particle size characterization*
F. El Bassri, C. Lefort, E. Capitaine, C. Louot, D. Pagnoux, V. Couderc, **P. Leproux**
SPIE Proceedings Volume 9703, Optical Biopsy XIV: Toward Real-Time Spectroscopic Imaging and Diagnosis; 970314, 2016

[AC_19] *Multiphoton imaging with a nanosecond supercontinuum source*
C. Lefort, R. P. O'Connor, V. Blanquet, F. Baraige, V. Tombelaine, P. Lévêque, V. Couderc, **P. Leproux**
SPIE Proceedings Volume 9712, Multiphoton Microscopy in the Biomedical Sciences XVI; 97121D, 2016

[AC_20] *M-CARS and EFISHG study of the influence of a static electric field on a non-polar molecule*
E. Capitaine, C. Louot, N. Ould-Moussa, C. Lefort, J. F. Kaneyasu, H. Kano, D. Pagnoux, V. Couderc, **P. Leproux**
SPIE Proceedings Volume 9712, Multiphoton Microscopy in the Biomedical Sciences XVI; 97120M, 2016

[AC_21] *Label-free imaging of acanthamoeba using multimodal nonlinear optical microscopy*
T. Kobayashi, Y. Cha, Y. Kaji, T. Oshika, **P. Leproux**, V. Couderc, H. Kano
SPIE Proceedings Volume 10498, Multiphoton Microscopy in the Biomedical Sciences XVIII; 104982J, 2018

[AC_22] *CARS molecular fingerprinting using a sub-nanosecond supercontinuum light source*
H. Kano, T. Akiyama, A. Inoko, T. Kobayashi, **P. Leproux**, V. Couderc, Y. Kaji, T. Oshika
SPIE Proceedings Volume 10498, Multiphoton Microscopy in the Biomedical Sciences XVIII; 104981P, 2018

[AC_23] *Generation of kilovolt, picosecond electric pulses by coherent combining in optoelectronic system*
S. Wehbi, F. El Bassri, D. Pagnoux, **P. Leproux**, D. Arnaud-Cormos, P. Leveque, A. Bertrand, V. Couderc
SPIE Proceedings Volume 11279, Terahertz, RF, Millimeter, and Submillimeter-Wave Technology and Applications XIII; 112791V, 2020

[AC_24] *Versatile supercontinuum generation by using χ(2) and χ(3) nonlinearities in PPLN crystal for direct multiplex CARS measurement*
S. Wehbi, T. Mansuryan, R. Jauberteau, A. Tonello, K. Krupa, S. Wabnitz, H. Kano, **P. Leproux**, S. Vergnole, V. Couderc
SPIE Proceedings Volume 11770, Nonlinear Optics and Applications XII; 1177017, 2021

[AC_25] *Toward whole brain label-free molecular imaging with single-cell resolution using ultra-broadband multiplex CARS microspectroscopy*
Y. Murakami, S. Miyazaki, D. Boildieu, Z. Rajaofara, D. Helbert, A. Magnaudeix, P. Carré, **P. Leproux**, S. Honjoh, H. Kano
SPIE Proceedings Volume PC11973, Advanced Chemical Microscopy for Life Science and Translational Medicine 2022; PC119731B, 2022

[AC_26] *Multiplex CARS microspectroscopy in the "long-pulse" regime: where are we now?*
H. Kano, **P. Leproux**
SPIE Proceedings Volume 11973, Advanced Chemical Microscopy for Life Science and Translational Medicine 2022; 1197306, 2022

[AC_27] *Modal analysis and experimental study of multimode graded-index microstructured fibres for highly efficient supercontinuum generation*
F. Shabana M.A., V. Tombelaine, G. Huss, A. N. Ghosh, T. Sylvestre, J. L. Auguste, F. Reynaud, **P. Leproux**
SPIE Proceedings Volume 12140, Micro-Structured and Specialty Optical Fibres VII; 1214003, 2022

Annexe 3 : bilan de la production scientifique

Articles	Communications internationales	Actes de congrès internationaux	Communications nationales	Brevets
Partie 1 - Architectures de sources supercontinuum à fibre microstructurée				
27	44 dont 7 invitées	11	20 dont 2 invitées	11
Partie 2 - Développement de sources supercontinuum dédiées à des applications biomédicales				
41	28 dont 6 invitées	6	6	2
Partie 3 - Microspectroscopie non linéaire multimodale sous excitation supercontinuum				
9	18 dont 4 invitées	8	4	1
Autres				
10	12	2	13 dont 1 invitée	0
TOTAL				
87	102 dont 17 invitées	27	43 dont 3 invitées	14

Annexe 4 : bilan des contrats de recherche

Titre	Type	Période	Rôle	Nombre de partenaires	Coût total	Financement XLIM
Partie 1 - Architectures de sources supercontinuum à fibre microstructurée						
Fibres Optiques à cristaux photoniques Nano Optimisées pour Télécommunications Et Applications Médicales (FONOTEAM)	Projet ANR PNANO	2005-2008	Simple participation	5		
SUPERcontinuum généré par fibre optique à cristal photonique pour l'accès multiple à répartition par CODE (SUPERCODE)	Projet ANR BLANC	2006-2009	Simple participation	4		
Développement d'un prototype de source laser polychromatique utilisant une fibre optique à cœur structuré (GeStruct)	Projet AVRUL-DIRECCTE Détection Innovation Laboratoires (DIL)	2011-2013	Porteur	3	70 k€	35 k€
SUPercontinuum broadband light sources covering UV to IR applications (SUPUVIR)	Projet MSCA-ITN du programme H2020	2016-2020	Partenaire (par l'inter-médiaire de LEUKOS)	10	4 M€	263 k€
Partie 2 - Développement de sources supercontinuum dédiées à des applications biomédicales						
Next Generation Photonic Crystal Fibres (NextGenPCF)	Projet intégré (IP) du programme FP6-IST	2006-2010	Partenaire et coordinateur du WP3 (10 partenaires)	20	12,2 M€	350 k€
Development of CARS micro-spectroscopy using compact sub-nanosecond supercontinuum	Projet bilatéral CNRS/JSPS	2008-2009	Responsable équipe française	2	N/A	20 k€
Développement d'un prototype de microscope CARS (SensiCARS)	Projet AVRUL-OSEO Détection Innovation Laboratoires (DIL)	2010-2012	Porteur	3	285 k€	50 k€
Development of novel molecular imaging method for visualization of	Partenariat Hubert Curien (PHC) SAKURA	2012-2013	Responsable équipe française	2	N/A	12 k€

functions of intravital lipids						
Study of chiral molecular fingerprint using an intense white light laser source in visible	Projet bilatéral CNRS/JSPS	2014-2015	Responsable équipe française	2	N/A	20 k€
Partie 3 - Microspectroscopie non linéaire multimodale sous excitation supercontinuum						
Nouveaux procédés de spectroscopie Raman pour l'analyse d'agents biologiques (NEOSPRAM)	Projet ASTRID (financement DGA, gestion ANR)	2014-2018	Coordinateur	2	856 k€	241 k€
Étude de nouveaux procédés de spectroscopie Raman : application à la cytométrie en flux	Bourse de thèse DGA	2014-2017	Responsable scientifique	N/A	N/A	120 k€
Towards coherent Raman endomicroscopy for brain tissue imaging (ENDOCRAM)	Projet international de coopération scientifique (PICS) CNRS	2015-2017	Responsable scientifique	2	N/A	21 k€
Nouveaux matériaux pour les sources laser supercontinuum appliquées à la bio-imagerie (NEMATUUM)	Projet Région NA (AAP ESR)	2017-2021	Coordinateur	6	618 k€	312 k€ (+ 49 k€ Labex)
Microscope pour l'Imagerie Multimodale (µMu)	Projet Région NA (R&D portée par des entreprises)	2020-2024	Partenaire et responsable scientifique « Imagerie multimodale »	3	973 k€	115 k€
Biomatériau hybride céramique-cellules humaines, élaboré par fabrication additive et bioimpression 3D couplées, pour des applications en chirurgie réparatrice osseuse (BELENOS)	Projet Région NA (AAP ESR)	2022-2025	Partenaire	4	174 k€	87 k€ (+ 87 k€ Labex)
Dynamique des microplastiques dans l'environnement par µspectroscopie CARS (DYNAPLAST)	Projet MITI CNRS (Programme Interne Blanc)	2022-2023	Porteur	3	N/A	32 k€
Development of functional molecular imaging method by coherent Raman spectroscopy using	Partenariat Hubert Curien (PHC) SAKURA	2023-2024	Responsable équipe française	2	N/A	12 k€

a white-light laser source						
Méthodes d'apprentissage profond pour l'analyse de données CARS hyperspectrales massives - Application à la bioimagerie (Deep'nCars)	Projet Région NA (AAP ESR)	2023-2026	Coordinateur	3	117 k€	58,5 k€ (+ 58,5 k€ MESR)
TOTAL						**1 943 k€**

Annexe 5 : activités d'enseignement

Depuis 2001, j'interviens essentiellement dans deux filières de la Faculté des Sciences et Techniques de Limoges :

- **en Physique** et plus particulièrement en optique, optoélectronique, électromagnétisme, traitement du signal, outils mathématiques pour la physique, CAO ;
- **en Technologies de l'Information et de la Communication (TIC)** et plus particulièrement en langages du web, bases de données, imagerie numérique et animation, communication par l'image, etc.

Depuis septembre 2008, date à laquelle j'ai pris la direction du département TIC de la Faculté des Sciences et Techniques, j'assure une grande partie de mes enseignements en TIC sur le « Campus Virtuel », une structure déployant depuis 1998 des formations à distance aux métiers du numérique et à destination des étudiants francophones, pouvant être localisés en France ou à l'étranger. Depuis 2021, je suis coresponsable du DEUST Webmaster et Métiers de l'Internet (DEUST WMI) et des années 1 et 2 de la licence professionnelle Métiers de l'Informatique - Applications Web (LP MI AW) (ces deux formations étant mutualisées à 50 %).

Liste détaillée des enseignements :

Année	Niveau	Diplôme	Intitulé	Type de formation	Nature	Effectifs	Volume horaire annuel
2002-2006	L3	Licence Sciences Physiques	Ondes et vibrations	FI - présentiel	TP	~ 25	24 h
2002-2005	L3	Licence EEA	Electromagnétisme	FI - présentiel	TD	~ 35	12 h
2003-2006	L3	Licence EEA	Optique	FI - présentiel	TD	~ 35	12 h
2005-2007	L3	Licence EEA	Mathématiques	FI - présentiel	TD	~ 35	12 h
2001-2007	L3	Licence EEA	Traitement du Signal	FI - présentiel	TP	~ 35	36 h
2001-2007	L3	Licence EEA	CAO Matlab Simulink	FI - présentiel	TP	~ 35	24 h
2002-2004	M1	Maîtrise EEA	Optoélectronique	FI - présentiel	Cours	~ 40	9 h
2002-2004	M1	Maîtrise EEA	Optoélectronique	FI - présentiel	TD	~ 40	24 h
2002-2006	M1	Maîtrise EEA	Travaux d'étude et de recherche	FI - présentiel	Encadrement	2/3	-
2004-2007	M1	Master EEA	Optoélectronique	FI - présentiel	Cours	~ 40	6 h
2004-2007	M1	Master EEA	Optoélectronique	FI - présentiel	TD	~ 40	8 h
2008-2009	M2	Master THEO	Nonlinear optics in PCF	FI - présentiel	Cours	~ 30	5,5 h

2002-	L1	DEUST WMI / LP MI AW	XML	FI/FC - distanciel	Cours/TD	~ 50	60 h
2002-2013	L1	DEUST WMI	Imagerie numérique	FI/FC - distanciel	Cours/TD	~ 50	60 h
2004-2018	L2	DEUST WMI	Techniques de communication par l'image	FI/FC - distanciel	Cours/TD	~ 25	27 h
2008-	L2	DEUST WMI / LP MI AW	Réalisation professionnelle	FI/FC - distanciel	Suivi de stages	~ 5	10 h
2013-	L2	DEUST WMI / LP MI AW	Contenus animés et interactifs	FI/FC - distanciel	Cours/TD	~ 15	27 h
2018-	L2	DEUST WMI / LP MI AW	Intégration multimédia	FI/FC - distanciel	Cours/TD	~ 15	54 h
2009-2016	L3	DU puis Licence Pro. iFOAD	Langages du Web	FI/FC - distanciel	Cours/TD	~ 15	30 h
2015-	M1	Master ARTICC	Fonctionnalités d'internet - Outils de travail collaboratif	FI/FC - distanciel	Cours/TD	~ 40	30 h
2021-	L1	DEUST WMI / LP MI AW	Bases de données	FI/FC - distanciel	Cours/TD	61	54 h
2021-	M2	Master EUR	Bio-engineering (Bioimaging)	FI - présentiel	Cours/TP	6	6 h
2022-	L2	DEUST WMI / LP MI AW	Tutorat	FI/FC - distanciel	Suivi d'étudiants en apprentissage	2	20 h
2022-	M2	Master EUR	Optical Nonlinearity and Materials (Introduction to nonlinear multimodal imaging)	FI - présentiel	Cours	6	1,5 h
2022-	M2	Master EUR	Design, fabrication and characterization of fiber-based laser systems	FI - présentiel	TP	4	3 h